Luminescent lanthanide-doped nano- and microparticles and hybrid materials towards biomedical applications

DISSERTATION

zur Erlangung des Grades eines Doktors
der Naturwissenschaften

vorgelegt von
M. Sc. Willis Collins Akeyo Muganda

eingereicht bei der Naturwissenschaftlich-Technischen Fakultät
der Universität Siegen
Siegen, 2024

Betreuer und erster Gutachter

Prof. Dr. Holger Schönherr

Universität Siegen

Zweiter Gutachter

Prof. Dr. Heiko Ihmels

Universität Siegen

Tag der mündlichen Prüfung

20.09.2024

“Children have a way of reminding us that the journey is more important than the destination” – Anonymous

Acknowledgement

First and foremost, I wish to express my heartfelt gratitude to Prof. Dr. Holger Schönherr for providing me with the invaluable opportunity to pursue my doctoral dreams in Chemistry. Overcoming significant challenges in the initial two years of my research, Prof. Dr. Schönherr welcomed me into his research group, marking a turning point in my academic journey. This support enabled me to secure a scholarship from the “Begabtenförderung der Konrad Adenauer Stiftung” (KAS). My sincere thanks extend to Deutschland Stipendium, DAAD, “Aktionsgemeinschaft zur Förderung wissenschaftlicher Projekte” (AWiPro e.V.) and Konrad Adenauer Stiftung for their generous financial support throughout my tenure at the University of Siegen. I am deeply grateful to Prof. Dr. Heiko Ihmels, Prof. Dr. Martin Gröger, and Dr. Stephan Vogt for their timely recommendations that were crucial to my scholarship application.

Special thanks are due to my former colleagues in the Inorganic Chemistry department at the University of Siegen. Prof. Dr. Claudia Wickleder, Dr. Matthias Adlung, and Jun.-Prof. Dr. Markus Suta (Heinrich-Heine-Universität Dusseldorf) provided invaluable assistance in mastering luminescence measurements, spectra interpretation, and solid-state synthesis. Additionally, I wish to extend my appreciation to the Micro- and Nanoanalytics Facility (MNaF) of the University of Siegen for direct access to Transmission Electron Microscope (TEM), Scanning Transmission Electron Microscope (STEM), Field Emission Scanning Electron Microscope (FESEM), Focused Ion Beam (FIB), Inductively Coupled Plasma Optical Emission Spectroscopy (ICP-OES), Powder X-ray Diffractometer (XRD), Dynamic Light Scattering (DLS) equipment, Fluorescence Lifetime Imaging Microscope (FLIM) and X-ray Photoelectron Spectroscope (XPS). Moreover, thanks to Kawaljit Kaur and Alexander Kleimann carrying out the XPS and Thermo-Gravimetric Analysis (TGA) measurements, respectively.

I would also like to thank my colleagues from Macromolecular Chemistry (Prof. Dr. Ulrich Jonas and Dipl. Laborchem Petra Frank) for granting me access to use the Microwave synthesis equipment, Rheometer and Fourier Transform Infra-red Spectroscope (FTIR). Many thanks also to Dr. Sergey Druzhinin, Dr. Daniel Wesner and Dr. Dipankar Das for enriching offline discussions, Dr. Mareike Müller and

Dipl. -Biol. Sabine Wenderhold-Reeb for their training on how to work in the S1 and S2 labs and insightful discussions. Dr. Mohammad Raoufi for inviting me to contribute to two review papers on nanomedicine, the former Chemistry Department and PC 1 secretaries Marie Luise Kleinschmidt, Rose-Marie Neidhardt, Melanie Dreute-Rüppel, and current secretaries Christine Zizka and Sandra Johnson for their assistance with bureaucratic paperwork. Dipl.-Ing. Gregor Schulte for his tremendous support and technical equipment maintenance, Bernd Meyer and Markus Rabe for designing some inhouse apparatus and cables that were used in some experiments reported in this Thesis, Dr. Lars Birlenbach and Alessa Schneider for ensuring lab safety, and all other PC1 members who contributed to making my lab experience memorable.

I extend my thanks to all the students who collaborated with me, especially Joshua Schumacher and Jonah Leon Decker for their contributions to this thesis and their friendship. Work challenges are lighter when colleagues support each other and share enjoyable moments after work. It has been a pleasure working with you all in the lab! Thanks also to former colleagues who indirectly contributed to my academic journey: Dr. Inga Lilge, Dr. Nowsheen Goonoo, Dr. Benedikt Steinhoff, Dr. Qimeng Song, Dr. Zhiyuan Jia, Dr. Hongsuh Choi, Dr. Anna Schulte, Dr. Abir Goswami, Jakob Derksen and Nicola Cusick. Special thanks to the personnel in the Dean’s office of Faculty IV, Dr. Bernd Klose and Annette Zaiane, for facilitating my documentation, inviting me to contribute to MINToringSi, and their mutual support. I am also deeply grateful for the guidance and support from Dr. Johannes Gold, Stefan Johann Schatz, Anja Wessel, and Heidrun Rühle from the KAS team.

Finally, I wish to express my profound gratitude to my family: Eva, daughter Zury, my mother Edith, and my brothers and sisters Wycliffe, Wendy, Wevyn, and Wilkens. Also, my in-laws Barbara and Slawomir Sobolewski and Adam Sobolewski for their unwavering support. Special thanks to dear friends: the family of Rolf and Annette Hackler, Dr. Matthias Hackler, Tim Hackler, the family of Prof. Dr. Dr. med. Kai Zacharowski and Dr. Paula Zacharowski, the late Dr. Wolfgang Böttger and Christine Böttger, Andreas Böttger, Dr. Wolfgang Huebinger, Dr. Kevin Volkmer, Joshua Bruch, Dr. med. Martin Hüttemann and Margret Hüttemann, Steve and Ratka Hoferick, and many others whom I may not have mentioned. Lastly, my thanks to Prof. Dr. Holger Schönherr, Prof. Dr. Heiko Ihmels, Prof. Dr.-Ing. Manuela S. Killian

and Prof. Dr. Toby Jenkins, for reviewing this Thesis and participating in my PhD defense commission, and to Prof. Dr. Jürgen Schnekenburger and Dr. Björn Kemper from the Biomedical Technology Center, University of Münster, Germany, for their successful cooperation leading to the patenting of part of the results published in this thesis.

This PhD thesis is dedicated to three men who have directly and positively influenced my life, shaping me into the person I am today.

Patrick Rens Muganda

Dr. Wolfgang Böttger

Prof. Dr. Holger Schönherr

Table of contents

List of abbreviations and acronyms

2D	2 dimensional
3D	3 dimensional
µg	microgram
µL	microliter
µm	micrometer
µs	microsecond
% wt /vol	Percent weight by volume
λ	Wavelength
AFM	Atomic force microscopy
ARGET	Activators regenerated by electron transfer
ATRP	Atom transfer radical polymerization
Au-NP	Gold nanoparticle
Bacillol AF	Aldehyde- and Fragrance-free fast-acting disinfectant
BMIM[BF_4]	1-butyl-3-methylimidazolium tetrafluoroborate
BMIM[Br]	1-butyl-3-methylimidazolium bromide
BMIM[Cl]	1-butyl-3-methylimidazolium chloride
α-CD	Alpha cyclodextrin
cif	Crystallographic information files
c.f	Confer
CFU	Colony forming unit
cm^{-1}	Wavenumber
CSNPs	Core-shell nanoparticles
Cu Kα	Copper K alpha radiation

DHM	Digital Holography Microscope
DLS	Dynamic light scattering
DMEM	Dulbecco's Modified Eagle's Medium
DMSO	Dimethyl sulfoxide
E. coli	*Escherichia* coli
EDX	Energy dispersive X-ray
EG	Ethylene glycol
E-gene	Envelope small membrane protein
em	Emission
ex	Excitation
FBS	Fetal Bovine Serum
FDA	Fluorescein diacetate
FIB	Focused ion beam microscopy
FLIM	Fluorescence life-time imaging
FESEM	Field emission secondary electron microscope
FTIR-ATR	Fourier transform infrared – attenuated total reflectance
G’	Storage modulus
G”	Loss modulus
HAADF	High-angle annular dark field
h	Hour(s)
ICSD	Inorganic crystal structure database
ICP-OES	Inductively coupled plasma optical emission spectrometry
ILs	Ionic liquids
IP	Imaging plate

IR	Infrared
IRF	Instrument response function
keV	Kilo-electron volts
kV	Kilo-volts
LB	Lysogeny broth
LT	Low temperature
M	Molar concentration
MACH 1	Phage-Resistant Chemically Competent *E*. coli
mg/mL	Milligram per millilitre
min	Minutes
M-L	Metal-ligand
Mmol	Milli moles
MPs	Microparticles
MRI	Magnetic resonance imaging
MTT	3-(4,5-dimethylthiazol-2-yl)-2,5-diphenyltetrazolium bromide
MUBiB	ω-Mercaptoundecyl bromoisobutyrate
ms	millisecond
NCs	Nanocrystals
NIBS	Non-invasive back scatter
NIPAAm/AAm	*N*-isopropylacrylamide/acrylamide
nm	Nanometer
NPs	Nanoparticles
ns	Nanosecond
OD	Optical density

ONC	Overnight culture
ORF1ab	Open reading frames ab
Pa	Pascal
PAA	Poly(acrylic acid)
PAAm	Polyacrylamide
PBS	Phosphate-Buffered Saline (pH ~ 7.4)
PCS	Photon correlation spectroscopy
PDEGMA	Poly(di(ethylene glycol) methyl ether methacrylate
PEG	Polyethylene glycol
PMT	Photomultiplier tube
PNIPAm	Poly(*N*-isopropylacrylamide)
pH	Potential of hydrogen
PI	Propidium iodide
PS	Polystyrene
PVP	Polyvinylpyrrolidone
QD	Quantum dots
RF	Radio frequency
rad s^{-1}	Radians per second
RdRp	RNA-dependent RNA polymerase
REX_3	Rare earth trihalide
rt	Room temperature
RTILs	Room temperature ionic liquids
S1	Bio-Laboratory safety level 1
S2	Bio-Laboratory safety level 2

SARS-CoV-2	Severe acute respiratory syndrome coronavirus 2
SE	Secondary electron
SEM	Secondary electron microscope
SDS	Sodium dodecyl sulphate
STEM	Scanning transmission electron microscope
t	Time
TCPS	Tissue Culture Polystyrene
TCSPC	Time correlated single photon counting
TEM	Transmission electron microscope
QPI	Quantitative Phase Imaging
v.	Version
W	Watts
XRD	X-ray diffraction analysis
ZS	Zetasizer

Abstract

Luminescent lanthanide materials are of great interest not only for biomedical applications due to their tuneable emission wavelengths that extend from the ultra-violet region into the near-infrared region. These materials are known to be non-toxic and resistant to photobleaching unlike traditional organic dyes. In this Thesis, the focus was laid on the synthesis of nanoscale and microscale fluoride containing luminescent lanthanide materials, such as (LaF_3:$Ce^{3+}Tb^{3+}$, TiO_2@SiO_2@LaF_3:$Ce^{3+}Tb^{3+}$, and $KSmF_4$:Ln^{3+} (Ln = Ce, Tb, Eu), which promise unique optical properties, as fluoride containing lanthanide materials are recognized for their strong luminescence and good optical stability due to their low phonon energies. To harness these properties for potential bioimaging applications, this Thesis thus focused on developing and optimizing synthetic routes for producing monodisperse lanthanide doped particles that bridge the length scales from the nano- (< 10 nm) to the microscale (> 1 µm). Furthermore, to enhance their scope by exploiting their surface features, these particles were incorporated into hydrogels and were modified with polymer brushes. The results confirm the successful synthesis of monodisperse particles with sizes ranging from < 10 nm to 15 µm with intense red and green luminescence due to Eu^{3+} and Tb^{3+} ions. Among the particles studied, the (LaF_3:$Ce^{3+}Tb^{3+}$) nanoparticles were investigated in cell toxicity tests, while the MgF_2 microbeads were tailor made for application in digital holography microscopy. The toxicity tests indicated that the NPs are non-toxic at concentrations below 0.0023 mg/mL in cell medium. These NPs were also incorporated into a biocompatible sodium alginate hydrogel matrix and the influence on the mechanical properties of the hydrogels was investigated. Rheological measurements revealed that nanoparticle inclusion significantly enhances the hydrogels' structural stability, supporting their potential use in drug delivery and bioimaging. The tomography phase microscopy results of spherical MgF_2 microparticles hinted at a very similar refractive index compared to human cells (1.360 ± 0.004). These particles were shown to provide the structural parameters required for precise calibration in digital holography, which enhances the accuracy and reliability of label-free live cell imaging. In addition, antibacterial tests with *E. coli* showed enhanced antibacterial activity compared to commercially purchased MgF_2. These results suggest that lanthanide-based particles can be further exploited in future biomedical applications.

Zusammenfassung

Lumineszierende Lanthanid-Materialien sind aufgrund ihrer einstellbaren Emissionswellenlängen, die von ultraviolettem Licht bis hin in den nahen Infrarotbereich reichen, auch für biomedizinische Anwendungen besonders interessant. Diese Materialien zeichnen sich durch ihre geringe Toxizität und hohe Photostabilität aus, was sie von traditionellen organischen Farbstoffen unterscheidet. In der vorliegenden Arbeit wurde der Fokus auf die Synthese von lumineszierenden Fluorid-haltigen Lanthanid-Verbindungen mit definierten nano- und mikroskaligen Dimensionen gelegt, wie beispielsweise LaF_3:$Ce^{3+}Tb^{3+}$, TiO_2@SiO_2@LaF_3:$Ce^{3+}Tb^{3+}$ und $KSmF_4$:Ln^{3+} (Ln = Ce, Tb, Eu). Diese Verbindungen sind bekannt für ihre starke Lumineszenz und hervorragende optische Stabilität, bedingt durch ihre niedrigen Phononenenergien. Um die vielversprechenden Eigenschaften dieser Materialien für Anwendungen im Bereich der Bioimaging-Technologien zukünftig nutzen zu können, wurde in dieser Arbeit die Entwicklung und Optimierung von Synthesemethoden zur Herstellung Lanthanid-dotierter Partikel mit definierter monomodaler Größenverteilung untersucht, und zwar mit Partikelgrößen von < 10 nm bis > 1 µm. Die so hergestellten Partikel wurden auch in Hydrogele integriert und mit Polymerbürsten modifiziert, um ihre Anwendungsbreite zu erhöhen. Die Ergebnisse zeigen, dass es gelungen ist, Partikel mit Größen von < 10 nm bis zu 15 µm mit engen monomodalen Größenverteilungen zu synthetisieren, die intensive rote und grüne Lumineszenz durch Eu^{3+}- und Tb^{3+}-Ionen aufweisen. Die (LaF_3:$Ce^{3+}Tb^{3+}$)-Nanopartikel wurden auf ihre Zelltoxizität hin untersucht, während die MgF_2-Mikroperlen speziell für Anwendungen in der digitalen Holographie-Mikroskopie entwickelt wurden. Die Toxizitätstests zeigten, dass die Nanopartikel bei Konzentrationen unter 0,0023 mg/mL im Zellmedium nicht toxisch sind. Weiterhin wurden diese Nanopartikel in eine biokompatible Natriumalginat-Hydrogelmatrix eingebettet, und deren Einfluss auf die mechanischen Eigenschaften der Hydrogele wurde untersucht. Rheologische Messungen zeigten, dass die Einbindung der Nanopartikel die strukturelle Stabilität der Hydrogele signifikant erhöht, was ihre potenzielle Verwendung in der Medikamentenfreisetzung und im Bioimaging unterstützt. Die Untersuchung der sphärischen MgF_2-Mikropartikel mittels Tomographie-Phasenmikroskopie ergab einen Brechungsindex, der dem von menschlichen Zellen sehr ähnlich ist (1,360 ± 0,004). Diese Partikel eignen sich

daher hervorragend für eine präzise Kalibrierung in der digitalen Holographie, wodurch die Genauigkeit und Zuverlässigkeit der markierungsfreien Echtzeit-Zell-Bildgebung verbessert wird. Zudem zeigten antibakterielle Tests mit *E. coli*, dass die antibakterielle Aktivität im Vergleich zu kommerziell erhältlichem MgF_2 verbessert ist. Insgesamt lassen diese Ergebnisse darauf schließen, dass Lanthanid-basierte Partikel in zukünftigen biomedizinischen Anwendungen vielversprechend eingesetzt werden können.

Chapter 1 Introduction

Lanthanides have recently reported to enable interesting applications in biomedicine and biotechnology.[1] Some applications include e.g. bioimaging,[2,3] biosensing,[4] bioprinting[5] and designing smart devices.[6–8] Probably the most interesting feature in these materials is the tuneable photoluminescence emission that can be altered by doping the host matrix with different lanthanide ions, energy transfer processes, or by modifying the host lattice matrix, enabling emission from ultraviolet, visible to the near infra-red region of the electromagnetic spectrum.[9] Apart from doping different materials with lanthanides, lanthanide NPs and lanthanide complexes have been extensively studied due to their unique optical properties, stability, and the ability to fine-tune their emission spectra.[1,10–14] Lately, researchers have shown that it is possible to dope hydrogels with luminescent nanomaterials such as lanthanide inorganic nanoparticles (NPs),[15,16] lanthanide based organic complexes,[17–21] quantum dots,[22–25] carbon nanotubes,[26] carbon dots,[24] fluorescent capsules[27] and embedded thin layers luminescent sheets.[28,29] Some applications of luminescent hydrogels reported in the literature include biosensors,[4,30–35] thermosensors,[36,37] optical switches,[29,38] pH sensors[28,39–41] and drug delivery.[42,43] In these applications, hydrogels serve as versatile platforms that provide a supportive, three-dimensional network capable of encapsulating and stabilizing the luminescent nanomaterials.[15] The role of the NPs in these hydrogels is to impart specific functionalities such as enhanced mechanical properties,[44] increased luminescence efficiency,[45] or targeted responsiveness to environmental stimuli,[46] thereby broadening the scope of potential applications.

Lanthanides as well as actinides exhibit interesting optical properties both in their trivalent and divalent states. This is due to the incompletely filled 4f electronic shells, which are shielded from crystal field splitting due to the high lying s, p and d orbitals.[47] The luminescence properties of divalent lanthanides have been studied extensively due to their peculiar parity-allowed 5d-4f transitions.[48–51] However, divalent lanthanides despite their attractive optical properties that could in principle enable interesting applications are highly unstable in water.[48] They readily oxidize to the trivalent states, hence limiting their application. Therefore, many researchers have focused on trivalent lanthanides for hydrogel systems in biomedical

applications.[31,39,52] Furthermore, their unique features, such as high photochemical stability, narrow emission bands due to the 4f-f transitions, empty 5d levels, charge transfer and energy transfer from neighboring ions or ligands and low toxicity make them outstanding.[47,53,54]

The choice of lanthanide(s) needed as dopant(s) depends on the application of the hydrogel. Thus, to design an efficient system requires careful consideration on the required excitation or emission wavelength and life times. However, trivalent lanthanides are also known for their complicated spectra.[9] Dieke and Crosswhite et al., published a report in 1963 showing the calculations of the energy levels for Ln^{3+} ions doped in a low-symmetry crystal, LaF_3 with levels labelled by term symbols or, for some higher levels, capital letters. The energy level diagram provides useful insights for interpretation and prediction of the emission energies of the different trivalent lanthanides, which is important in tuning the luminescent properties. In the past, a lot of focus on the design and applications of trivalent lanthanides was on ceramics and NPs. However, there is little information that has been reported and understood about luminescent biopolymeric hydrogels prepared from Eu^{3+} or Tb^{3+} ions as crosslinkers. Thus, energy transfer,[55] upconversion and downconversion[56] luminescence systems are suddenly becoming interesting for future applications of trivalent lanthanides doped hydrogels.

For these applications, the choice of the host matrix is crucial. The use of fluoride is critical because it forms highly stable and low-phonon-energy matrices with lanthanides, enhancing their luminescent properties.[57,58] Fluoride based lanthanide NPs can be prepared using ionic liquids (ILs) and room temperature ionic liquids (RTILs).[59–63] ILs and RTILs are salts in nature below 100°C usually in liquid state or volatile solids at room temperature.[64] They are made up of asymmetric organic cations and inorganic or organic anions, but in liquid state preferably consist of single and short-lived ion pairs.[63] Furthermore, they have many advantages as choice of solvent for NP synthesis: negligible vapor pressure, high thermal stability and low melting point.[65] ILs and RTILs are a good substitute for synthesis that require HF or other F^- sources in combination with water. Thus, reducing the risks associated with the use or generation of HF during or after the synthesis.[66–68] The resulting NPs usually have high crystallinity and can be dispersed in both polar and non-polar solvents.[69]

Attempts to use ILs as solvent and also fluoride source to develop monodisperse NPs and MPs are still not well established. For example, Lunstroot et al., successfully prepared LaF_3 NPs doped with Eu^{3+} and Nd^{3+} via IL but could not control the particle size.[70] Bartůněk et al., reported agglomerates of LaF_3 using two different kind of IL i.e. 1-butyl-3-methylimidazolium hexafluorophosphate (BMIM[PF_6]) and 1-butyl-3-methylimidazolium chloride (BMIM[Cl]).[71] Most challenging is to systematically prepare monodisperse fluoride MPs . Xu and Zhu et al., have reported a method to prepare different alkaline earth fluorides (MgF_2, CaF_2 and SrF_2) using BMIM[BF_4].[72] However, their results indicated polydisperse MPs with a wide range of size distribution and impurity below 70 % of the final product.

In this Thesis, different fluoride NPs and MPs composed of lanthanides or doped with lanthanides [LaF_3:$Ce^{3+}Tb^{3+}$, XYF_4: Eu^{3+} (X=K, Rb, Cs und Y=Sm / Eu) NPs and MgF_2: X^{3+} (X= Eu, Tb)] have been synthesized. The aim was to create materials with enhanced luminescent properties for potential applications in bioimaging and biosensing. LaF_3 host lattice is beneficial because of the low vibrational energies thus reducing the possibilities of quenching excited states.[73] Zhou et al., synthesized for the first time LaF_3 NPs,[74] of which Stouwdam and van Veggel et al., improved the synthesis to dope with luminescent material and modify the NPs surface.[75] The resulting NPs were able to be dispersed in organic solvents, opening avenues for new biological applications. Liu et al., reported a simple method for preparing LaF_3:$Ce^{3+}Tb^{3+}$ and LaF_3:Tb^{3+} water-soluble nanoparticles that could potentially activate photodynamic therapy for deep cancer treatment.[75–77] Zhu et al., designed a sonochemical method using 1-butyl-3-methylimidazolium tetrafluoroborate ([BMIM][BF_4]) as IL to prepare highly luminescent LaF_3:Tb^{3+} NPs with controlled morphologies and sizes.[59] Microwave synthesis has also been previously used to prepare polyethyleneimine functionalized crystalline LaF_3:$Ce^{3+}Tb^{3+}$ NPs with mean size of 12 nm.[78] The preparation of XYF_4 host lattice has been reported to occur in the CaF_2- type in $KTlF_4$, KYF_4, $KTbF_4$ and $KErF_4$ as a bulk material.[79] Hence, increasing interest in the photoluminescence field in using such hosts especially as a nanomaterial.[80–84] Most common has been the application of $NaGdF_4$ as a host material for doping with lanthanides due to its stability, low vibrational energy and the ability to mediate energy exchanges between lanthanide dopants.[85]

Motivated by the current trend in designing luminescent NPs and biopolymers with different functionalities, the work reported in this Thesis is also aimed at developing a simple strategy combining photoluminescence and NP interaction with sodium alginate hydrogel to create a multifunctional material that can be used in various potential biomedical applications such as imaging, sensing, and cell proliferation. Furthermore, such hydrogels are cheap and require less preparation time.[86] The crosslinker, which is in the acetate form of Eu^{3+} also acts as an activator for red luminescence. Likewise, the NPs contribute to green luminescence and energy transfer from Tb^{3+} to Eu^{3+}. Moreover, these combined effects enhance the gel strength that aids attachment and proliferation of NIH 3T3 fibroblasts. Another aim was the unprecedented synthesis of monodisperse (3 nm - 5 nm) and highly crystalline $XYF_4:Eu^{3+}$ (X=K, Rb, Cs und Y=Sm / Eu) NPs that can be dispersed in polar solvents. Furthermore, the research extends to developing functionalized nanoassemblies for future biomedical applications.

Chapter 2 Motivation and objectives

For over two decades, nanomaterials have emerged as important ingredient for biomedical applications such as drug or gene delivery tools, photothermal therapy agents, photo sensitizers, biosensors, theranostic and antibacterial agents due to their unique characteristics.[87,88] In addition, it has been widely reported that NPs could induce non-apoptotic cell death in cancer cells by inducing cytotoxicity in cancer cells, which triggers different forms of programmed cell death.[89] This potential by NPs to trigger non-apoptotic cell death in cancer cells can also be explained by the possibility of co-administration of different cancer treatment methods.

These developments have led to efforts recently concentrated in modification of known existing NPs to offer a single system with wide range of applications. For example, core-shell NPs (CSNPs) were designed to incorporate photophysical properties in nanomaterials.[90] This is done by doping the core and shell with different dopants (possibly lanthanides or transition metals). The shell usually acts as a protective layer to prevent surface quenching. However, if the shell is optically active the absorption is improved as well as light to heat conversion is possible.[91] It is known in the literature that PEG and SiO_2 shells increase biocompatibility due to ease for further biofunctionalization for targeted response and in vivo experiments.[92] Most recently, the need for smart materials has motivated scientists to come up with multifunctional biomaterials.

Whitesides et al., reported in a review article how smart materials like soft robotics will revolutionize the future of medicine.[93] This is because of the countless biological functional soft structures that nature has to offer. Hydrogels are an example of interesting soft matter scaffold due to the structural similarity to extracellular matrix of various tissues.[94] Hence, making hydrogels the best choice for mimicking biological structures. Hydrogel properties can be modified depending on the desired application (drug delivery, tissue repair, bioimaging and biosensing). In most cases, organic dyes have been used to prepare fluorescent hydrogels, which are needed for applications requiring visual tracking, imaging, or sensing within biological systems. However, it is also known that these dyes suffer photobleaching[95] and are toxic at higher doses.[96] Currently, reports have shown that lanthanides offer alternatives to functionalize hydrogels, thus making them photoluminescent.[30,31,52,97,98]

To date, there exists a challenge however to develop stable and non-toxic biopolymeric photoluminescent hydrogels for biomedical applications.

The main objective of the research done and reported in this Thesis was to investigate the synthesis and properties of photoluminescent nanomaterials that can be potentially used for various biomedical applications. A particular focus was laid on lanthanide-doped NPs and MPs because of their unique tuneable optical properties, controllable particle size and size distribution.

In Chapter 4, the focus is on the synthesis, stabilization, and optical properties of lanthanide-doped luminescent NPs and CSNPs. The study involves synthesizing LaF_3:$Ce^{3+}Tb^{3+}$ NPs, TiO_2@SiO_2@LaF_3:$Ce^{3+}Tb^{3+}$ NPs, and $KSmF_4$:Ln^{3+} (Ln = Ce, Tb, and Eu) NPs, optimizing synthetic methods to achieve stable photoluminescence and controlled particle size, and enhancing structural and luminescent properties by functionalizing TiO_2 nanoparticles with LaF_3:$Ce^{3+}Tb^{3+}$ to create TiO_2@SiO_2@LaF_3:$Ce^{3+}Tb^{3+}$ CSNPs. The photoluminescence of synthesized NPs is investigated in both dry (powder) and liquid (NP solution) states, and their potential applications in bioimaging and sensing evaluated by characterizing their optical properties.

Building upon the foundational work in Chapter 4, Chapter 5 further focuses into the fabrication of hybrid sodium alginate hydrogel-lanthanide-doped luminescent NP materials for biomedical applications. This chapter integrates luminescent NPs into biocompatible hydrogels by incorporating LaF_3:$Ce^{3+}Tb^{3+}$ NPs into sodium alginate hydrogels crosslinked with trivalent lanthanide ions. The mechanical strength and optical properties of these hydrogels are enhanced for potential biomedical applications. Further, the biocompatibility and cytotoxicity is assessed through toxicity assays using various cell lines to ensure safe application in biological systems. The suitability of hydrogel-NP hybrids for drug delivery and bioimaging is also evaluated.

Transitioning from hydrogels to solid bead structures, Chapter 6 describes the synthesis of spherical micrometer-sized MgF_2 beads for digital holography via the self-assembly of nanowhiskers. This chapter focuses on the development of monodisperse micrometer-sized MgF_2 beads for use as calibration standards in digital holography, tailored for label-free quantitative in vitro live cell imaging.

Various synthesis methods, including microwave heating, solvothermal, and hydrothermal techniques, are investigated to optimize the desired bead size and properties.

Finally, Chapter 7 explores the functionalization of nanoassemblies for future biomedical applications, focusing on the enhancement of photoluminescent properties and biocompatibility. The photoluminescent properties of MgF_2 beads are enhanced by functionalizing them with Tb^{3+} and Eu^{3+} ions to impart distinctive green and red emissions, respectively. Biocompatibility and functionality are further improved by modifying MgF_2 beads with polymer brushes (PDEGMA-*block*-PAA) to enhance stability, responsiveness to environmental stimuli, and biocompatibility. Additionally, the antibacterial efficacy of MgF_2 nanowhiskers is evaluated against *Escherichia coli* to explore their potential as antibacterial agents.

Chapter 3 State of the art in luminescent lanthanide-doped nano- and microparticles and hybrid materials for biomedical applications

This Chapter highlights the past and recent advances in application of luminescent lanthanide doped NPs. Moreover, it aims to give an understanding of how lanthanide luminescence can be coupled to soft matter for biomedical applications. In addition to doping resulting in the desired optical properties, the design (size, shape etc.) of both NPs and MPs determine some important properties. These need to be understood if a desired bio-functionality is targeted. However, due to various intrinsic factors such as electronic structure, crystal field environment, and energy transfer processes, the choice of the host material is also critical in defining the photoluminescence of these particles.

3.1 Luminescence of trivalent lanthanides

The crystal structures of rare earth trihalides are known to change along the lanthanide series due to the so-called lanthanide contraction.[99] High coordination numbers occur in lighter lanthanides with small ligands like fluorides. Lanthanum and cerium trifluorides adopt the tysonite structure with 11-fold RE^{3+} coordination.[100] Energy flow in lanthanides is due to transitions from excited singlet states via intersystem crossing to triplet states and hence to the ground state of the lanthanide ion. Figure 3.1 shows a simplified illustration of the relevant energy levels of different trivalent lanthanides.[101] Eu and Tb exhibit potential strong red and green emission, respectively, which are thus attractive for biomedical labeling and imaging. Compared to currently used fluorophores, lanthanide-based emitters offer distinct advantages such as enhanced brightness and exceptional photostability.[58] Traditional organic dyes and fluorescent proteins often suffer from photobleaching, where their fluorescence diminishes upon prolonged exposure to light, and can exhibit lower quantum yields.[102] Lanthanide complexes, however, maintain their luminescence over longer periods and under intense illumination, making them highly suitable for long-term imaging applications.[103] The 4f→5d transitions in most trivalent lanthanides are too high in energy, especially in the UV or vacuum-UV region of the electromagnetic spectrum, to be applied in visible light promoted

photochemical reactions.[104,105] For the Ce^{3+}, the 4f→5d transition is lower than the other trivalent lanthanides. The emission can be tuned to shift to the visible region via coordination chemistry.[106] Understanding these transitions, whether they involve allowed f-d transitions or electronic rearrangements within the 4f shell (f-f transitions), is crucial for optimizing the photoluminescent properties of lanthanide-based materials. The allowed f-d transitions are more intense compared to f-f transitions and are generally observed in the UV/visible range.[107] However, the electric-dipole f-f transitions are forbidden by Laporte's selection rules.[106,107] This is not entirely the case for the magnetic-dipole f-f transitions. Thus, f-f transitions are sharp and undergo long life times in the excited states, which makes the trivalent lanthanides containing compounds unique since they do not easily undergo photobleaching.[103]

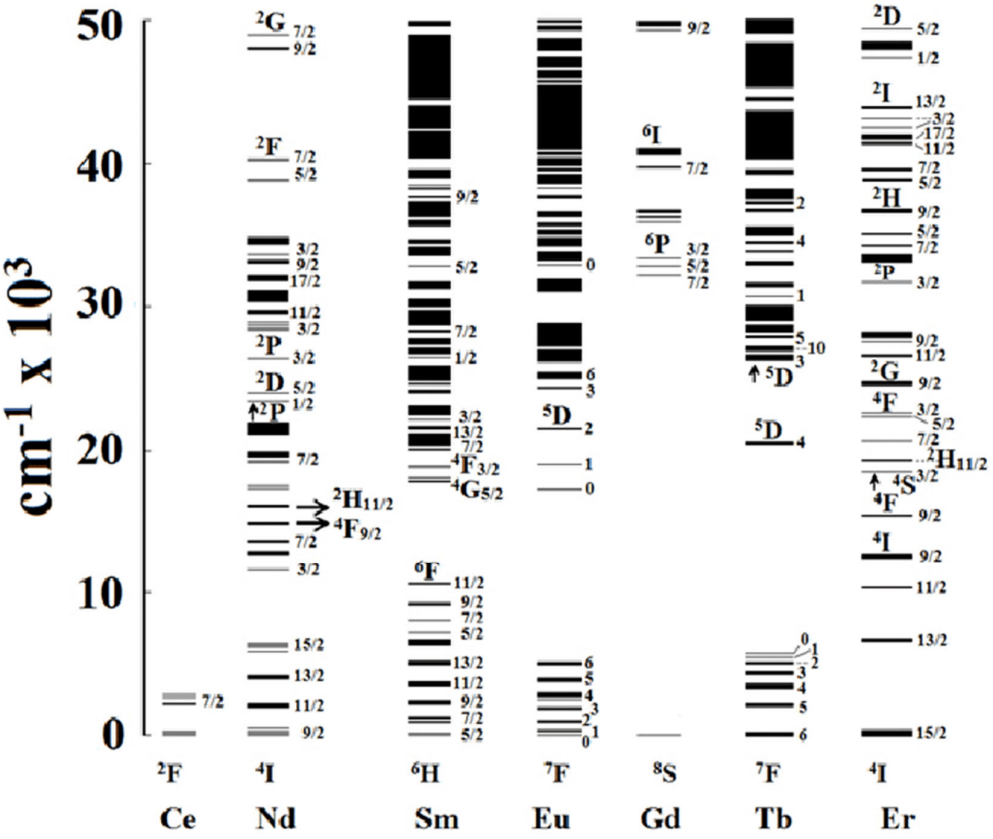

Figure 3.1: Energy level of the $4f^n$ configuration of luminescent trivalent lanthanide ions. This Figure is reproduced with permission from Quoc Minh Le, Q.; Phan, T. K.; Luu, T. Q.; Nguyen, V. T.; Tran, Q. A.; Trinh, Q. T.; Nguyen, D. M.; Pham, N. Q.; Pham, T. V.; Hoang, T. M. Development of a fluorescent label tool based on lanthanide nanophosphors for viral biomedical application. *Adv. Nat. Sci: Nanosci. Nanotechnol.*, **2012**, *3* (035003), 1–10. Copyright 2012 IOP Publishing.

The aforementioned features of trivalent lanthanide luminescence allow diverse applications in lighting, information technology, lasers, forensics, sensors and biomedical applications[108]. In this Thesis emphasis is made on understanding the luminescence properties of NPs and MPs in different environments and conditions. In recent years, NPs and MPs have been extensively developed and utilized in experimental research involving cellular and bacterial systems. The next section provides a detailed literature review on the state-of-the-art biomedical applications of these particles.

3.2 Biomedical applications of NPs doped with trivalent lanthanides

The use of trivalent lanthanides in NPs has led to significant advancements in biomedical fields. These lanthanide-doped NPs possess unique optical,[109] magnetic,[110] and redox properties,[111] making them versatile for imaging,[112] diagnostics,[113] and therapy.[114]

Ln^{3+}-doped NPs exhibit remarkable luminescent properties within the visible and near-infrared (NIR) regions of the electromagnetic spectrum. This luminescence arises from intra-configurational transitions within the 4f orbitals of the lanthanide ions, shielded by the 5s and 5p orbitals.[115] This shielding results in sharp emission lines and long luminescence lifetimes, making these NPs highly suitable for bioimaging applications.[109] For instance, Eu^{3+} and Tb^{3+} ions are known for their bright red and green emissions, respectively, which can be exploited in various imaging techniques to provide clear and distinguishable signals.[116] Figure 3.2 depicts different luminescence mechanism that can lead to downshifting, upconversion or quantum cutting.[117]

The high surface area to volume ratio of these NPs further enhances their functionality.[109] By modifying the surface chemistry of Ln^{3+}-doped NPs, it is possible to attach various targeting ligands, such as antibodies, peptides, or small molecules, to facilitate specific binding to biological targets.[118–120] This specificity is particularly beneficial in applications like targeted drug delivery and precision imaging, where distinguishing between healthy and diseased tissues is crucial.[121]

One of the significant applications of Ln^{3+}-doped NPs is their use as MRI contrast agents.[110] The paramagnetic nature of certain Ln^{3+}-doped NPs, particularly those doped with gadolinium (Gd^{3+}), makes them excellent candidates for use as MRI contrast agents.[110,122] Traditional gadolinium-based chelates can dissociate and release toxic Gd^{3+} ions, whereas Gd^{3+}-doped NPs provide a safer alternative due to their stable crystal structure, minimizing ion leakage.[123] The high concentration of paramagnetic ions within each NP enhances the MRI signal, offering superior contrast.[124] Moreover, these NPs can be engineered to exhibit dual-modal imaging capabilities by combining MRI with optical imaging, thus providing complementary information and improving diagnostic accuracy.[125]

Lanthanide-doped upconversion NPs (UCNPs), doped with lanthanides such as erbium (Er^{3+}), ytterbium (Yb^{3+}), and thulium (Tm^{3+}), have been explored as biomarkers.[126] UCNPs convert NIR light into visible light through a multi-photon process, reducing photobleaching and autofluorescence while allowing deeper tissue penetration, making them suitable for in vivo imaging applications.[127] These properties make UCNPs particularly suitable for applications requiring high sensitivity and specificity, such as early cancer detection and real-time tracking of cellular processes.[128] The ability to simultaneously visualize multiple targets using different emission wavelengths from various lanthanide ions can significantly enhance multiplexing capabilities in bioimaging.[112]

The redox behavior of Ln^{3+} NPs, particularly cerium oxide (CeO_2) NPs, has been utilized for their enzyme-mimicking properties.[111,129–133] CeO_2 NPs exhibit reversible redox cycling between Ce^{3+} and Ce^{4+}, enabling them to mimic natural enzymes such as superoxide dismutase (SOD) and catalase.[111] This antioxidant capability is beneficial for long-term treatments of diseases associated with oxidative damage, such as neurodegenerative and cardiovascular diseases.[134–137] The ability to scavenge reactive oxygen species (ROS) provides protective effects against oxidative stress, making CeO_2 NPs promising candidates for various therapeutic applications.[135] Additionally, the catalytic activity of these nanoparticles can be fine-tuned by controlling their size, shape, and surface properties, allowing for the design of more efficient and specific enzyme mimics.[136]

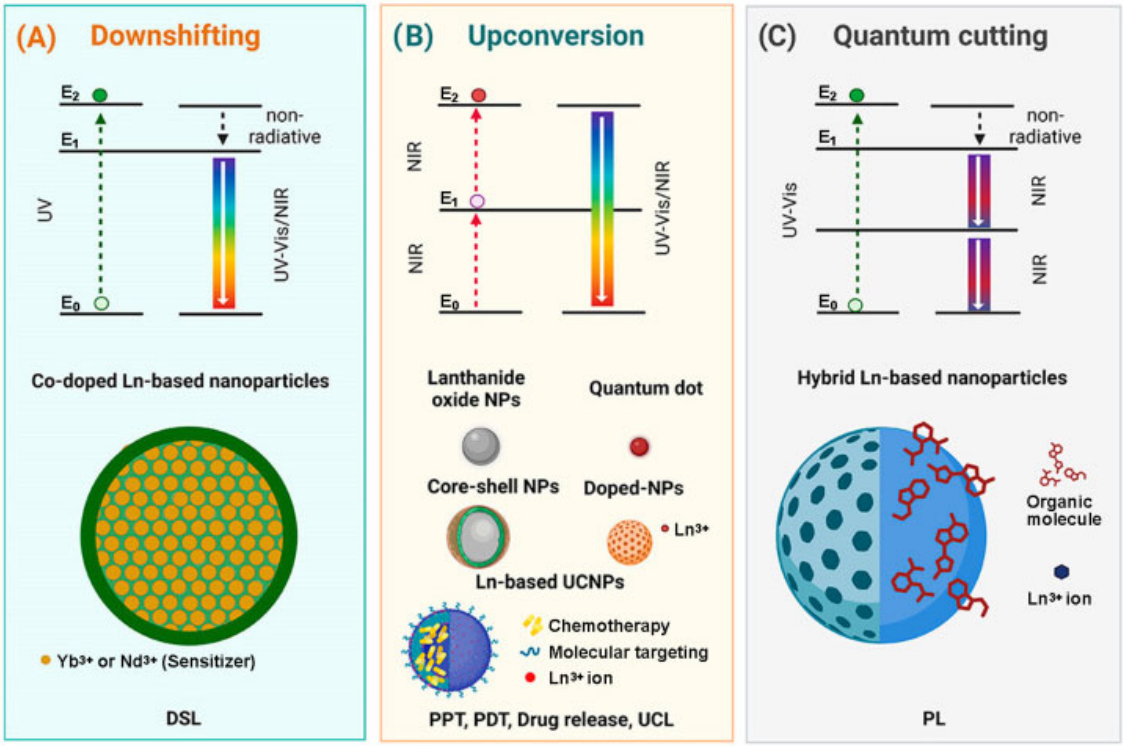

DSL: Downshifting Luminescence; PTT: Photothermal therapy; PDT: Photodynamic therapy; UCL: Upconversion Luminescence; PL: Photoluminescence

Figure 3.2: (A) Downshifting mechanism associated with Co-doped Ln-based NPs; (B) Upconversion mechanism associated with Ln_2O_3 NPs, QDs, Core–shell Ln-based NPs, Ln-doped NPs and multimodal Ln-based platforms, and (C) Quantum cutting mechanism associated with hybrid Ln-based nanoparticles. Reproduced with permission from Ferro-Flores, G.; Ancira-Cortez, A.; Ocampo-García, B.; Meléndez-Alafort, L. Molecularly Targeted Lanthanide Nanoparticles for Cancer Theranostic Applications. *Nanomaterials*, **2024**, *14* (3), 1–25. Copyright 2024 MDPI.

Ln^{3+}-doped NPs with persistent luminescence properties are gaining popularity as bioimaging probes.[138] These NPs can store photons and emit NIR light for extended periods after the initial excitation, allowing long-term imaging without continuous external illumination.[138–140] Persistent luminescent NPs are advantageous for tracking biological processes over extended periods, such as tumor imaging and monitoring.[141,142] For example, Wu et al. developed transactivator of transcription (TAT) peptide-conjugated persistent luminescent NPs for labeling adipose-derived stem cells and macrophages, facilitating cell tracking without selective labeling.[143,144] This innovation allows for non-invasive, long-term tracking of cell movements and interactions in live subjects, providing valuable insights into cellular dynamics and disease progression.

Zhao et al. introduced a background-interference-free persistent luminescent metal-organic framework for tumor site-activated imaging, enhancing tumor detection sensitivity and specificity.[113] This approach leverages the unique properties of persistent luminescent NPs to provide high-contrast images with minimal background noise, which is critical for accurately identifying and characterizing tumors. Furthermore, Zhao's team developed a long persistent luminescence hydrogel that integrates tumor-targeted persistent luminescent NPs with alginate hydrogel, enabling tumor-specific labeling and autofluorescence-free tracking of tumor metastasis.[114] This hydrogel system offers a versatile platform for localized and sustained imaging of metastatic sites, potentially improving the monitoring and treatment of cancer metastasis.[114]

The recent COVID-19 pandemic highlighted the need for rapid and sensitive diagnostic tools. Ln^{3+}-doped NPs have been used in multiplexed nucleic acid assays to improve the detection rate of SARS-CoV-2, the virus responsible for COVID-19.[145] Probes doped with terbium (Tb^{3+}), holmium (Ho^{3+}), and europium (Eu^{3+}) were designed to detect SARS-CoV-2's ORF1ab gene, RdRp gene, and E gene respectively, providing high sensitivity detection without complex nucleic acid amplification procedures.[145–147] This method offers a robust and reliable approach for early detection and monitoring of viral infections, which is crucial for effective disease management and control.[146] The incorporation of Ln^{3+}-doped NPs into diagnostic assays not only enhances sensitivity and specificity but also allows for the development of portable and user-friendly diagnostic devices, facilitating widespread testing and early intervention.[147]

3.3 Designing and applications of nanoparticle – hydrogel hybrid materials

The application of NPs in consumer products has led to the rise of regulations and restrictions due to concerns about their safe use. Steinhoff et al. recently published results showing the fate of NPs in the environment.[148] To mitigate the environmental and health risks posed by NPs, it is essential to develop strategies that enhance their stability and control their release. One promising approach involves using hydrogels to effectively encapsulate and immobilize NPs, potentially reducing their mobility and impact on the environment. This method allows for innovative applications such as

environmental remediation and safer consumer products, while also improving hydrogel properties, such as increased mechanical strength and enhanced stimuli response. A good example between silica NPs-hydrogel composite has been reported already in the literature, of which the NPs were modified with polyethylene glycol.[149,150] The resulting material had improved tissue adhesive property, mechanical strength and bioactivity compared to bare silica NPs. Likewise, gold NPs immobilized in poly *N*-isopropyl amide hydrogel has improved thermal response and mechanical strength.[151]

Figure 3.3 highlights 5 different strategies for innovatively developing hydrogel-NP conjugates with uniform distribution. The simplest method being hydrogel formation in a NP suspension. Sershen et al., prepared optically responsive opto-mechanical NP-hydrogel composites using this approach.[44] Au-NPs were added into a solution of monomer (95/5 molar ratio of *N*-isopropylacrylamide/acrylamide (NIPAAm/AAm) followed by addition of ammonium persulfate initiator and tetramethylethylenediamine accelerator. Other authors have also used similar approach and reported positive results in intra-ocular lens applications,[152] NP stability and reduce aggregation[153] (however, NPs may leach out of the hydrogel matrix at low crosslinking density)[154–156], improved photocatalysis[157] and tumor metastasis tracking.[114]

In a different approach, NPs can be incorporated in a hydrogel matrix after gelation. Pardo-Yissar inserted Au-NPs in a PAAm gel after electro-polymerization to study the solvent switchable electronic properties of hydrogel-Au-NPs composite material.[158] Wang et al came up with a different strategy and demonstrated that is possible to manipulate the thermo-responsive nature of PNIPAm hydrogels by loading nanoparticle precursors into a gel. Thus, reactive NPs formation in a preformed gel. New methods are coming up using NPs as crosslinkers to form hydrogels. Souza et al., developed a bacteriophage molecular network by spontaneous assembly of phage with Au-NPs.[159] The formed hydrogel was able to maintain the cell surface receptor binding and internalized attribute of the peptides. Skardal et al., utilized multivalency and thiophilicity of Au-NPs to crosslink thiolated hyaluronic acid commercially available in to biodegradable, cytocompatible, printable and extrudable hydrogels.[160]

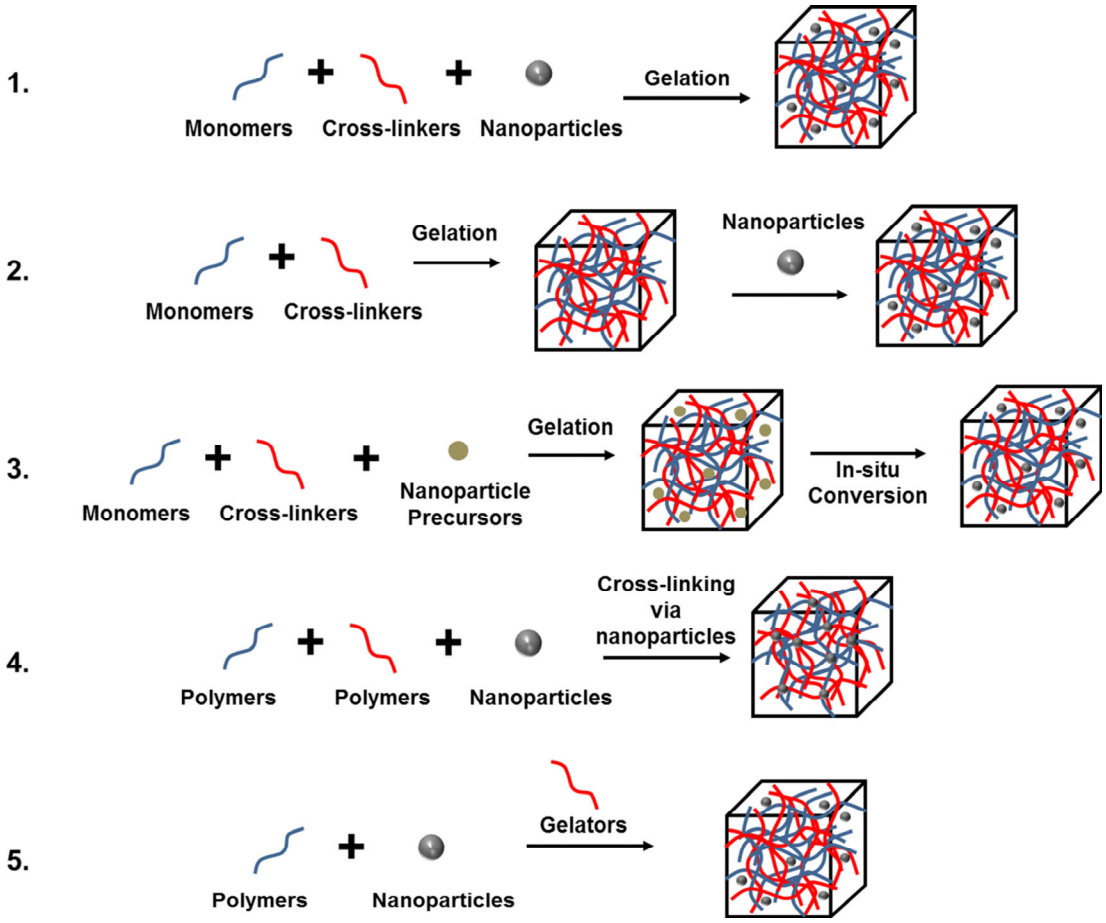

Figure 3.3. Diagram illustrating five different strategies to develop hydrogel-NP conjugates with uniform distribution: 1) Preparing the hydrogel in a NP suspension, 2) physically embedding of the NPs into hydrogel matrix after the gelation process, 3) reactive NP formation inside a preformed gel, 4) Using NPs as crosslinkers to form hydrogels, 5) gel formation using a combination of NPs, polymers, and precise gelators Reproduced with permission from Thoniyot, P.; Tan, M. J.; Karim, A. A.; Young, D. J.; Loh, X. J. Nanoparticle–Hydrogel Composites: Concept, Design, and Applications of These Promising, Multi-Functional Materials. *Adv. Sci.*, **2015**, *2* (1400010), 1–13. Copyright 2015 Wiley-VCH.

In another study, Zhang et al., prepared semiconductors NP-based hydrogel by self-initiated polymerization in the presence of sunlight or visible light.[161] The semiconductor NPs were used as inorganic initiators for the polymerization of *N,N*-dimethylacrylamide. A more innovative method has also been reported using NPs, polymers and distinct gelator molecules. Precisely, Wu et al., incorporated silica NPs in to a conducting polymer hydrogel for Si-based anodes.[162] The hydrogel was formed in situ to generate a good 3D network structure based of silica NPs coated with the conducting polymer.

The progress made in NP-hydrogel composites, particularly through the incorporation of lanthanide-doped NPs for stable photoluminescent properties and improved structural properties, offers valuable insights for the synthesis of MPs. Techniques used to achieve uniform distribution and stability of NPs within hydrogels can be adapted for the fabrication of MPs, ensuring precise control over size, morphology, and functional properties. MPs are particularly relevant in biomedical applications due to their capacity for controlled drug release at targeted sites, which enhances therapeutic efficacy while minimizing adverse effects.[163] In summary, the NP-hydrogel composite provides a multifunctional and stimuli responsive properties. To date, only metal NP-hydrogel, metal-oxide NP-hydrogel, nonmetal NP-hydrogel and polymeric NP-hydrogel composite systems have been well investigated and not the RE fluoride NP-hydrogel counterparts.[15]

Applying the advanced principles and techniques developed in NP-hydrogel composites offer possibilities to design multifunctional MPs tailored for various biomedical applications. This integrative approach broadens the scope and utility of these materials, enhancing their effectiveness in therapeutic and diagnostic contexts.

3.4 Fabrication of tailored microparticles for biomedical applications

Currently, there is no reported synthetic method for preparing monodispersed MgF_2 beads larger than 2 μm in diameter. The latest report by Xu et al.,[72] claimed to prepare micro sized spherical particles with wide size distribution ranging from 200 nm and 2 μm. Typical known synthesis routes for preparing MgF_2 nanoparticles and micro sized beads include precipitation, ammonia route, sol-gel via hydrogen fluoride acid (HF) or acetate, microwave assisted ionic liquid solvothermal, ultra-sonification and synthesis via sea water. Precipitation can be used to prepare uniform MgF_2 particles of different morphologies by changing the pH and ionic strength, while avoiding complexation of interaction ions. Spherical, cubic, prismatic and platelet colloidal particles are formed due to diffusional growth or aggregation of individual single particles. It is however challenging to control the particle size for particles greater than 2 μm.[72,164,165]

Likewise, synthesis via ammonia from the reaction of Mg^{2+} and F^- in aqueous solution is useful in achieving controlled sizes (from ~6 to max. 300 nm) and morphologies (from a spherical and a cubical form), which can be produced by means of an appropriate F: Mg ratio.[164]

The sol-gel synthesis via HF requires an inert atmosphere under Ar gas and a Schlenk apparatus. The purification process of the particles is tedious and involves large amounts of alcohol as a solvent. The resultant size distribution is between 10 – 20 nm.[166] Similarly, sol-gel via acetate is not convenient for large scale synthesis. This is because in the first step of the reaction between magnesium and methanol large amounts of hydrogen is released.[167] Unfortunately, redesigning the synthesis with commercially available magnesium ethoxide as a starting material cannot be considered, since this is insoluble in methanol or in ethanol.[167] Hence, no transparent sols are available due to the deposition of a protective MgF_2-layer onto the suspended solid $Mg(OEt)_2$ precursor particles.[167]

An alternative route with $MgCl_2$ as educt is quite easy to perform but suffers from the stoichiometric formation of HCl from $MgCl_2$ as result of the reaction with HF.[167,168] HCl is very corrosive, a practical application of such sols is not recommended. However, the synthesis route via ionic liquids can be used as a substitute for fluorine source rather than working with large volume of HF. Ultra-sonification method has only been reported for preparing active MgF_2 biofilms.[169] Hence, application in synthesis of particles is not possible. Lastly, synthesis using sea water from the Baltic Sea has been reported as a low-cost method.[170] However, environmental challenges limit the application of the sea water for industrial synthesis. Furthermore, the effects of other chemical species in the sea water have not been fully understood and investigated on how they affect the size distribution of the particles.

Doping MgF_2 beads with activators such as trivalent lanthanides is beneficial in further functionalization of the beads. This has been shown by Cortelletti et al., for small CaF_2, SrF_2 particles and bulk material.[171] Thus, developing photoluminescent MgF_2 beads that emit in the visible or near infra-red region, which can be used as label free markers

Chapter 4 Synthesis, stabilization and optical properties of lanthanide-doped luminescent NPs ($LaF_3:Ce^{3+}Tb^{3+}$, $TiO_2@SiO_2@LaF_3:Ce^{3+}Tb^{3+}$ and $KSmF_4:Ln^{3+}$ (Ln = Ce, Tb and Eu)

4.1 Introduction

This Chapter covers the synthesis and characterization of lanthanide-doped luminescent nanoparticles (NPs). The overall objective was to prepare multifunctional NPs that luminesce in the visible range of the electromagnetic spectrum using trivalent lanthanides (Ln^{3+}) as dopant. Furthermore, the NPs were modified for applications in cell studies.

$LaF_3:Ce^{3+}Tb^{3+}$ was chosen because doping of LaF_3 with lanthanides is known[74] and different synthetic methods were anticipated to afford stable photoluminescence in NPs. Thereafter, $LaF_3:Ce^{3+}Tb^{3+}$ was used to functionalize TiO_2 NPs. These particles were considered as a carrier, since they are well established NPs and known for their interesting photocatalytic properties, as discussed in Chapter 3 of this Thesis,[172] among others. However, since photocatalysis is detrimental for many biological and industrial processes,[172] a core-shell synthesis strategy with a shell of SiO_2 synthesized around the TiO_2 core has been used to prepare $TiO_2@SiO_2@LaF_3:Ce^{3+}Tb^{3+}$ NPs. SiO_2 shells supress the unwanted generation of reactive oxygen species (ROS), provided that they shield the underlying TiO_2 completely.[173] Initially, $LaF_3:Ce^{3+}Tb^{3+}$ NPs were synthesized using an autoclave method, exploiting stabilization using PVP and citric acid. A modified synthesis route was developed to create core-shell NPs of $TiO_2@SiO_2@LaF_3:Ce^{3+}Tb^{3+}$. Additionally, this Chapter explores the preparation of $KSmF_4$: Ln^{3+} (Ln = Ce, Tb and Eu) perovskite-like NPs, focusing on their modification, stabilization, and dispersion in aqueous media for subsequent cell studies.

The luminescence properties of these nanoparticles were investigated in both dry (powder) and liquid (NP solution) states to gain comprehensive insight into their optical behaviour. The findings of this Chapter are used as a basis and motivation for further evaluation on toxicity and experiments with hydrogels and cells *(see Chapter 5)*.

4.2 Results and discussion

4.2.1 Stepwise synthesis and powder X-Ray diffraction patterns

In the first step of the developed protocol, the synthesis of TiO_2 NPs was carried out by employing a controlled hydrolysis reaction of titanium tetrachloride ($TiCl_4$). This reaction was facilitated by mixing two ionic liquids, namely 1-butyl-3-methylimidazolium chloride (BMIM[Cl]) and 1-butyl-3-methylimidazolium bromide (BMIM[Br]), in a solution containing Milli-Q water and ethanol *(see Figure 4.1)*. The utilization of microwave heating allowed for rapid and efficient synthesis under controlled conditions. Notably, the ionic liquids served as co-surfactants during the synthesis process, exerting a significant influence on the resulting crystalline phases of TiO_2 nanoparticles, as evidenced by powder X-ray diffraction (XRD) analysis *(Figure 4.2)*. Specifically, variations in the concentrations of BMIM[Cl] and BMIM[Br] were found to possess an impact on the relative abundance of the (001) and (101) crystallographic planes, thereby influencing the size and morphology of the TiO_2 nanoparticles applications.

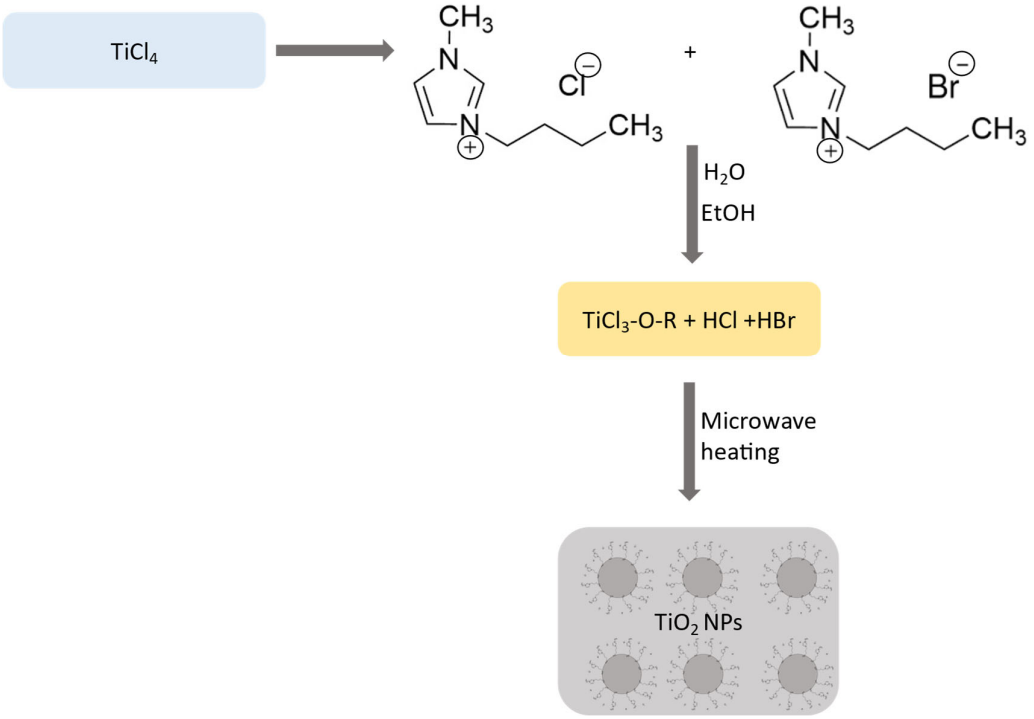

Figure 4.1: First synthesis scheme for preparing TiO_2 NPs.

Figure 4.2 shows a XRD powder pattern of core TiO_2 NPs after the first step of the synthesis *(see Figure 4.1)* and sintering at 400°C. The XRD pattern revealed characteristic peaks corresponding to the anatase phase of TiO_2. The most intense peak was observed at 2θ = 25.3°, corresponding to the (101) crystallographic plane of the anatase phase of TiO_2. Additional peaks were observed at 2θ values of approximately 37.8°, 48.0°, 53.9°, 55.1°, and 62.7°, corresponding to the (004), (200), (105), (211), and (204) crystallographic planes, respectively. The peaks correlate to the reference spectrum of anatase adopted from the ICSD.[174] The broad peaks observed in the XRD pattern suggest the presence of small crystallite sizes, a characteristic feature of anatase TiO_2 nanoparticles.

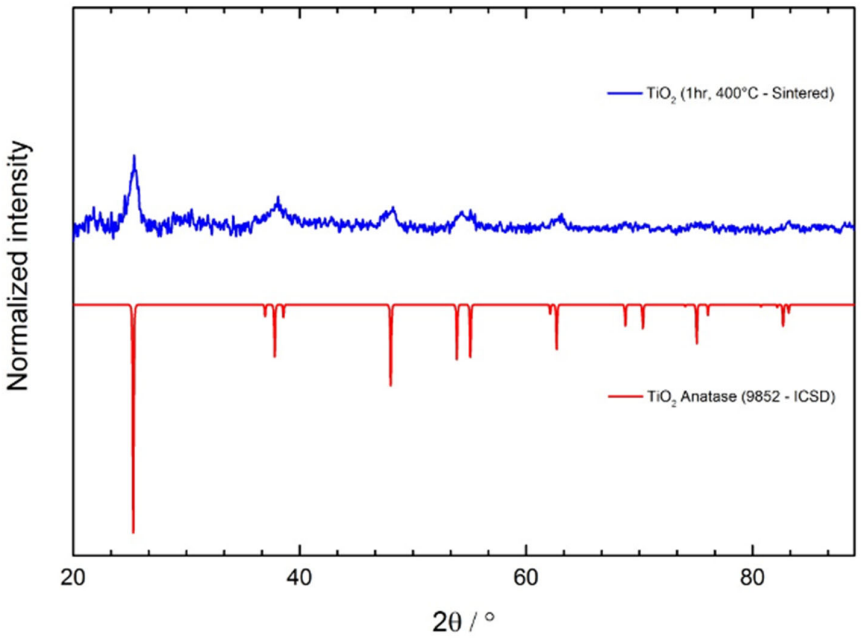

Figure 4.2: Powder XRD pattern of TiO_2 NPs after 1 h sintering at 400°C compared to standard reference (9852-ICSD).[174]

However, the signal to noise ratio is limited and clear peak broadening is observed, which is a typical feature for smaller NPs less than 20 nm.[175] According to the literature, peak broadening can be caused by several factors; the crystallite size, instrumental profile, type of instrument used for nanophase analysis, presence of microstrain, different types of microstrain, solid solution inhomogeneity, and temperature factors.[176]

In practice, the instrumental profile influences the upper limit of crystallite size that can be analyzed.[176,177,178,179,180] Hence, the occurrence of any impurities cannot be estimated using the XRD powder pattern. The excess ionic liquid remaining on the surface of the NPs was removed by sintering at 400°C for 1 h.

Furthermore, the successful formation of TiO_2@SiO_2 core-shell nanoparticles was achieved via the Stöber synthesis[181] method *(see Figure 4.3)*. This approach, known for its simplicity and versatility, offers several advantages, including precise control over particle size, uniformity, and the ability to incorporate additional functionalities through surface modification. The synthesis of SiO_2-encapsulated TiO_2 NPs was carried out in two steps. First, TiO_2 nanoparticles were prepared as shown in Figure 4.1, followed by careful purification, drying and sintering. Subsequently, the Stöber-inspired synthesis was employed to encapsulate the TiO_2 NPs with a silica shell. $TiCl_4$ served as the TiO_2 precursor, while TEOS was used as the SiO_2 precursor. The reaction conditions were optimized to achieve a uniform SiO_2 coating around the TiO_2 NPs. The resulting core-shell NPs were characterized using SEM, TEM, FTIR spectroscopy, and XRD. The successful synthesis of TiO_2@SiO_2 CSNPs represent a pivotal advancement in the fabrication of multifunctional nanomaterials with tailored properties for biomedical applications.

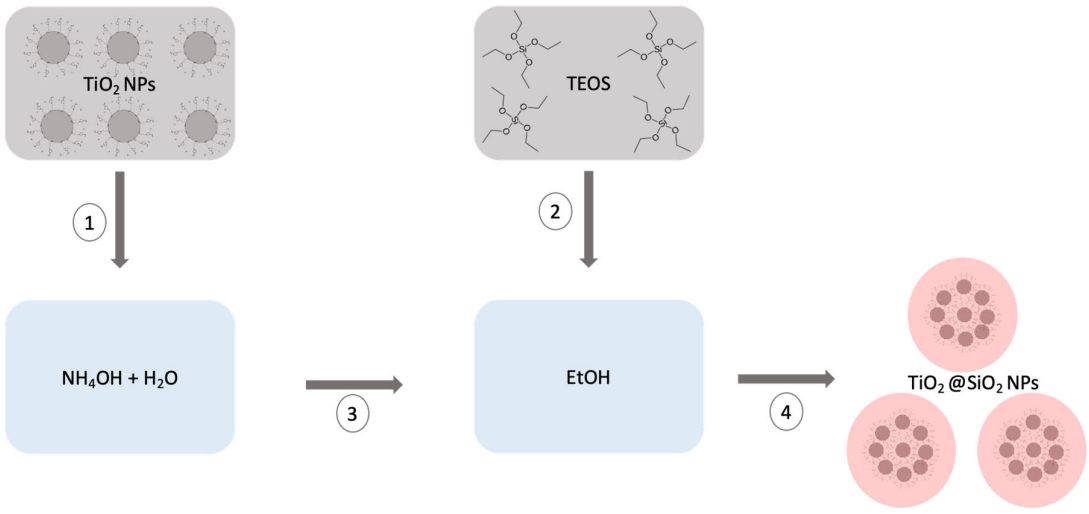

Figure 4.3: Second step of the synthesis scheme for preparing TiO_2@SiO_2 NPs sintered at 400°C for 1 h.

Powder XRD analysis of the synthesized TiO_2@SiO_2 CSNPs revealed notable observations, namely distinct reflections corresponding to both TiO_2 and SiO_2 NPs. Peaks due to SiO_2 were observed because the TiO_2@SiO_2 undergoes a drying step after synthesis. Drying is known to enhance the crystallinity of the SiO_2 shell.[182] The substantial thickness of the amorphous silica shell may obscure any weak diffraction peaks of the TiO_2 core.[183] Additionally, the amorphous nature of the silica could attenuate X-rays, contributing to the absence of TiO_2 peaks. This absence underscores the complexity of CSNP characterization and suggests the need for further investigation using complementary techniques such as transmission electron microscopy (TEM) or energy-dispersive X-ray spectroscopy (EDX) for a comprehensive understanding of the nanoparticles' composition, structure, and morphology *(refer to Section 4.2.3)*.

The synthesis of TiO_2@SiO_2 core-shell nanoparticles was followed by the incorporation of a LaF_3:$Tb^{3+}Ce^{3+}$ layer using 1-butyl-3-methylimidazolium tetrafluoroborate (BMIM[BF_4]), as shown in Figure 4.4. Initially, TiO_2 nanoparticles were synthesized and then coated with SiO_2 NPs shell using the Stöber method to form TiO_2@SiO_2 core-shell nanoparticles. Unlike conventional methods that utilize NaF or NH_4F as fluorine sources,[184,185] BMIM[BF_4] serves a dual role as both a fluorine source and a solvent, simplifying the synthesis process and reducing the need for additional reagents. BMIM[BF_4] offers high thermal stability and tunable solvation behavior, allowing for precise manipulation of the reaction environment, resulting in improved reproducibility and uniformity of the final product.[186] The chemical reactions I, II and III describe the formation of LaF_3:$Tb^{3+}Ce^{3+}$ layer.

$$La(NO_3)_{3(aq)} + 3BMIM[BF_4]_{(aq)} \rightarrow LaF_{3(s)} + 3BMIM[NO_3]_{(aq)} + 3BF_{3(aq)} \quad (I)$$

$$Tb(NO_3)_{3(aq)} + 3BMIM[BF_4]_{(aq)} \rightarrow TbF_{3(s)} + 3BMIM[NO_3]_{(aq)} + 3BF_{3(aq).} \quad (II)$$

$$Ce(NO_3)_{3(aq)} + 3BMIM[BF_4]_{(aq)} \rightarrow CeF_{3(s)} + 3BMIM[NO_3]_{(aq)} + 3BF_{3(aq)} \quad (III)$$

Tb and Ce were used as co-dopants and replaced some of the La sites in the crystal structure and hence the overall reaction is simplified and is given by the chemical reaction IV.

$$La(NO_3)_{3(aq)} + 3BMIM[BF_4]_{(aq)} \rightarrow LaF_{3(s)} + 3BMIM[NO_3]_{(aq)} + 3BF_{3(aq)} \quad (IV)$$

To prepare the final shell consisting of LaF_3:$Tb^{3+}Ce^{3+}$ in the CSNPs, the use of correct stoichiometric amounts of the educts is necessary. This is because during the synthesis some appreciable amount of TiO_2 and SiO_2 is lost in the washing steps *(see section 4.4.5.3)*. Furthermore, NPs that aggregate before addition of LaF_3:$Ce^{3+}Tb^{3+}$ are sieved out, thus altering the final concentration of NPs. At the end of the synthesis grinding of the CSNPs was necessary to remove any sticking of the NPs due to excess ionic liquids on the surface of the NPs that dry together with the NPs. Hence, the washing steps were vital immediately after the synthesis and again after drying-grinding process.

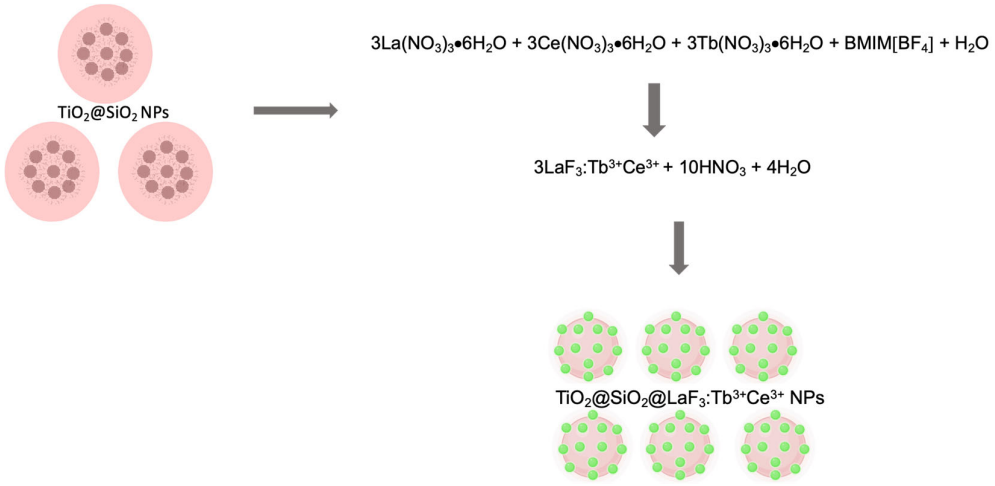

Figure 4.4: Final synthesis step scheme for preparing TiO_2@SiO_2@LaF_3:$Tb^{3+}Ce^{3+}$ NPs.

Table 4.1 provides an overview of the synthesis, characterization, and properties of various NPs investigated in this Chapter. The characterization of the NPs included XRD for crystal structure determination, and TEM along with STEM-EDX for particle size and morphology analysis. DLS was utilized for size distribution analysis of LaF_3:$Ce^{3+}Tb^{3+}$.

Figure 4.5 shows the powder XRD pattern of synthesized LaF_3:$Ce^{3+}Tb^{3+}$ NPs via BMIM[BF_4] *(No. 3 on Table 4.1)* to investigate crystallinity and phase composition of the reaction product obtained. The resulting XRD pattern *(Figure 4.5)* revealed prominent diffraction peaks corresponding to the (100), (110), (111), and (200) crystallographic planes of the fluorite-type LaF_3 lattice,[187] indicative of well-defined crystallinity. Notably, the observed peak positions at 2θ = 28.5°, 32.7°, 47.1°, and 56.4° closely matched reference values for LaF_3,[187] affirming the successful synthesis of the targeted material. The XRD pattern exhibited broad peaks,

consistent with high crystallinity and phase purity of the nanoparticles *(Figure 4.5)*. However, the reflections are slightly shifted with respect to the reference LaF_3 (23972 ICSD database)[187] and significantly broadened, which signifies the formation of nanocrystals.

Table 4.1: Summary of NPs synthesized (including conditions and characterization methods).

NPs	Route	Structure	Size
TiO_2	Via BMIM[Cl] and BMIM[Br] *(a)*	XRD & TEM	TEM
$TiO_2@SiO_2$	Stöber synthesis via TEOS[181]	XRD & STEM-EDX	STEM
$LaF_3:Ce^{3+}Tb^{3+}$	Via EG and $BMIM[BF_4]$ *(b), (c), (d)*	XRD & STEM-EDX	STEM & DLS
$TiO_2@SiO_2@LaF_3:Ce^{3+}Tb^{3+}$	Via EG and $BMIM[BF_4]$ *(b), (c), (d)*	XRD & STEM-EDX	STEM
$KSmF_4:Ln^{3+}$ (Ln = Ce, Tb and Eu)	Protocol according to Wang et al.[85]	XRD & TEM-EDX	TEM

*(a)*Microwave parameters: 10 min, 10 bar, 100°C, 100 W.
*(b)*Microwave parameters: 30 min, 10 bar, 120°C, 100 W.
*(c)*Room temperature and low temperature luminescence.
*(d)*Toxicity tests with NIH 3T3 and PaTu 8988t cells *(see Chapter 5)*.

This XRD analysis reveals that the $LaF_3:Ce^{3+}Tb^{3+}$ nanoparticles possess a crystalline structure similar to that of pure LaF_3 *(reference from ICSD database)*. The positions of the diffraction peaks *(2θ = 28.5°, 32.7°, 47.1°, and 56.4°)* match closely with the reference pattern, indicating that the doped nanoparticles maintain the same phase as the undoped LaF_3. Differences in peak width suggest some changes due to doping and possibly nanoparticle size effects. Overall, the pattern confirms successful incorporation of Ce^{3+} and Tb^{3+} into the LaF_3 lattice without significant impurities or secondary phases.

In the synthesis of $TiO_2@SiO_2@LaF_3:Ce^{3+}Tb^{3+}$ NPs the ionic liquid $BMIM[BF_4]$ was used, which has the advantage of controlling the growth of the nanocrystals and also act as source for fluoride ions.[186,188] Hence, no HF is formed as in the conventional method using NaF that requires excess water.

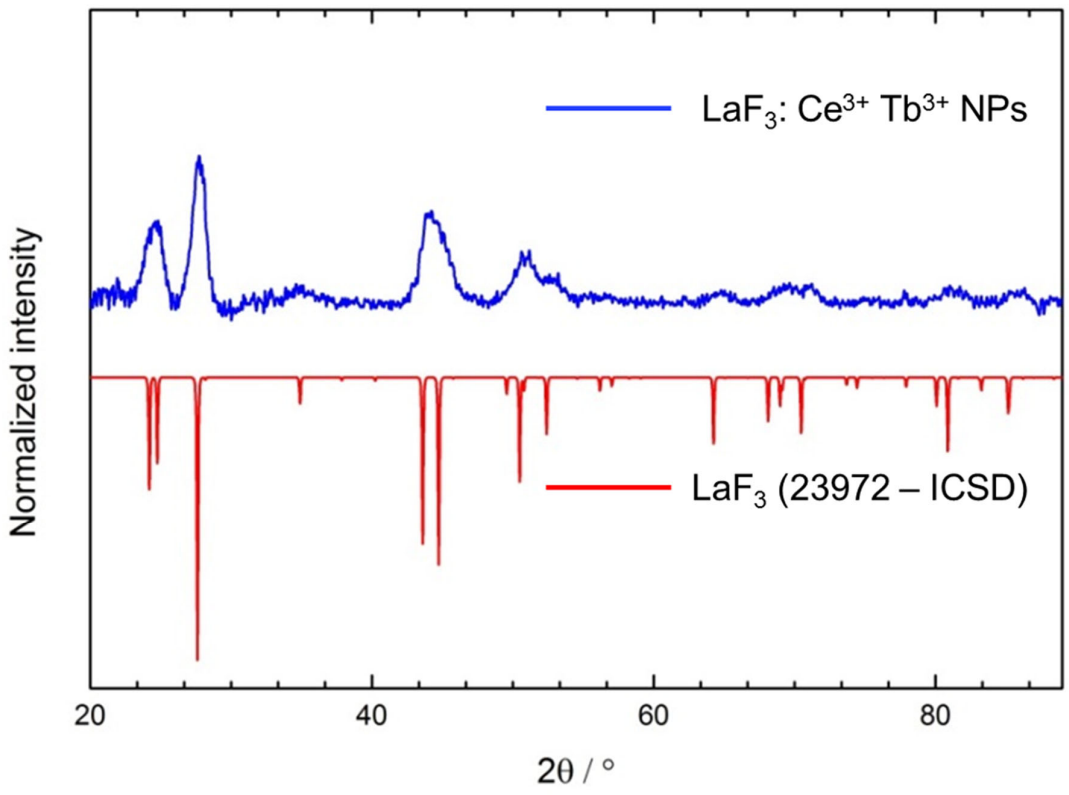

Figure 4.5: Powder XRD pattern of LaF_3:$Ce^{3+}Tb^{3+}$ NPs compared to standard reference (23972-ICSD).[187]

Figure 4.6 shows the XRD powder pattern of the final TiO_2@SiO_2@LaF_3:$Ce^{3+}Tb^{3+}$ NPs *(synthesis procedure see Figure 4.4)*. The XRD peaks corresponding to TiO_2, SiO_2 and LaF_3 are denoted in Figure 4.6 as red, blue and green asterisks, respectively. Again, the peaks are broad and signal to noise ratio is low. The LaF_3 peaks indicate the successful formation of the outer layer, while the SiO_2 peaks suggest partial crystallinity in the SiO_2 layer. The peaks attributed to the anatase phase of TiO_2 are less intense, likely due to effect of a shielding SiO_2 shell. The presence of crystalline SiO_2 peaks, despite the expectation of amorphous SiO_2, can be attributed to synthesis conditions or post-synthesis effects leading to partial crystallization. To improve signal to noise ratio, data acquisition time is increased. However, this can also damage the imaging plate. For this measurement, the recording time for the instrument was set to 10 minutes. To gather independent information on the NP composition, ATR - FTIR spectroscopy was used as a complementary technique to confirm the composition of the CSNPs *(see Figure 4.7)*.

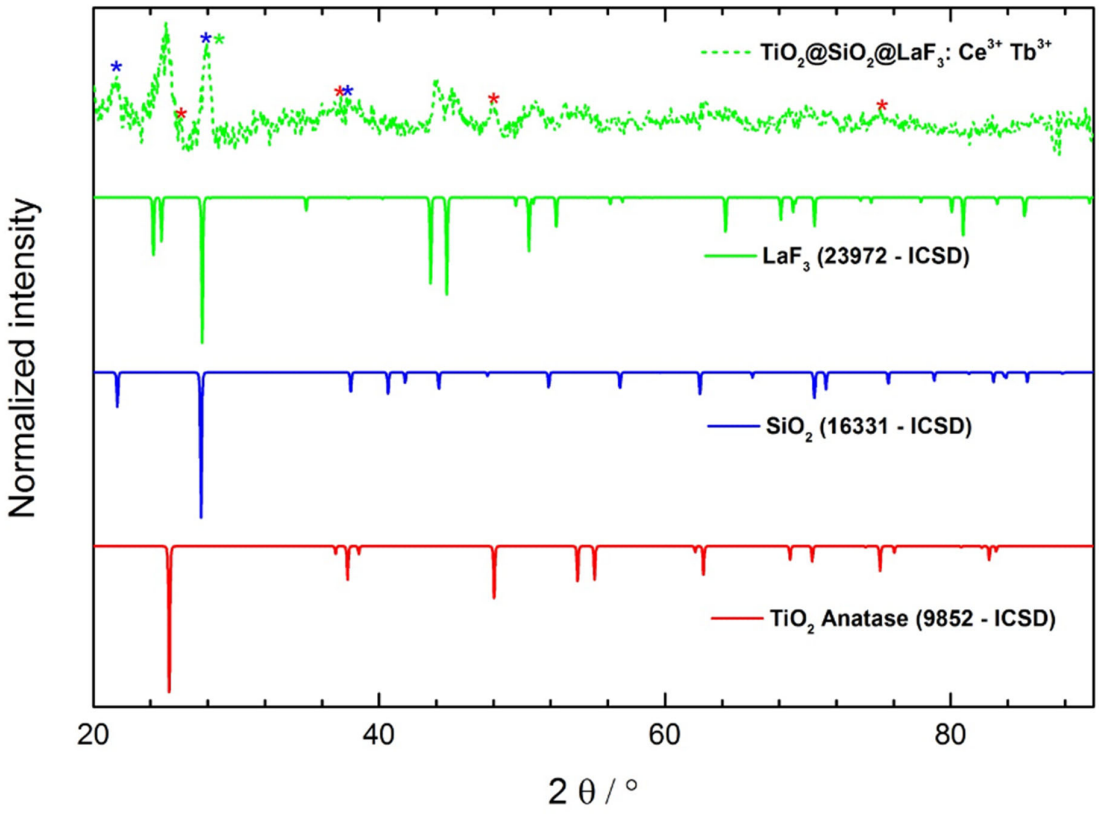

Figure 4.6: Powder XRD pattern of TiO_2@SiO_2@LaF_3:$Ce^{3+}Tb^{3+}$ NPs.

As shown in Figure 4.7 the expected peaks of anatase phase of TiO_2, SiO_2 and LaF_3 NPs in TiO_2@SiO_2@LaF_3:$Ce^{3+}Tb^{3+}$ were all observed, which is in agreement with results reported in the literature.[189,190–192] Doping of LaF_3 with Ce^{3+} and Tb^{3+} did not lead to any changes in the FTIR spectra *(compare Figure 4.7)*. This is in contrast to the XRD data *(Figure 4.6)*, where the peaks were shifted to lower 2θ values. This shift by 1.5° is tentatively attributed to the strain in the crystal lattice and distorted symmetry.[177]

For the ATR - FTIR spectroscopy measurements a ZnSe crystal and a Tensor 27 FTIR spectrometer (Bruker Optik GmbH, Ettlingen, Germany) was used. Two different TiO_2 samples were taken as reference for monitoring changes after the addition of SiO_2 and LaF_3 *(see Figures 4.2 and 4.3)*. The samples investigated included TiO_2 NPs sintered at 400°C for 1 h, 2 h, CSNPs TiO_2(400°C, 2h)@SiO_2 and TiO_2(400°C, 2h)@SiO_2@LaF_3:$Ce^{3+}Tb^{3+}$. The FTIR spectra of TiO_2 samples subjected to various treatments reveal key structural and compositional information in the wavenumber range from 4000 to 400 cm^{-1}.

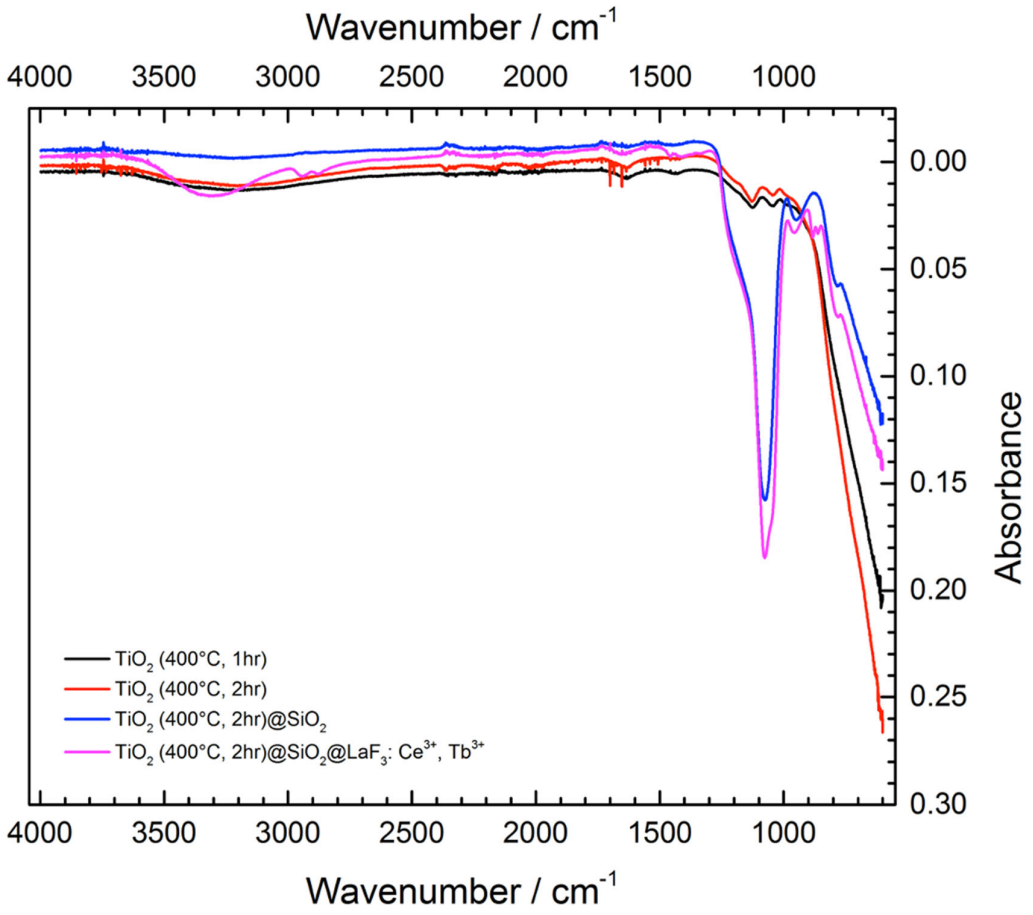

Figure 4.7: ATR-FTIR spectra of TiO_2@SiO_2@LaF_3:$Ce^{3+}Tb^{3+}$ NPs.

Broad absorption bands around 3400 and 3500 cm^{-1} correspond to O-H stretching vibrations, indicative of surface hydroxyl groups or adsorbed water molecules.[193] Additionally, the bands between 1620 cm^{-1} and 1640 cm^{-1} are attributed to H-O-H bending modes, further supporting the presence of hydroxyl groups or adsorbed water on the TiO_2 surface.[194]

Table 4.2: FTIR spectroscopy band position and assignment of TiO_2@SiO_2@LaF_3:$Ce^{3+}Tb^{3+}$ NPs.

Band Position (cm^{-1})	Assignment	Description
3400 - 3500	O-H stretching vibrations[193] *(a)*	Surface OH groups or adsorbed water molecules
1620 - 1640	H-O-H bending modes[194] *(a)*	OH groups or adsorbed water
800 - 400	Ti-O and Ti-O-Ti stretching vibrations[195] *(a)*	Intrinsic to the TiO_2 lattice structure
1200 - 1000	Si-O-Si stretching vibrations[196] *(b)*	Incorporation of SiO_2 in TiO_2 matrix
500 - 600	La-F stretching vibrations[197] *(c)*	Incorporation of LaF_3 in CSNPs
1100	Asymmetric stretching vibrations of Si-O-Si[196] *(d)*	Presence of SiO_2
800	Symmetric stretching vibrations of Si-O-Si[196] *(d)*	Presence of SiO_2
950	Si-OH bending vibrations[196] *(d)*	OH groups on SiO_2 surface
3400	O-H stretching vibrations[193,196] *(d)*	OH groups on SiO_2 surface

*(a)*Sample composed of only TiO_2.
*(b)*Sample composed of TiO_2(400°C, 2h)@SiO_2.
*(c)*Sample composed of TiO_2(400°C, 2h) @SiO_2@LaF_3: $Ce^{3+}Tb^{3+}$.
*(d)*Sample composed of TiO_2@SiO_2@LaF_3:$Tb^{3+}Ce^{3+}$.

The region of 800-400 cm^{-1} is characterized by prominent bands corresponding to Ti-O and Ti-O-Ti stretching vibrations, intrinsic to the TiO_2 lattice structure.[195] Comparative analysis of the samples treated at 400°C for 1 h and 2 h reveals that the latter exhibits more well-defined bands, suggesting an enhancement in crystallinity or changes in particle size with extended thermal treatment duration.[198,199] Incorporation of SiO_2 is evidenced by the additional Si-O-Si stretching vibrations observed in the range from 1200 to 1000 cm^{-1}, confirming the successful integration of silica into the TiO_2 matrix.[200]

The spectrum of TiO_2 (400°C, 2h)@SiO_2@LaF_3:Ce^{3+} Tb^{3+} displays distinct spectral features, particularly in the Ti-O region, highlighting modifications in the lattice structure due to the incorporation of LaF_3:$Ce^{3+}Tb^{3+}$.

The FTIR spectrum of TiO_2@SiO_2@LaF_3:$Tb^{3+}Ce^{3+}$ CSNPs confirms the presence of both silica and lanthanum fluoride. The broad band around 3400 cm^{-1} is attributed to O-H stretching vibrations from Si-OH groups, indicating the presence of hydroxyl groups on the silica surface.[196] The strong band at 1100 cm^{-1} corresponds to the asymmetric stretching vibrations of Si-O-Si bonds, while the band at 800 cm^{-1} is due to symmetric stretching vibrations of Si-O-Si.[196] Additionally, the band at 950 cm^{-1} is assigned to Si-OH bending vibrations.[196] Bands in the 500-600 cm^{-1} region, corresponding to La-F stretching vibrations, confirm the successful incorporation of LaF_3 into the core-shell structure.[197] Observed changes in band positions and intensities align with established literature values,[193–200] affirming the structural and compositional modifications introduced in different sets of NPs.

4.2.2 DLS measurements

LaF_3:$Ce^{3+}Tb^{3+}$ NPs were prepared according to the procedure highlighted in Figure 4.4 for further estimation of the particle size distributions. In particular, DLS was employed to estimate the hydrodynamic diameter and related particle size distributions of LaF_3:$Ce^{3+}Tb^{3+}$ NPs and also to monitor the stability of the dispersions in water.

Figure 4.8 shows the size distribution by number of LaF_3:$Ce^{3+}Tb^{3+}$ NPs dispersed with a concentration of 0.5 mg/mL in Milli-Q water. The NPs investigated here were prepared in situ using a mixture of PVP and EG in a ratio of 1:1. PVP was chosen as a stabilizer due to its non-toxicity,[201] non-ionic.[202] PVP, which is a stable polymer with inert physiochemical features over a wide range of pH conditions,[203,204] is comprised of a hydrophilic side groups and a hydrophobic aliphatic backbone.[205] These characteristics renders PVP soluble in aqueous and non-aqueous solvents.[206]

In the DLS analysis it was assumed that the scatterers are spherical in shape. Panel B in Figure 4.8 shows a broad apparent size distribution of LaF_3:$Ce^{3+}Tb^{3+}$ NPs observed less than 5 minutes after preparation of the solution. The distribution peaks

at an apparent hydrodynamic diameter of 50 nm and extends to large particle sizes of close to 1 µm. In addition, a shoulder is observed at 300 nm.

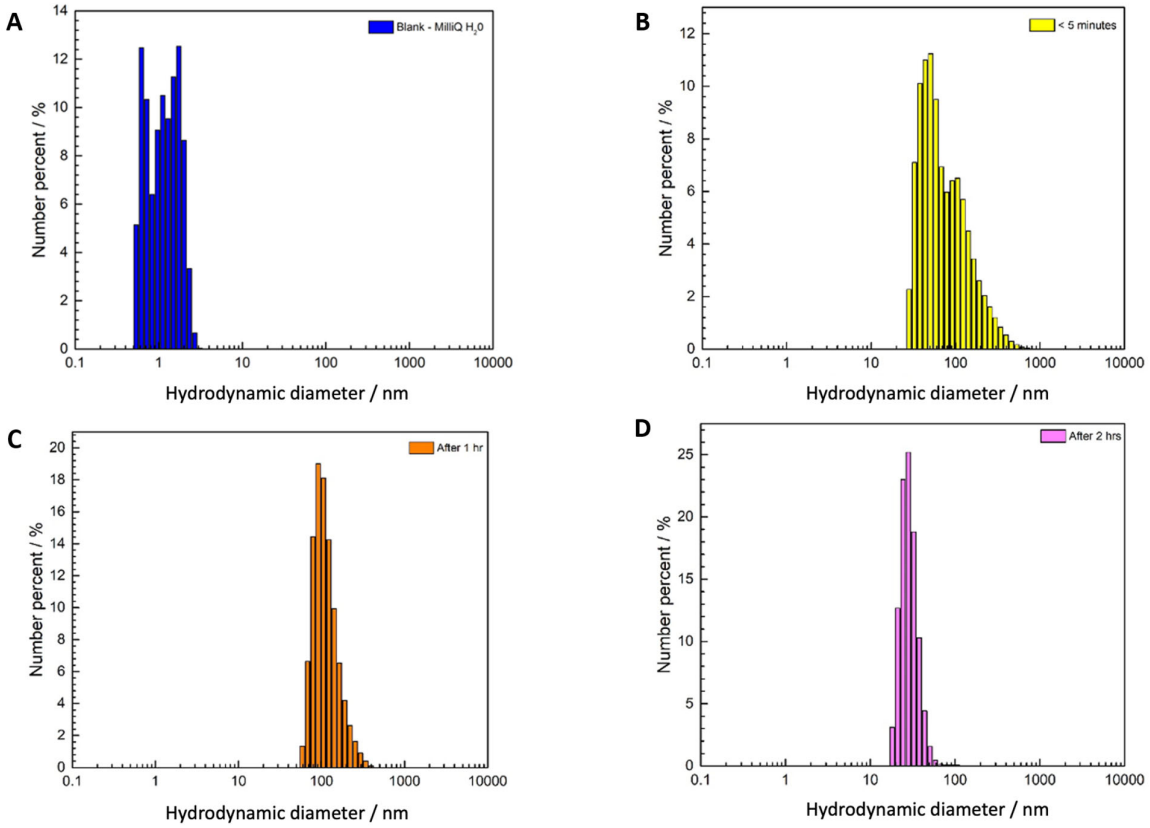

Figure 4.8: DLS size distributions of blank and $LaF_3:Ce^{3+}Tb^{3+}$ NPs at different times A) blank Milli-Q water, B) < 5 min, C) after 1 h and D) after 2 h.

Panel C and D show the DLS distribution by number for the different dispersions after certain storage times (quiescent solution stored at 25°C). The distributions shift markedly to smaller apparent hydrodynamic diameters, showing the originally observed apparent size is not stable. The greater abundance of smaller NPs over time may be attributed to an equilibration of the NP suspension. Initially, larger aggregates or clusters may dominate the size distribution due to incomplete dispersion. However, with time there may be a breakdown of larger aggregates into smaller nanoparticles. Here the surface stabilization agent PVP may contribute to promote a uniform dispersion and to prevent reaggregation. Consequently, individual nanoparticles become more prevalent. Since the particles were found by TEM analyses *(see Figure 4.10)* to be non-spherical the stated *apparent* values of the hydrodynamic diameters do *not* correspond to the *actual* NP size.[207]

In a different experiment, the effect of various PVP concentrations on LaF_3:Ce^{3+} Tb^{3+} NPs was analyzed. 1 mL of 5 mg/mL NPs concentration were dispersed in a suspension composed of 4 mL Milli-Q water and 25 mmol PVP in different ratios *(see Experimental section 4.4.3)*. The optimum ratio was found to be 0.5 mL : 6 mL (Milli-Q water : PVP). As shown in Figure 4.9, the narrow size distribution indicates the presence of NPs, whose apparent hydrodynamic diameter ranges between 5 and 10 nm ± 2 nm.

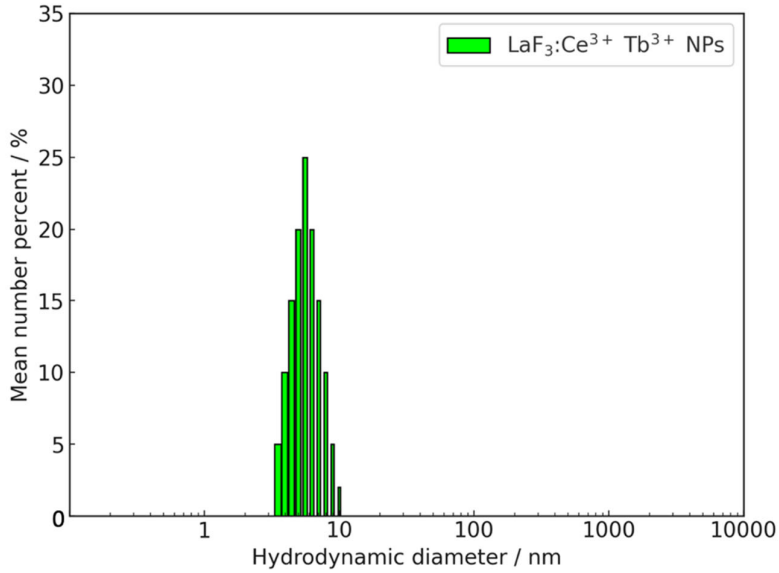

Figure 4.9: DLS size distribution of 5 mg/mL NPs concentration of LaF_3:$Ce^{3+}Tb^{3+}$ NPs dispersed in a suspension of Milli-Q water and 25 mmol PVP.

The mechanism of preventing NP aggregation by using PVP involves according to the literature a combination of steric, electrostatic, and hydrophilic/hydrophobic interactions between the polymer molecules and the NP surface.[203] By adsorbing onto the surface and forming a protective layer, PVP has been reported to help maintain the stability and dispersibility of nanoparticles in solution.[208] The chain length of PVP plays an important role in the stability of NPs and can also influence the particle growth.[209] As a shape-controlling agent, specific crystal faces can be favored, while hindering others during the synthesis. Li et al., successfully prepared LaF_3:Ln^{3+} up–down conversion fluorescent colloidal NCs by a microwave-assisted polyol method and PVP.[210] The results showed that surface-tethered PVP chains make the NCs highly water dispersible. A similar observation was made in this experiment as shown in Figure 4.9.

4.2.3 Morphology investigations by TEM and STEM

DLS, as used above, is a valuable technique for analyzing the size distribution and hydrodynamic properties of spherical NPs in solution. However, DLS alone may not provide sufficient information for a comprehensive understanding of NP characteristics. For instance, while DLS provides information about the diffusion of scatterers, the calculation of the hydrodynamic diameter of NPs with help of the Stokes – Einstein equation requires independent confirmation that they are indeed spherical. The Stokes-Einstein Equation 1 is given by:

$$D = \frac{k_B T}{6\pi\eta r_h} \quad (1)$$

where:

- D is the diffusion coefficient (measured in m^2s^{-1})
- k_B is the Boltzmann constant (1.38×10^{-23} JK^{-1}),
- T is the absolute temperature (K)
- η is the dynamic viscosity of the medium (Pa·s)
- r_h is the hydrodynamic radius of the spherical particle (m).

Given that the Stokes-Einstein equation assumes spherical particles, verifying the shape of the NPs independently is crucial. In addition, the DLS data does not offer any insights into the morphology, crystallinity, or surface structure of the NPs. To unveil these parameters and gain a more complete understanding of NP properties, TEM and STEM were employed in this study. TEM and STEM offer high-resolution imaging capabilities, allowing direct visualization of individual NPs and determination of their size, shape, and internal structure. By complementing DLS data with TEM and STEM analysis, a more comprehensive characterization of the NPs was achieved, facilitating a deeper understanding of their structure-property relationships and guiding further development for various applications.

In this section, TEM images of individual TiO_2, SiO_2 and LaF_3:$Ce^{3+}Tb^{3+}$ and CSNPs of TiO_2@SiO_2@LaF_3:$Ce^{3+}Tb^{3+}$ are discussed. Figure 4.10 shows TEM images of LaF_3:$Ce^{3+}Tb^{3+}$ NPs prepared in 1:1 ratio of EG:PVP.

Both sphere- and rod-like shaped NPs are present. From the images, it can also be seen that the NPs are highly crystalline due to the presence of lattice fringes. The size of the NPs (in terms of length and width) as calculated from the TEM images are 10 nm ± 2 nm and 30 nm ± 5nm for spheres and rod-like shaped NPs, respectively *(see Figure 4.11)*.

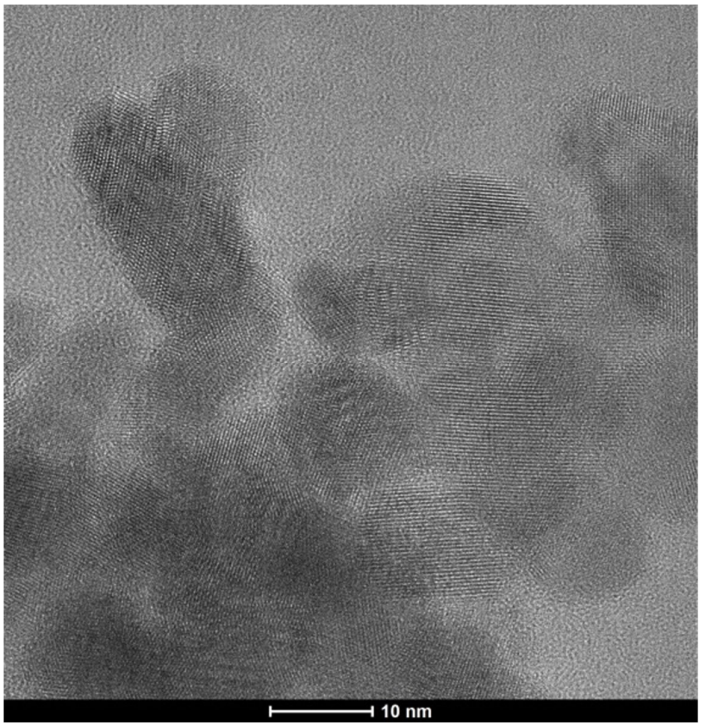

Figure 4.10: TEM images of highly crystalline $LaF_3:Ce^{3+}Tb^{3+}$ NPs prepared in 1:1 ratio of EG:PVP and dispersed in a suspension of Milli-Q water and 25 mmol PVP.

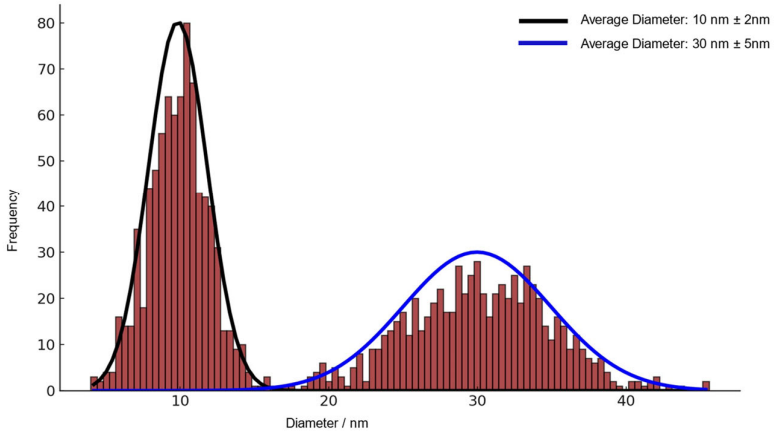

Figure 4.11: Histogram of $LaF_3:Ce^{3+}Tb^{3+}$ NP size with Gaussian fits representing the average diameter in nm. Refer to Figure 4.12 (raw data).

The different shapes are likely a consequence to the presence of both EG and PVP as solvents during the synthesis. Most authors have reported rod-like shapes for LaF_3 NPs prepared in different synthesis routes.[60,211–216] As alluded to above, by using PVP it is possible to control the growth of the NPs on a particular crystal plane due to the long polymer chains, e.g. by favoring the production of spheres. The TEM image in Figure 4.12 presents clearer lattice fringes.

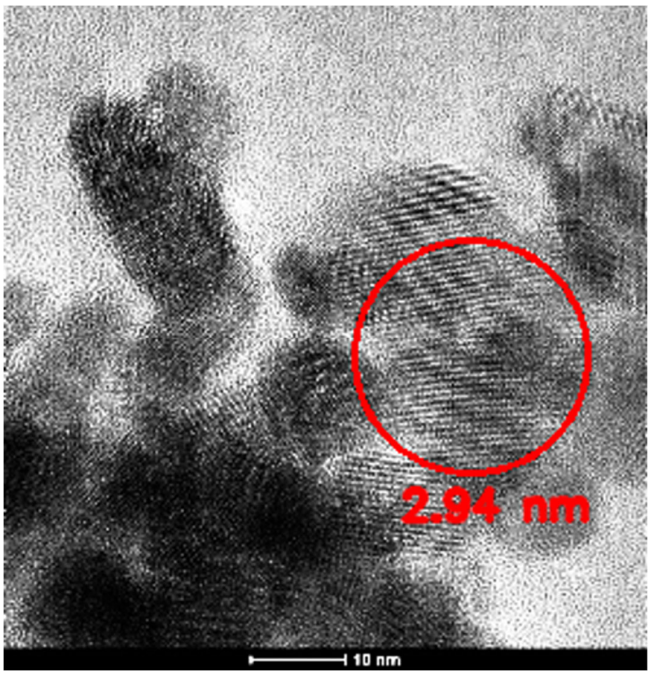

Figure 4.12: Enhanced pixels of 2D image of 4.10 (circled red area shows area used for lattice fringes analysis).

For this analysis ImageJ was used to enhance contrast and measure distances. The lattice fringes were identified, marked, and the distances between them were measured in pixels. The average distance between the lattice fringes was approximately 20 pixels. To convert pixel measurements to nanometers, the scale bar was referenced *(refer to Section 4.4.2)*.

The known interplanar spacings for LaF_3 are as follows: (1,0,0): 6.22 nm, (1,1,0): 3.59 nm, (0,0,1): 7.03 nm, (1,0,1): 4.66 nm, and (1,1,1): 3.20 nm.[187] Hence, the measured spacing of ~ 3 nm agrees with the interplanar spacing of the (1,1,1) plane, which is 3.20 nm, suggesting that the observed fringes correspond to the (1,1,1) planes of LaF_3. The highlighted upper area of the image, marked with a red circle, indicates the region analyzed.

Figure 4.13 shows a TEM image of TiO_2 NPs after 1 h 400°C sintering. NPs size range between 2 and 6 nm ± 1 nm. Sintering is known to increase particle size and rate of agglomeration.[217] However, in this case individual NPs can be identified and their sizes estimated *(see Figure 4.14)*. BMIM[Cl] and BMIM[Br] used during the synthesis creates a protection on the surface of the NPs. Thus, high surface energies on the NPs, which are responsible for agglomeration, are minimized. If the NPs are left longer than 1 h at 400°C in the oven, TiO_2 NPs gradually change color from white to light grey and eventually dark grey. This color change is a result of the decomposed thin ionic liquid layer on the surface of the NPs.

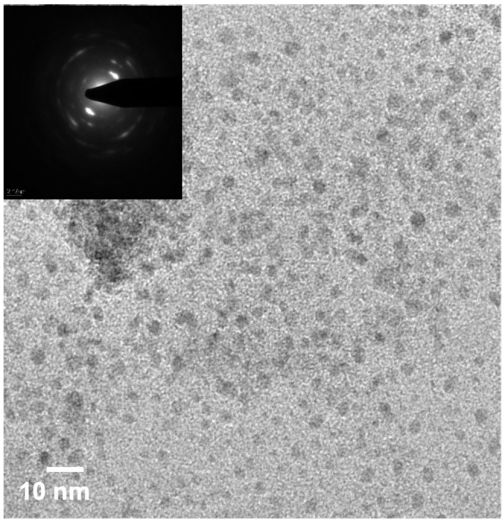

Figure 4.13: TEM image of TiO_2 NPs after 1 h 400°C sintering (inset – selected area electron diffraction).

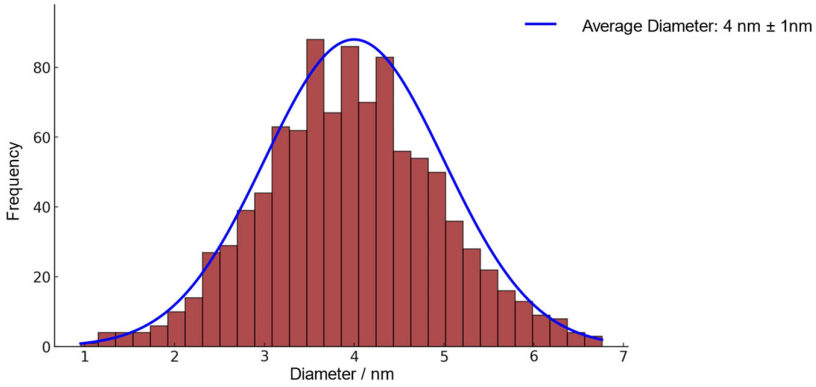

Figure 4.14: Size distribution of the TEM image of TiO_2 NP after 1 h 400°C (gaussian fit representing the average distance in nm). Refer to Figure 4.13 with raw data.

Selected area electron diffraction (SAED) pattern *(Figure 4.13, inset)* was examined to measure the radii of the diffraction rings. The interplanar spacings (d-spacings) corresponding to each ring were calculated using the following Equation 2:

$$d = \frac{\lambda L}{R} \quad (2)$$

where λ is the electron wavelength (0.0251 Å for a 200 kV TEM), L is the camera length (100 cm), and R is the radius of the diffraction ring. The measured values of R and the corresponding calculated d-spacings are presented in Table 4.3. These d-spacings were then compared with standard values for the anatase phase of TiO_2.

Table 4.3: SAED Analysis of TiO_2 NPs.

Ring Index	Measured Radius (mm)	Calculated d-Spacing (Å)	Reference*
1	5.0	5.02	-
2	7.4	3.39	3.52 (101)
3	9.3	2.70	-
4	10.4	2.41	2.37 (004)
5	12.5	2.01	1.89 (200)

*Standard d-Spacing for Anatase TiO_2 (Å) according to Horn et al.[174]

The results show that the calculated d-spacings are in reasonable agreement with the standard d-spacings for anatase.[174] Specifically, the d-spacing calculated for the second ring (3.39 Å) is close to the (101) plane of anatase, which has a standard d-spacing of 3.52 Å and the d-spacing for the fourth ring (2.41 Å) corresponds well with the (004) plane of anatase, with a standard d-spacing of 2.37 Å. In addition, d-spacing for the fifth ring calculated as 2.01 Å is near the standard d-spacing for the (200) plane of anatase, of which is 1.89 Å.

The obtained TiO_2 NPs were redispersed in Milli-Q water and used for the synthesis of TiO_2@SiO_2 via the Stöber synthesis, as mentioned already above.[181] Previous studies used only XRD and UV spectroscopy to support the formation TiO_2@SiO_2 NPs.[173,218] In contrast, many applications prefer using SiO_2 as core and TiO_2 as shell.[182] This is mainly due to the ease of modification of SiO_2 with TEOS chains on the surface of the NPs.

The STEM results *(c.f. Figures 4.15 and 4.16)* obtained from this experiment clearly show the formation of TiO_2@SiO_2 NPs. Furthermore, the presence of TEOS (7 – 8 nm ± 0.3 nm) on the surface of the SiO_2 NPs can be confirmed. Panel (a) reveals the morphology and distribution of pure SiO_2 NPs, showcasing well-defined, spherical particles with a uniform size distribution, as highlighted by the 200 nm scale bar. In contrast, panel (b) depicts the TiO_2@SiO_2@ NPs, illustrating a core-shell structure with a thin TEOS layer formed on the particle's surface, as indicated by the measurements of 7 – 8 nm ± 0.3 nm. The high-resolution STEM image in panel (c) provides a closer examination of the TiO_2@SiO_2@ NPs, revealing a more complex and less uniform structure compared to the pure SiO_2 NPs, with a scale bar of 100 nm. The subsequent elemental mapping panels offer insight into the compositional distribution within the NPs. Panel (d) displays the silicon (Si) mapping, where Si is represented in blue, indicating its presence throughout the nanoparticles. Panel (e) shows the titanium (Ti) mapping in red, highlighting the distribution of Ti within the NPs. Finally, panel (f) integrates the Si and Ti mappings, providing a comprehensive view of the core-shell structure, with Si in blue and Ti in red, confirming the spatial distribution of these elements within the NPs.

To investigate the purity of the NPs, EDX and elemental mapping in the STEM mode were done. No impurities other than the expected contamination peaks of C and Cu were observed. The C peak originates mainly from the carbon film on the TEM grid and slightly from the TEOS on the surface of the NPs.[207,219,220] The small Cu-Kα peak occurs also due to the TEM grid, which is coated with copper.[207,219,220]

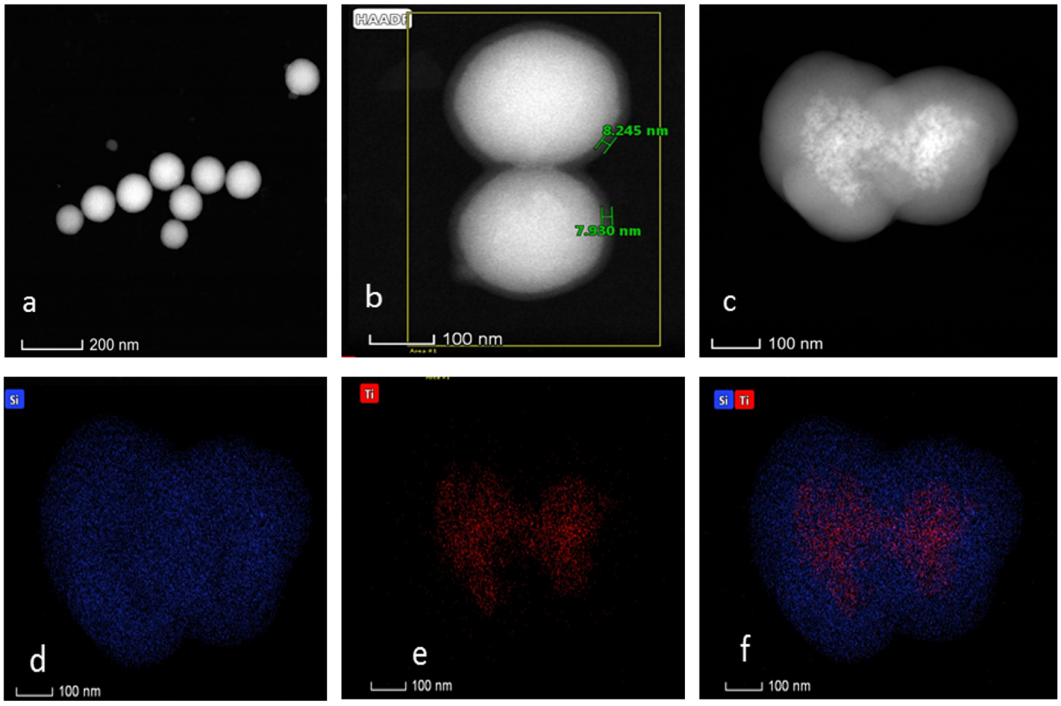

Figure 4.15: STEM images of TiO_2@SiO_2 NPs a) Pure SiO_2 NPs b) TiO_2@SiO_2@TEOS NPs, c) TiO_2 NPs embedded in the center of SiO_2 NPs; d-f) elemental mapping d-Si, e-Ti and f-Si&Ti.

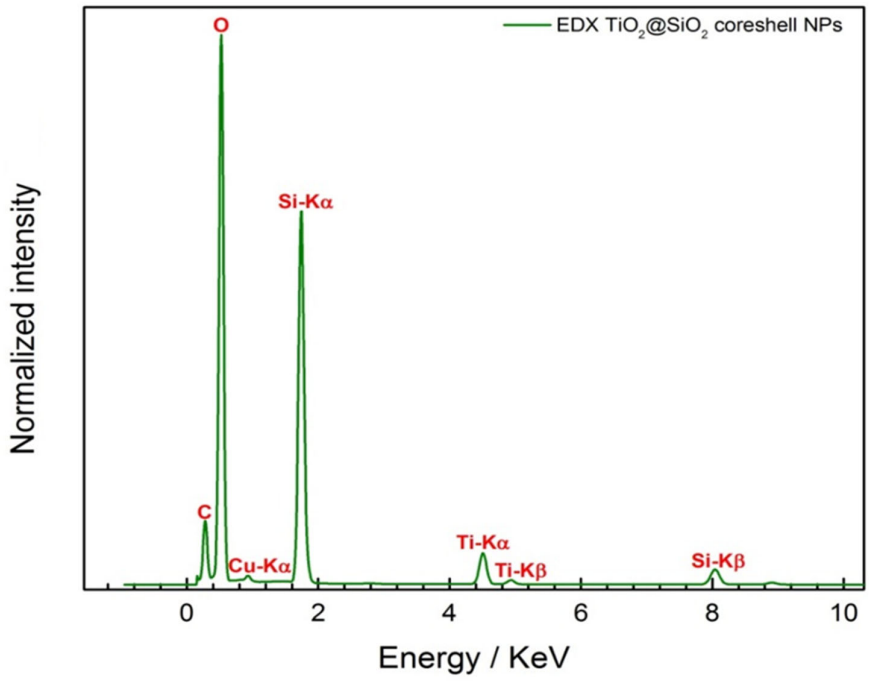

Figure 4.16: STEM-EDX data of TiO_2@SiO_2 NPs on a carbon-coated (Cu) TEM grid.

Table 4.4: STEM-EDX peak positions and energy in keV of TiO_2@SiO_2 CSNPs.

Energy (keV)*	Element	Signal Type
0.277	C	Kα
0.525	O	Kα
0.93	Cu	Lα
1.74	Si	Kα
4.51	Ti	Kα
4.931	Ti	Kβ
8.047	Si	Kβ

*Results energy (keV) compared to JEOL database[220]

Figure 4.17 shows a STEM image of TiO_2@SiO_2@LaF_3:$Ce^{3+}Tb^{3+}$ CSNPs, which provide evidence of CSNPs formation. LaF_3:$Ce^{3+}Tb^{3+}$ was apparently formed randomly on the surface of the SiO_2 in a raspberry-like structure, as shown in Figure 4.17. EDX analysis of the NPs cluster, as shown in Figure 4.18, provides detailed insights into the elemental composition and distribution. Panels (a) to (h) illustrate the spatial distribution of various elements within the cluster.

Panel (a) presents the high-angle annular dark-field (HAADF) image, offering an overview of the NP morphology. Panels (b), (c), and (d) display the EDX maps for Silicon (Si), Oxygen (O), and Titanium (Ti), respectively. The Si signal is observed to be weaker at the center of the cluster, while the Ti signal is stronger in these regions, suggesting a non-uniform SiO_2 shell, potentially with variations in thickness or composition.

Panels (e), (f), and (g) show the distribution of Tb^{3+}, Ce^{3+} and La^{3+}. The co-localization of Tb, Ce, and La signals, particularly at the periphery of the NP cluster, indicates the formation of LaF_3:$Ce^{3+}Tb^{3+}$ patches on the surface of the SiO_2 shell. This is further validated by the composite map in panel (h), which combines Si, Ti, and La signals, highlighting the distinct regions where these elements overlap.

The STEM-EDX spectrum, as shown in Figure 4.18, does not exhibit any signals for any impurities other than Cu and C peaks, which originate from the TEM grid made of copper and a thin carbon film. All the energies (keV) represented agree with the standard energies reported in the literature.[221]

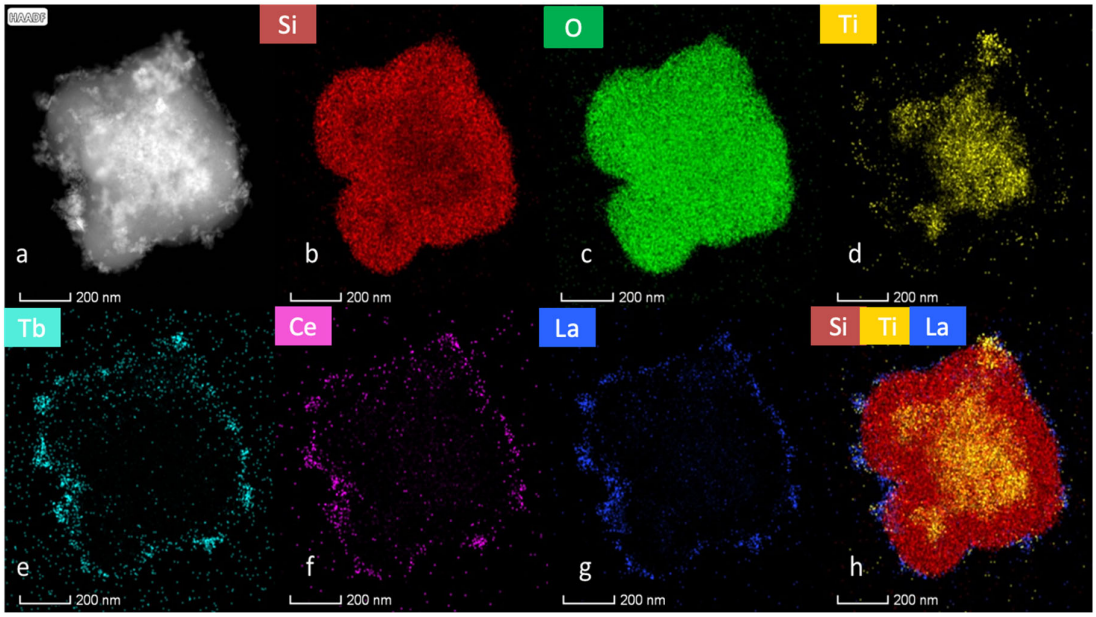

Figure 4.17: STEM images of TiO_2@SiO_2@LaF_3:$Ce^{3+}Tb^{3+}$ NPs a) CSNPs as prepared, b) Si signal, c) O signal, d) Ti signal, e) Tb signal, f) Ce signal and g) La signal, h) superimposed Si, Ti and La signals.

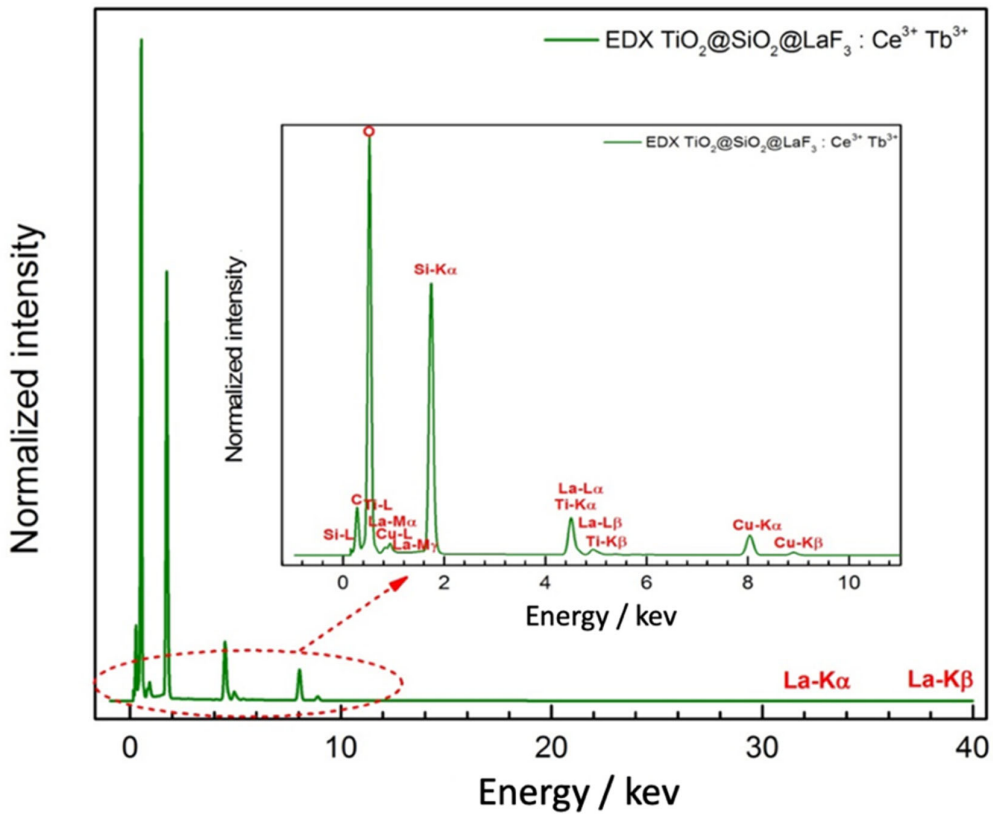

Figure 4.18: STEM-EDX of TiO_2@SiO_2@LaF_3:$Ce^{3+}Tb^{3+}$ NPs on a carbon-coated (Cu) TEM grid.

Table 4.5: STEM-EDX peak positions and energy in keV of TiO_2@SiO_2@LaF_3:$Ce^{3+}Tb^{3+}$ CSNPs.

Peak	Energy (keV)*
Si-L	0.099
C	0.277
Ti-L	0.452
O	0.525
La-Mζ	0.640
La-Mα	0.910
Cu-L	0.930
La-Mγ	1.250
Si-Kα	1.739
Ti-Kα	4.508
La-Lα	4.651
La-Lβ	4.634
Ti-Kβ	4.933
Cu-Kα	8.040
Cu-Kβ	8.904
La-Kα	33.442
La-Kβ	37.797

*Results energy (keV) compared to JEOL database[220]

4.2.4 $KSmF_4$:Ln^{3+} (Ln = Ce, Tb, Eu) NPs

$KSmF_4$:$Ce^{3+}Tb^{3+}$ and $KSmF_4$:Eu^{3+} NPs were successfully prepared using a modified method derived from Wang et al.[85] This synthesis involves a high-temperature decomposition method, in which precursors are dissolved in oleic acid and 1-octadecene, followed by heating to 300°C under an inert atmosphere to form monodisperse NPs. The resulting NPs were highly crystalline with uniform sizes of less than 5 nm, as evidenced by TEM imaging. Figure 4.19 shows the TEM image of $KSmF_4$:$Ce^{3+}Tb^{3+}$ NPs, which appear to be monodispersed with a narrow size distribution of 5 nm ± 2 nm.

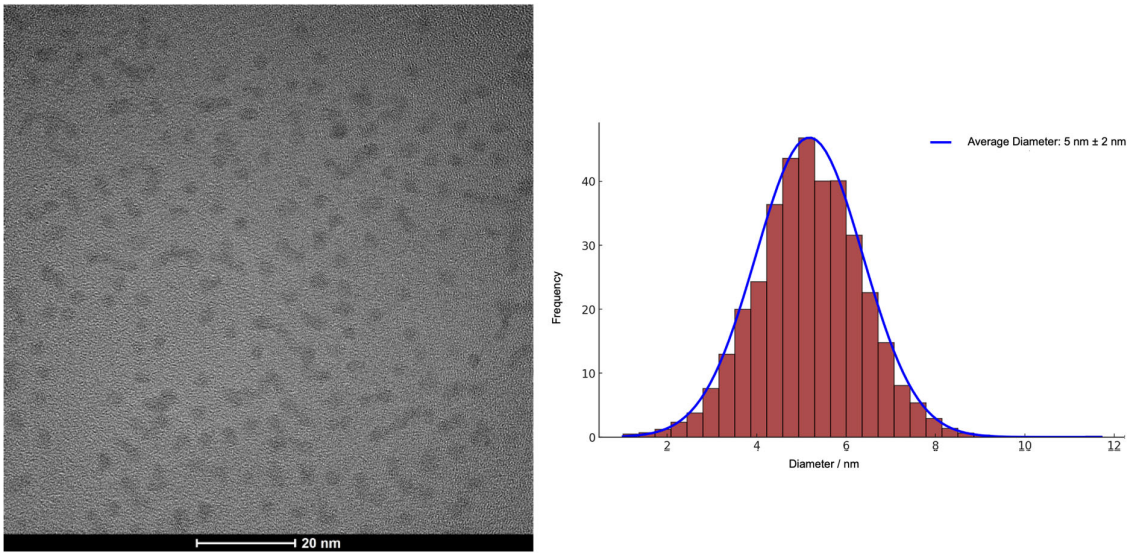

Figure 4.19: TEM image (left) and size distribution (right) of $KSmF_4:Ce^{3+}Tb^{3+}$ NPs.

Figure 4.20 displays the TEM image of $KSmF_4:Eu^{3+}$ NPs. Similar to Figure 4.19, the NPs are uniformly distributed with sizes of 5 nm $\pm$ 2 nm. Figure 4.21 provides the TEM-EDX spectra (left) and SAED pattern (right) of $KSmF_4:Ce^{3+}Tb^{3+}$ NPs. The EDX spectra reveal characteristic peaks at approximately 1 keV, 4-5 keV, and 6-7 keV, corresponding to Samarium (Sm) Lα, Cerium (Ce) Lα and Lβ, and Terbium (Tb) Lα and Lβ emissions, respectively. Additionally, a peak around 0.5 keV is attributed to Fluorine (F) Kα emission. The SAED pattern displayed in Figure 4.21 (right) shows a series of concentric rings, indicative of a polycrystalline structure. Each ring corresponds to a specific set of crystallographic planes, which can be indexed to determine the crystal structure of the $KSmF_4:Ce^{3+}Tb^{3+}$ NPs.

The innermost ring corresponds to the (001) plane, followed by the (100) plane, the (101) plane, the (110) plane, the (200) plane, the (210) plane, the (211) plane, and finally the outermost ring corresponds to the (220) plane.[222,223] The sharpness and clarity of these rings suggest high crystallinity, confirming the successful synthesis of the NPs. The indexing of these rings to specific planes aligns well with the expected crystallographic planes of the $KSmF_4$ structure, further validating the high-quality crystalline nature of the synthesized NPs.

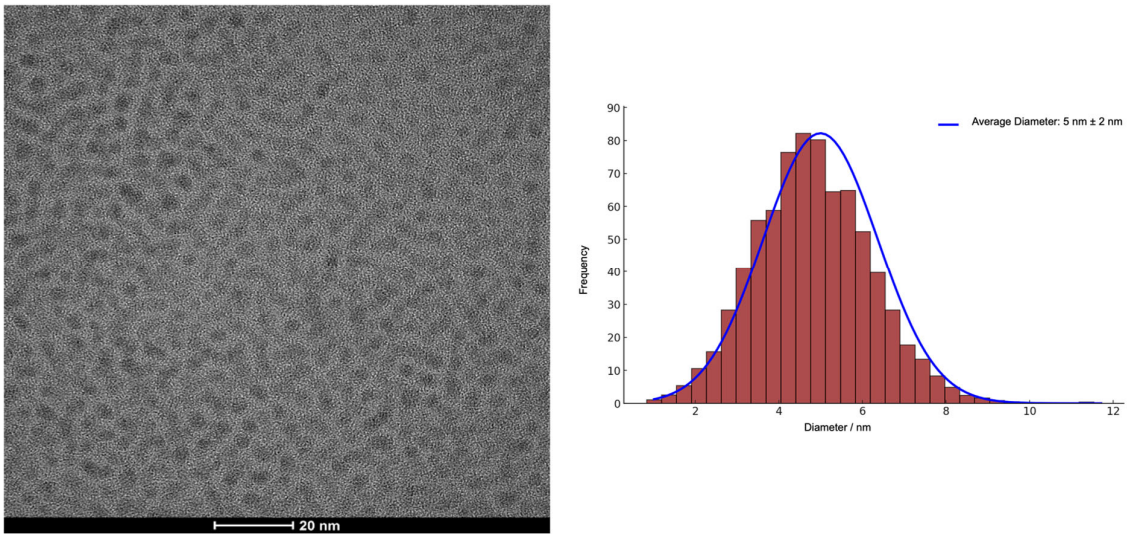

Figure 4.20: TEM image (left) and size distribution (right) $KSmF_4:Eu^{3+}$ NPs.

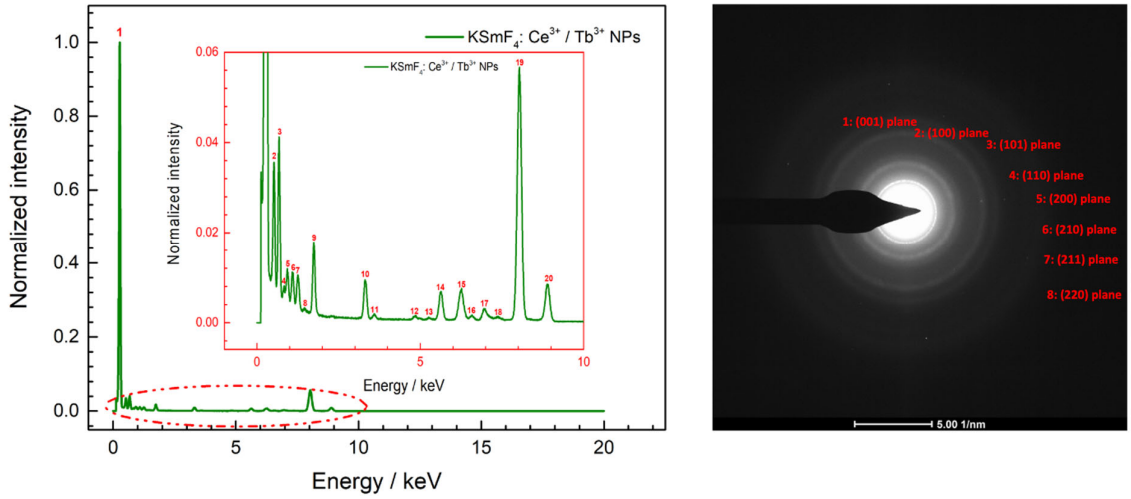

Figure 4.21: TEM-EDX spectra (left) and selected area electron diffraction data (right) of $KSmF_4:Ce^{3+}Tb^{3+}$ NPs.

To enhance the stability and applicability of these NPs in aqueous environments, a ligand exchange process was employed. According to principles outlined by Branca et al., the hydrophobic oleate ligands were replaced with cyclodextrin, a hydrophilic ligand.[224] This ligand exchange enabled the NPs to be dispersed in Milli-Q water, improving their stability and potential for luminescent applications. However, no emission was observed from the prepared $KSmF_4:Ce^{3+}Tb^{3+}$ and $KSmF_4:Eu^{3+}$ NPs *(Figure 4.22)*. This lack of emission could be attributed to the presence of Sm^{3+}, which can act as a quenching center.[106] Non-radiative energy transfer from Ce^{3+}, Tb^{3+}, and Eu^{3+} to Sm^{3+} ions can significantly reduce luminescence.[107]

The overlapping energy levels between Sm^{3+} and the dopant ions facilitate non-radiative transitions, further quenching the emission. High concentrations of Sm can also lead to concentration quenching, where cross-relaxation processes between Sm ions and the dopants increase the probability of non-radiative decay.[106] Additionally, structural distortions caused by the incorporation of Sm ions into the $KSmF_4$ lattice might affect the local environment of Ce^{3+}, Tb^{3+}, and Eu^{3+}, promoting non-radiative decay pathways.

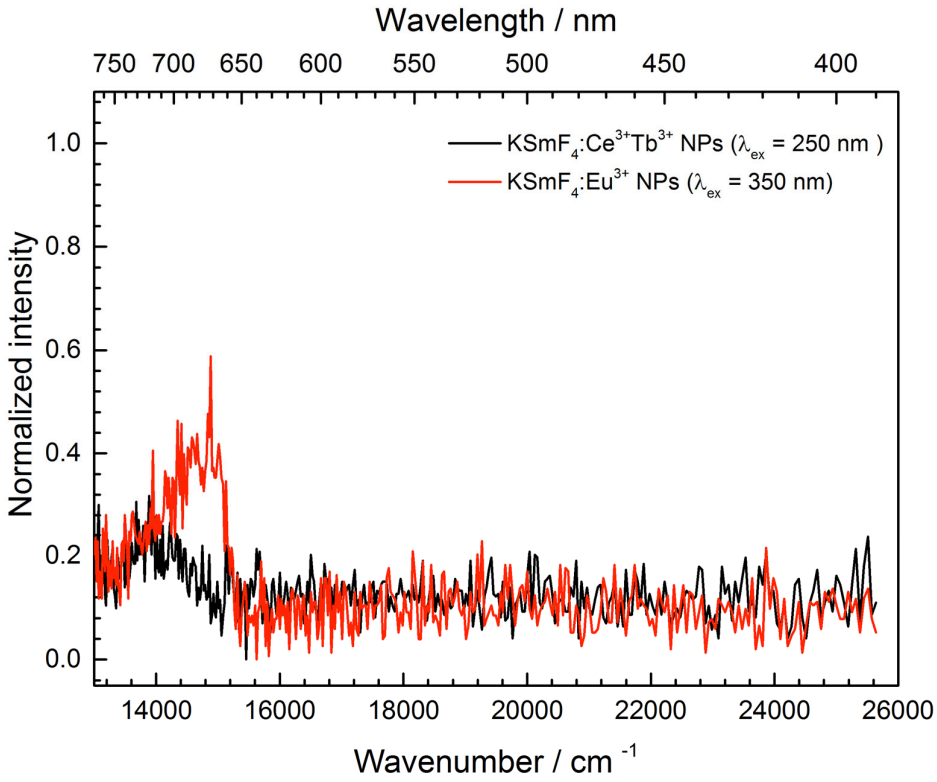

Figure 4.22: Emission spectra of $KSmF_4:Ce^{3+}Tb^{3+}$ and $KSmF_4:Eu^{3+}$ NPs excited at 250 nm and 350 nm, respectively.

These findings contrast with previous studies, such as those by You et al., which required prolonged synthesis times and high-temperature annealing to achieve NP formation, often without clear evidence of crystallinity.[225] The current methodology not only reduces synthesis time and temperature, but also results in NPs that are stable in aqueous solutions post-ligand exchange with cyclodextrin, overcoming stability issues observed in earlier methods. The improved synthesis technique, yielding highly crystalline and monodisperse $KSmF_4:Ce^{3+}Tb^{3+}$, and $KSmF_4:Eu^{3+}$ NPs, demonstrates significant potential for multifunctional applications.

4.2.5 Photoluminescence spectra

The spectral data presented in Figure 4.23 show the absolute intensity of emissions in cps (counts per second) across different wavenumbers and corresponding wavelengths. These data were acquired from a sample of LaF_3:$Ce^{3+}Tb^{3+}$, incorporating PVP as a stabilizing agent *(refer to Figure 4.9)*, under varying thermal conditions (25°C, 35°C, 45°C, 55°C, and 65°C). The motivation for conducting temperature-dependent measurements is to understand the thermal stability of the luminescent properties and investigate energy transfer dynamics. The spectra reveal distinct peaks predominantly those of the $^5D_4 \rightarrow {}^7F_{6\text{-}3}$ transitions of Tb^{3+}, marked by the green dotted line.

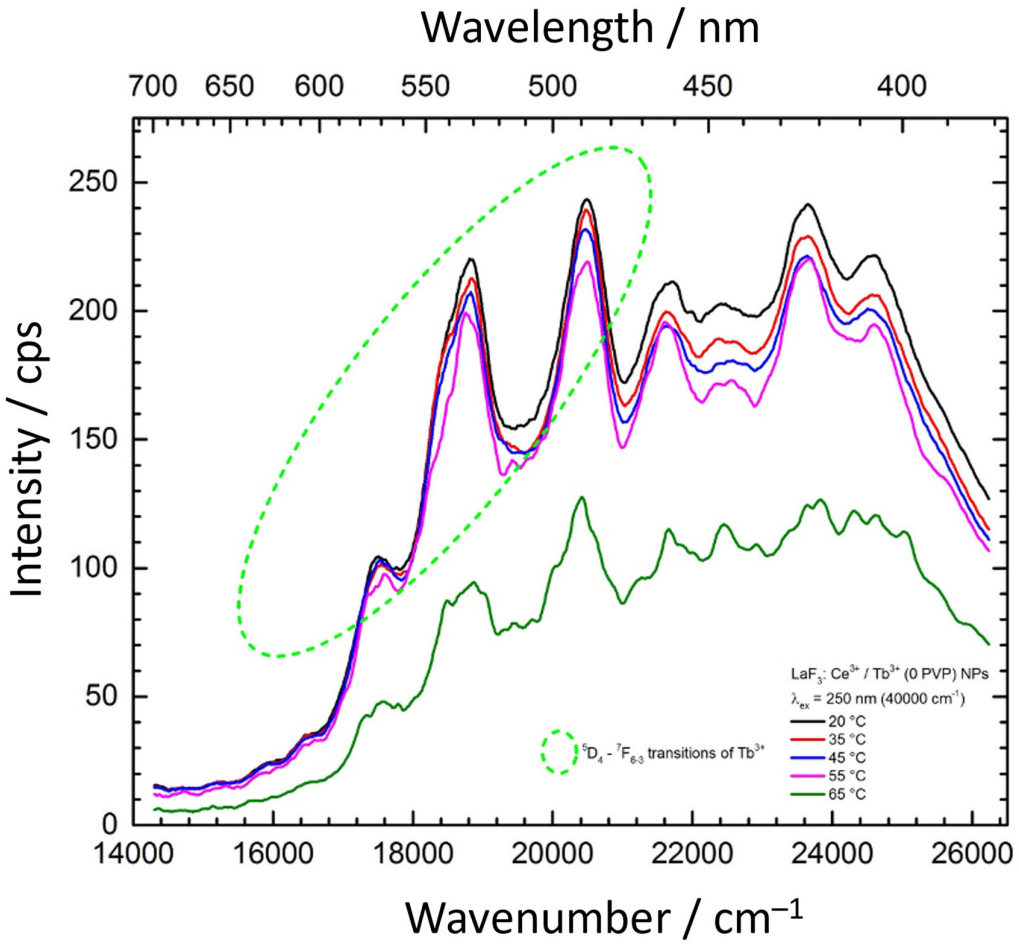

Figure 4.23: Temperature dependent emission spectra of LaF_3:$Ce^{3+}Tb^{3+}$ NPs prepared in 1:1 ratio of PVP and EG and dispersed in Milli-Q water measured after storage time of 10 minutes at 250 nm (40000 cm^{-1}) excitation wavelength.

Notably, the consistent emission peaks between 17000 cm^{-1} and 23000 cm^{-1} are attributed to the characteristic f-f transitions of Tb^{3+}. The results indicate a temperature-dependent variation in emission intensity, where an increase in temperature from 25°C to 55°C generally leads to a decrease in emission intensity. A further increase to 65°C causes a drastic drop in emission intensity. This behaviour suggests that at higher temperatures, the PVP-stabilized NPs lose their steric stabilization in solution. This results in agglomeration of particles, thus consequently reduced emission intensity in the spectra. The additional set of peaks, around 24000 cm^{-1} represents the 4f-5d transitions of Ce^{3+}. These results are in agreement to other literature values.[59,60,226–229]

Table 4.6: Emission bands of $LaF_3:Ce^{3+}Tb^{3+}$ NPs prepared in 1:1 ratio of PVP and EG and dispersed in Milli-Q water (storage time 10 min) measured at 250 nm (40000 cm^{-1}) excitation wavelength.

Peak Position (cm^{-1})	Peak Position (nm)	*Transition (a) & (b)
17000	588	$^5D_4 \rightarrow {}^7F_6$ of Tb^{3+} (a)
18000	556	$^5D_4 \rightarrow {}^7F_5$ of Tb^{3+} (a)
20000	500	$^5D_4 \rightarrow {}^7F_4$ of Tb^{3+} (a)
22000	455	$^5D_4 \rightarrow {}^7F_3$ of Tb^{3+} (a)
24000	417	4f-5d transitions of Ce^{3+} (b)

*Transitions compared to references from: (a) Carnall et al., *J. Chem. Phys*., **1989**[230] & (b) Dorenbos, *J. Phys. Condens. Matter.,* **2003**[107]

Figure 4.24 shows normalized emission spectra of $LaF_3:Ce^{3+}Tb^{3+}$ NPs stabilized with citrate, for excitation at 250 nm as well as 350 nm. The spectrum obtained with an excitation wavelength of 250 nm (solid green line) shows prominent peaks around 18000 cm^{-1} (~555 nm), 20000 cm^{-1} (~500 nm), and 22000 cm^{-1} (~455 nm), with smaller peaks near 24000 cm^{-1} (~417 nm). The high overall intensity indicates that excitation at 250 nm effectively induces strong luminescence from the Tb^{3+} ions in the NPs.

These peaks correspond to characteristic electronic transitions of Tb^{3+} ions, particularly the $^5D_4 \rightarrow {}^7F_J$ transitions, with the strong peak around 555 nm linked to the $^5D_4 \rightarrow {}^7F_5$ transition. Similar results have been observed in other studies, where the $^5D_4 \rightarrow {}^7F_5$ transition at 545-555 nm is a dominant emission band in Tb^{3+}-doped materials.[231]

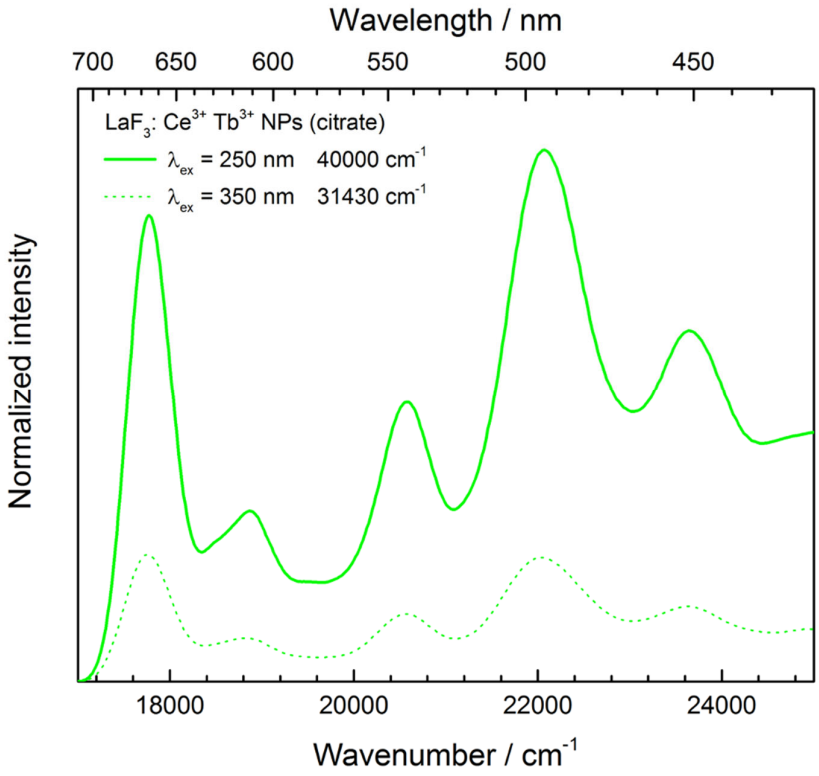

Figure 4.24: Emission spectra of LaF_3:$Ce^{3+}Tb^{3+}$ NPs stabilized with citrate and dispersed in Milli-Q water measured at 250 nm (40000 cm^{-1}) and 350 nm (31430 cm^{-1}) excitation wavelengths.

In contrast, the spectrum obtained with an excitation wavelength of 350 nm (dashed green line) shows similar peaks, but with significantly lower intensity, indicating that 350 nm is less effective in exciting the Tb^{3+} ions. The peaks correspond to the same electronic transitions, but the reduced efficiency suggests that 350 nm is not the optimal excitation wavelength for maximizing emission from these ions. This observation aligns with findings from the literature, where the excitation of Ce^{3+} at shorter wavelengths (around 250 nm) has been shown to result in more efficient energy transfer to Tb^{3+} ions, leading to stronger emission compared to longer wavelengths.[232]

The comparative analysis reveals that 250 nm excitation is far more efficient due to better matching with the absorption bands of the Ce^{3+} ions, facilitating effective energy transfer to the Tb^{3+} ions. This difference in intensity underscores an efficient energy transfer mechanism from Ce^{3+} to Tb^{3+} at 250 nm, leading to strong emission, whereas at 350 nm, the energy transfer is less efficient, resulting in weaker emission.

Figure 4.25 shows photoluminescence spectra of $LaF_3:Ce^{3+}Tb^{3+}$, excited at 250 nm and 344 nm, recorded at temperatures of 10 K and 300 K. These spectra offer significant insights into the material's luminescent behavior. The spectra at 10 K were measured to reduce thermal quenching effects, to resolve fine spectral features (especially the region around 400 nm), and to understand energy transfer mechanisms. This approach provides a comprehensive understanding of the intrinsic luminescent properties.

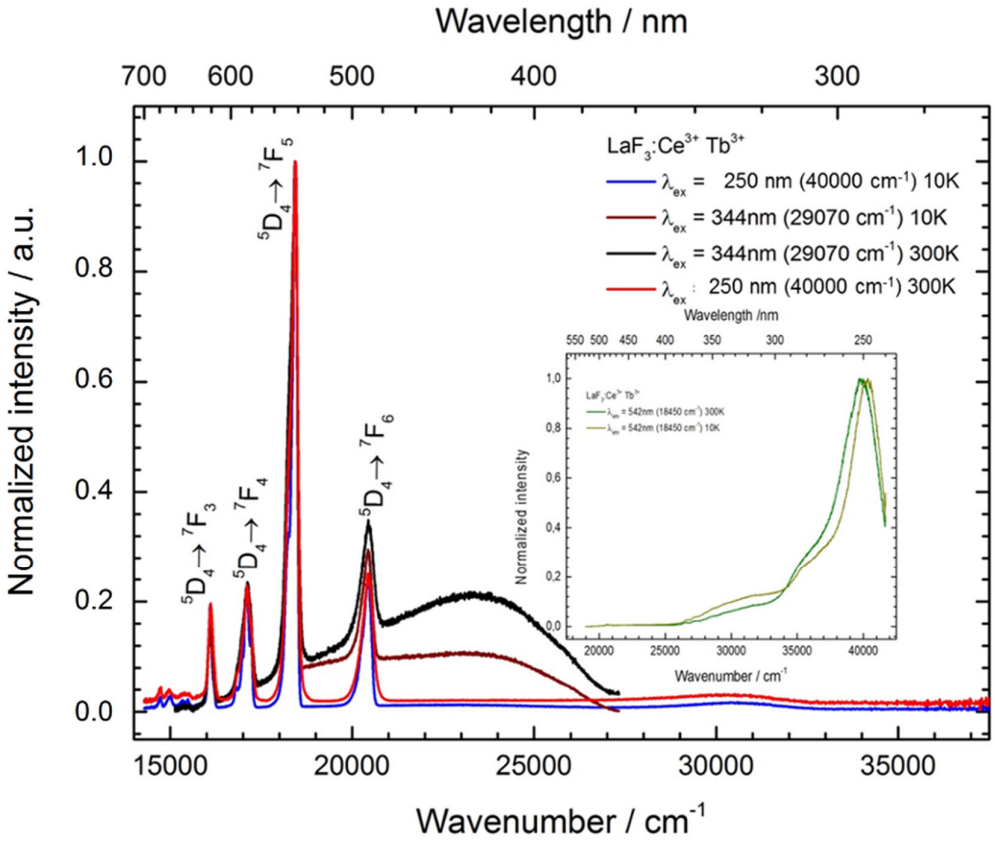

Figure 4.25: 10K and 300K emission spectra measured at excitation wavelengths 250 nm (40000 cm^{-1}) and 344 nm (29070 cm^{-1}), respectively, for dried $LaF_3:Ce^{3+}Tb^{3+}$ NPs. The inset shows the 10 K and 300 K excitation spectra at emission wavelength 542 nm (18,450 cm^{-1}).

The spectra reveal several prominent peaks, notably around 16200 cm^{-1} (617 nm), 18940 cm^{-1} (528 nm), 21000 cm^{-1} (476 nm), and 24000 cm^{-1} (417 nm). These peaks correspond to the well-known transitions $^5D_3 \rightarrow {}^7F_5$, $^5D_4 \rightarrow {}^7F_4$,$^5D_4 \rightarrow {}^7F_5$, and $^5D_4 \rightarrow {}^7F_6$, respectively.[228] The intensity of these transitions is appreciably higher at 10 K compared to 300 K, and excitation at 250 nm yields the most significant intensities. This trend is indicative of reduced vibrational effects in the different excited states.[107]

Observed spectral features agree with the literature, affirming the positions and characteristics of the Tb^{3+} transitions within the LaF_3 matrix.[213,233] Additionally, the variation in luminescence intensity with excitation wavelength underscores the absorption properties and energy transfer dynamics of Ce^{3+} and Tb^{3+} ions. Higher energy excitation at 250 nm populates higher energy levels more effectively, facilitating energy transfer and resulting in improved luminescence.[107]

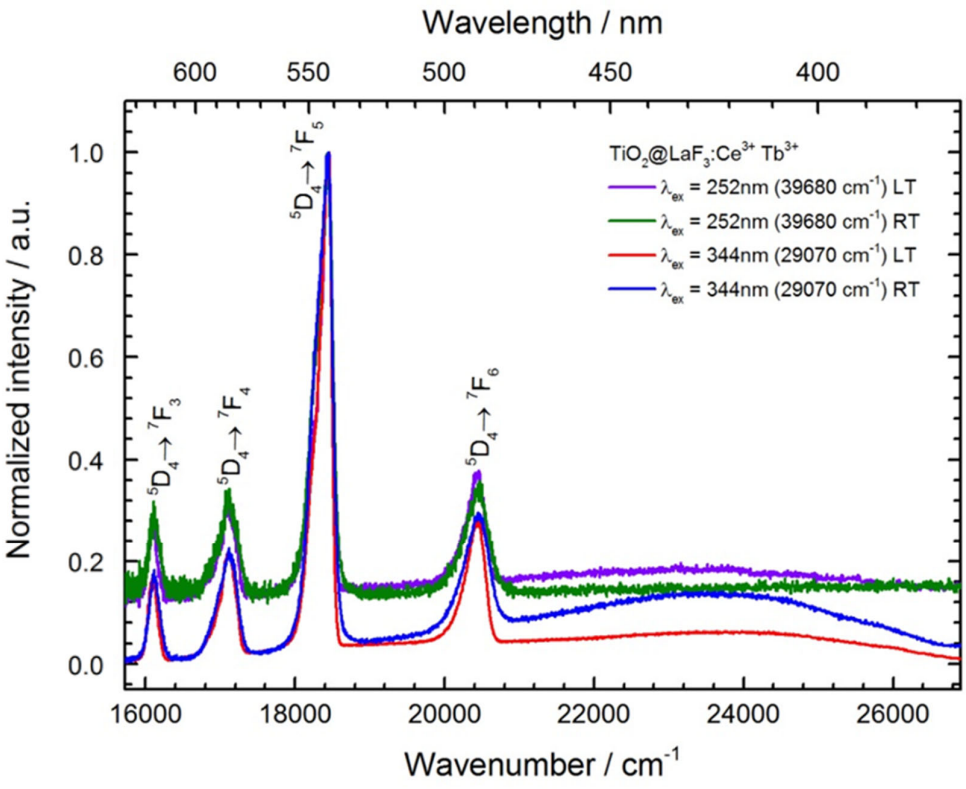

Figure 4.26: 10K and 300K emission spectra measured at excitation wavelengths 252 nm (39680 cm^{-1}) and 344 nm (29070 cm^{-1}), respectively, for dried CSNPs TiO_2@SiO_2@LaF_3:$Ce^{3+}Tb^{3+}$.

Comparatively, similar studies on LaF_3:$Ce^{3+}Tb^{3+}$ NPs have reported analogous peak positions and transitions, yet variations in intensities and temperature dependence are noted. For instance, Liu et al.,[76] observed similar higher intensity at lower temperatures. Furthermore, Chen et al.,[234] documented similar excitation wavelength dependence also with slightly shifted peak positions, likely due to differences in crystal field environments and nanoparticle size effects.[235]

Figure 4.26 shows 10 K and 300 K emission spectra of TiO_2@SiO_2@LaF_3:$Ce^{3+}Tb^{3+}$ CSNPs measured at 252 nm and 344 nm excitation wavelengths. The excitation spectra *(see Figure 2.27)* were measured at 542 nm emission wavelength. Compared to the sample with only LaF_3: $Ce^{3+}Tb^{3+}$ NPs, the excitation band at 344 nm is more intense and broader in both 10 K and 300 K. This is possible because part of the UV excitation energy required is absorbed by the TiO_2 and SiO_2 in the NPs.[236] However, these effects do not entirely quench the emission of the Tb^{3+}. Both crystalline TiO_2 and SiO_2 NPs are known to quench the photoluminescence of lanthanides especially TiO_2 NPs in anatase and rutile phases.[237,238] This is because SiO_2 readily absorb UV light thus reducing the excitation intensity, whereas, TiO_2 especially anatase is known to have many oxygen vacancies that eventually lowers the site symmetry.[237] Low site symmetry favors self-trapped excitons, which eventually quench the photoluminescence.[239–241]

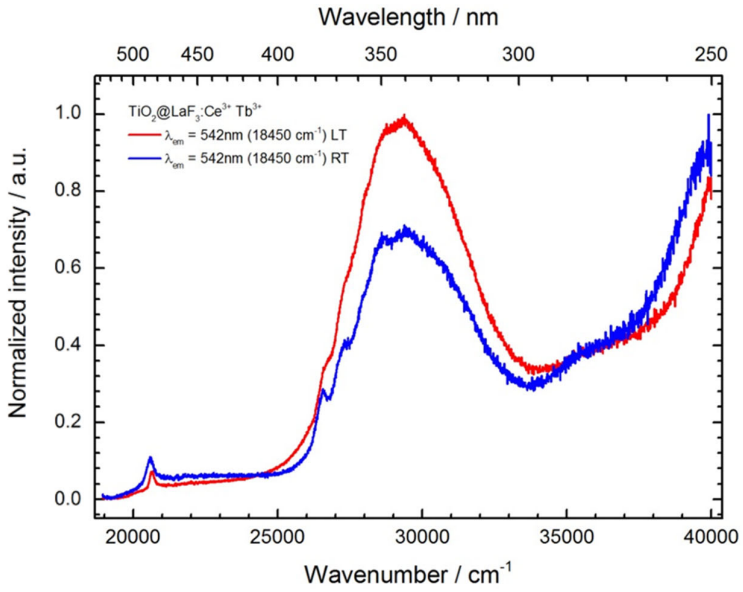

Figure 4.27: 10K and 300K excitation spectra measured at emission wavelength 542 nm (18450 cm^{-1}) for dried CSNPs TiO_2@SiO_2@LaF_3:$Ce^{3+}Tb^{3+}$.

4.3 Conclusion

This Chapter reported on the synthesis, stabilization, and optical properties of lanthanide-doped luminescent NPs and CSNPs, specifically LaF_3:$Ce^{3+}Tb^{3+}$, TiO_2@SiO_2@LaF_3:$Ce^{3+}Tb^{3+}$, and $KSmF_4Ln^{3+}$ (Ln = Ce, Tb and Eu). The primary objectives were to synthesize multifunctional NPs exhibiting stable photoluminescence for potential applications in bioimaging and sensing technologies.

The synthesis of TiO_2 NPs was achieved via controlled hydrolysis of $TiCl_4$ using the ionic liquids BMIM[Cl] and BMIM[Br], demonstrating a rapid and efficient method facilitated by microwave heating. The resulting TiO_2 NPs predominantly exhibited the anatase phase, confirmed through XRD analysis, with post-synthesis sintering at 400°C to remove excess ionic liquids without altering NP size significantly. This method underscores a novel approach to synthesizing TiO_2 NPs with controlled size and morphology, suitable for subsequent functionalization. Utilizing the Stöber synthesis method, TiO_2 NPs were successfully encapsulated within a uniform silica shell, forming TiO_2@SiO_2 CSNPs. Characterization via SEM, TEM, STEM, FTIR spectroscopy and XRD revealed the amorphous nature of the SiO_2 shell, which masked the TiO_2 peaks. This encapsulation strategy offers moiety for suitable biological applications.

Employing BMIM[BF_4] as a fluorine source and solvent, TiO_2@SiO_2@LaF_3:$Ce^{3+}Tb^{3+}$ core-shell NPs were synthesized, resulting in a shell of LaF_3:$Ce^{3+}Tb^{3+}$ NPs. XRD and FTIR spectroscopy analyses confirmed the formation and structural integrity of these multilayered NPs. This method presents simplified synthesis route for creating complex core-shell structures, reducing the need for multiple reagents and synthesis steps.

$KSmF_4Ln^{3+}$ (Ln = Ce, Tb and Eu) NPs were synthesized using a modified known protocol. Ligand exchange with cyclodextrin improved their dispersion in aqueous environments, though luminescence was quenched by Sm^{3+} acting as a quenching center. This experiment highlights a novel synthesis and post-synthesis modification approach that enhances NP stability in aqueous environments, crucial for potential biomedical applications. Thus far there were no reports on NP synthesis of this nature and only bulk materials are known.

Temperature-dependent photoluminescence studies of LaF_3:$Ce^{3+}Tb^{3+}$ NPs revealed stable emission characteristics, with efficient energy transfer from Ce^{3+} to Tb^{3+} at an excitation wavelength of 250 nm. Despite partial quenching by the TiO_2 and SiO_2 layers, TiO_2@SiO_2@LaF_3:$Ce^{3+}Tb^{3+}$ CSNPs exhibited notable photoluminescence. Identification of optimal excitation wavelengths that maximize luminescence is crucial for designing effective bioimaging agents and constitutes a novel finding in this study. This is the first time photoluminescence of TiO_2@SiO_2@LaF_3:$Ce^{3+}Tb^{3+}$ CSNPs is reported.

In summary, this research successfully synthesized and characterized various lanthanide-doped luminescent NPs, each with unique properties and potential applications. The novel synthesis methods and comprehensive characterization techniques employed here provide a foundation for further explorations in nanoparticle-based luminescent materials. These findings highlight the potential of such NPs for bioimaging and sensing applications. The results presented in this Chapter also lay a solid foundation for future research aimed at optimizing these NPs for specific biomedical applications, considering their optical properties and biocompatibility in detail.

4.4 Materials and methods

BMIM[Cl] (99%), BMIM[Br] (99%) and BMIM[BF_4] (99%) were purchased from io-li-tech, Heilbron Germany. $TiCl_4$ metal basis (99.99%), $La(NO_3)_3$•$6H_2O$ (99.999%), $TbNO_3)_3$•$6H_2O$ (99.999%), $CeCl_3$•$7H_2O$ (99.999%), from Alfa Aesar, Germany. $EuCl_3$•xH_2O (99.99%) Reacton Germany. $Eu(NO_3)_3$•xH_2O (99.9%), ChemPur Germany, Lanthanum (III), Terbium (III), Cerium (III), Samarium (III) and Europium (III) acetates (99.999%) Alfa Aesar Germany. TEOS (99+%), NH_4F (96%), NH_4OH (50% v/v aq. Solution), KOH pellets (85%), Trisodium citrate dihydrate (99%), NaF (99%), ethylene glycol (99+%), ethanol denatured (90%), ethanol anhydrous (99+%), methanol (99.8%), cyclohexane (99+%), alpha-cyclodextrin (97%), Polyvinylpyrrolidone, M.W. 10,000 Alfa Aesar Germany. *Trace*CERT®, 1 g/L La, Tb & Ce in nitric acid (nominal concentration), Sigma Aldrich Germany. SiO_2 nanopowder 10-20 nm particle size, 99.5% trace metals basis from Sigma Aldrich Germany. H_2SO_4 (95–97%) purchased from Riedel de Haën. Milli-Q water (resistivity of 18.2 MΩ cm), from a Millipore Direct Q8 system, (Millipore Advantage A10 system, Schwalbach, Germany) with a Millimark Express 40 as filter (Merck, Germany).

4.4.1 XRD sample preparation

Before the measurement was done, the crystals had to be ground as fine powder. This was done in order to obtain spherical particles, which enhances the random orientation of the crystals. Silicon grease was spread on a thin polyethylene foil clipped on the sample holder for fixation of the powder sample. SiO_2 was used as calibration standard for the measurement. The calibration standard was placed on the first slide, and then followed by the other samples *(c.f. figure 4.35)*. After sample application, the top was covered with a thin plastic foil to prevent sample mixing.

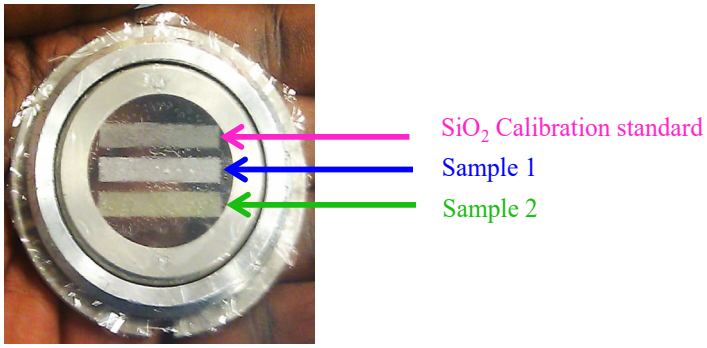

Figure 4.35: XRD sample holder with three-sample application slides.

The separator is then mounted on to the clamp in the instrument adjacent to the camera, which contains an imaging plate (IP) for recording the measurement. The measurement is run for 10 minutes. Measurements were performed using STOE-Stadi powder diffractometer, (Karlsruhe) with Cu Kα radiation (λ = 1.54 Å). The read-out process of the IP was achieved using a Typhoon FLA 7000 instrument with a 650 nm laser, 25 μm pixel size, grid mode, Photomultiplier tube (PMT) 1000 and a reading time of 4 minutes. Samples were identified using STOE Win XPOW software48 and further processing was performed with origin v. 9.0.63. The resulting diffraction patterns were compared to crystallographic information files (cif) from the inorganic crystal structure database (ICSD) database, Karlsruhe.[242]

4.4.2 DLS, TEM and STEM sample preparation

The stability of the NPs in dispersion was investigated in a Nanosizer ZS, Malvern Instruments using polystyrene cuvettes from Sarstedt AG & Co. KG, Germany. All samples prepared for DLS, TEM and STEM were filtered using polytetrafluoroethylene (PTFE) 0.45 μm filter (from Thermo Fischer Scientific, Germany) to remove any dust particles accumulated in the air. The glass tubes and glass petri dishes used for storage were rinsed with ethanol and filtered Milli-Q water several times before usage. A series of dilution steps (1:10, 1:25, 1:50, 1:100 and 1:250) of the NP solution was made. Before pipetting, samples were sonicated for 10 minutes and mixed thoroughly using a 1000 μL Eppendorf pipette. For TEM and STEM samples, 50 μL solution was pipetted and dropped on a carbon-coated copper grid (Plano, 200 mesh), dried overnight in a desiccator (0.1 mbar, Ar atmosphere). After drying, the samples must be covered and sealed with Parafilm to prevent any contamination. Caution must be taken when handling the TEM grid with tweezers. The tweezers must be washed with Milli-Q water after each sample handling. TEM grid is handled only from the edges. All samples were investigated and images with appreciable number of NPs selected for analysis. The morphology and size of the NPs was analyzed using a FEI Talos F200X electron microscope (Thermo Fisher Scientific, Waltham) that is equipped with a Super-X EDX detector, at an acceleration voltage of 200 kV and HAADF detector for STEM images. Colors for atomic mapping were chosen arbitrarily based on the HAADF detector response for individual experiment. Hence, each STEM measurement resulted to a different color signal for each atom.

To determine the size distribution of NPs from TEM images, ImageJ software is used. The scale bar, is read from the software in pixels and recalculated to nm. The calculated distance in nm was determined by multiplying the measured distance in pixels by the ratio of the scale bar length in nanometers to the scale bar length in pixels. Using the formula: distance in nm = (distance in pixels / scale bar length in pixels) * scale bar length in nanometers, the distance between the lattice fringes is thus estimated in nm. Images recorded have not been edited or painted using any software and are reported as captured by the instrument.

4.4.3 Stabilization of NPs with citric acid and PVP

To stabilize LaF_3:$Ce^{3+}Tb^{3+}$ NPs with citric acid, 3.0000 g ± 0.0002g of trisodium citrate dihydrate was dissolved 35 mL Milli-Q water. The solution was neutralized by stepwise addition of NH_4OH, until pH 6 was attained. The pH was controlled using Whatman® indicator papers from Millipore Sigma. For this experiment NaF (0.2660 g) was used instead of BMIM[BF_4]. 3 mL Milli-Q water was added to the NaF and stirred until all the powder dissolved. The other lanthanide salts were dissolved in 3 mL methanol and transferred to the solution containing NaF and stirred for 2 h. LaF_3:Ce^{3+} Tb^{3+} NPs eventually precipitated, when excess ethanol was added to the mixture. The mixture was transferred into a polypropylene (PP) 50 mL centrifuge tube from VWR™ and centrifuged (Fischer Scientific AccuSpin Instrument) @ 5000 rpm for 5 minutes to separate NPs from the solution. The solvent was decanted and 5 mL of anhydrous ethanol added. The centrifugation was repeated 5 times with ethanol and Milli-Q water, alternatingly. The second and third samples are also redispersed in ethanol and prepared for particle size distribution experiment (DLS and STEM analysis), luminescence measurements and cell studies. For stabilization experiment with PVP needed for synthesizing TiO_2@SiO_2@LaF_3:$Ce^{3+}Tb^{3+}$ CSNPs, ethylene glycol (EG) initially used in procedure 4.4.5.3 was substituted and progressively decreased from 20 mL to 0 mL, while the PVP volume was correspondingly increased from 0 mL to 20 mL. The experimental conditions began with 20 mL of EG and 0 mL of PVP, followed by incremental reductions of 2 mL in EG, accompanied by equivalent increments in PVP. This gradient continued until the final condition of 0 mL EG and 20 mL PVP was achieved.

4.4.4 Photoluminescence measurements

The luminescence spectra of the NPs were measured as dry powder (fluorolog 3-22 Jobin Yvon fluorescence spectrometer) and as dispersion (Varian Cary 100 Bio Spectrophotometer with baseline correction) in Milli-Q water. The instrument is fitted with a 450W and 150W xenon lamp. The former was used for emission, excitation and quantum yield measurements, while the latter was used for lifetime measurements. Recording and evaluation of the luminescence spectra was done with FluorEssence v.3.5,[243] embedded in an OriginPro © v. 8.0.[244] A He-cryostat (Janis, Wilmington) with a regulation unit for temperature control (Lake Shore) for measurements at 10K and temperature dependent measurements between 10K and 300K. For both excitation and emission spectra, correction of the signal is required. In the emission spectra, the signal was corrected with respect to the sensitivity of the photomultiplier tube. For the excitation spectra, the correction was done with respect to a reference detector, which is a Si- diode to correct for the lamp spectrum. Before the emission and excitation measurements were performed, a synchronous measurement was undertaken to determine the approximate maximum positions of the emission and excitation wavelength. A fixed offset was chosen, while the emission and excitation wavelengths were varied. During emission measurements, the excitation wavelength was kept fixed, while the emission wavelength was varied over an energy range lower than the excitation energy.

4.4.5 Synthesis procedure

4.4.5.1 TiO_2 NPs via ionic liquids

TiO_2 cores were prepared by adding equal amounts of BMIM[Cl] and BMIM[Br] (0.5000 g), followed by stirring in 50 mL microwave glass vessel. 700 µL of anhydrous ethanol and 300 µL of Milli Q were added to the ionic liquid mixture followed by mild stirring to avoid splashing of the contents. 500 µL of $TiCl_4$ were carefully added while stirring and a clear yellow solution was formed. Stirring was done until all the white and yellow flakes were completely dissolved. $TiCl_4$ was handled only in the fume hood due to its corrosive nature. The solution is left to cool down to approximately 25°C before transferring to the CEM microwave. The reaction was left to run for 10 minutes at 10 bar, 100°C, 100 W. The glass vessel was removed only after the temperature in the microwave dropped below 30°C.

Transfer the contents in to a 50 mL centrifuge tube followed by centrifuging @ 5000 rpm for 5 minutes to separate the NPs from the solution. Decant the solvent and add 1 mL of anhydrous ethanol. Thereafter, centrifuge 6 times with ethanol and Milli-Q water alternately. The whole experiment was repeated 3 times. One portion of the sample is dried at 60°C in an oven overnight and prepare for XRD. The excess ionic liquid remaining on the surface of the NPs was removed by sintering at 400°C for 1 h. The second sample is redispersed in 1 mL ethanol for second step of preparing TiO_2@SiO_2 CSNPs. The third sample is also redispersed in ethanol and prepared for particle size distribution experiment (DLS and TEM analysis).

4.4.5.2 TiO_2@SiO_2CSNPs

The freshly prepared TiO_2 NPs were added to 3.0 mL NH_4OH, 28.8 mL H_2O and 26.5 mL ethanol in a beaker. In the normal Stöber synthesis 27.5 mL ethanol is used.[181] In a separate beaker 1.5 mL TEOS was added to 30 mL ethanol and stirred for 5 minutes. The beaker containing NPs was added to the second beaker dropwise while stirring. The mixture was sonicated for 10 minutes and left to stir for 2 h. Followed by centrifuging 6 times with ethanol and Milli-Q water alternately @5000 rpm for 5 minutes. The whole experiment was repeated 3 times. One portion of the sample is dried at 60°C in an oven overnight and prepared for XRD.

The second sample is redispersed in 1 mL ethanol for third step of preparing TiO_2@SiO_2@LaF_3:$Ce^{3+}Tb^{3+}$ CSNPs. The third sample is also redispersed in ethanol and prepared for particle size distribution experiment (DLS and STEM analysis).

4.4.5.3 TiO_2@SiO_2@LaF_3:$Ce^{3+}Tb^{3+}$ CSNPs

LaF_3:$Ce^{3+}Tb^{3+}$ NPs were prepared according to a known literature protocols but modified for further investigations.[226,228] 500 µL Milli-Q water was added to a mixture of $La(NO_3)_3$•$6H_2O$ (0.4179 g), $TbNO_3)_3$•$6H_2O$ (0.1019 g) and $CeCl_3$•$7H_2O$ (0.0559 g). To the solution 20 mL ethylene glycol was added and stirred for about 10 minutes to form a homogenous mixture. 10 mL BIMIM[BF_4] was dropwise added to the mixture while stirring for 10 minutes. Even after adding BMIM[BF_4], the resulting pH of the solution remains between 6.5 and 7.0. Hence, there was no indication for the presence of HF. The final solution was sonicated for another 30 minutes to initiate the formation of crystal nucleus. Thereafter, the contents were transferred to a 50 mL microwave glass vessel and inserted in the microwave. The reaction is set to start

under high stirring at 120°C, 100 W and for 30 minutes. High stirring is necessary due to efficiently homogenize ethylene glycol and BMIM[BF_4] respectively. The glass vessel is removed only after the temperature in the microwave has dropped below 30°C. Contents are transferred into a 50 mL centrifuge tube and centrifuged @ 5000 rpm for 5 minutes to separate the NPs from the solution. The solvent was decanted and 5 mL of anhydrous ethanol added. Followed by centrifuging 6 times with ethanol and Milli-Q water alternately @5000 rpm for 5 minutes. The whole experiment was repeated 3 times. One portion of the sample is dried at 75°C for 3 h and prepared for XRD. The second sample is redispersed in 1 mL ethanol and sonicated for 1 h with a mixture of TiO_2@SiO_2 CSNPs, 3 mL Milli-Q water and 2 mL ethanol. After 1 h the mixture is transferred in to a 50 mL centrifuge tube and centrifuged @ 5000 rpm for 5 minutes to separate the CSNPs from the solution. Solvent is again decanted and 5 mL of anhydrous ethanol added to it. Followed by centrifuging 6 times with ethanol and Milli-Q water alternately @5000 rpm for 5 minutes. The second and third samples are also redispersed in ethanol and prepared for particle size distribution experiment (DLS and STEM analysis), luminescence measurements and cell studies.

4.4.5.4 $XYF_4:Ln^{3+}$ (X = K, Rb, Cs, Y = Sm / Eu, Ln = Ce, Tb, Eu) NPs

The $XYF_4:Ln^{3+}$ (X = K, Rb, Cs, Y = Sm / Eu, Ln = Ce, Tb, Eu) NPs were prepared according to the protocol for preparing $NaGdF_4$ by Wang et al.[85] A further ligand exchange experiment has also been done using cyclodextrin and was adopted as reported in the literature. [224]

Chapter 5 Fabrication of hybrid sodium alginate hydrogel – lanthanide doped luminescent NP materials for biomedical applications

5.1 Introduction

The application of NPs in consumer products have led to the rise of regulations and restrictions due its safe use. Steinhoff et al., recently published results showing the fate of NPs in the environment.[148] To overcome challenges associated with environmental and health risks, strategies must be developed on how to incorporate NPs in safe matrix, such as hydrogels. NP incorporation can also lead to improved hydrogel properties like mechanical strength and stimuli response in biological applications. A good example for hybrid hydrogel - NP materials realized with a silica NPs-hydrogel composite has been reported already in the literature: Here silica NPs were modified with polyethylene glycol.[149,150] The resulting material had improved tissue adhesive property, mechanical strength and bioactivity compared to bare silica NPs. Likewise, gold NPs immobilized in poly(*N*-isopropyl amide) hydrogels possess improved thermal response and mechanical strength of the hydrogels.[151]

Integration of hydrogels with NPs has shown significant potential for enhancing material properties and expanding application possibilities.[245] This Chapter explores the potential toxicity of lanthanide doped luminescent NPs prepared in the Chapter 4 and tailoring the NPs for potential biomedical applications. The NPs are embedded in a sodium alginate hydrogel, which is crosslinked with trivalent lanthanide ions. The primary focus is laid on investigating the optical and mechanical properties of these hybrid materials in both dry and swollen states, aiming to interrogate their suitability for future biomedical applications, such as drug delivery and bioimaging.

Sodium alginate hydrogel, renowned for its biocompatibility and gel-forming capabilities,[246–250] was crosslinked using Eu^{3+} ions. Concurrently, luminescent NPs, specifically LaF_3:$Ce^{3+}Tb^{3+}$, were synthesized *(refer to section 4.2.1 in Chapter 4)* and incorporated into the hydrogel matrix *(see Figure 5.1)*. This dual modification was designed to leverage the unique optical properties of lanthanides, alongside the mechanical enhancements provided by the NPs, thus, creating a hybrid material with superior characteristics.

For the first time, this study focused into the mechanical properties and luminescent behavior of sodium alginate hydrogel–NP hybrid, assessing their performance through a series of experiments. The influence of NP concentration on the hydrogel's mechanical strength was systematically analyzed using rheological measurements. Additionally, the potential of this hybrid material for bioimaging was evaluated using NIH 3T3 cells, aiming to replace traditional organic dyes with luminescent Eu^{3+} ions as emitters.

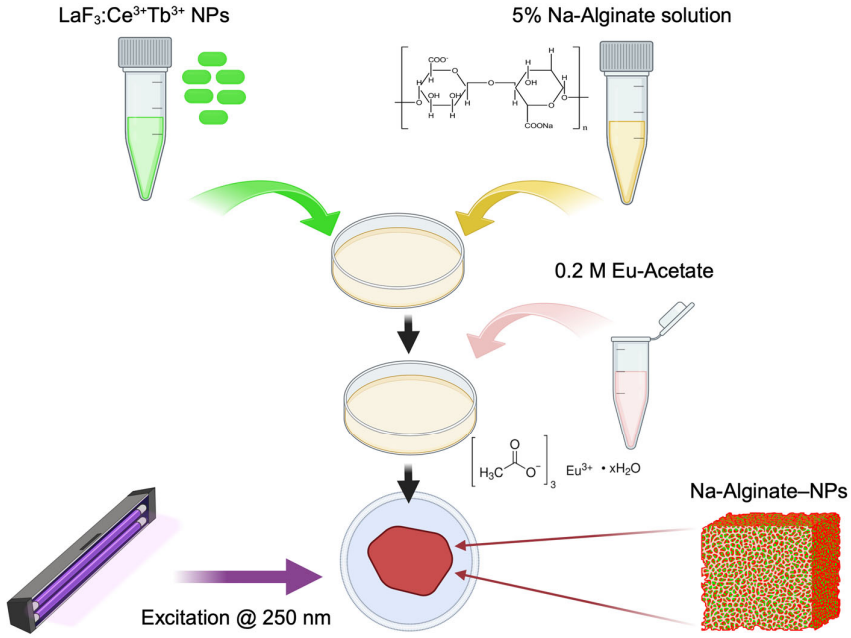

Figure 5.1: Preparation of sodium alginate hydrogel–LaF_3:$Ce^{3+}Tb^{3+}$ NPs hybrid material (illustration created in BioRender app).

5.2 Results and discussion

5.2.1 Toxicity studies of $LaF_3:Ce^{3+}Tb^{3+}$ NPs and $TiO_2@SiO_2@LaF_3:Ce^{3+}Tb^{3+}$ CSNPs

For potential applications in biological systems, the luminescent materials should be non-toxic. Hence, a comprehensive suite of assays was employed using NIH 3T3 fibroblasts and PaTu 8988t cells to study the biocompatibility and cytotoxic potential of $LaF_3:Ce^{3+}Tb^{3+}$ NPs and $TiO_2@SiO_2@LaF_3:Ce^{3+}Tb^{3+}$ CSNPs. Over a period of 48 h, time-lapse microscopy facilitated the real-time monitoring of dynamic cellular processes and morphological alterations induced by the NPs. Concurrently, viability assays, specifically the live-dead staining and the MTT assay, were conducted using different NP concentrations to assess immediate cytotoxic effects and metabolic activity, respectively. The concentrations tested spanned from 0.0001 mg/mL to 0.005 mg/mL. This range was selected to encompass a spectrum of potential cellular responses, enabling to pinpoint the concentration at which the nanoparticles exhibited optimal functionality with minimal cytotoxicity.

Figures 5.2, 5.3, and 5.4 illustrate the impact of $LaF_3:Ce^{3+}Tb^{3+}$ NPs and $TiO_2@SiO_2@LaF_3:Ce^{3+}Tb^{3+}$ CSNPs on cell viability, as measured by absorbance in the MTT assay,[251] across varying cell densities for NIH 3T3 and PaTu 8988t cells. Each figure is detailed to analyze how different concentrations of NPs influence cellular metabolic activity, reflecting cytotoxicity through absorbance changes.

Figure 5.2 presents the effect of $LaF_3:Ce^{3+}Tb^{3+}$ NP concentrations on NIH 3T3 cells. Panel A shows results for a cell density of 25,000 cells. At the lowest NP concentration, the absorbance is approximately 0.6, suggesting a high level of metabolic activity. However, as the NP concentration increases, absorbance decreases to around 0.5 at the highest concentration tested. This indicates a moderate cytotoxic effect, as higher NP concentrations slightly reduce the metabolic activity of the cells.

In Panel B, for a cell density of 50,000 cells, the absorbance values are more stable, fluctuating narrowly around 0.5. This suggests that at this cell density, the cells maintain their metabolic activity despite the varying NP concentrations. This stability implies a certain resilience of the cells to the NPs at this concentration range.

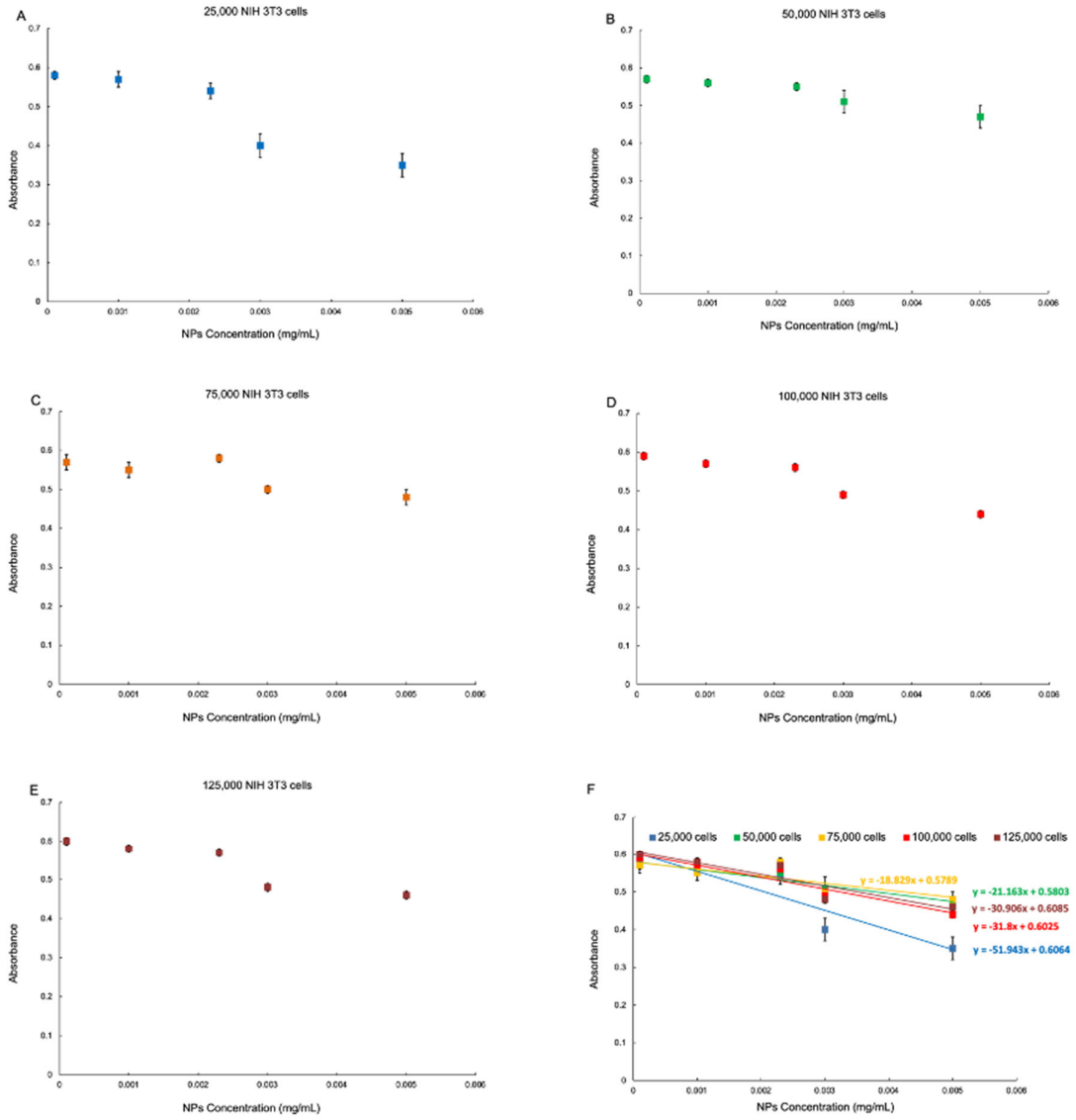

Figure 5.2: Effect of LaF_3:$Ce^{3+}Tb^{3+}$ NPs concentrations on absorbance of formazan formed in the MTT assay across different NIH 3T3 cell densities A) 25,000, B) 50,000, C) 75,000, D) 100,000, E) 125,000 and F) all cell densities with a linear fit to determine slope.

Panel C depicts the results for 75,000 cells, where absorbance remains relatively consistent at approximately 0.5, with only slight fluctuations. This indicates minimal impact on cell viability, reinforcing the observation that NIH 3T3 cells at this density are not significantly affected by the NP concentrations tested. Panel D, with 100,000 cells, presents an interesting trend where absorbance slightly increases from about 0.5 to 0.6 with increasing NP concentrations. This unexpected rise is due to errors

associated with cell counting. Hence, the possibility of higher cell densities than 100,000 cells cannot be ruled out.

In Panel E, for 125,000 cells, absorbance values remain steady around 0.5, with minimal variation across NP concentrations. This stability indicates robust metabolic activity at the highest cell density, demonstrating that NIH 3T3 cells maintain their viability and functionality even in the presence of higher NP concentrations.

Panel F consolidates the absorbance data across all tested cell densities. The steeper decrease in absorbance observed for lower cell concentrations suggests a heightened sensitivity or increased toxicity of the cells to the NPs. This observation indicates that cells in lower concentrations are apparently more adversely affected by the presence of NPs, potentially due to a lack of buffering capacity that is present in higher cell concentrations.[252] Conversely, higher cell concentrations may exhibit a buffering effect, thereby mitigating the impact of NPs on absorbance measurements.[252,253] Such a buffering effect implies a form of protective mechanism that lessens the overall toxic impact of the nanoparticles.

Figure 5.3 shows the impact of $LaF_3:Ce^{3+}Tb^{3+}$ NP on PaTu 8988t cells across different densities. Panel A, for 25,000 cells, displays a noticeable decrease in absorbance from approximately 0.7 at the lowest NP concentration to around 0.4 at the highest concentration. This significant drop indicates a pronounced cytotoxic effect, with higher NP concentrations substantially reducing the metabolic activity of the cells.

Panel B, representing 50,000 cells, shows a similar trend, with absorbance decreasing from about 0.7 to 0.4 as NP concentration increases. The results suggest that even at this higher cell density, the higher concentrations of NPs adversely affect cell viability and metabolic activity. For 75,000 cells, as depicted in Panel C, the absorbance decreases steadily from approximately 0.6 to 0.3 with increasing NP concentrations. This consistent decline reinforces the observation that higher NP concentrations are detrimental to cell health across varying densities of PaTu 8988t cells. Panel D, for 100,000 cells, shows absorbance decreasing from about 0.5 to 0.3 with increasing NP concentrations. This further supports the cytotoxic effect of NPs at higher concentrations, indicating a significant reduction in metabolic activity.

In Panel E, with 125,000 cells, absorbance values decrease from around 0.45 to 0.3 with increasing NP concentrations. Despite the highest cell density, the negative impact of NPs on cell viability remains evident, showcasing a similar trend across all densities.

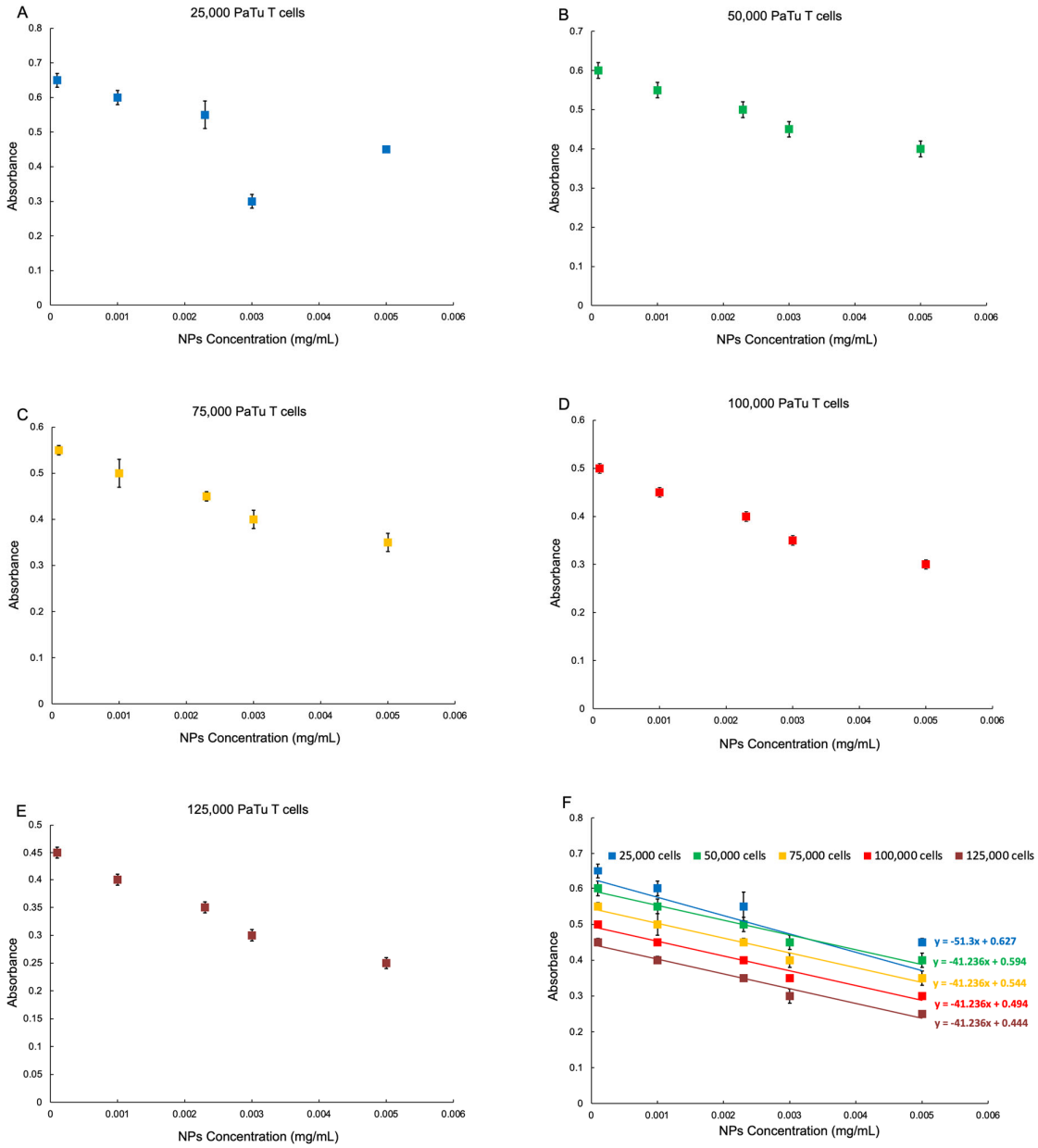

Figure 5.3: Effect of LaF_3:$Ce^{3+}Tb^{3+}$ NPs concentrations on absorbance of formazan during MTT assay across different PaTu 8988t cell densities A) 25,000, B) 50,000, C) 75,000, D) 100,000, E) 125,000 and F) all cell densities with a linear fit to determine slope.

Panel F provides a comprehensive comparison of absorbance across all cell densities at each NP concentration. The data indicate that, irrespective of the cell density, increasing NP concentrations consistently lead to a decrease in absorbance, highlighting a dose-dependent cytotoxic effect.

Comparing Figures 5.2 and 5.3, it is evident that PaTu 8988t cells exhibit a higher sensitivity to $LaF_3:Ce^{3+}Tb^{3+}$ NPs than NIH 3T3 cells. The extent of the decrease in absorbance is more pronounced in PaTu 8988t cells, suggesting that they are more susceptible to the cytotoxic effects of these NPs. While NIH 3T3 cells show moderate decreases or stability in absorbance, PaTu 8988t cells consistently exhibit substantial reductions, indicating a significant impact on their viability. Additionally, the effect of the conditions varies with the cell density. At lower cell numbers, the observed effects are different compared to those at higher cell numbers. This suggests that cell density plays a crucial role in the response of both NIH 3T3 and PaTu 8988t cells to the conditions being tested.

Figure 5.4 illustrates the impact of $TiO_2@SiO_2@LaF_3:Ce^{3+}Tb^{3+}$ CSNPs concentrations on absorbance in NIH 3T3 cells. Panel A shows that for 25,000 cells, absorbance decreases from approximately 0.5 at the lowest concentration to about 0.4 at the highest concentration, indicating a clear cytotoxic effect of CSNPs at higher concentrations.

Panel B, for 50,000 cells, shows a decrease in absorbance from about 0.45 to 0.3 with increasing CSNP concentrations. This trend suggests that higher CSNP concentrations negatively impact cell viability and metabolic activity. For 75,000 cells, depicted in Panel C, absorbance decreases from around 0.4 to 0.25 with increasing CSNP concentrations. This consistent decline indicates a significant cytotoxic effect of the CSNPs at higher concentrations. Panel D, for 100,000 cells, shows absorbance decreasing from about 0.35 to 0.2 with increasing CSNP concentrations. This further supports the observation of a substantial reduction in metabolic activity due to the cytotoxic effects of the CSNPs. In Panel E, with 125,000 cells, absorbance values decrease from approximately 0.35 to 0.15 with increasing CSNP concentrations. Despite the higher cell density, the adverse impact of CSNPs on cell viability remains evident, indicating strong cytotoxicity. Panel F consolidates the absorbance data across all cell densities, demonstrating a consistent decrease in

absorbance with increasing CSNP concentrations across all tested densities. This highlights a clear dose-dependent cytotoxic effect of the CSNPs on NIH 3T3 cells.

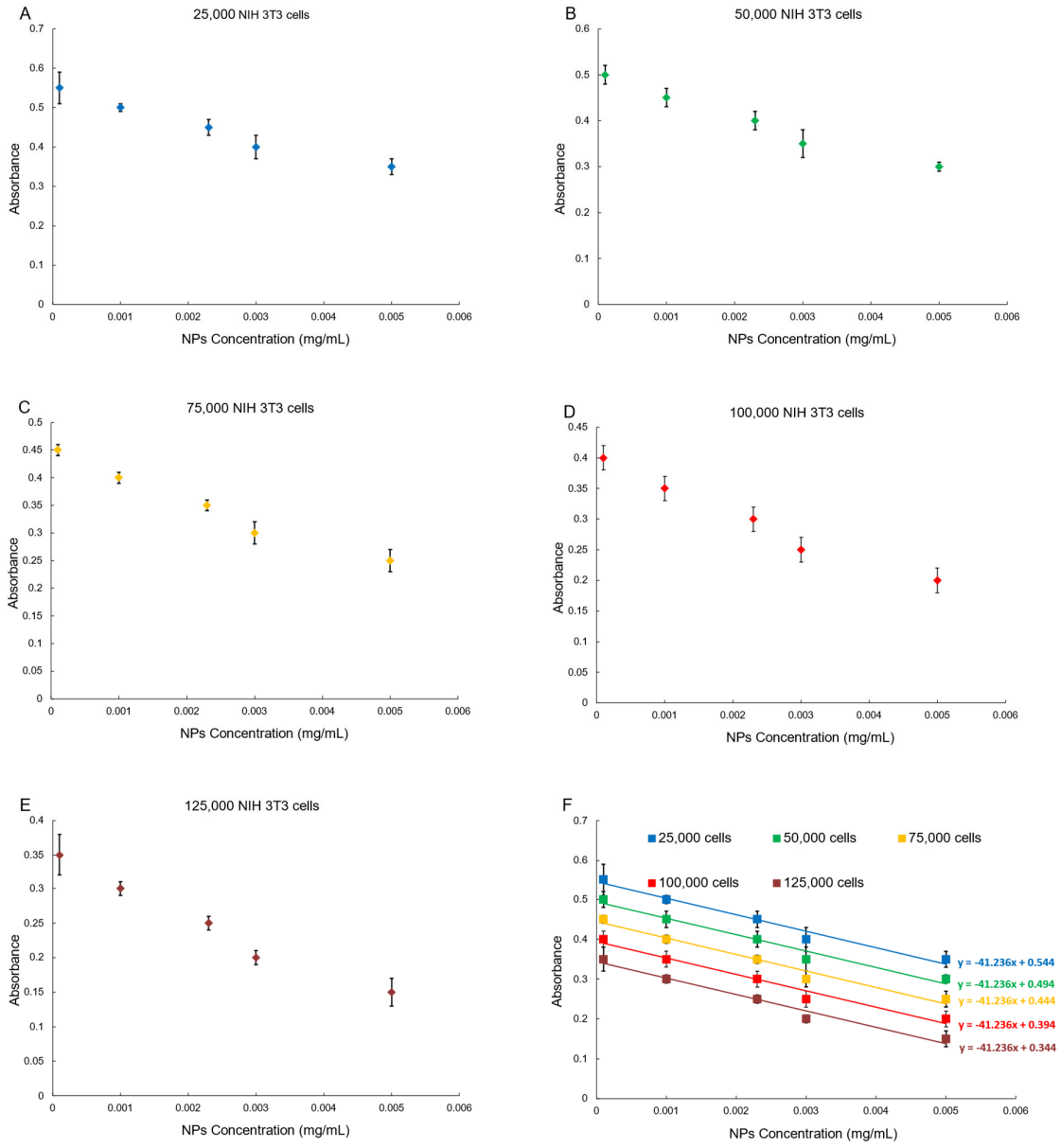

Figure 5.4: Effect of TiO_2@SiO_2@LaF_3:$Ce^{3+}Tb^{3+}$ CSNPs concentrations on absorbance of formazan during MTT assay across different NIH 3T3 cell densities A) 25000, B) 50000, C) 75000, D) 100000, E) 125000 and F) all cell densities with a linear fit to determine slope.

Comparing Figures 5.2 and 5.4 reveals distinct differences and similarities in the response of NIH 3T3 cells to different nanoparticle types. Both figures investigate the effect of NP concentrations on NIH 3T3 cells using the MTT assay, but with different

nanoparticles: $LaF_3:Ce^{3+}Tb^{3+}$ NPs in Figure 5.2 and $TiO_2@SiO_2@LaF_3:Ce^{3+}Tb^{3+}$ CSNPs in Figure 5.4.

In Figure 5.2, $LaF_3:Ce^{3+}Tb^{3+}$ NPs show relatively stable absorbance values with only moderate cytotoxicity. The cells exhibit resilience, particularly at higher densities, with minimal impact on metabolic activity across the tested NP concentrations. However, in Figure 5.4, $TiO_2@SiO_2@LaF_3:Ce^{3+}Tb^{3+}$ CSNPs induce a more pronounced decrease in absorbance, indicating stronger cytotoxicity. The consistent decline in absorbance across all cell densities suggests that the core-shell structure of the CSNPs enhances their cytotoxic effect compared to $LaF_3:Ce^{3+}Tb^{3+}$ NPs.

Higher cell densities in both figures generally correlate with higher absorbance values, indicating greater metabolic activity. However, the decrease in absorbance with increasing NP concentrations is more pronounced in Figure 5.4, suggesting that the $TiO_2@SiO_2@LaF_3:Ce^{3+}Tb^{3+}$ CSNPs are more effective at reducing cell viability and metabolic activity. The results indicate that NIH 3T3 cells are more sensitive to the CSNPs, possibly due to the core-shell structure enhancing the cytotoxic potential.

Low cell concentrations are particularly susceptible to cytotoxic effects when exposed to NPs, as the limited number of cells can be overwhelmed by the high surface reactivity and potential toxicity of NPs.[253] This heightened vulnerability arises from the reduced collective defensive mechanisms within sparse cell populations, often leading to pronounced cytotoxic responses that may not accurately represent the biological system's resilience. Moreover, statistical variability increases significantly at low cell densities, where minor fluctuations in cell numbers can disproportionately affect assay results, thus diminishing reproducibility and obscuring true NP-induced cytotoxicity.[252] Additionally, the metabolic conversion of MTT to formazan, a fundamental aspect of the assay, can be insufficient at low cell numbers, resulting in sub-detectable formazan levels and potential false negatives regarding NP toxicity.[251]

Conversely, high cell concentrations introduce a distinct set of challenges, particularly when NPs are involved. The phenomenon of metabolic saturation becomes prominent at elevated cell densities, where the high metabolic activity can

rapidly convert MTT to formazan, often exceeding the assay's linear detection range and leading to inaccurate cell viability measurements. [252,253]

This effect is compounded by the limited diffusion of both MTT and formazan in densely packed cell environments, exacerbated by the presence of NPs that may further restrict molecular movement. Such conditions result in heterogeneous formazan distribution and uneven colorimetric signals.[254] Additionally, the turbidity associated with high cell densities, intensified by the particulate nature of NPs, interferes with absorbance readings due to significant light scattering, thereby distorting spectrophotometric data.[251]

Figure 5.5 illustrates the calculated slopes versus NPs concentration (mg/mL), with the aim of further understanding how $LaF_3:Ce^{3+}Tb^{3+}$ NPs and $TiO_2@SiO_2@LaF_3:Ce^{3+}Tb^{3+}$ CSNPs concentration relate to different cell densities and types. First, a linear fit is done on each plot of individual cell density's absorbance versus NP concentration. The evaluation, conducted using the absorbance of formazan during the MTT assay, highlights the differential cytotoxic effects and optimal NPs concentrations for NIH 3T3 fibroblast cells and PaTu 8988t cells.

For NIH 3T3 cells *(see Figure 5.5-A)*, the slopes indicate that $LaF_3:Ce^{3+}Tb^{3+}$ NPs caused a gradual decrease in cell viability with increasing concentration, particularly notable at higher cell densities (100,000 and 125,000 cells). Conversely, PaTu 8988t cells *(see Figure 5.5-B)* exhibit a more pronounced reduction in slope across all cell densities, signifying a higher sensitivity to $LaF_3:Ce^{3+}Tb^{3+}$ NPs. This sensitivity suggests that lower concentrations below 0.001 mg/mL of these NPs could be effective for applications involving PaTu 8988t cells, while NIH 3T3 cells might tolerate higher concentrations.

When comparing the effects of $LaF_3:Ce^{3+}Tb^{3+}$ NPs with $TiO_2@SiO_2@LaF_3:Ce^{3+}Tb^{3+}$ CSNPs NIH 3T3 cells *(refer to Figure 5.5-C)*, it is observed that the slopes for CSNPs decrease more uniformly across different cell densities. This uniformity indicates a consistent cytotoxic response, unlike the significant slope decrease observed with $LaF_3:Ce^{3+}Tb^{3+}$ NPs, especially at higher concentrations and cell densities.

The analysis of slopes revealed that the NPs concentration varies depending on the cell type and NP composition. PaTu 8988t cells require lower NPs concentrations (below 0.001 mg/mL) to achieve the desired cytotoxic effect, whereas NIH 3T3 cells show relative effects up to 0.023 mg/mL.

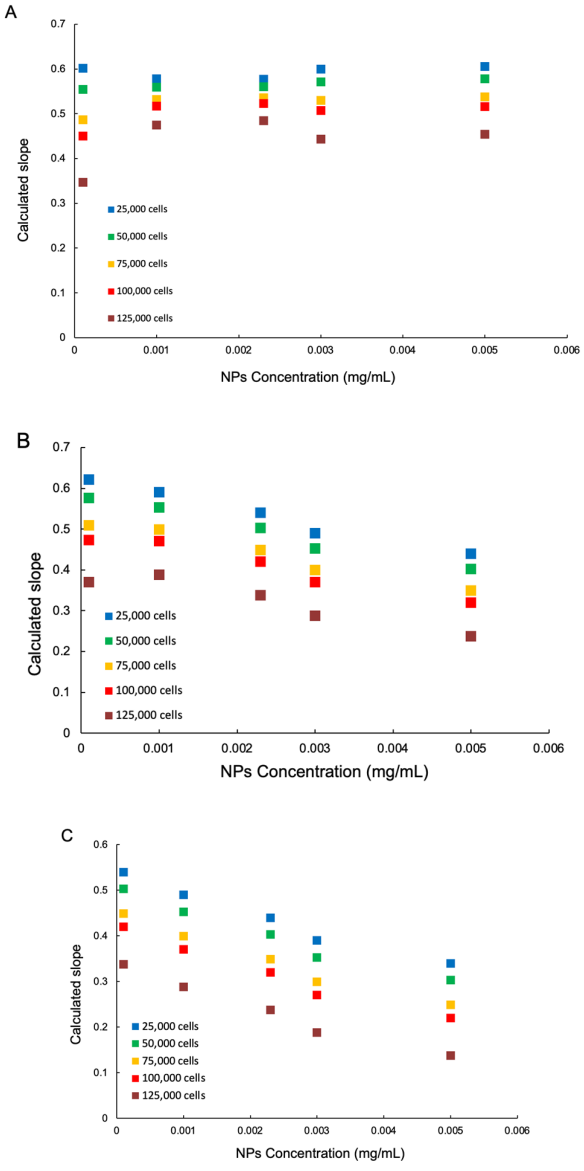

Figure 5.5: Calculated slopes versus NPs concentration of; A) effect of $LaF_3:Ce^{3+}Tb^{3+}$ NPs concentrations on absorbance of formazan during MTT assay across different NIH 3T3 cell densities (25,000 | 50,000 | 75,000 | 100,000 | 125,000 cells); B) effect of $LaF_3:Ce^{3+}Tb^{3+}$ NPs concentrations on absorbance of formazan during MTT assay across different PaTu 8988t cell densities (25,000 | 50,000 | 75,000 | 100,000 | 125,000 cells); C) effect of $TiO_2@SiO_2@LaF_3:Ce^{3+}Tb^{3+}$ CSNPs concentrations on absorbance of formazan during MTT assay across different NIH 3T3 cell densities (25,000 | 50,000 | 75,000 | 100,000 | 125,000 cells).

This comparative analysis highlights the higher cytotoxicity of TiO_2@SiO_2@LaF_3:$Ce^{3+}Tb^{3+}$ CSNPs compared to LaF_3:$Ce^{3+}Tb^{3+}$ NPs towards NIH 3T3 cells. The steeper declines in both cell viability and absorbance indicate an impact on cellular health and metabolic activity at higher NP concentrations. These findings suggest the importance of considering NP composition in toxicity assessments. While TiO_2@SiO_2@LaF_3:$Ce^{3+}Tb^{3+}$ CSNPs may offer specific functional advantages, their increased cytotoxicity necessitates careful evaluation when considering their use in biomedical applications.

0.0023 mg/mL was selected as a relative concentration for the time-lapse experiment using NIH 3T3 cells with LaF_3:$Ce^{3+}Tb^{3+}$ NPs because at this concentration absorbance declines drastically to lower values *(see Figure 5.6)*. The NIH 3T3 cell line, known for its robust growth and predictable responses, provides a consistent model for such evaluations. Given that higher NP concentrations typically exhibit increased cytotoxic effects, a moderate concentration that is 0.0023 mg/mL minimizes potential cytotoxicity while still allowing for effective observation of NP interactions over time. The time-lapse images show the NIH 3T3 fibroblasts at various incubation times with LaF_3:$Ce^{3+}Tb^{3+}$ NPs at this concentration.

At the 5-minute mark NIH 3T3 cells are not attached on the TCPS surface. NPs are dispersed in the cell medium and no changes in the cell morphology can be observed. After 12 h, cells with elongated filopodia are attached on the TCPS surface. Furthermore, cells begin to proliferate. After 24 h, cells increase in number and begin to occupy the entire TCPS surface. A distinct cell nucleus can be observed in each individual cell structure. Cells further increase in number even after 48 h indicating positive cellular response. At this stage, no cell anomalies can be noted under the light microscope. This observation suggests that the concentration of NPs in the cell medium do not directly interfere with cell growth. Also, there is no indication of cytotoxicity due to cellular uptake of NPs at this concentration.

To critically test the promising results from MTT assays and time-lapse experiments, live/dead staining was conducted to provide an additional layer of validation and deeper insights into the effects of nanoparticles on cell viability and morphology.

The MTT assay primarily measures cell metabolic activity, which correlates with cell viability, but does not directly distinguish between live and dead cells, while time-lapse imaging offers dynamic visual information, but may not precisely quantify cell death. Live/dead staining uses specific dyes to directly label living cells with a green-fluorescent dye (fluorescein diacetate) and dead cells with a red-fluorescent (propidium iodide) dye, offering a clear and immediate distinction between viable and non-viable cells.

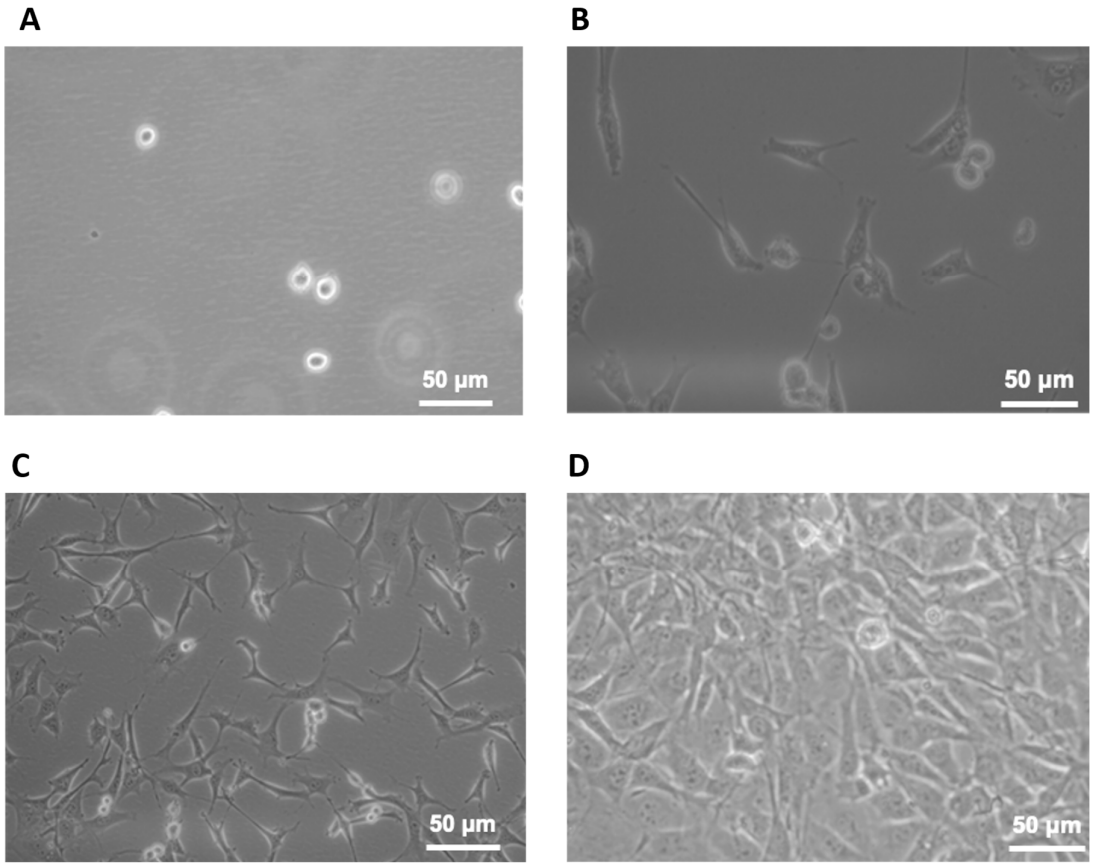

Figure 5.6: Time-Lapse Microscopy of NIH 3T3 Fibroblasts interacting with 0.0023 mg/mL LaF_3:$Ce^{3+}Tb^{3+}$ NPs (25 nm ± 5 nm) in cell medium over different incubation periods: (A) 5 min, (B) 12 h, (C) 24 h, and (D) 48 h, respectively.

This technique serves as a confirmatory method to validate the findings from the MTT assays and time-lapse imaging, ensuring that the observed metabolic activity and morphological changes correlate accurately with the actual viability status of the cells, thus increasing the robustness and reliability of the experimental results.

Furthermore, live/dead staining offers additional information about subtle cytotoxic effects that might not significantly alter metabolic activity detected by MTT assays or observable changes in time-lapse imaging.[251,255]

This sensitivity is particularly useful in identifying low levels of cytotoxicity that could have long-term implications for cell health. Integrating live/dead staining with MTT assays and time-lapse imaging provides a comprehensive cytotoxicity profile, covering metabolic activity, dynamic cellular behavior, and direct viability assessment. However, floating dead cells flushed with PBS during the washing step in sample preparation for fluorescence imaging cannot be accounted for.

Figure 5.7 shows results from a live/dead staining cytotoxicity experiment with LaF_3:$Ce^{3+}Tb^{3+}$ NPs (25 nm $\pm$ 5 nm) at a concentration of 0.0023 mg/mL on NIH 3T3 fibroblasts. The experiment compared two different cell densities: 400,000 cells and 200,000 cells, both with and without NP treatment. In the control group of 400,000 cells without NPs, robust green fluorescence indicated a high viability rate with minimal cell death, confirming the healthy state of the cells. Similarly, in the 400,000 cells treated with NPs, the cells continued to exhibit substantial green fluorescence, suggesting that the NPs did not exert severe cytotoxic effects at this concentration. The minimal presence of red fluorescence in this group further supported the conclusion that cell death was not significantly increased as observed in Figure 5.5.

For the lower cell density of 200,000 cells without NPs, the cells displayed green fluorescence, indicating high viability similar to the higher density control. The sample containing 400,000 cells exhibited a faint red fluorescence in the absence of NPs, indicating minimal cell death. Nevertheless, this observation lacks the statistical robustness required for a conclusive evaluation of cell viability, potentially stemming from artifacts introduced during the fluorescence measurement process. When treated with NPs, the 200,000 cells still showed predominant green fluorescence, indicating high cell viability. As with the higher cell density, there was no significant increase in red fluorescence, suggesting that the NPs did not induce notable cytotoxicity at this concentration.

The live/dead staining results corroborate findings from time-lapse experiments, confirming that LaF_3:$Ce^{3+}Tb^{3+}$ NPs at a concentration of 0.0023 mg/mL exhibit minimal cytotoxicity towards NIH 3T3 fibroblasts.

However, MTT data *(see Figure 5.2)* suggest that there is a certain percentage of cells that 10 - 15 % of cells die after 48 h. It is worth noting that the cell concentration maximum in MTT was 125000 cells compared to live/dead staining and time-lapse experiment was at 200000 and 400000 cells after 24 and 48 h respectively. Hence, the noted cell death in MTT cannot directly be accounted for in live/dead staining or time-lapse experiments.

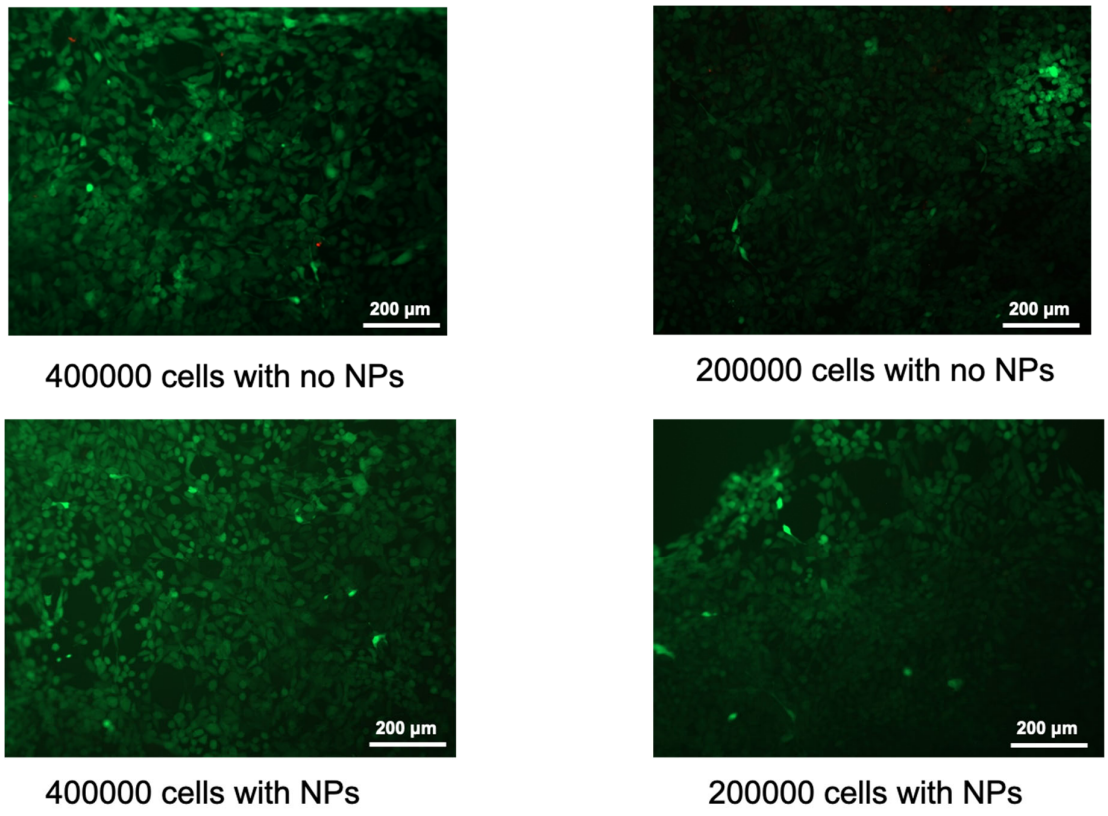

Figure 5.7: Live-dead staining cytotoxicity experiment with NIH 3T3 fibroblasts incubated for 48 h in cell medium. The left image shows an experiment done after 48 h with 400,000 cells (either with or without NPs) and the right image shows an experiment done after 24 h with 200000 cells (either with or without NPs). 0.0023 mg/mL LaF_3:$Ce^{3+}Tb^{3+}$ NPs dispersed in cell medium (25 nm ± 5 nm) was used for the experiments with NPs.

5.2.2 Investigation of the interaction of NPs with NIH 3T3 cells using ICP-OES

To investigate the interaction of nanoparticles (NPs) with cells, i.e., to clarify whether or not NPs were taken up or adhered to cells, ICP-OES was used for the final analysis of the cell medium, cells, and NPs. A simplified sample preparation method was developed for the elements Cerium (Ce), Lanthanum (La), and Terbium (Tb) in organic matrices.

The digestion of all organic components of the mixture followed the procedure described in the Experimental Section. The cell medium was collected after the experiment to determine the concentration of Ce, La, and Tb, and was digested to ensure complete dissolution of any NPs. The cells were separated from the medium and digested to remove all organic matter and release incorporated NPs, while the NPs themselves were isolated and digested similarly. Calibration curves for the standards used in the experiment displayed excellent linear regression with a precision (R^2) of 0.999, as shown in Figure 5.8. Manganese (Mn) with an emission line at 257.611 nm was used as the internal standard, with the Mn ratio plotted against concentration in parts per billion (ppb) providing insights into the accuracy of pipetting during the experiment *(refer to Figure 5.9)*. The internal standard effectively monitored the signal-to-background ratio, maintaining it within accepted limits (> 3% of overall intensity).[256] A straight line in the Mn ratio plot indicates high accuracy, leading to correct calibration with the standards. This approach ensures the reliability of the ICP-OES analysis, confirming the precision and accuracy of the measurements for Ce, La, and Tb in the samples.

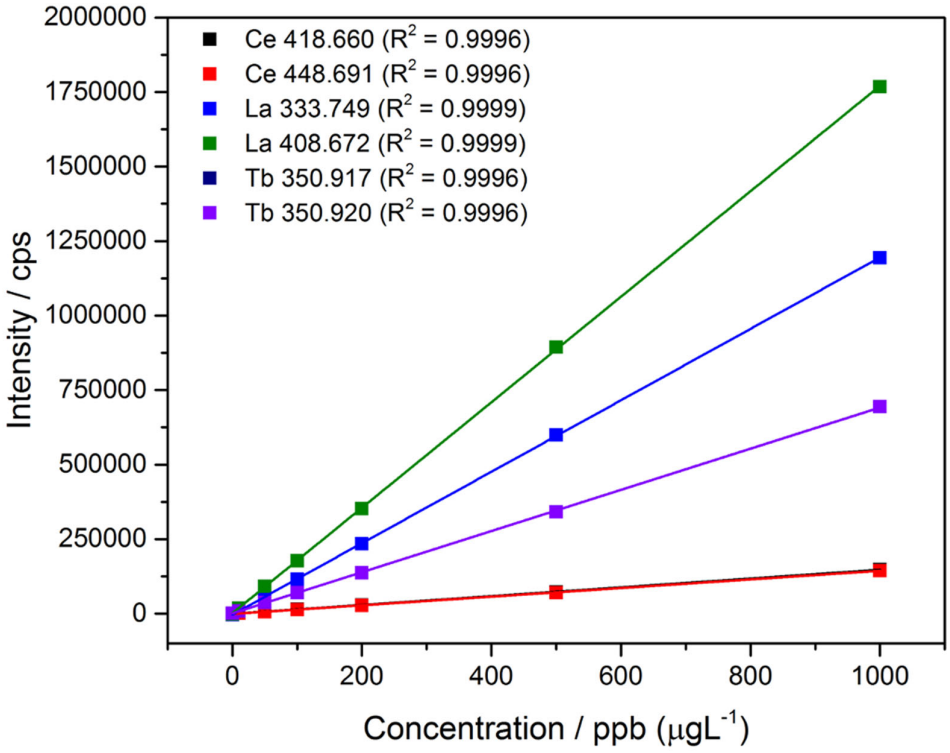

Figure 5.8: ICP-OES Calibration curves of Ce 418.660 nm, Ce 448.691 nm, La 333.749 nm, La 408.672 nm, Tb 350.917 nm and Tb 350.920 nm measured in 2 % HNO_3 solution.

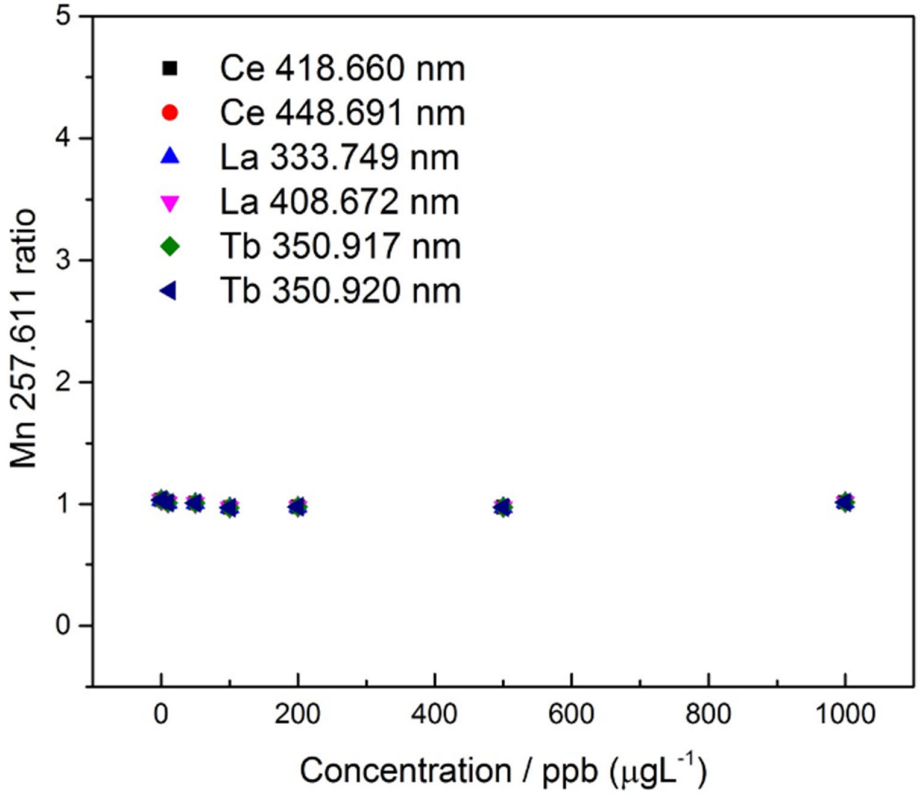

Figure 5.9: ICP-OES internal standard Mn 257.611 nm ratio plotted against concentration in ppb (μgL^{-1}) 2 % HNO_3 solution.

The recorded average of each Mn intensity signal was 18584.7, of which the highest and lowest values were capped at 1.03594 and 0.97311 respectively. From Table 5.1, Ce concentrations for both emission lines (418.660 nm and 448.691 nm) were found to be below the LOD. The results indicate a deep surge of concentration of the analytes after MTT assay with high errors. However, this was expected due to the complexity of the experiment especially during digestion and dilution processes. The difference in concentration is due to the loss of analytes in the mentioned processes. Hence, the reported results are relative and cannot be used in singularity to justify NPs interaction with cells. Despite, the ambiguity in the experiment, detection of La and Tb rare earth elements in LaF_3:1%Ce^{3+}3% Tb^{3+} are recorded even in high organic matrices. Almost no chemical interference of La and Tb signals was noted.

Table: 5.1 Determination of elemental composition (Ce, Tb & La) of the NPs before and after toxicity via ICP-OES.

Emission line	Concentration of analyte in the NPs solution (µg/L) before MTT	Concentration of analyte in the NPs solution (µg/L) after MTT	LOD (µg/L)	LOQ (µg/L)
Ce 418.660	119	4.0	8.06	24.51
Ce 448.691	118	5.8	3.18	9.65
La 333.749	699	3.6	0.01	0.03
La 408.672	676	2.9	0.54	1.46
Tb 350.917	198	4.2	2.0	6.09
Tb 350.920	198	4.3	2.01	6.13

The experiment highlights the need for more refined sample preparation techniques to minimize analyte loss and improve detection accuracy, especially for Ce. The stability of the Mn internal standard underscores its importance in correcting signal fluctuations and ensuring measurement accuracy. The varying LOD and LOQ values emphasize the necessity of optimizing detection methods for each element, and the successful detection of La and Tb suggests that the methods are well-suited for analyzing these elements. Future studies should focus on improving sample preparation, exploring alternative analytical techniques, expanding elemental analysis, and conducting long-term studies to better understand NP interactions with cells.

5.2.3 Toxicity studies of sodium alginate hydrogel–lanthanide doped luminescent NPs hybrid materials

NIH 3T3 cells were cultured to investigate effects of Na-Alginate NPs on cell proliferation and adhesion. Initially, NIH 3T3 cells were seeded on TCPS without any hydrogel–NP matrix to serve as a control for MTT assay *(see Figure 5.10)*. To prepare the experimental samples, all chemicals and glassware were sterilized using steam in the autoclave. A 0.2 M solution of Eu^{3+} (europium acetate) was employed as a cross-linker, with the pH adjusted to 7 using a buffer solution.

The hydrogel was cleaned by soaking it in Milli-Q water for five minutes, followed by incubation at 37°C in CO_2 atmosphere cell culture incubator to evaporate any toxic vapors due residual acetic acid, a step that was repeated six times or more until the hydrogel exhibited a clear pink color, indicating color of the cell medium. NIH 3T3 cells were subsequently injected into the hydrogel and incubated with fresh medium, which was replaced every 12 h without washing the hydrogel.

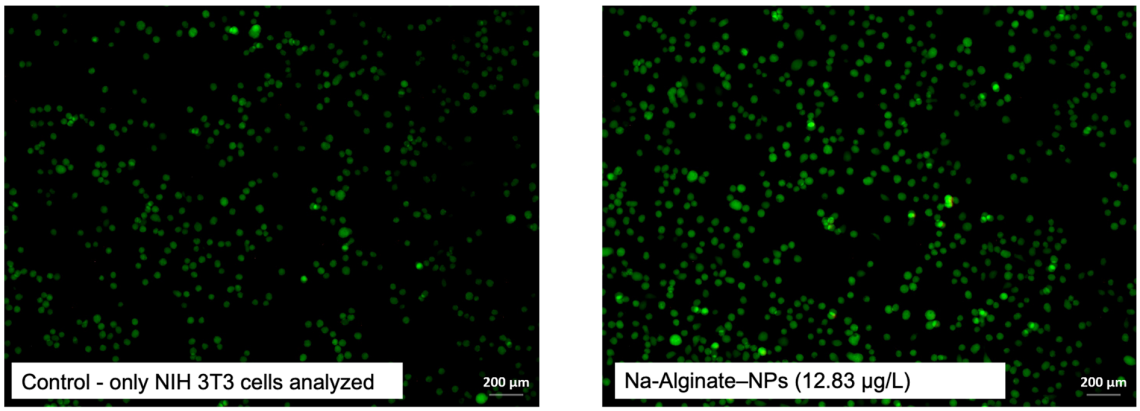

Figure 5.10: Live dead staining assay of (left) control and (right) with Na-Alginate sample containing 12.8 µg/L NPs.

The control image, depicting NIH 3T3 cells without Na-Alginate-NP treatment, shows an even distribution and consistent cell density. In contrast, the image of the treated cells, incubated with Na-Alginate-NPs at a concentration of 12.8 µg/L, reveals a significantly higher cell density and a more clustered distribution pattern. This observation suggests that the presence of Na-Alginate-NPs may enhance both cell proliferation and adhesion properties. The treated cells' increased density from 125,000 to 160,000 cells and clustering indicate that the Na-Alginate-NPs provide a supportive microenvironment that promotes cellular activities more effectively than the control conditions. Green fluorescence is indicative of viable cells, whereas red fluorescence, which is not prominently observed here, would denote non-viable cells. The predominance of green fluorescence in both panels suggests a high viability of NIH 3T3 cells under the tested conditions. These findings give insight to the potential of Na-Alginate-NPs in tissue engineering and regenerative medicine applications, where enhanced cell growth and adhesion are critical for successful outcomes.

Several studies have explored before the impact of alginate-based materials on cell proliferation and adhesion. For instance, a study by Mohandas et al. demonstrated that alginate hydrogels loaded with zinc oxide NPs (ZnO) significantly improved fibroblast proliferation and collagen deposition in wound healing applications.[257] This study reported that the incorporation of ZnO NPs enhanced the mechanical properties of the hydrogel and supported higher rates of cell proliferation compared to untreated controls. Similarly, Zhang et al. found that alginate-based dressings containing ZnO NPs were biocompatible with NIH 3T3 fibroblasts and showed improved wound healing rates, indicating the potential for enhanced cell proliferation and adhesion.[258] In another study, Harper et al. observed that the presence of sodium ions in alginate hydrogels affected the viscosity and gelation properties, which in turn influenced cell attachment and proliferation.[259] Their findings suggested that the ionic environment and molecular weight of the alginate played significant roles in the hydrogel's effectiveness as a cellular scaffold.

5.2.4 Mechanical properties of sodium alginate hydrogel–$LaF_3:Ce^{3+}Tb^{3+}$ NPs hybrid material

In this study, a series of experiments were conducted to investigate the mechanical properties and applications of sodium alginate hydrogels crosslinked with Eu^{3+} ions. The hydrogels were prepared by mixing 5% sodium alginate solution with a 0.2 M Eu^{3+} solution, forming a robust gel *(see Figure 5.1)*. To optimize gel quality, various formulations were tested by altering the amount of crosslinker, while keeping the alginate concentration constant. For rheological analysis, samples were prepared with a constant alginate and Eu^{3+} concentration, while varying the concentration of NPs and balancing the total concentration with Milli-Q water. The NPs, at a concentration of 0.0462 g/L, were introduced into the hydrogel matrix in varying amounts, ensuring thorough dispersion to investigate their impact on the mechanical properties of the gels. The swelling behavior of the hydrogels was evaluated gravimetrically, measuring the equilibrium swelling percentage. Additionally, the hydrogels were tested for biocompatibility by incorporating NIH 3T3 cells, ensuring a pH-adjusted environment and repeated soaking steps to remove any residual toxic vapors.

In this experiment, the mechanical properties of $LaF_3:Ce^{3+}Tb^{3+}$ NPs are not determined in isolation, but as a hybrid composite together with sodium alginate hydrogel. To obtain meaningful results, it was necessary to prepare uniform sizes of the hydrogel-NP matrix. Figure 5.11 shows the FESEM microstructure of sodium alginate hydrogel without (left) and with (right) NPs after 48 h freeze drying. The sample containing 500 μL solution of NPs (12.8 μg/L) was chosen for freeze drying due to the midpoint volume of NPs. 100 μL (2.6 μg/L) or 1000 μL (25.6 μg/L) solution of NPs are two extremes that may not give a good representation of the samples especially after the several washing steps. The left image depicts the hydrogel without NPs, characterized by a distinct porosity and fiber network. The pores appear uniformly distributed with a specific average size, and the fibers are densely packed, forming a connected network. In contrast, the right image shows the hydrogel with 500 μL of NP solution, revealing noticeable structural modifications. The presence of NPs seems to affect the porosity, as evidenced by changes in pore size and distribution.

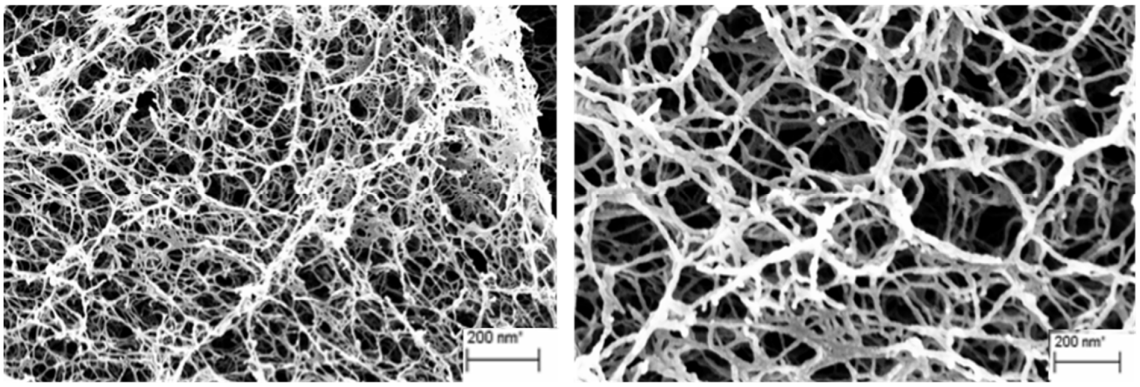

Figure 5.11: FESEM images of sodium alginate hydrogel without (left) and with 500 μL solution of NPs (12.8 μg/L) (right) NPs.

Quantitative analysis of the fiber thickness *(see Figure 5.12)* reveals significant differences between the two samples. Without NPs, the average fiber thickness is approximately 98 nm with a standard deviation of 18 nm. In the presence of NPs, the average fiber thickness increases to about 151 nm with a standard deviation of 29 nm. Thicker fibers are known to enhance the structural reinforcement of the hydrogel.[250]

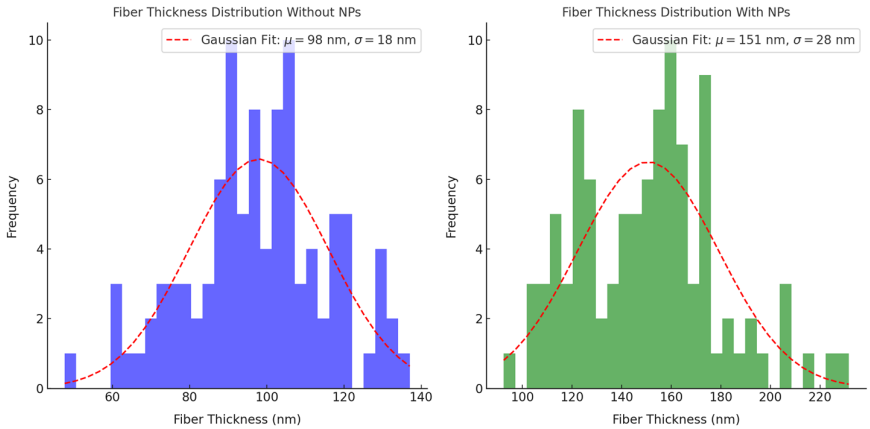

Figure 5.12: Histograms of fiber thickness from FESEM images of sodium alginate hydrogel without (left) and with 500 µL solution of NPs (12.8 µg/L) (right) NPs.

In general, the inclusion of NPs at this concentration significantly modifies the structural properties of the sodium alginate hydrogel. The reduction in pore size and increase in fiber thickness suggest that NPs may enhance the mechanical stability and functionality of the hydrogel, likely contributing to its improved performance in potential applications. Das et al., reported similar microstructures, but of a functionalized alginate (Alg)-based terpolymeric semi-interpenetrating (semi-IPN) hydrogel, synthesized via free radical polymerization.[250] It was not possible to visualize the NPs using the same magnification for the hydrogel microstructure investigation. For this reason, other methods have been used to confirm the effects of NPs in the hydrogel matrix.

Figure 5.13 shows results of rheological measurements done on sodium alginate hydrogel–LaF_3:$Ce^{3+}Tb^{3+}$ NPs hybrid material. From the rheology experiment, it was possible to confirm the existence of a hydrogel structure due to the phase shift below 45°.[260] The viscoelasticity was proven from the frequency and amplitude sweep measurements. Notably, the increase in NPs concentration is directly proportional shear stress in Pa *(c.f. Figure 5.13)*. Adibnia and Hill et al., showed that silica NPs increase the mechanical strength of hydrogels if embedded in hydrogels.[261] Hence, one may conclude increased mechanical strength of the resulting hydrogel-NP hybrid material. Low concentrations of NPs result in a less rigid hydrogel network, which increases the swelling properties. Tunability of the mechanical strength via NPs can thus be an insight for possible biomedical applications such as drug release or targeted cell apoptosis studies.

This is the first time, mechanical properties of fluoride NPs doped with lanthanides and lanthanide crosslinked hydrogels have been reported. Sershen et al., used a similar method of hydrogel formation in a gold (Au) nanoparticle suspension.[44] The Au NPs were immersed in *N*-isopropylacrylamide/acrylamide (NIPAAm/AAm) monomers and crosslinked with initiator ammonium persulfate (APS) and accelerator tetramethylethylenediamine (TMEDA). Other studies have used this method as a strategy to stabilize silica NPs.[153] Liu et al., proved that it is possible to prepare photo-modulable thermos-responsive hydrogels using titania nanosheets as photocatalytic crosslinkers immersed in bisfunctional monomer *N,N'*-methylenebisacrylamide (MBAAm).[157]

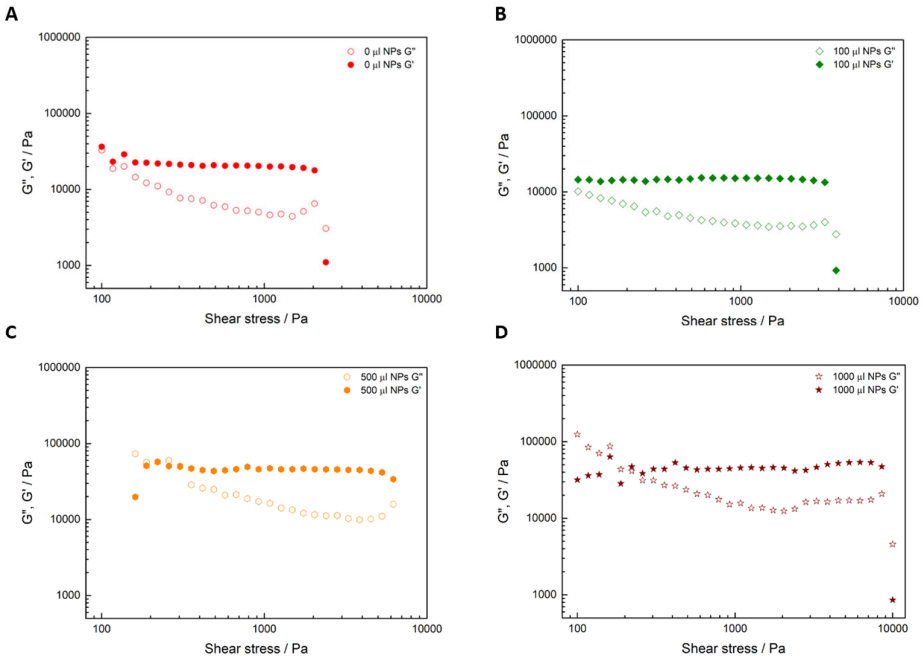

Figure 5.13: Influence of NPs 0 µL (0 µg/L), 100 µL (2.6 µg/L), 500 µL (12.8 µg/L), 1000 µL (25.6 µg/L) in the rheological properties of sodium alginate hydrogel crosslinked with Eu^{3+}.

From Figure 5.13, Panel A, corresponding to 0 µL NPs (0 µg/L), shows a decrease in both the storage modulus (G') and loss modulus (G") with increasing shear stress, indicating a reduction in the hydrogel's elastic properties under stress. Panel B, with 100 µL NPs (2.6 µg/L), demonstrates that G' remains relatively stable across the range of shear stress, suggesting a more robust elastic structure at this NP concentration. Similarly, G" exhibits stability, with a slight decline at higher shear stress levels.

In Panel C, representing 500 µL NPs (12.8 µg/L), both G' and G'' show minor decreases as shear stress increases, yet they maintain higher values compared to lower NP concentrations, indicating enhanced elastic and viscous properties. Panel D, at 1000 µL NPs (25.6 µg/L), reveals that G' remains stable with a slight increase at higher shear stress values, indicating strong elastic behavior. G'' also maintains elevated levels, emphasizing significant improvements in both elastic and viscous properties.

The influence of shear stress is evident across all panels, with higher shear stress generally causing a decrease in both G' and G''. However, this effect is less pronounced at higher NP concentrations, indicating that the presence of NPs enhances the hydrogel's structural stability and resistance to deformation. The data suggest that increasing NP concentration not only improves the hydrogel's rheological properties but also its ability to withstand shear stress, maintaining a predominantly elastic behavior (G' > G'') across all concentrations. Grosskopf et al., observed similar results when a fixed polymer concentration and different NP concentration was used.[262] In higher NP content, there was an observed increase in the G″ overshoot during yielding. This indicates that substantial deformation energy is dissipated due to the de-caging of nanoparticles during the yielding process.[263–265]

Figure 5.14 illustrates that the hydrogel with 1000 µL NPs (25.6 µg/L) reaches its maximum swelling capacity relatively quickly and maintains a stable swelling ratio after about 35 minutes. This indicates good stability and water absorption characteristics at this NP concentration. Panel D in the rheological analysis revealed that with 1000 µL NPs (25.6 µg/L), both the storage modulus (G') and loss modulus (G'') remained stable across increasing shear stress, indicating a robust elastic structure and enhanced rheological properties. Similarly, the swelling ratio plot showed that the hydrogel's swelling ratio increased rapidly in the first 25 minutes, reaching a plateau around 35 minutes, where it maintained a constant swelling ratio of approximately 7.0 x 10%.

This consistency suggests that the hydrogel, with the addition of 1000 µL NPs (25.6 µg/L), achieved a stable maximum swelling capacity. The correlation between the two datasets highlights that the increased NP concentration not only improves

the hydrogel's elasticity and viscosity but also ensures its structural integrity and stability during water absorption.

Consequently, the incorporation of 1000 µL NPs (25.6 µg/L) significantly enhances the hydrogel's ability to withstand mechanical stress and maintain its functional properties over time.

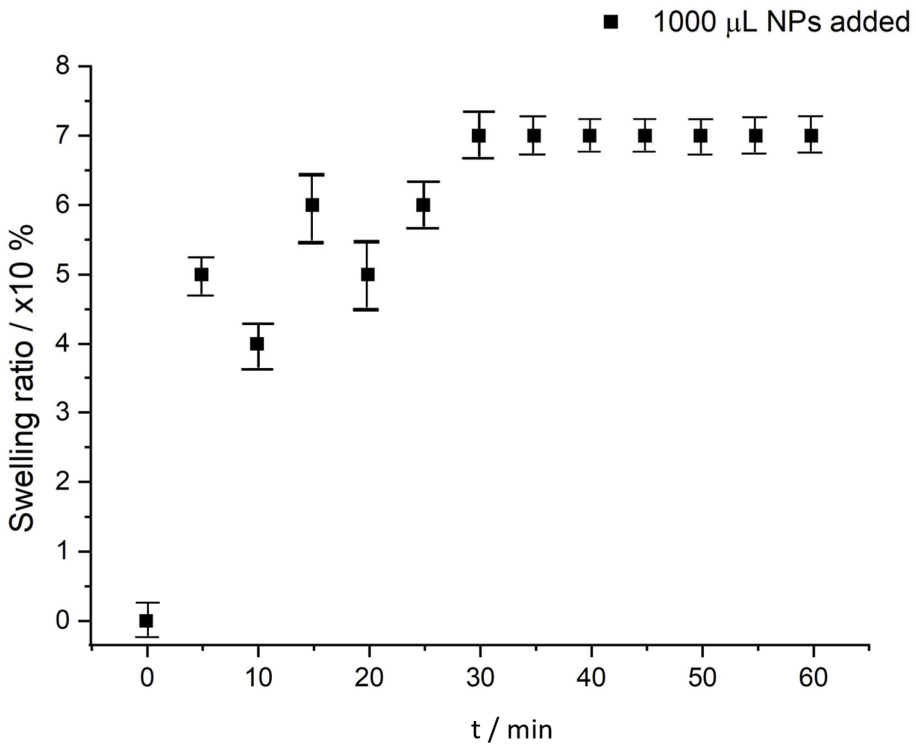

Figure 5.14: A graph of swelling ratio versus time, t (min).

5.2.5 NP release and luminescence properties

In Figure 5.15, luminescence data of $LaF_3:Ce^{3+}Tb^{3+}$ NPs embedded in sodium alginate hydrogel is shown. The red emission detected when excited at 250 nm indicates an energy transfer from Tb^{3+} in the NPs to Eu^{3+} used as crosslinker in the hydrogel. Co-doping of the NPs with Ce^{3+} was to enhance the green emission due to Tb^{3+}. The Ce^{3+} excitation energy lies between 200 nm and 375 nm, which originates from allowed 4f→5d transitions. Emission due to the NPs alone is observed at 553 nm, when excited at 250 nm. Thus, resulting green emission at 553 nm originates from an energy transfer from higher 5d states in Ce^{3+} that populate lower 5d states of Tb^{3+} between 420 nm and 450 nm. Hence, using 250 nm as excitation energy for

the hydrogel-NPs hybrid system not only leads to the emission of Tb^{3+} but most of the energy in the lower 5d states is transferred to Eu^{3+}. Furthermore, stark f-f transitions in Eu^{3+} are also induced leading to the orange color and not the deep red emission typical for Eu^{3+}. At lower excitation energy (350 nm), almost all electrons in lower excited states of Ce^{3+} and those in higher ground states of Tb^{3+} that have overlapping energies are promoted to the excited 5d states in Tb^{3+}. Hence, only green emission is detected leaving almost no electrons that cross over to Eu^{3+} excited states.

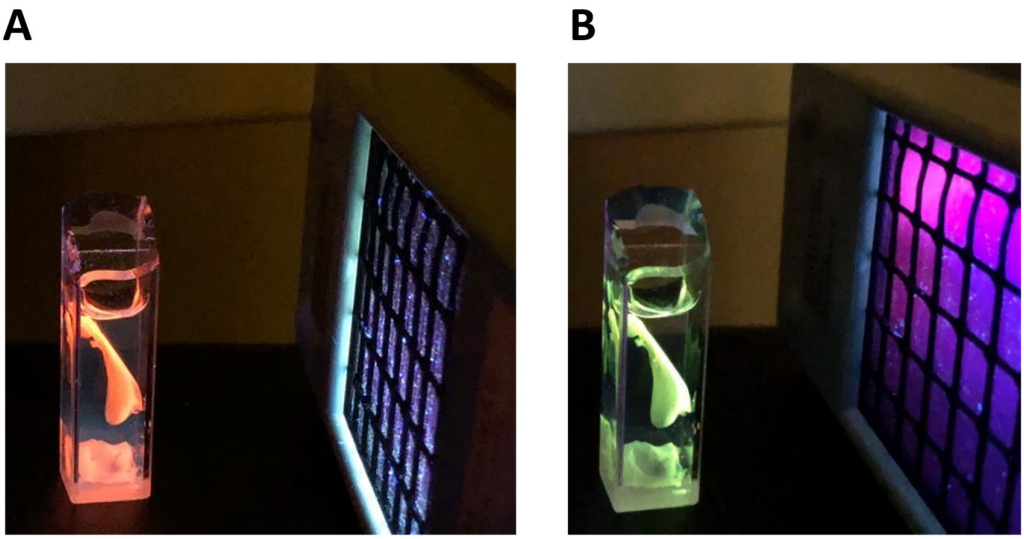

Figure 5.15: Photograph of sodium alginate–LaF_3:$Ce^{3+}Tb^{3+}$ NPs hybrid material suspended in Milli-Q water and illuminated using a UV lamp A) excited @ 250 nm B) @ 350 nm.

Figure 5.16 shows the measured emission spectra of the Eu^{3+}-sodium alginate hydrogel - LaF_3:$Ce^{3+}Tb^{3+}$ NPs hybrid system. The emission detected at 478 nm is attributed to the organic components in sodium alginate in original state. Depending on the pigmentation or impurities of the alginate derivative, the emission can range between 400 nm and 500 nm.[246] From the spectra, emission band of Tb^{3+} @ 553 nm is much lower than Eu^{3+} @ 617 nm due to two main reasons. First, the energy transfer from Tb^{3+} to Eu^{3+} and secondly due to high concentration of Eu^{3+} ions in the hydrogel matrix compared to Tb^{3+} ions in the NPs.

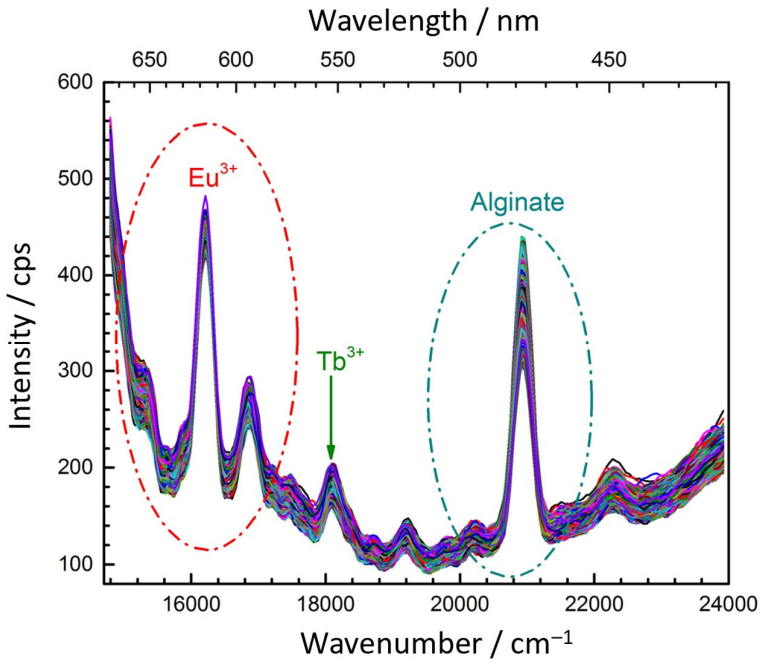

Figure 5.16: Emission spectra of LaF_3:$Ce^{3+}Tb^{3+}$ NPs embedded in sodium alginate hydrogel crosslinked with 0.2M Eu^{3+} measured at 378 nm excitation wavelength.

Time dependent emission spectra were monitored for 20 h at 37°C, which is approximately the time and temperature used for cell studies with NIH 3T3 cells. Notably, the intensity of major emission peaks (alginate, Tb^{3+} and Eu^{3+}) decrease over time. Moreover, green emission due Tb^{3+} is almost diminished after 15 h *(c.f. Figure 5.17)*. At this time, detecting green emission requires; large optical slits and high voltage during measurement, hence low signal to noise ratio. In contrast, red emission due to Eu^{3+} remains appreciable and is detected even after 15 h. Between the first 7 h, NPs are slowly released from the hydrogel matrix. The hydrogel begins to swell in water and bound NPs detach. In fact, the intense Eu^{3+} peak at 617 nm shows an increase in emission intensity, meaning that the concentration of NPs decreases from the hydrogel and aggregate at the bottom of the cuvette cell. Thus, the red emission is not compromised. After 7 h, the emission due to sodium alginate hydrogel begins to shrink because small pieces of the hydrogel fragmented over time. However, after 12 h this emission and corresponding emission due to Eu^{3+} decrease over time but at similar rates. The emission due Tb^{3+} drastically diminishes.

Nevertheless, it does not mean that no green emission is detected but rather the NPs are not any longer suspended in the hydrogel and solution but form aggregates at the bottom of cuvette cell. Further detection of NP aggregates will require filtering solution, drying and measuring luminescence in dry state or redispersed in a colloidal solution.

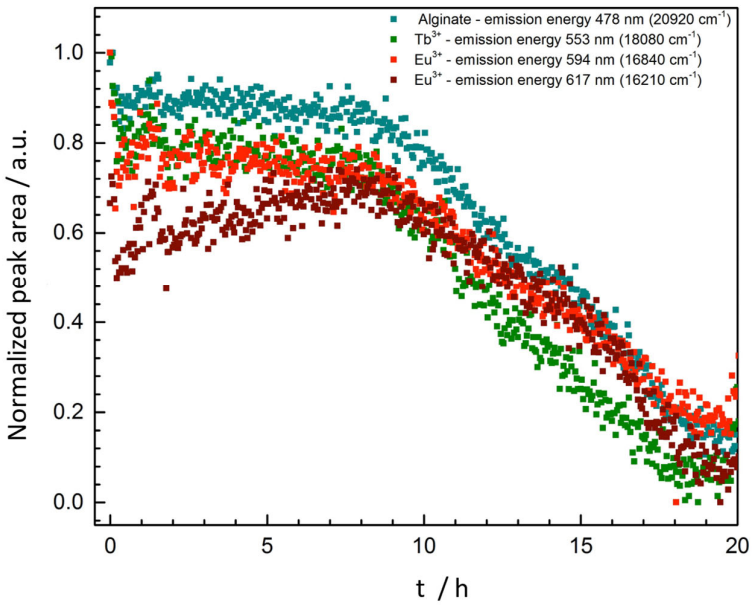

Figure 5.17: Peak area analysis of selected energetic bands from the emission spectra of LaF_3:$Ce^{3+}Tb^{3+}$ NPs and Eu^{3+} crosslinked sodium alginate hydrogel.

5.2.6 Bioimaging using sodium alginate hydrogel–LaF_3:$Ce^{3+}Tb^{3+}$ NPs

The Na-Alginate–LaF_3:$Ce^{3+}Tb^{3+}$ NP hybrid system was used for bioimaging experiment with NIH 3T3 fibroblast cells cultured on TCPS substrates. The cells were incubated for 24 h to allow for adhesion and proliferation. Figure 5.18 shows NIH 3T3 cells attached on TCPS without the hydrogel-NP matrix, displaying typical cell growth and attachment with visible cell structures such as the nucleus and filopodia. The calculated cell density in this image was approximately 1.05×10^5 cells per cm². However, hydrogel samples without embedded NPs degraded after 12 h, preventing cells from attaching to the hydrogel surface. The TCPS surface was hindered by hydrogel remnants floating and segregating at the interface between the TCPS and cell medium, interfering with cell metabolism and leading to cell death. In contrast, samples containing 12.8 µg/L NPs solution showed that cells could

proliferate and attach, as illustrated in Figure 5.18. NIH 3T3 cells are known to adhere in normal condition after 6 h.[266]

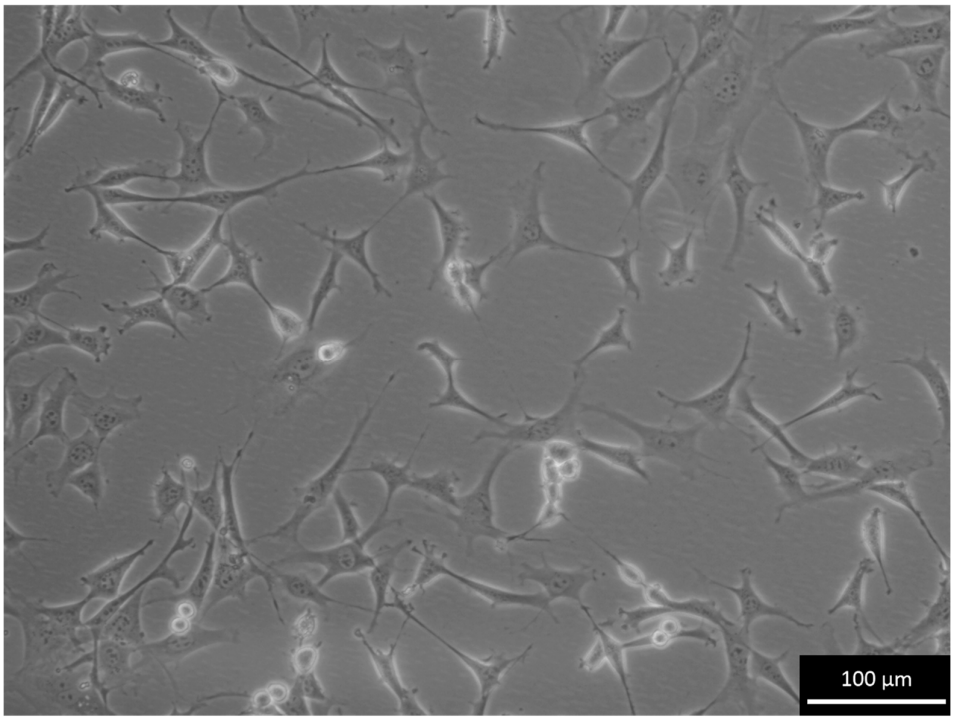

Figure 5.18: Light microscopy image of NIH 3T3 cells attached on TCPS without hydrogel-NP matrix taken after 24 h incubation.

Most cells grew inside the hydrogel with adhesion occurring between 9 and 10 h, although sometimes delayed up to 12 h due to direct injection into the hydrogel matrix. Some cells migrate to the top surface of the hydrogel. After 24 h, cell medium was replaced, prompting further cell migration outward through the hydrogel network in search of nutrients. Encapsulated cells within the hydrogel matrix *(see Figure 5.19)* exhibited more elongated shapes compared to those outside, likely due to active internal processes such as cytoskeletal rearrangement and variations in local adhesive forces and cell density.[267] This phenomenon of delayed cell adhesion has also been observed with ZnO NPs in 3D cell culture with NIH 3T3 cells by Sambale et al.[268] Cell encapsulation was maintained for up to 48 h before the hydrogel matrix began to fragment. This study marks the first instance of NIH 3T3 cells being encapsulated in a Eu^{3+} ionically crosslinked Na-Alginate–LaF_3:$Ce^{3+}Tb^{3+}$ NP hybrid system. The delayed adhesion and subsequent migration patterns observed indicate potential applications in tissue engineering and regenerative medicine, where controlled cell growth and migration are crucial.

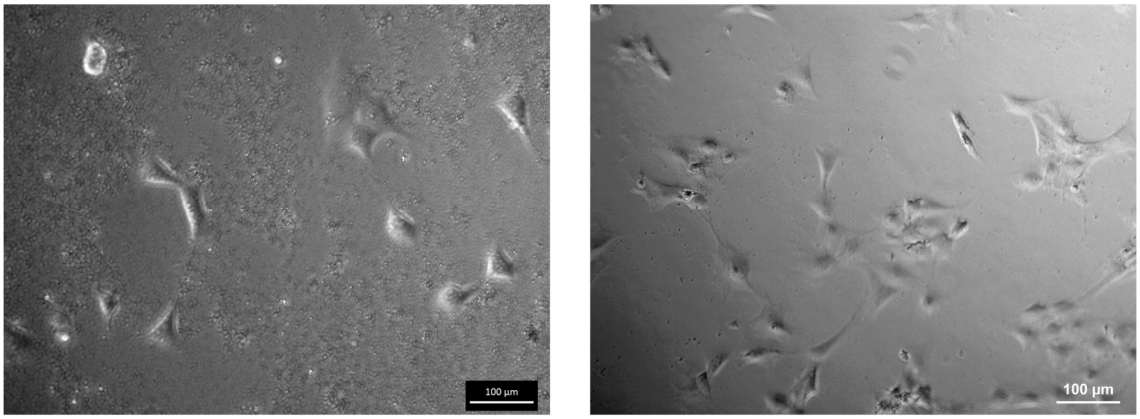

Figure 5.19: (Left) Top side image of hydrogel-NP matrix taken after 24 h incubation with NIH 3T3 cells as seen under light microscopy. (Right) Image shows a cross-section cut along the horizontal axis parallel to the TCPS surface of the hydrogel-NP matrix taken after 24 h incubation with NIH 3T3 cells.

To investigate bioimaging via FLIM, first an experiment was designed to mimic NIH 3T3 cell encapsulation in a hydrogel hybrid system. Dye-labeled (with Nile red) and unlabeled polystyrene (PS) cubes were used instead of NIH 3T3 cells, (prepared according to procedure in 5.4.5). Eu^{3+} ions are replaced with Ca^{2+} as crosslinker in preparing Na-Alginate hydrogel.

In the first experiment (A), dyed PS cubes were incorporated in to a hydrogel matrix that is not dye-labeled and investigated via FLIM *(see Figure 5.20 panel A)*. Dye-labeled PS cubes were clearly detected with no emission interference from the undyed hydrogel. Contrary to the first experiment, in the second experiment (B), undyed PS cubes were embedded in a dye-labeled hydrogel (5-aminofluorescein dye). Dark cubic-shaped “voids” were detected, and a strong signal from the 5-aminofluorescein dye in the hydrogel was observed *(see Figure 5.20 panel B)*. The signal-to-noise ratio was low at the cube edges due to varying orientations.[269]

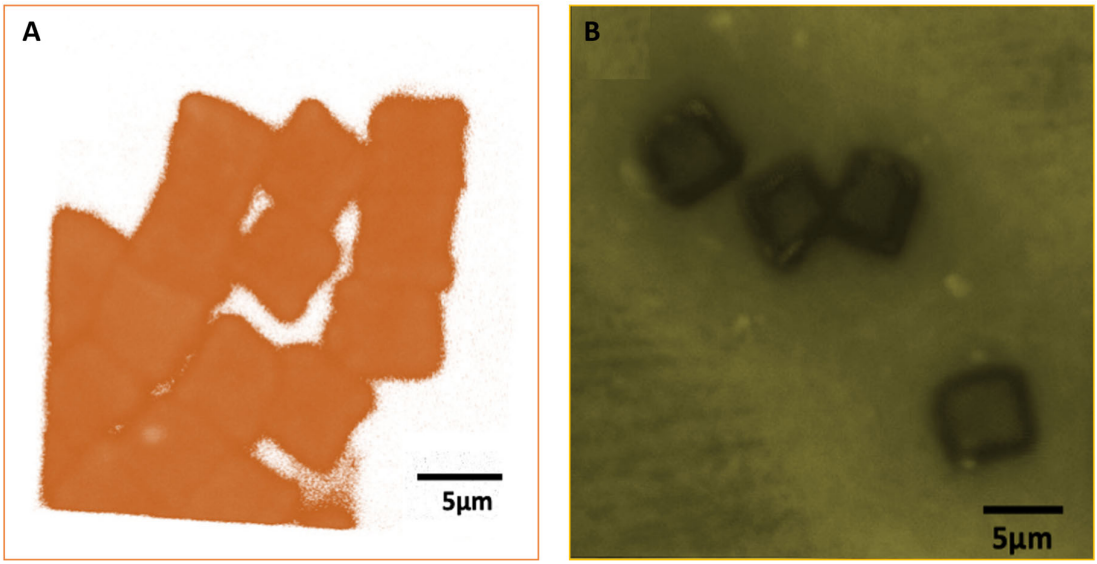

Figure 5.20: FLIM measurement of (A) Nile Red stained 5 µm PS cubes incorporated in Ca^{2+} crosslinked sodium alginate hydrogel; (B) unstained 5 µm PS cubes incorporated in Ca^{2+} crosslinked sodium alginate hydrogel stained with 5-aminofluorescein.

The observations suggest that Na-Alginate hydrogel may be a candidate for bioimaging of encapsulated cells. These observations are supported by previous study on alginate based bioinks for 3D printing.[270]

In this regard, an attempt to use live NIH 3T3 cells was made, but for this purpose with NP–Na-Alginate hydrogel crosslinked with Eu^{3+} ions. NIH 3T3 cells were incubated with NP–Na-Alginate hydrogel in cell medium for 24 h. Thereafter, the cells were washed in PBS and soaked in PBS for investigation under fluorescence light microscope. Initially, no fluorescent emission due to Eu^{3+} was detected. The excitation spectra of Eu^{3+} typically span between 250 nm and 420 nm depending on the site symmetry and crystal field splitting.[107] However, the organic components in the matrix also exhibit photoluminescence in the visible range, necessitating high energy between 250 nm and 350 nm to induce red emission. This was challenging to probe since the available optical fluorescence microscope was limited to excitation wavelengths above 420 nm, precluding proper excitation of Eu^{3+}.

To address this limitation, live-dead staining was conducted following standard protocols using propidium iodide (PI) and fluorescein diacetate (FDA) *(see Appendix IV)*.

Figure 5.21 shows a fluorescence light microscope image of the hydrogel-NP hybrid system. In this staining assay, green and red spots typically indicate live and dead cells, respectively. The image predominantly shows green spots and a uniform red background. Some green shadowed spots are visible beneath the red uniform color, indicating cells encapsulated within the hydrogel matrix at a shorter distance from the outer surface. Cells deeper in the matrix were obscured by the intense red color. The red background is not an unambiguous indicator of dead cells, as the hydrogel itself absorbed the PI dye. Potential energy transfer from the lowest energetic states of PI dye to Eu^{3+} might have enhanced the red emission from Eu^{3+}, although this phenomenon was not explored in this thesis. Carneiro Neto et al., reported theoretical calculations proving the existence of an intramolecular energy transfer for both singlet-triplet intersystem crossing and ligand-to-metal (and vice versa) between a multitude of ligand and Eu^{3+} energetic states.[271]

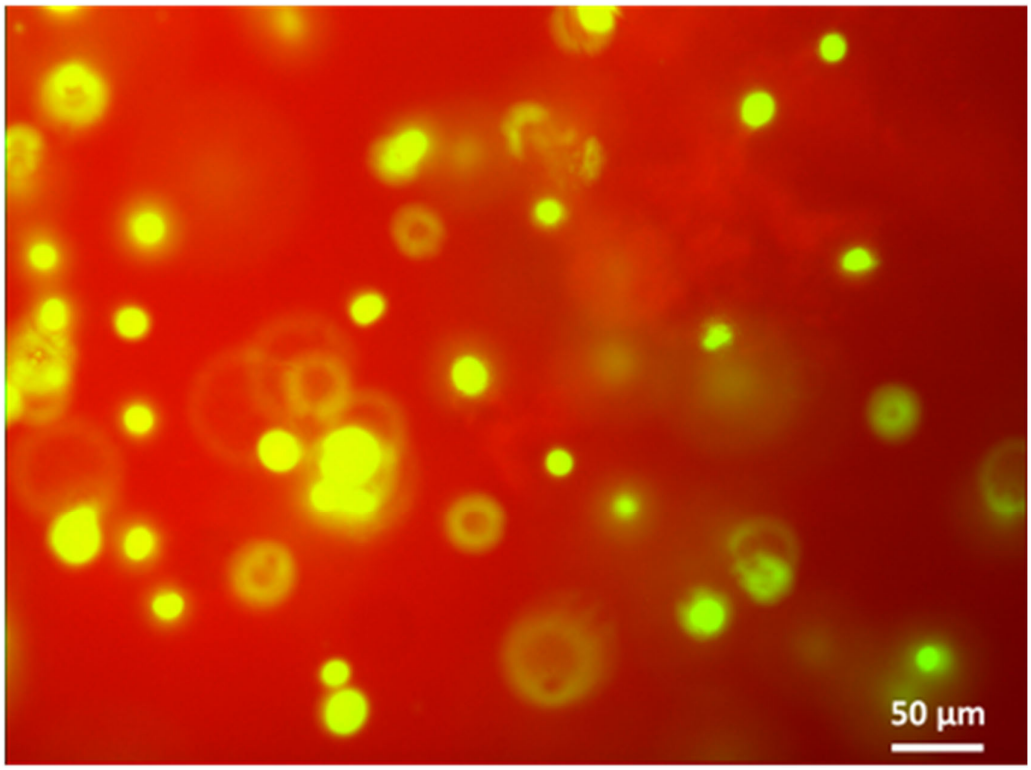

Figure 5.21: Live-dead staining and imaging of NIH 3T3 cells using a fluorescence microscope.

5.3 Conclusion

This Chapter focused on the analysis of potential toxicity of the NPs synthesized in Chapter 4. Furthermore, it was investigated how to prepare a biocompatible NP–Hydrogel hybrid system that can be potentially used bioimaging. The hybrid system was developed by first mixing NPs solution with Eu^{3+} solution (used as crosslinking agent) before mixing with Na-Alginate solution. This was followed by investigation of mechanical and optical properties.

Initially, toxicity assays using NIH 3T3 fibroblasts and PaTu 8988t cells demonstrated a dose-dependent decrease in cell viability for LaF_3:$Ce^{3+}Tb^{3+}$ NPs. At a concentration of 0.0023 mg/mL, abrupt and significant changes in absorbance were detected, indicating this concentration as a critical threshold for investigating cytotoxicity. TiO_2@SiO_2@LaF_3:$Ce^{3+}Tb^{3+}$ CSNPs exhibited higher cytotoxicity due to their incoherent structure, which disintegrates over time and forms large aggregates in the cell medium. These aggregates hinder cell attachment as they cover a large area of the TCPS, and the particle dissolution increases the turbidity of the cell medium, interfering with MTT and formazan absorption. PaTu 8988t cells, compared to NIH 3T3 cells, are generally more sensitive to certain NPs. Consequently, live/dead staining was performed only using the NIH 3T3 cell line. MTT, live/dead staining, and ICP-OES analyses further validated minimal cytotoxicity at the 0.0023 mg/mL concentration, confirming efficient cellular interaction without significant adverse effects. This toxicity assessment provided an understanding of NP biocompatibility, emphasizing the importance of selecting appropriate concentrations for safe application in biological systems.

The synthesis process of hydrogel–NP hybrid systems involved the formation of sodium alginate hydrogels crosslinked with Eu^{3+} ions, coupled with the incorporation of LaF_3:$Ce^{3+}Tb^{3+}$ luminescent NPs. The hydrogel–NP hybrid systems were systematically analyzed to understand the impact of NP concentration on mechanical properties *(see Figure 5.12)* and luminescent behavior *(see Figure 5.15)*. Rheological measurements revealed that the inclusion of NPs significantly enhances the mechanical strength of the hydrogels.

Overall, the presence of NPs increases the hydrogel's structural stability and resistance to deformation, with higher NP concentrations improving rheological properties and maintaining predominantly elastic behavior (G' > G'').

FSEM was used to observe the microstructural changes in the hydrogel matrix. The presence of NPs resulted in a notable increase in fiber thickness and a decrease in pore size, indicating enhanced structural reinforcement.

The luminescent properties of the hybrid materials were also investigated. From the results energy transfer from Tb^{3+} in the NPs to Eu^{3+} in the hydrogel matrix, leading to distinctive emission spectra. Green emission from Tb^{3+} and red emission from Eu^{3+} were both detected, with the intensity of these emissions varying over time. This behavior suggests the potential for these materials to be used in bioimaging applications where specific wavelength emissions are required.

Biocompatibility studies using NIH 3T3 cells confirmed that the sodium alginate hydrogel-NP hybrids support cell proliferation and adhesion. Na-Alginate–NP hybrid system with cells exhibited higher density and better adhesion compared to the control, indicating that the hydrogel-NP environment promotes cellular activities effectively.

5.4 Materials and methods

$EuCl_3 \cdot xH_2O$ (99.99%) Reacton Germany. $Eu(NO_3)_3 \cdot xH_2O$ (99.9%), ChemPur Europium (III) acetate (99.999%) Alfa Aesar Germany. Ethanol denatured (90%), ethanol anhydrous (99+%), Alginic acid sodium salt, low viscosity, $CaCl_2$ (93%), Alfa Aesar Germany. 5-Aminofluorescein (isomer I) (95%), nile red (98%), TCI Germany. NIH 3T3 cell lines were obtained from Dr. Jürgen Schnekenburger (Biomedical Technology Center of the Medical Faculty Münster, Germany). Milli-Q water (resistivity of 18.2 MΩ cm), from a Millipore Direct Q8 system, (Millipore Advantage A10 system, Schwalbach, Germany) with a Millimark Express 40 as filter (Merck, Germany). Phosphate-buffered saline (PBS) solution with a pH of 7.4 purchased from Sigma Aldrich was autoclaved before use. Freshly prepared LaF_3: Ce^{3+} Tb^{3+} NPs and PS cubes. The PS cubes were prepared according procedure from Song and Schönherr et al.[269]

5.4.1 Preparation of sodium alginate hydrogel

5% of sodium alginate solution was prepared in Milli Q water. 500 µL of this solution was mixed with 300 µL of 0.2 M Eu^{3+} solution to form a gel. The quality of the gel can be optimized by changing the amount of crosslinker and keeping the amount of alginate constant or vice versa *(see Figure 5.22)*.

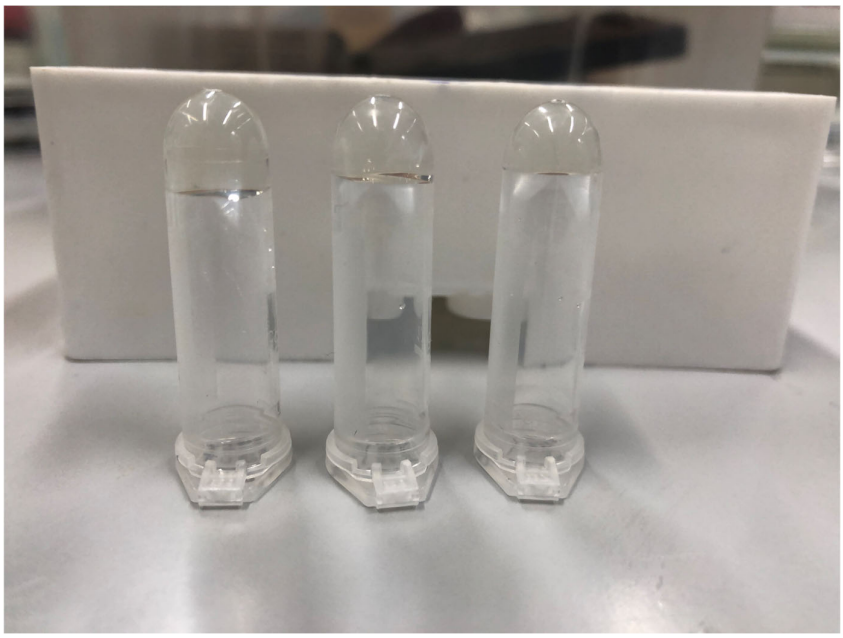

Figure 5.22: Images of freshly prepared sodium alginate hydrogel crosslinked with Eu^{3+}.

5.4.2 Preparation of samples for rheology measurements

The samples for rheology were prepared as shown in Table 5.2 Alginate and Eu^{3+} solutions are kept constant and only the volume of NPs is varied. Milli Q water is topped up on each varied amounts of NPs to create a balanced ration of water to alginate solution.

Table 5.2 Rheology samples (preparation and concentration of different materials).

Sample No.*	NPs (0.0462 g/L) volume (µL)	Milli Q volume (µL)	Total volume (µL)	Final NPs concentration in gel matrix (µg/L)
1	0	1000	1800	0.0
2	50	800	1800	1.3
3	100	600	1800	2.6
4	200	400	1800	5.1
5	400	200	1800	10.2
6	500	500	1800	12.8
7	600	100	1800	15.4
8	800	50	1800	20.5
9	1000	0	1800	25.6

*500 µL of 5 % Alginate and 300 µL 0.2 M Eu^{3+} volume added to all samples.

5.4.3 Preparation of samples for rheology measurements

The swelling ratio of the hydrogel was done gravimetrically. After preparing the hydrogel, a section was cut and freeze dried for 96 h. The dried sample was dipped in to a buffer solution at 37°C for 1 h. After every 5 minutes the wet hydrogel was removed the buffer solution and excess liquid on the surface of the hydrogel wiped with a cleantech tissue that leaves no fibers. The wet hydrogel is weighed until an equilibrium is attained. The percentage of swelling was calculated as shown in Equation 3:

$$Swelling\ \% = \frac{W_{wet} - W_{dry}}{W_{dry}} \times 100\ \% \quad (3)$$

W_{wet} and W_{dry} denote the weight of the wet and dried hydrogel, respectively.

5.4.4 Preparation of samples for cell studies

NIH 3T3 mouse fibroblasts were obtained from Dr. Jürgen Schnekenburger at the Biomedical Technology Center of the Medical Faculty in Münster, Germany. The statistical analysis of the cell counts was conducted using a one-sided ANOVA test. Cell culture was done according to protocol developed and modified by Lilge et al.[272]

All chemicals and glass ware were sterilized in the autoclave before use. 1 mL of 0.2 M europium acetate was used as cross linker and pH adjusted to 7 using buffer solution (pH 10.00 at 20°C). The hydrogel is first soaked in 3 mL milli Q water for 5 minutes and incubated at 37°C to evaporate any toxic vapors. This step is repeated at least 6 times or more with cell medium in the hydrogel has a clear pink color resembling the cell medium. The NIH 3T3 cells are then injected in to the hydrogel and incubated with fresh medium. After every 12 h the cell medium has to be changed but no washing of the hydrogel is necessary.

5.4.5 Preparation and imaging of 5 µm PS cubes

PS microcubes with 5 µm edge length were prepared using titanium-coated silicon or glass substrates according to a standard protocol from Song et al., and Steuber et al.[273] The substrates, cut to 2 cm x 2 cm, were cleaned by sequential rinsing with Milli-Q water, ethanol, and chloroform (for glass substrates), followed by a final ethanol wash and nitrogen drying. PS was dissolved in toluene (6 wt%), with Nile Red dye (1.57 mM) added for dye-doped microcubes. Drops of this solution were spin-coated onto the substrates using a spin coater (30 s, 1200 rpm). The substrates were then vacuum-dried overnight at 140°C or in a desiccator for four days. The PS microcube structure was created using nanoimprint lithography with a PDMS stamp and the Eitre 3 nanoimprinter (Obducat, Sweden). Fluorescence microscopy was performed using time-resolved confocal microscopy with an IX 71 inverted microscope (Olympus, Hamburg, Germany), employing a pulsed diode laser (LDHD-C-485, PicoQuant, Berlin, Germany) at 482 nm. Fluorescence emission was collected with a 60x water immersion objective (UPlanSApo 60x / 1.20 N.A., Olympus) and detected by a single-electron avalanche photodiode (PD1CTC, Micro Photon Devices, Bolzano, Italy) after passing through a dichroic mirror (z500dcxr, Chroma, Bellows Falls, USA) and an emission filter (HQ510lp, Chroma) and a 50 µm pinhole. Data acquisition and analysis were conducted using SymPhoTime software and Matlab R2020b. Images were typically 80 µm x 80 µm, with the xy-plane defined orthogonal to the substrate or water-air interface. Time-correlated single-photon counting (TCSPC) was used for fluorescence measurements. Lifetimes of Nile Red were determined by fitting a multi-exponential function to the intensity spectrum, fixing one lifetime at 0.05 ns to remove residuals. Integration times were set at 1.6 ns and 32 ns, with fit quality assessed by residuals analysis.

5.4.6 ICP-OES sample preparation and experimental procedure

The concentration of the NPs before and after toxicity studies was determined using ICP-OES (ARCOS, SPECTRO Analytical Instruments GmbH, Kleve, Germany) fitted with a “Smart Analyzer Vision” software, version 6.01.0951. The standard curves of Ce, La and Tb emission lines were determined using OriginPro 2015.[244] Internal standard (Mn 257.611 nm) was used to successfully monitor the signal to background ratio, which was within accepted limits > 3% of the overall intensity. The parameters for the measurement were as follows; End-on Position (EOP / axial view), 1200 W plasma power, 13 L/min cool gas flow, 0.8 L/min Auxiliary gas flow, 0.9 L/min Nebulizer gas flow, gas: Argon (5.0), 2 mL/min Sample flow rate. ICP calibration standards were prepared by diluting the ICP stock solutions (La, Tb, and Ce) with Milli-Q water to the desired concentration with 2 % HNO_3. The samples with cell medium were digested with 2% HNO_3 before measurement. The concentration of samples prepared for analysis were as follows; 0 (blank), 10 µg/L, 50 µg/L, 100 µg/L, 200 µg/L, 500 µg/L and 1 mg/L.

Chapter 6 Synthesis of spherical micrometer-sized MgF_2 beads for digital holography via self-assembly of nanowhiskers

6.1 Introduction

Despite the fact that fluorescence labelling is an established approach to enable localization studies in fluorescence microscopy and benefits from high signals for many fluorophore-labelled antibodies,[274] certain challenges in live cell imaging cannot be avoided.[275–277] Among others, long term in vitro studies are hampered by photo bleaching.[278] To address this issue, some advanced photostable dyes and emitters like green fluorescent protein (GFP) for improved long term experiments have been newly developed .[279] However, such protein-based types of dyes require extra genetic engineering before use.[280,281]

Alternatively, label-free methods are increasingly recognized for their potential in biological and medical imaging due to their ability to circumvent the limitations associated with fluorescent or chemical labels, such as time-consuming preparation, potential toxicity, and sample alteration.[282] These imaging modalities may also enable the acquisition of qualitatively different data and hence new insight. These methods encompass a range of techniques, including phase-contrast microscopy, differential interference contrast microscopy, quantitative phase imaging (QPI), and notably, digital holography.[283–286]

Filed Patent & Abstract Submission for Scientific Paper

Kemper, B.; Schnekenburger, J.; Muganda, W. C. A.; Schönherr, H. Teststandards for Labelfree Imaging (TL-IM). **Germany Patent.**

Kemper, B.; Schnekenburger, J.; Muganda, W. C. A.; Schönherr, H. Teststandards for Labelfree Imaging (TL-IM). **European Patent.**

Kemper, B.; Decker, J. L.; Muganda, W.C.A.; Barroso, Á.; Marzi, A.; Wiegmann, S.; Ketelhut, S.; Greve, B.; Liedtke, T.; Schönherr, H.; Schnekenburger, J. Microspheres with Optical Properties Similar to Living Cells for Benchmarking Label-Free Quantitative Phase Imaging and Flow Cytometry. Abstract of Paper, SPIE Photonics West Label-Free Biomedical Imaging and Sensing (LBIS), 2025.

Digital holography employs a coherent light source, typically a laser, which is bifurcated into a reference beam and an object beam.[287,288] The object beam is directed at the sample and the light scattered by the sample interferes with the reference beam. The resulting interference pattern, or hologram, is captured with a digital sensor, such as a charge coupled device (CCD) or complementary metal oxide semiconductor (CMOS) camera. Subsequently, the recorded hologram undergoes computational processing through algorithms designed to reconstruct the phase and amplitude information of the light field. This process results in a three-dimensional image of the sample, elucidating its structure and other inherent properties without necessitating labels.[287]

The applications of digital holography are diverse, with a significant impact on biological imaging.[288] The technique enables real-time visualization and study of live cells, allowing for detailed observation of cell morphology, motility, and dynamic processes without the need for staining.[282] This capability is particularly advantageous for monitoring cell cultures, tracking cell growth, and detecting morphological changes in response to various conditions or treatments.[285] Additionally, digital holography facilitates quantitative phase imaging, which measures the optical thickness of cells, thereby providing critical data on cell mass, volume, and refractive index.[289] This technique is instrumental in investigating cell-cycle dynamics, identifying cellular abnormalities, and aiding in the diagnosis of diseases.[289,290] Furthermore, digital holography proves effective in evaluating cell viability and health, detecting pathological changes, and understanding cellular responses to various stimuli.[284] In essence, digital holography offers a non-invasive, high-resolution imaging modality that delivers both qualitative and quantitative insights, solidifying its role as an invaluable tool in biological and medical research.[274]

In digital holography and other label-free imaging techniques, the need for calibration is paramount to ensure accuracy and reliability of the measurements.[282] Calibration is essential to correct for any systematic errors and to achieve precise quantitative analysis of the samples. Proper calibration allows for the accurate reconstruction of the phase and amplitude information of the light field, which is critical for obtaining high-quality 3D images and quantitative data.[287]

The required properties of a calibration specimen include homogeneity, stability, and a well-defined refractive index. The refractive index of the calibration specimen should closely match that of the biological cells being studied to ensure that the imaging system is accurately tuned for the target samples.[291] For example, human cells typically possess a refractive index in the range of 1.37 to 1.40.[292] Therefore, a calibration specimen with a refractive index within this range would be ideal.

Among the different materials that could be potentially interesting for this purpose, MgF_2 stands out. MgF_2 is known to possess a refractive index similar to that of human cells, approximately 1.38 at wavelengths of 540 - 720 nm.[293] This similarity makes MgF_2 an excellent candidate for use as a calibration standard in digital holography, ensuring that the imaging system is properly calibrated to accurately reflect the properties of human cells.[294] As calibration standard a well-defined size and shape are also indispensable. However, there are no reports in literature on how to synthesize monodisperse MgF_2 bead of cell-like dimensions, i.e., diameters of 5 μm and beyond. Hence, the main objective of the work reported in this Chapter was to develop an approach that enables one to synthesize monodisperse spherical MgF_2 beads with diameters between 5 and 15 μm that can be used for label-free quantitative in vitro live cell imaging with digital holographic microscopy.

6.2 Results and discussion

6.2.1 Synthesis via microwave heating

The synthesis of nano- and micro-sized MgF_2 materials via microwave heating was explored to understand how the different parameters, including source of Mg, dwell times, and synthesis conditions, affect the final product shape and size (distribution). Initially, magnesium acetate tetrahydrate ($Mg(CH_3COO)_2•4H_2O$) and magnesium nitrate hexahydrate ($Mg(NO_3)_2•6H_2O$) were utilized as starting materials. Specifically, 0.5000 g of $Mg(CH_3COO)_2•4H_2O$ was dissolved in 2.0 mL of Milli-Q water. Subsequently, 3.0 mL of the ionic liquid BMIM[BF_4] was introduced into the solution, which was then stirred to form a homogeneous mixture. The reaction mixture was subjected to microwave heating at 100°C and 100 bar, with dwell times ranging from 5 to 30 minutes and a power setting of 200 watts. Post-reaction, the product underwent washing and drying before characterization using TEM, STEM-EDX, and FESEM.

Additionally, alternative syntheses using $Mg(NO_3)_2•6H_2O$ (0.3840 g) were conducted to investigate the effects of different sources of Mg on the final properties. Key variables, including dwell time, temperature, solvent, and source of Mg, were systematically varied to identify adequate strategies for preparing uniform spherical micro-sized MgF_2 particles.

Figure 6.1 summarizes the synthesis strategy for preparing nano- and micro-sized MgF_2 materials. The microwave heating method proved to be efficient, requiring less time and yielding a variety of nanosized structures, such as nanowhiskers, spherical NPs, and combinations of both in a single structure. Notably, the formation of nanowhiskers appeared to be important for the subsequent self-assembly process that led to the creation of spherical NPs. TEM images *(see Figure 6.2)* showed nanowhiskers with lengths ranging between 50 nm and 200 nm with average size of 120 nm ± 20 nm.

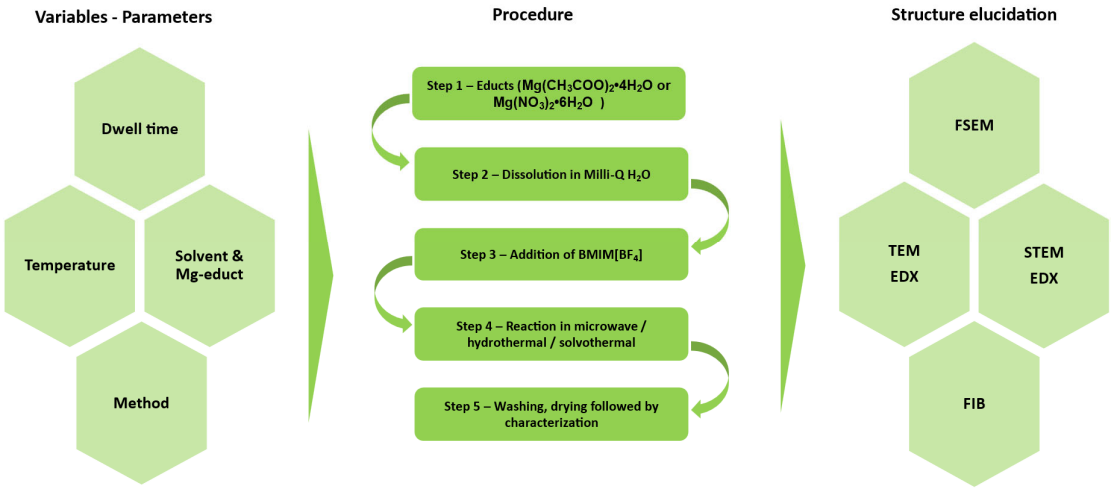

Figure 6.1: Summary of synthesis strategy for preparing MgF_2 nano- and micro-sized particles.

Microwave heating significantly reduced the reaction time and resulted in the formation of various nanosized structures, including nanowhiskers, spherical NPs, and hybrid structures combining both morphologies. The TEM images showed elongated structures consistent with nanowhiskers.

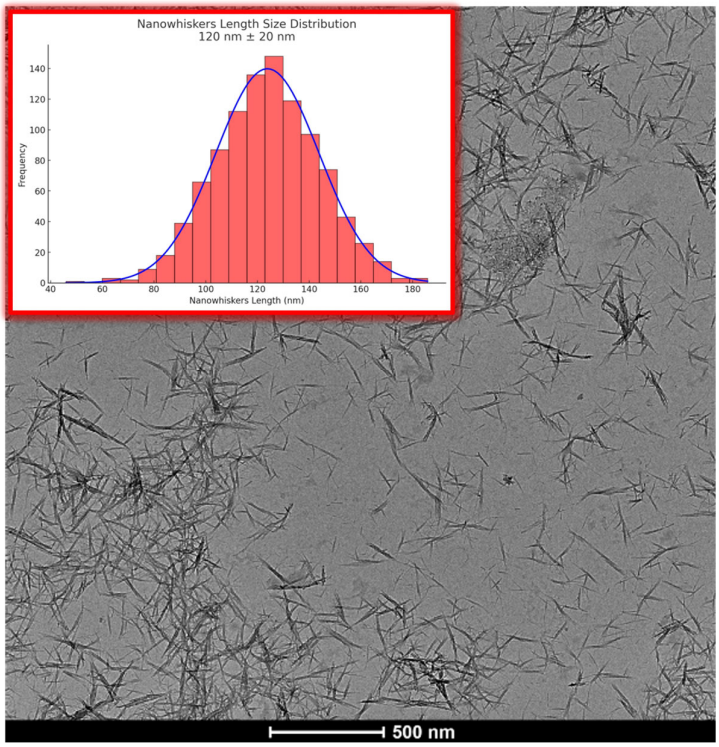

Figure 6.2: TEM image of MgF_2 nanowhiskers prepared in the microwave at 100°C and 5 minutes dwell time.

Increasing the dwell time in the microwave reaction chamber, while maintaining a power of 200 W, a temperature of 100°C, and a maximum pressure of 100 bar, influenced the growth of the nanowhiskers. After 10 minutes, the whiskers thickened at the center and merged to form NPs with sizes ranging from 80 nm to 100 nm ± 20 nm, as shown in Figure 6.3. These observations align with the findings of Bao et al., who reported similar structures of MgF_2 via solvothermal synthesis. However, Bao's synthesis required HF as the fluoride source and longer aging times (7 days) before the material could be applied directly. In contrast, the synthesis reported in this Thesis required only 24 h and used BMIM[BF_4] instead of HF as source for fluoride.

One may speculate that the observation of clustering of NPs into a sludge with BMIM[BF_4] and this formation begin with heating BMIM[BF_4] above its melting temperature (71°C). This heating presumably leads to the dissociation of $[BF_4]^-$ anions, which are subsequently replaced by water molecules in the solution. The hydrogen bond formation between water molecules and $[BMIM]^+$ lowers the thermal conductivity and the viscosity of BMIM[BF_4]. Consequently, the formed nanowhiskers are attracted together into a paste, where the growth into spheres is initiated *(see Figure 6.4)*.

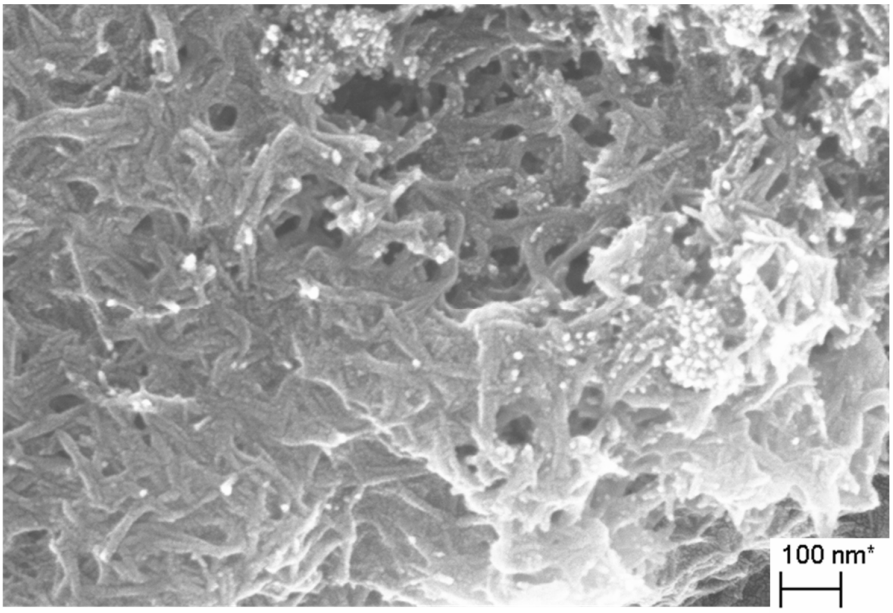

Figure 6.3: FESEM image of MgF_2 nanowhiskers and NPs prepared in the microwave at 100°C and 10 minutes dwell time.

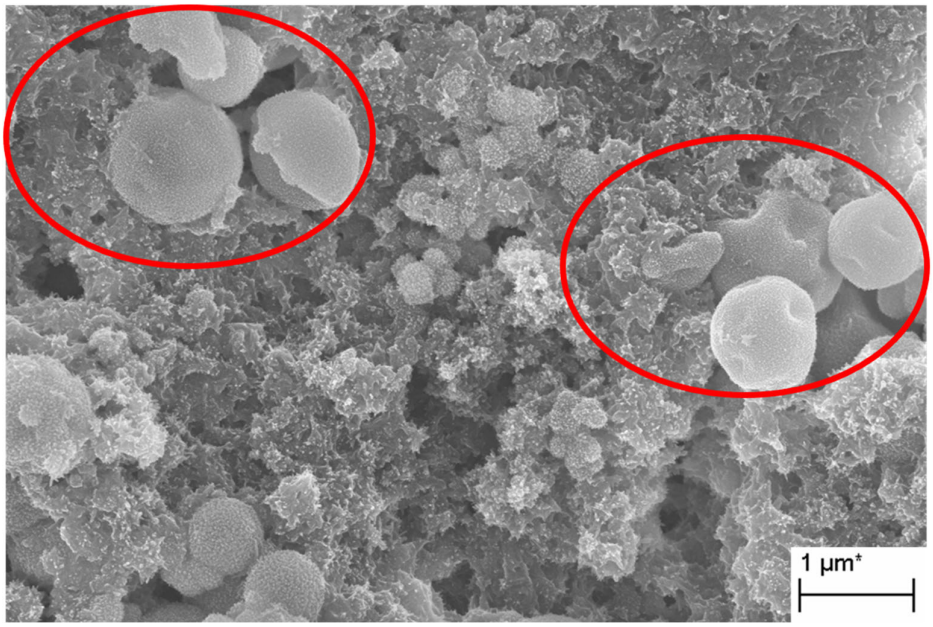

Figure 6.4: FESEM images of MgF_2 nanowhiskers and NPs prepared in the microwave at 100°C and 30 minutes dwell time. The red circles show deformed particles.

At 30 minutes dwell time, the NPs grew to a larger size, becoming polydisperse with diameters between 100 nm and 800 nm. Growth was apparently restricted and further heating resulted in deformed particles, some with depressions and others burst as indicated by the red-marked regions in Figure 6.4.

To obtain micro-sized beads larger than 5 µm, the temperature and dwell time were increased to 200°C and 2 h, respectively. The TEM observations of the reaction product show a bimodal distribution of spherical particles (1.2 µm ± 0.2 µm and 0.3 µm ± 0.1 µm), as shown in Figure 6.5. Further increasing the dwell time, while keeping other parameters constant resulted in smaller particles (0.74 µm ± 0.1 µm), with the outer surface of the particles forming platelets instead of needle-like structures *(see Figure 6.6)*. Smaller particles (0.3 µm ± 0.05 µm) apparently merged to form larger particles, likely due to the transformation of needle-like structures into spherical particles and the formation of hollow structures.

Sintering the particles at higher temperatures (500°C) further increased the particle sizes to 1.6 µm ± 0.2 µm and the particle surface become smoother. At such elevated temperatures neighboring particles merged and formed larger particles, as depicted in Figures 6.6 and 6.7.

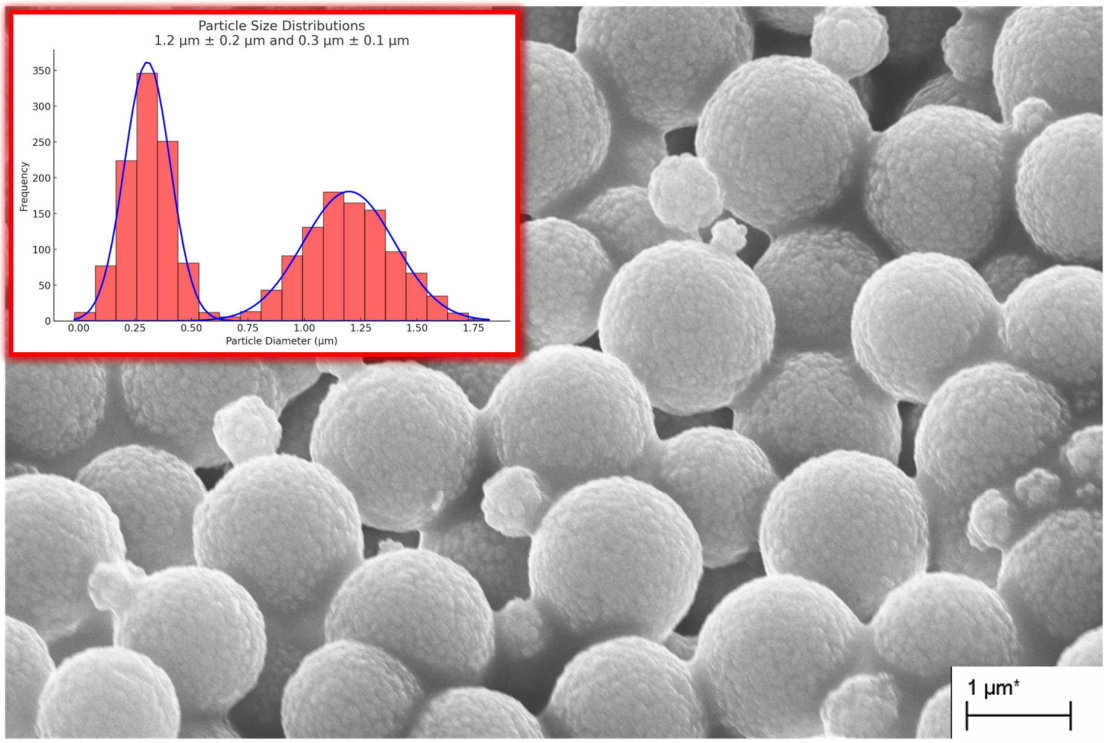

Figure 6.5: FESEM images of MgF_2 microparticles prepared in the microwave at 200°C and 2 h dwell time. Inset shows beads size distribution.

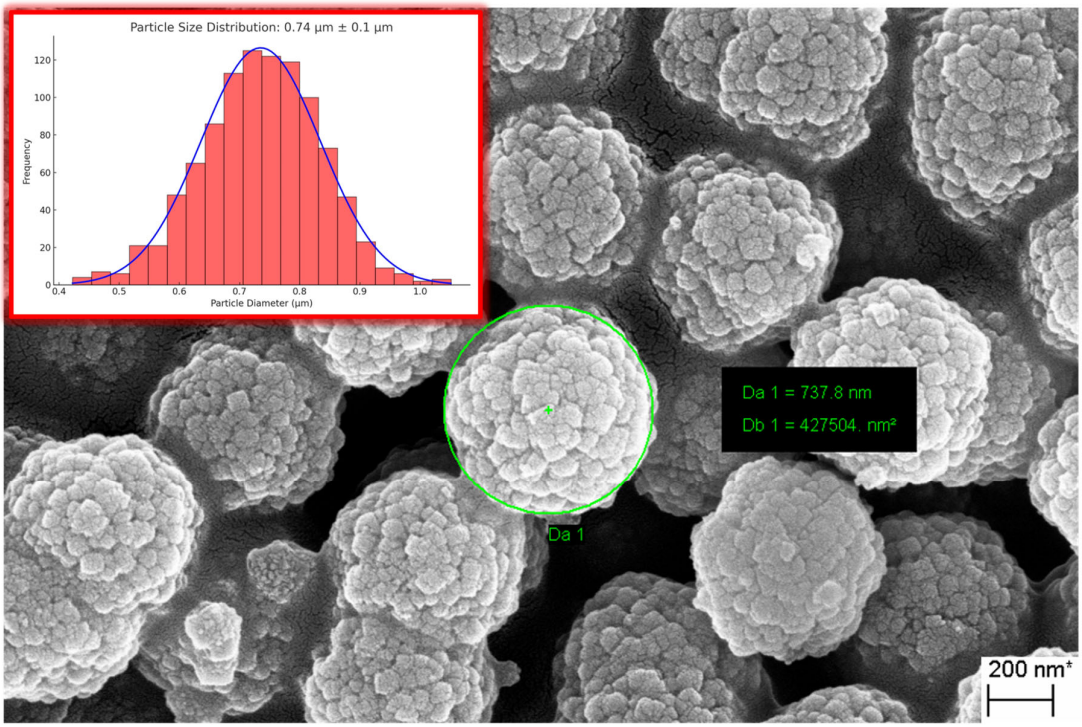

Figure 6.6: FESEM images of MgF_2 microparticles prepared in the microwave at 200°C and 5 h dwell time. Inset shows beads size distribution.

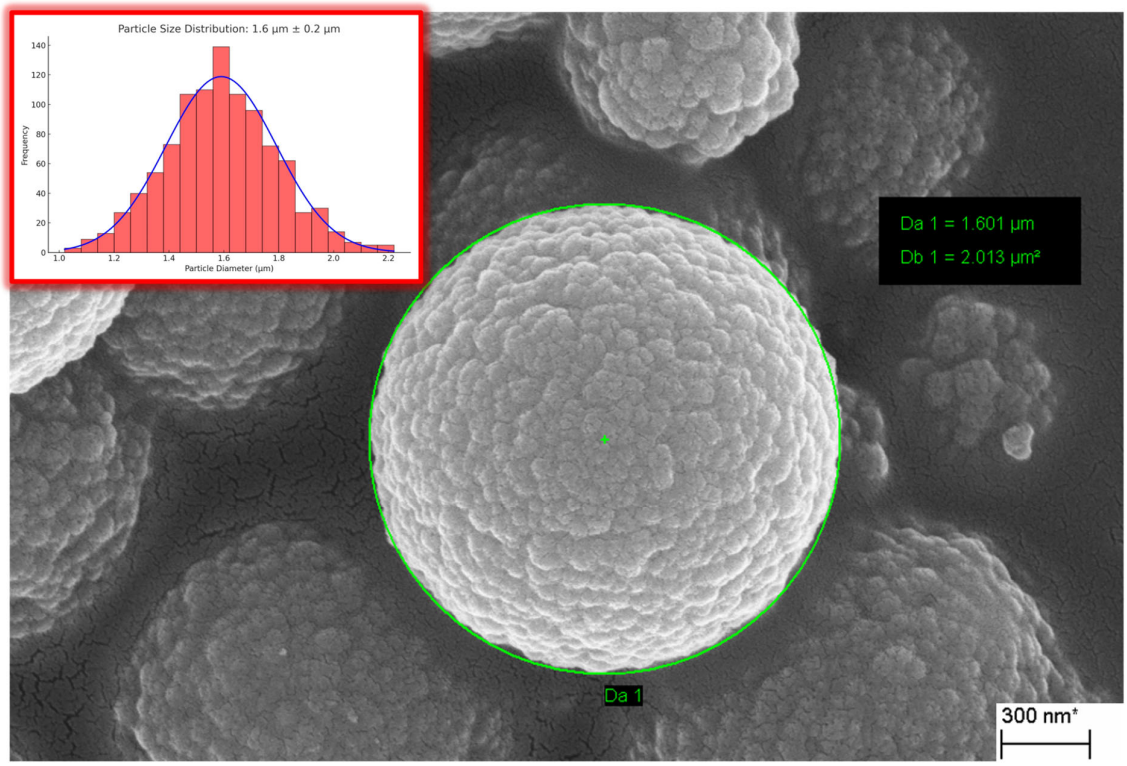

Figure 6.7: FESEM images of MgF_2 microparticles prepared in the microwave at 200°C and 5 h dwell time, followed by sintering at 500°C for 2 h. Inset shows beads size distribution.

The microwave synthesis method proved efficient for the synthesis of defined MgF_2 structures. The formation of nanowhiskers as a precursor to spherical NPs demonstrated a significant reduction in reaction time compared to traditional methods, highlighting the advantages of microwave-assisted synthesis. The microscopy observations show particle formation that is consistent with nucleation and growth mechanisms described in the literature.[295] For instance, Xu et al. reported on the use of microwave-assisted synthesis for alkaline earth metal fluorides, which demonstrated the effectiveness of microwave heating in achieving rapid and efficient synthesis.[72] Furthermore, Cai et al. explored the molecular characteristics of BMIM[BF_4] and water mixtures, providing insights into the role of ionic liquids in particle synthesis.[296] These comparisons underscore the advantages of microwave-assisted methods in reducing synthesis time and achieving desired morphologies with greater control and efficiency.

6.2.2 Solvothermal Synthesis

The solvothermal synthesis of MgF_2 micro-sized beads was undertaken to explore the effects of different solvents and synthesis conditions on particle growth and morphology. The objective was to prepare spherical micro-sized MgF_2 beads using various solvents and understand their impact on the resulting particle size and structure. Initially, $Mg(NO_3)_2 \cdot 6H_2O$ was used as the starting material. Different solvents, including Milli-Q water, ethanol, oleic acid, and octadecene, were employed to investigate their influence on the synthesis process.

In the initial experiment, 0.3840 g of $Mg(NO_3)_2 \cdot 6H_2O$ was dissolved in 10.0 mL of Milli-Q water, followed by sonication to ensure complete dissolution. The solution was then transferred to a reflux setup and heated to 180°C for 2 h. The resulting product was washed with ethanol and dried before characterization using FESEM. Figure 6.8 shows the FESEM image of the prepared MgF_2, revealing a fragmented and cracked morphology, with individual grains exhibiting relatively smooth surfaces interspersed with irregularities.

Despite sonication, the MgF_2 particles exhibited a pronounced tendency to agglomerate immediately after the synthesis, highlighting the challenges in achieving stable dispersions when Milli-Q water is used as the solvent *(see Figure 6.9)*.

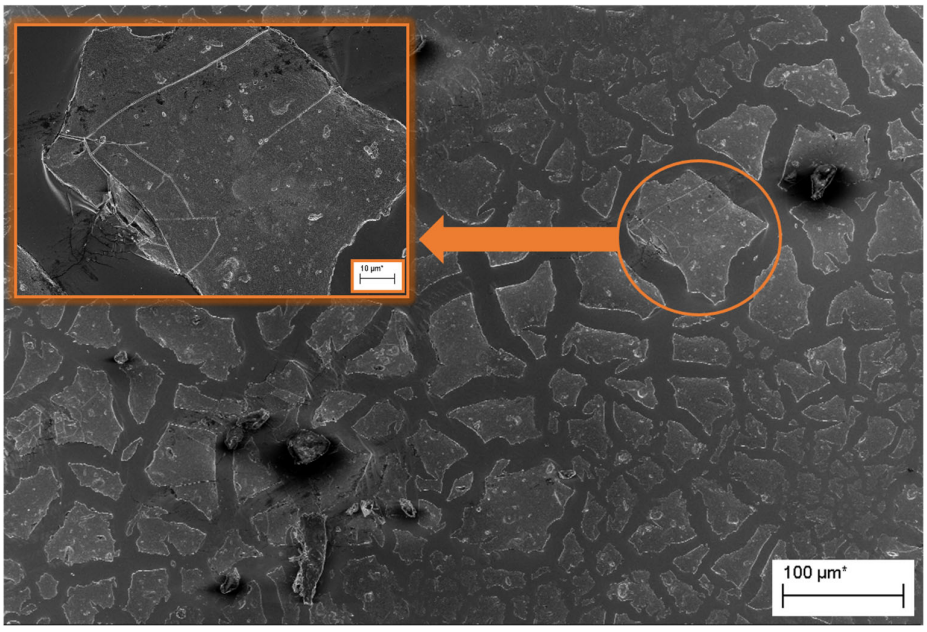

Figure 6.8: FESEM image of MgF_2 prepared at 180°C for 2 h within atmospheric pressure via solvothermal synthesis without ethanol (contents scratched from the glass flask surface).

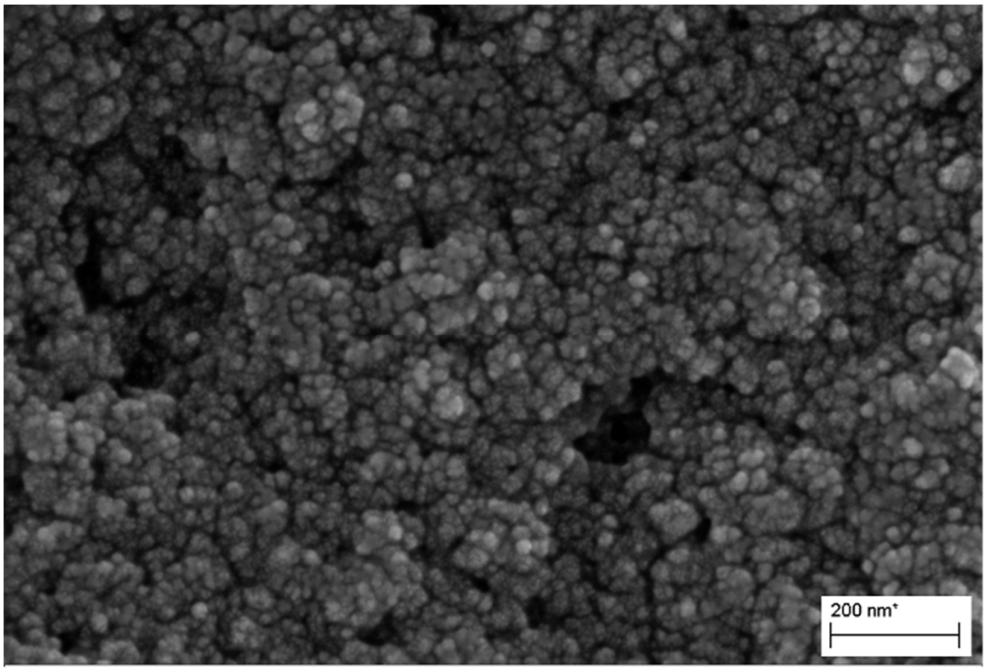

Figure 6.9: FESEM image of MgF_2 prepared at 180°C for 2 h within atmospheric pressure via solvothermal synthesis after 10 minutes of sonication.

These findings suggest that pure Milli-Q water is not an ideal medium for synthesizing isolated MgF_2 particles. To address the agglomeration issue, a mixture of Milli-Q water and ethanol in a 1:1 ratio was employed. This modification significantly influenced the morphology of the resulting MgF_2 particles. After 2 h of heating at 180°C, micro-sized beads with sizes of 2.6 µm ± 0.1 µm were formed *(see Figure 6.10)*. In some instances, the beads were observed to coalesce leading to oriented attachment *(see Figure 6.11)*.

Coalescence and oriented attachment are known phenomenon in nucleation and growth of particles.[295] They may be similar but differ in the orientation of the crystal planes along the grain boundary. Coalescence has in fact no preference for attachment.[297] However, in oriented attachment the common crystallographic arrangement occurs that is patterned to the crystal planes.[298] Hence, particles rotate while in contact to each other until there is match between the crystal orientation.[299] This is mainly due to Coulombic attraction.[295] In this case, the particles are not only coalescing, but orient with time and form cubic structures that appear to be sliced in to halves *(c.f. figure 6.11 – inset)*.[300,301]

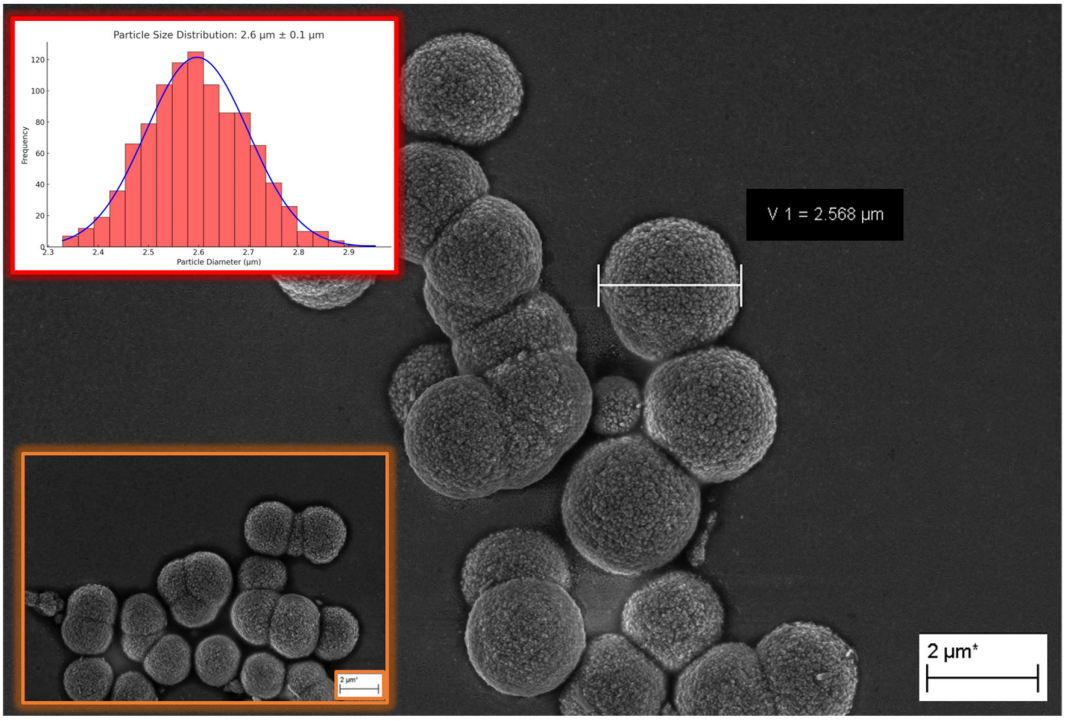

Figure 6.10: FESEM image of MgF_2 beads prepared via solvothermal synthesis at 180°C in a mixture of ethanol and water (1:1) for 2 h within atmospheric pressure conditions – the orange inset image shows coalescence and red shows beads size distribution.

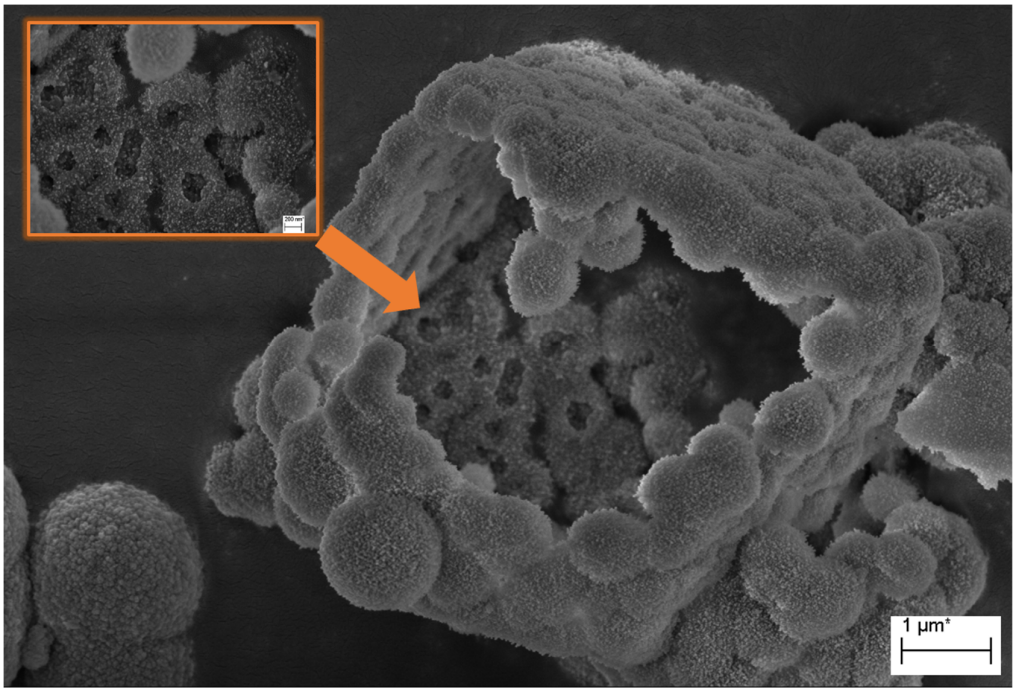

Figure 6.11: FESEM image of MgF_2 beads prepared via solvothermal synthesis at 180°C in a mixture of ethanol and water (1:1) for 2 h within atmospheric pressure conditions – the inset image shows oriented attachment.

Next, the use of oleic acid as a solvent was investigated. The resulting MgF_2 beads exhibited a coral stony-like structure, with sizes of approximately 0.5 µm ± 0.1 µm *(see Figure 6.12)*. Despite the unique morphology, the beads were prone to agglomeration, suggesting that oleic acid does not form a protective layer around the bead surface to reduce agglomeration.

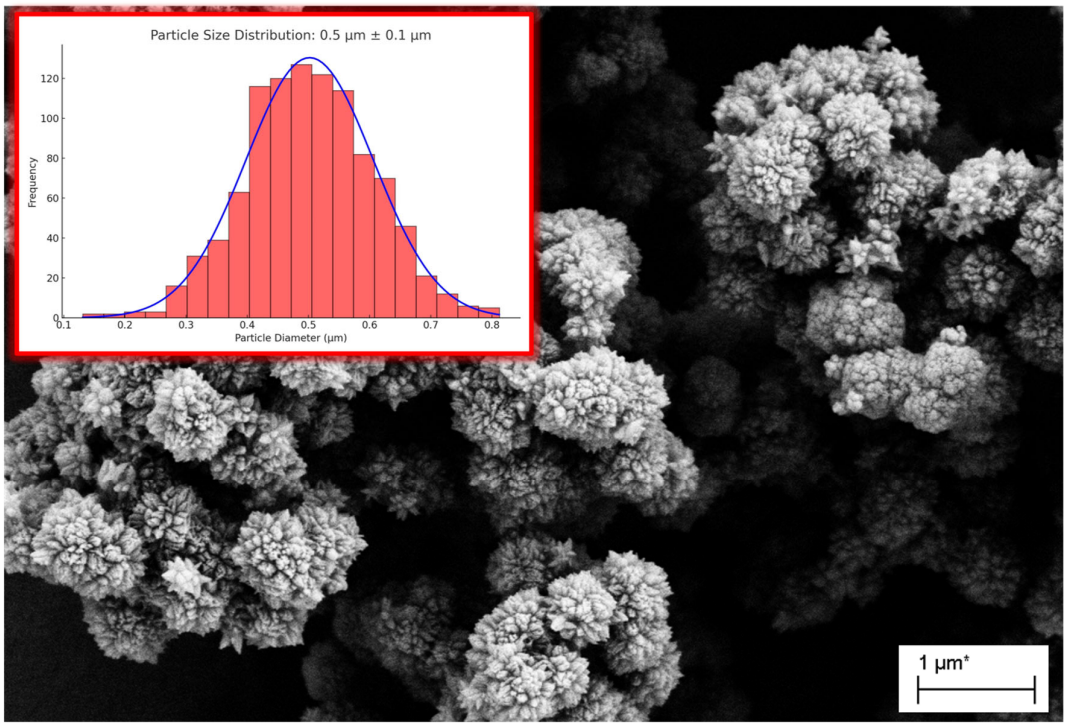

Figure 6.12: FESEM image of MgF_2 beads prepared via solvothermal synthesis using oleic acid as a solvent at 180°C for 2 h under atmospheric pressure conditions. Inset shows beads size distribution.

Similarly, the use of octadecene as a solvent resulted in beads with a more defined and uniform structural features compared to those prepared with oleic acid, with sizes of approximately 1.5 µm ± 0.1 µm *(see Figure 6.13)*. The beads synthesized using octadecene exhibited a higher surface area, making them suitable for potential core-shell synthesis. However, both oleic acid and octadecene did not lead to the formation of larger beads compared to the ethanol and water mixture.

To further explore the potential of core-shell synthesis, octadecene and Milli-Q water were used in combination. This approach resulted in a linear increase in particle size with each added layer of MgF_2, as shown in Figure 6.14. Attempts to add a sixth layer were unsuccessful, as re-addition of the starting material during synthesis triggered new nucleation sites rather than growth on the formed core-shell beads.

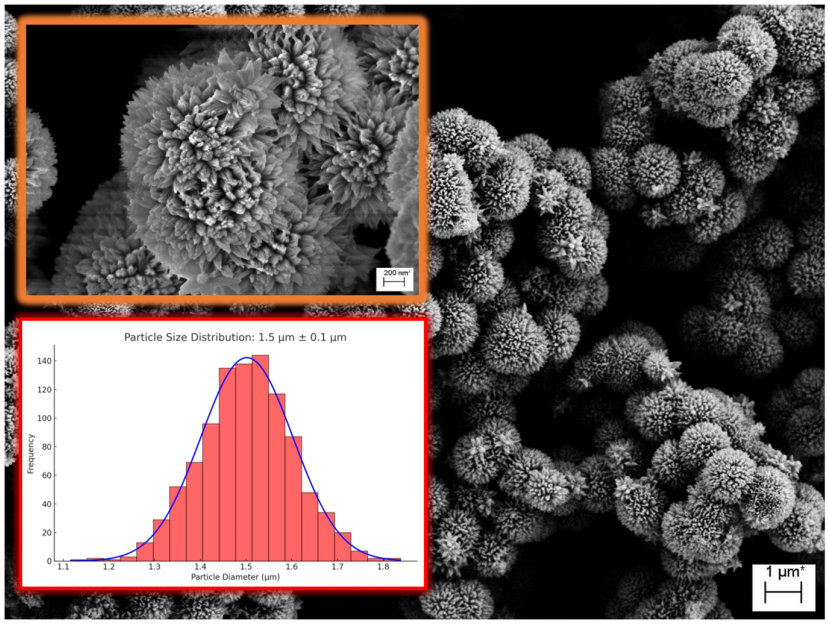

Figure 6.13: FESEM image of MgF_2 beads prepared via solvothermal synthesis using octadecene as a solvent at 180°C for 2 h within atmospheric pressure conditions. The inset image in orange shows a close-up of the beads surface and red Inset shows beads size distribution.

The choice of solvent significantly affects the size and morphology of MgF_2 particles. The mixture of ethanol and water proved effective in promoting the formation of micro-sized beads through coalescence and oriented attachment. The use of oleic acid and octadecene yielded unique structures but showed differences in agglomeration behavior. The core-shell strategy using octadecene and water was effective for controlled particle size increase however only limited to 2.6 µm ± 0.1 µm.

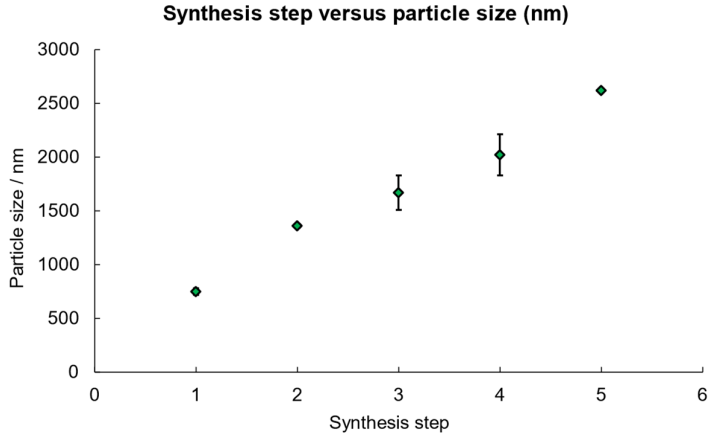

Figure 6.14: Plot of particle size (nm) versus synthesis step of MgF_2@MgF_2@MgF_2@MgF_2@MgF_2 CS beads via solvothermal synthesis using octadecene and Milli Q water.

The results of the present study align with those reported in the literature. Wang et al. highlighted the effectiveness of using solvents like oleic acid for controlled particle growth.[85] Similarly, Niederberger and Cölfen discussed the importance of oriented attachment in particle growth.[298] The insights provided by Thanh et al. into nucleation and growth mechanisms in nanoparticle synthesis resonate with the observations of coalescence and oriented attachment in this study.[295]

In addition to the aforementioned studies, the work by Niederberger and Pinna also demonstrates the importance of selecting appropriate solvents in solvothermal synthesis to control particle size and morphology.[302] Their research emphasizes how different solvent environments can lead to varying growth rates and nucleation behaviors, corroborating the findings of the current study. The study by Wang et al. on the synthesis of MgF_2 nanoparticles using a similar solvothermal method with different solvents further supports the conclusion that solvent choice critically influences the structural properties of the resulting particles.[303] Wang et al. observed that using alcohol-based solvents led to the formation of well-defined spherical particles, which is consistent with the formation of micro-sized beads in the present work when using a mixture of ethanol and water.

Moreover, the core-shell synthesis approach demonstrated in this study aligns with the work of Liu et al., who reported on the incremental growth of core-shell structures by successive layer deposition.[304] Their findings underscore the feasibility and effectiveness of using solvothermal methods to achieve precise control over particle size and morphology through stepwise addition of reactants.

6.2.3 Hydrothermal Autoclave Synthesis

The hydrothermal synthesis of spherical micro-sized MgF_2 beads was conducted to explore the effects of prolonged heating and high temperatures on particle size and morphology. The primary objective was to produce monodispersed MgF_2 beads of 5 micrometer size and to understand how varying dwell times and temperatures influence the structural properties of the resulting particles. $Mg(NO_3)_2 \cdot 6H_2O$ was used as the starting material, and the synthesis was carried out in an autoclave to facilitate high-pressure and high-temperature conditions.

Initially, $Mg(NO_3)_2 \cdot 6H_2O$ was dissolved in a mixture of Milli-Q water and BMIM[BF_4] and stirred vigorously to ensure complete dissolution. The solution was then transferred to a Teflon-lined autoclave, which was heated to 200°C for varying dwell times, ranging from 8 h to 7 days. After the reaction, the products were washed with ethanol and dried before characterization using FESEM.

The initial experiment with an 8-h dwell time resulted in compact, monodispersed beads with sizes of approximately 1.20 µm ± 0.02 µm. The FESEM image *(see Figure 6.15)* shows that the beads were composed of platelets, indicating that the dwell time was sufficient to achieve significant particle growth while maintaining a uniform morphology.

Extending the dwell time to 7 days resulted in a noticeable decrease in bead size, with the formation of petal-like structures and some melted formations observed *(see Figure 6.16)*. This observation suggests that prolonged heating at 200°C leads to the disintegration of the platelets from larger particles, with detached pieces rearranging to form individual particles resembling petals. Additionally, some particles exhibited melted structures, indicating that continuous heating influenced the internal pressure and structural integrity of the particles.

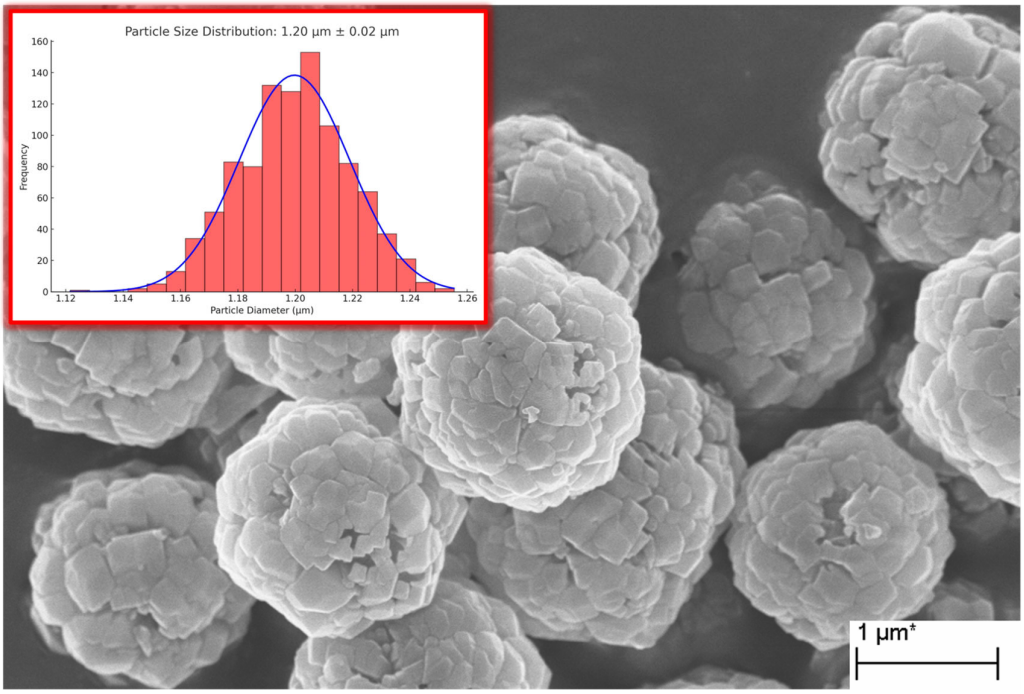

Figure 6.15: FESEM image of MgF_2 beads prepared via hydrothermal synthesis in an autoclave at 200°C and for 8 h. Inset – beads size distribution.

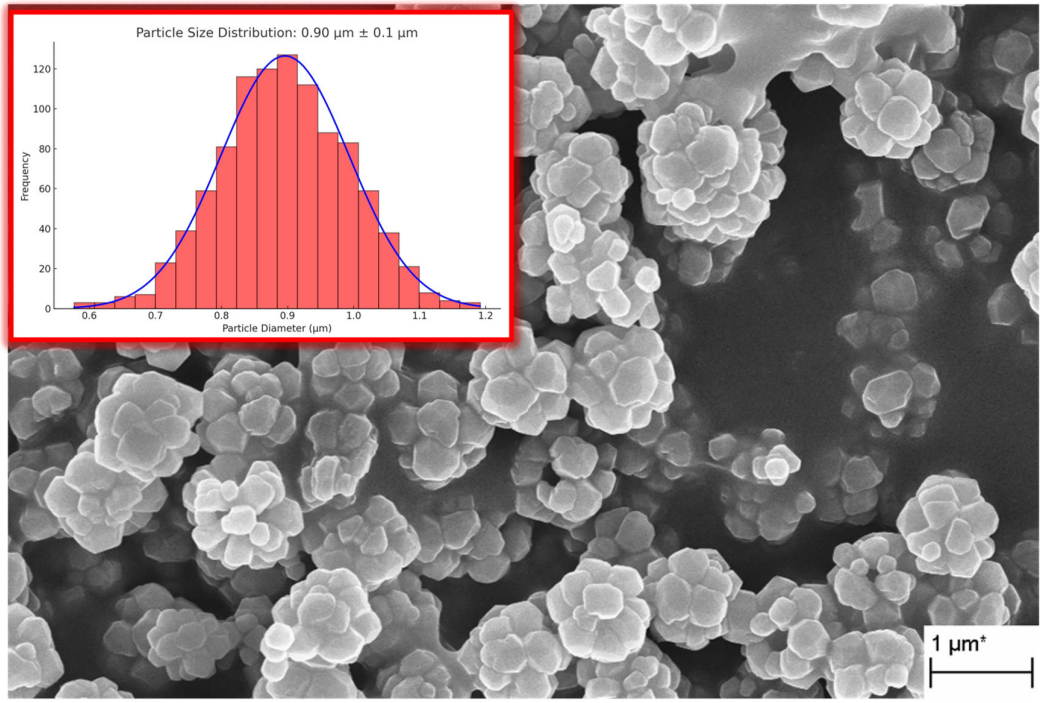

Figure 6.16: FESEM image of MgF_2 beads prepared via hydrothermal synthesis in an autoclave at 200°C for 7 days. Inset – beads size distribution.

To improve the synthesis, the amount of Milli-Q water was reduced to half and a dwell time of 4 days was selected. The initial quality of BMIM[BF_4] is crucial, as it is hygroscopic. To minimize the impact of water uptake, pipetting was conducted in an inert dry atmosphere. The heating steps, both at the onset and during the reaction, were also critical. The formation of the first nuclei, influenced by temperature and concentration, determines the growth and morphology of each bead.[295] Figures 6.17 and 6.18 display FESEM images of 5 µm MgF_2 beads successfully synthesized under the optimized conditions described above. Similarly, as seen in Figure 6.11, coalescence, oriented attachment, and intraparticle growth are also evident *(refer to Figure 6.18)*.

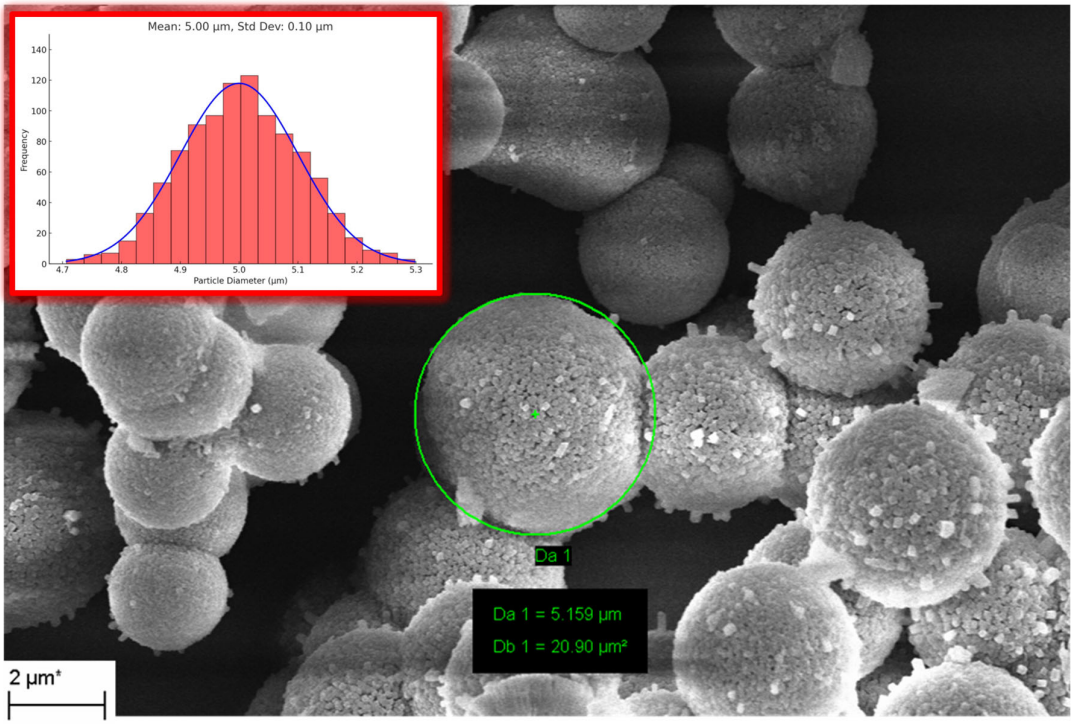

Figure 6.17: FESEM image of 5 µm MgF_2 beads prepared in an autoclave at 200°C and for 4 days. Inset – beads size distribution. The green circle shows the bead size and surface area in µm and μm^2 respectively.

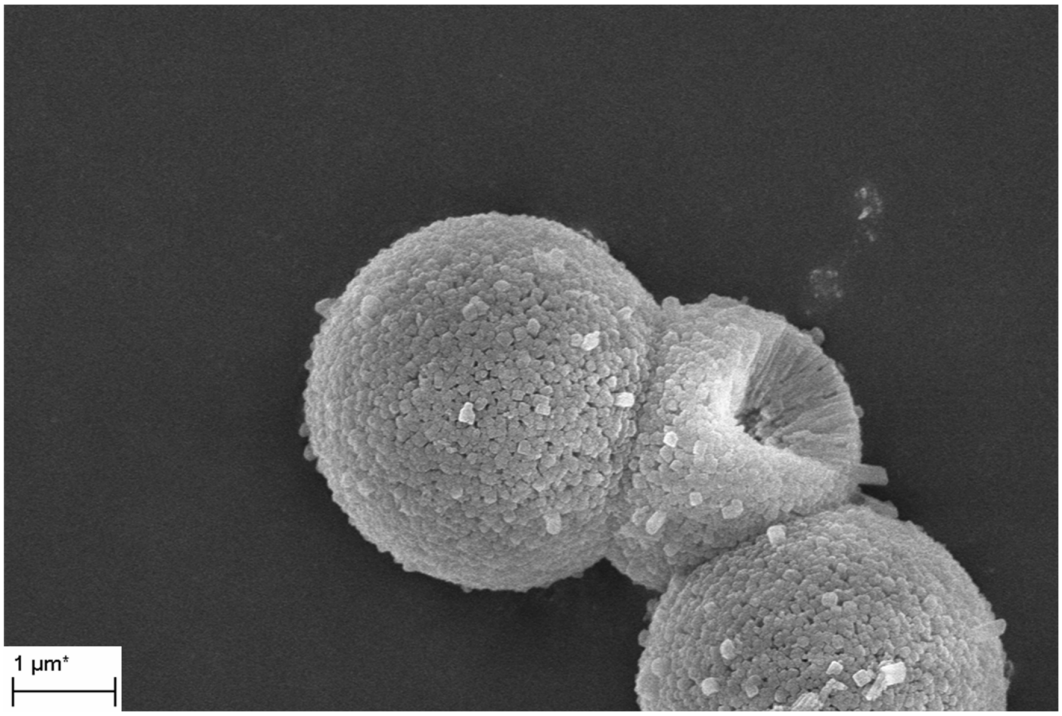

Figure 6.18: FESEM image of 5 µm MgF_2 beads prepared in an autoclave at 200°C and for 4 days. Image showing coalescence and orientated attachment of 3 MgF_2 beads.

Further experiments were conducted to investigate the effects of temperatures exceeding 200°C. The melting point of MgF_2 is approximately 1255°C, so the beads from the 8-h synthesis were sintered at 1200°C in an inert atmosphere for 6 h to trigger the formation of larger beads. This process yielded microporous beads ranging from 15 µm to 25 µm in size *(see Figure 6.19-A)*. The resulting beads were not purely composed of MgF_2, as X-ray diffraction (XRD) analysis indicated the formation of oxyfluorides upon exposure to air *(see Figure 6.19-B)*. The measured diffraction pattern, represented by the green line, exhibits prominent peaks at 2θ values around 25°, 45°, and 53°, indicating the presence of well-defined crystalline phases. Comparison with calculated patterns for MgF_2 (ICSD-759777 and ICSD-422263),[305,306] CaF_2 (ICSD-1130),[307] and MgO (ICSD-9863)[308] reveals some peaks that are associated to both calculated patterns of MgF_2 and MgO. MgF_2 can exist in either the orthorhombic or monoclinic crystal system, contingent on the degree of distortion from its tetragonal crystal structure.[309,310] At elevated temperatures exceeding 600°C, significant alterations in symmetry occur, inducing distortions along various planes within the crystal lattice.[311,312]

Consequently, MgF_2 undergoes comparative analysis with four distinct crystal systems to ascertain its crystalline phase. CaF_2, with its well-characterized cubic fluorite structure,[307] and MgO, which adopts a rock-salt structure,[308] serve as crucial reference points. These comparisons provide insights into the potential structural transformations and distortions that MgF_2 may undergo at high temperatures. The distinct thermal properties and responses to high temperatures of CaF_2 and MgO offer a valuable perspective on the stability and phase transitions of MgF_2.[313] Furthermore, the differences in ionic sizes and coordination environments—Mg^{2+} in MgF_2, Ca^{2+} in CaF_2, and Mg^{2+} in MgO—shed light on how ionic radii and coordination preferences influence crystal structure and phase stability under varying conditions.[314] This alignment, particularly with the peaks at 2θ values corresponding to 38°, 45°, 63°, 77° and 80° confirms that MgF_2 is not the predominant crystalline phase in the sintered sample.

The hydrothermal synthesis method demonstrated that both dwell time and temperature significantly impact the size and morphology of MgF_2 particles. Shorter dwell times at 200°C resulted in uniform, monodispersed beads, while prolonged heating led to structural disintegration and the formation of petal-like particles.

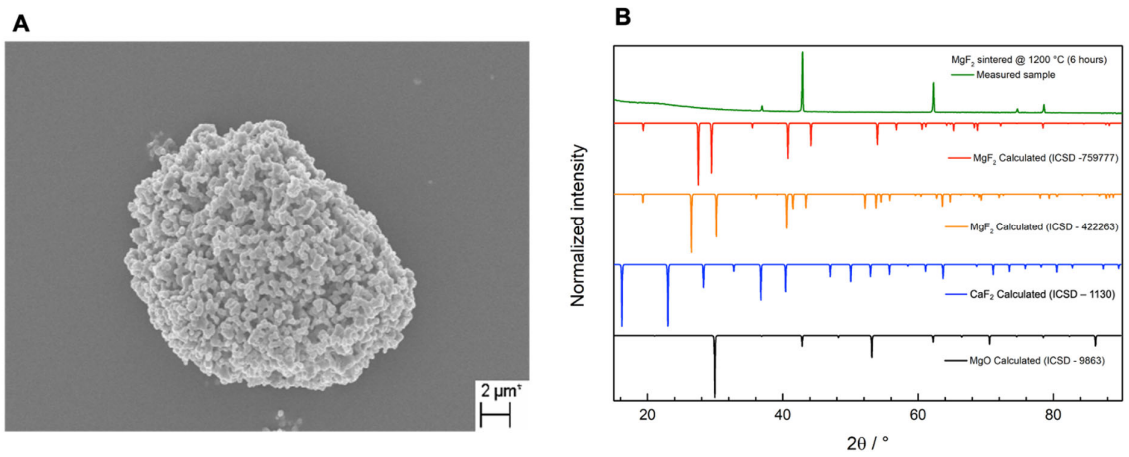

Figure 6.19: A) FESEM image of MgF_2 beads *(refer to sample in Figure 6.17)* sintered at 1200°C for 6 h. B) XRD of MgF_2 compared to other standards obtained from ICSD (red line represents MgF_2 orthorhombic crystal system, orange line corresponds to MgF_2 monoclinic crystal system, blue line represents CaF_2 crystal system and black line MgO).

High-temperature sintering induced substantial particle growth and the formation of microporous structures, albeit with the inclusion of oxyfluorides especially at 1200°C. The findings from the synthesis of MgF_2 beads prepared in an autoclave at 200°C, for 4 days *(refer to Figures 6.18 and 6.19)* align with existing literature on hydrothermal synthesis and particle growth mechanisms. Duncanson and Stevenson reported on the thermal properties and transformations of MgF_2, highlighting the role of temperature in inducing structural changes.[315] Zhao et al. provided insights into pressure-induced superheating, which can explain the melting and rearrangement of particles observed in the present study during prolonged heating.[316] The observations of petal-like structures and the formation of oxyfluorides are consistent with the work of Peng et al., who discussed shape control and growth mechanisms in nanocrystals under high-temperature conditions.[300]

When comparing the three synthesis methods—microwave, solvothermal, and hydrothermal—several key differences and advantages become apparent. Each method offered distinct pathways and conditions for achieving the objective of preparing MgF_2 beads, specifically targeting the formation of beads approximately 5 µm in size. Microwave synthesis *(see Section 6.2.1)* offered a significantly reduced reaction time and enabled the formation of various nanosized structures, including nanowhiskers and spherical NPs.

This method's efficiency in producing nanoscale structures in a short period is notable, especially when aiming for rapid synthesis and uniform particle sizes. However, the microwave method primarily yielded smaller nanoparticles and did not achieve the target bead size of 5 µm. The synthesis parameters did not favor the growth of larger particles despite the accelerated reaction kinetics.

The solvothermal synthesis *(Section 6.2.2)* provided greater versatility in manipulating particle size and morphology through the choice of solvent and synthesis conditions. The use of different solvents such as ethanol, oleic acid, and octadecene demonstrated the method's ability to produce a range of particle structures, from micro-sized beads to coral stony-like formations. The solvothermal approach also facilitated the development of core-shell structures, which were achieved by sequentially adding layers in a controlled manner. While this method produced larger particles compared to the microwave synthesis, it still fell short of consistently achieving the target 5 µm bead size.

The hydrothermal synthesis *(Section 6.2.3)* proved to be the most successful method for achieving the target bead size of 5 µm. The ability to control the dwell time and temperature in a high-pressure autoclave allowed for the precise manipulation of particle growth. Shorter dwell times at 200°C resulted in uniform, monodispersed beads, while prolonged heating led to significant structural transformations, including the formation of petal-like particles structures. High-temperature sintering further promoted particle growth, resulting in microporous beads ranging from 15 to 25 µm but with oxyfluoride impurities.

6.2.4 Structure elucidation of MgF_2 beads via STEM-EDX and FIB

Figure 6.20 presents a STEM-EDX analysis of MgF_2 beads, revealing a composition of 32.1 atom-% Mg and 64.2 atom-% F, thereby maintaining the stoichiometric ratio of 1:2. The remaining minor fraction of other elements, comprising 3.7 atom-%, is attributed to carbon and copper originating from the TEM grid utilized during the analysis and silicon from the semi-conductor detector. The F-Kα (0.677 keV) signal is more intense than the signal of Mg-Kα (1.253 keV). However, the C-Kα (0.277 keV) signal due to the carbon film from the TEM grid is not clearly visible, because it is almost overlapping with F-Kα signal. Cu-Kα (8.040 keV) and Cu-Kβ (8.904 keV) are detected due to the Cu on the TEM grid.

The signal at 1.74 keV is attributed to Si-Kα, which emanates from the detector made of Si-crystal. No other impurities were detected indicating high purity (above 99 %) formation of MgF_2 beads.

Conversion from atom-% to mass-% in EDX analysis is elucidated by considering the atomic weights of Mg (24.305 u) and F (18.998 u).[220] The mass-% is derived through calculation of total mass contribution for each element, followed by normalization against the total mass contribution of all detected elements.[219] This approach ensures a precise representation of the material composition, as EDX quantification is inherently dependent on the mass of the constituent elements, which directly influences the emitted X-ray intensity and energy.

Atomic mapping was done to confirm results as obtained by EDX. The spatial distribution of the detected Mg and F signals correlates well with the shape of MgF_2 beads. Furthermore, the detected energies in keV agree with the known literature values.[317]

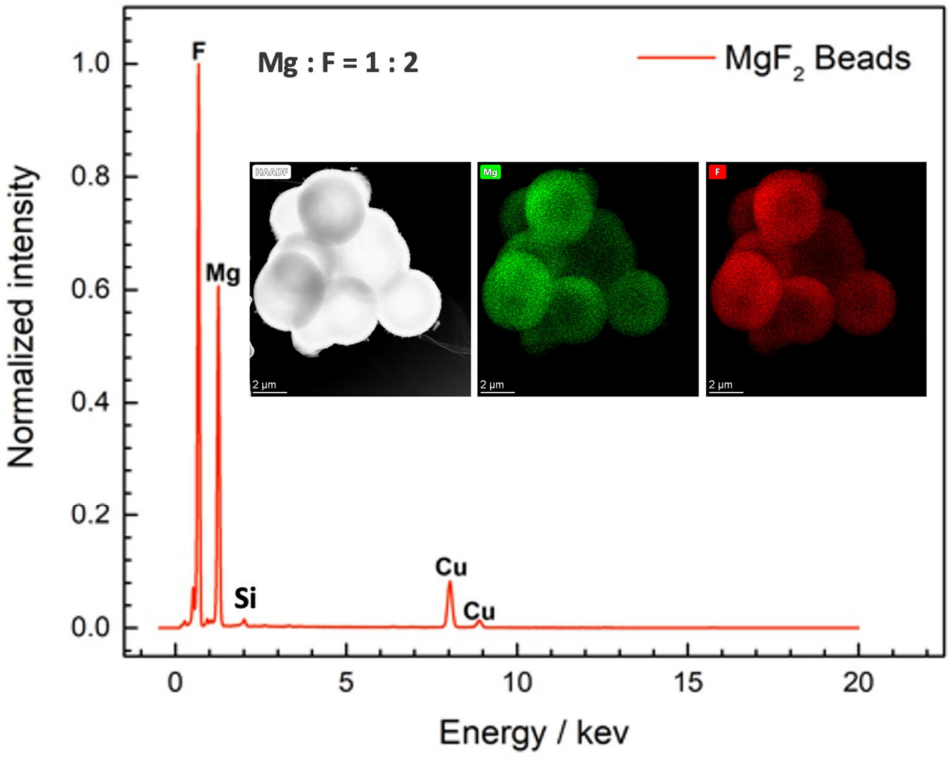

Figure 6.20: STEM – EDX analysis of 5 µm MgF_2 beads prepared in an autoclave at 200°C and for 4 days. Inset – atomic mapping using HAADF detector – scale bar represents 2 µm (green – Mg signal, red – F signal and grey – MgF_2 beads).

In the STEM images (green and red) some dark black spots in the central part of the beads are seen that seem to extend outwards. These dark spots are an indication of a hollow structure. Therefore, an experiment was done using focused ion beam (FIB) to investigate whether the beads are hollow in nature. With FIB part of the material is removed using a focused Ga ion beam, followed by SEM analysis. Figure 6.21 shows a FIB analysis of MgF_2 beads at different cross-section and stages (A to F) during detection. Hollow structures that possess different diameters are observed. Image F shows a close-up of a single bead that has presumably undergone coalescence / oriented attachment and intraparticle growth. From the cross-section it is also possible to observe how cylindrical structures detected in 6.18 merge or grow together. Hence, the facets of each individual cylindrical structure align corresponding to a neighbouring structure (oriented attachment). The beads are seen as an assembly of cylindrical structures that likely grew from the center.

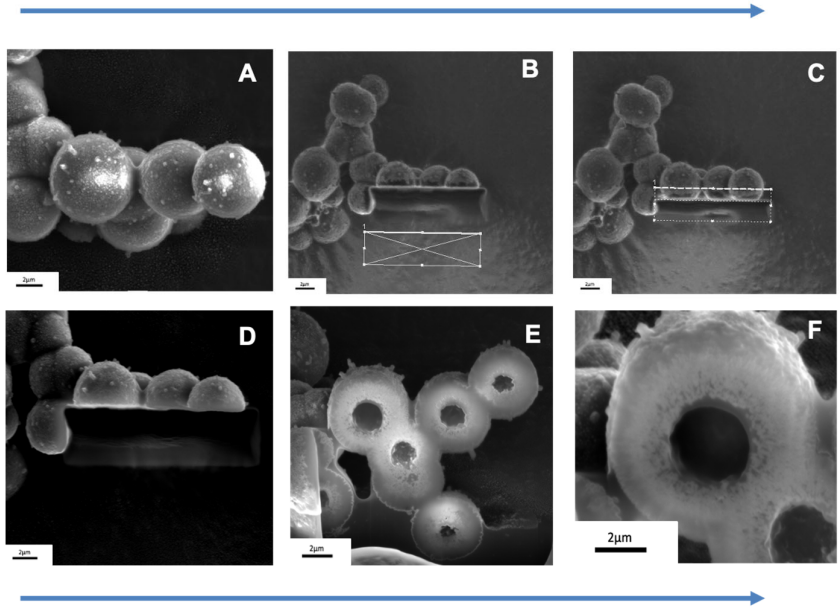

Figure 6.21: FIB analysis of 5 µm MgF_2 beads prepared in an autoclave at 200°C and for 4 days. The arrows indicate the direction of slicing the beads. The scale bar represents 2 µm.

Characterization of optical and morphological particle properties were performed utilizing commercial tomographic phase microscopy (TPM) and a custom built digital holographic microscopy (DHM) system facilitating multi-modal bright field and quantitative phase imaging (QPI). TPM as well as bright field and DHM QPI were conducted at *Biomedical Technology Center (BMTZ), University of Münster, Germany* by Álvaro Barroso and Kai Eder.

Figure 6.22 shows tomographic phase microscopy images of MgF_2 beads, illustrating a TPM refractive index measurement as well as the 3D particle morphology retrieved from TPM refractive index tomograms. Evaluation of DHM QPI images recorded with a 20x microscope objective (NA=0.4) *(Refer to Figure 7.40 in the appendix)* performed as described with details in [ref: Steike et al. 2022] (n=5),[318] indicates a refractive index of 1.351 ± 0.005 and a bead diameter of 4.8 ± 0.2 µm.

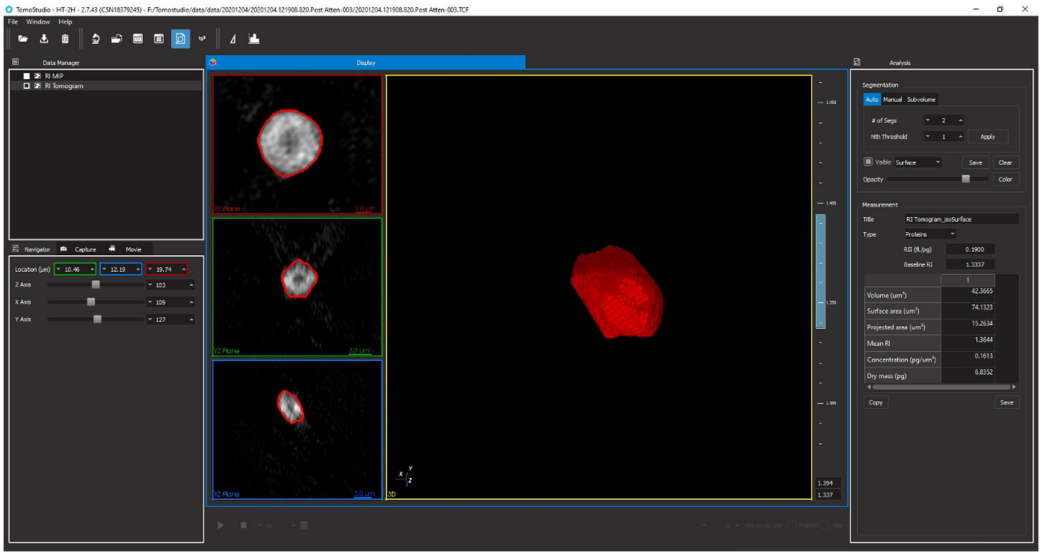

Figure 6.22: Tomographic phase microscopy of MgF_2 beads prepared in an autoclave at 200°C and for 4 days. Displayed are cross-section planes through a representative measured refractive index (RI) tomogram and a rendered 3D representation of the retrieved RI tomogram. The images of the XY, YZ, and XZ planes highlight the microparticle's dimensions and morphology. The measurement data on the right panel include the volume (42.4 µm³), surface area (74.1 µm²), projected area (15.3 µm²) and the mean refractive index (1.364).

Corelative TPM measurements on n=5 other particles as illustrated in Figure 6.22 yielded a slightly higher refractive index of 1.360 ± 0.004 and a diameter of approximately 5.0 ± 0.2 µm. The results from these label free quantitative imaging techniques underscores the robustness of the methodology in characterizing the physicochemical properties of MgF_2 beads, thereby advancing the understanding of their potential applications in various high-temperature and optical environments. Notably, the measured refractive index of MgF_2 beads is comparable to that of mammalian cells, which typically ranges from 1.34 to 1.40.[318–320] This similarity suggests potential biomedical applications for MgF_2 beads, as their optical properties align well with those of biological tissues,[321] making them suitable for use in imaging and diagnostic tools that rely on light interaction with biological structures.

6.3 Conclusion

In summary, this Chapter elucidated the synthesis and characterization of micrometer-sized MgF_2 beads tailored for use in digital holography for label-free, quantitative in vitro live cell imaging. The exploration spanned three distinct synthesis methods—microwave heating, solvothermal, and hydrothermal—each optimized to achieve beads with the desired size and structural properties.

The synthesis via microwave heating demonstrated efficiency in producing nanoscale structures, including nanowhiskers and spherical nanoparticles. However, while the reaction time was significantly reduced, the microwave approach primarily yielded smaller nanoparticles rather than the target 5 μm beads. On the other hand, the solvothermal synthesis method offered greater control over particle size and morphology through the strategic selection of solvents. The formation of core-shell structures further underscored its versatility, although it fell short of consistently producing 5 μm beads. The ethanol and water mixture were notably effective, promoting the formation of micro-sized beads through coalescence and oriented attachment.

Hydrothermal autoclave synthesis proved most effective, successfully yielding monodispersed MgF_2 beads of the target size. By precisely controlling temperature and dwell time within a high-pressure autoclave, uniform bead growth was facilitated. High-temperature sintering promoted particle enlargement but resulted in oxyfluoride impurities. Structural analysis via STEM-EDX and FIB confirmed the high purity of the MgF_2 beads, with atomic mapping and cross-sectional imaging revealing the presence of hollow structures and oriented attachment, critical for understanding the growth mechanisms.

Detailed protocols for the preparation of MgF_2 nanowhiskers, nanoparticles, and 5 μm beads are provided, ensuring reproducibility and clarity for future research. Overall, the findings from this chapter advance our understanding of the synthesis parameters essential for tailoring MgF_2 beads for digital holography applications. The insights gained lay a robust foundation for further refinement of synthesis techniques, ultimately enhancing the application of these beads in biological and medical imaging.

6.4 Materials and methods

BMIM[BF_4] (99%) purchased from io-li-tech, Heilbronn Germany. $NaH_2PO_4 \cdot 2H_2O$ (99.9%), $Mg(NO_3)_2 \cdot 6H_2O$ (99.97%), $Mg(CH_3COO)_2 \cdot 4H_2O$ (99.99%) from Alfa Aesar, Schwerte Germany. Oleic aicd (99%), octadecene (90%), ethanol denatured (90%), ethanol anhydrous (99+%), Alfa Aesar, Schwerte Germany. Milli-Q water (resistivity of 18.2 MΩ cm), from a Millipore Direct Q8 system, (Millipore Advantage A10 system, Schwalbach, Germany) with a Millimark Express 40 as filter (Merck, Darmstadt Germany).

6.4.1 Preparation of MgF_2 nanowhiskers and NPs

In a separate experiment $Mg(NO_3)_2 \cdot 6H_2O$ was used instead of $Mg(CH_3COO)_2 \cdot 4H_2O$ to investigate the effect of a different Mg source.

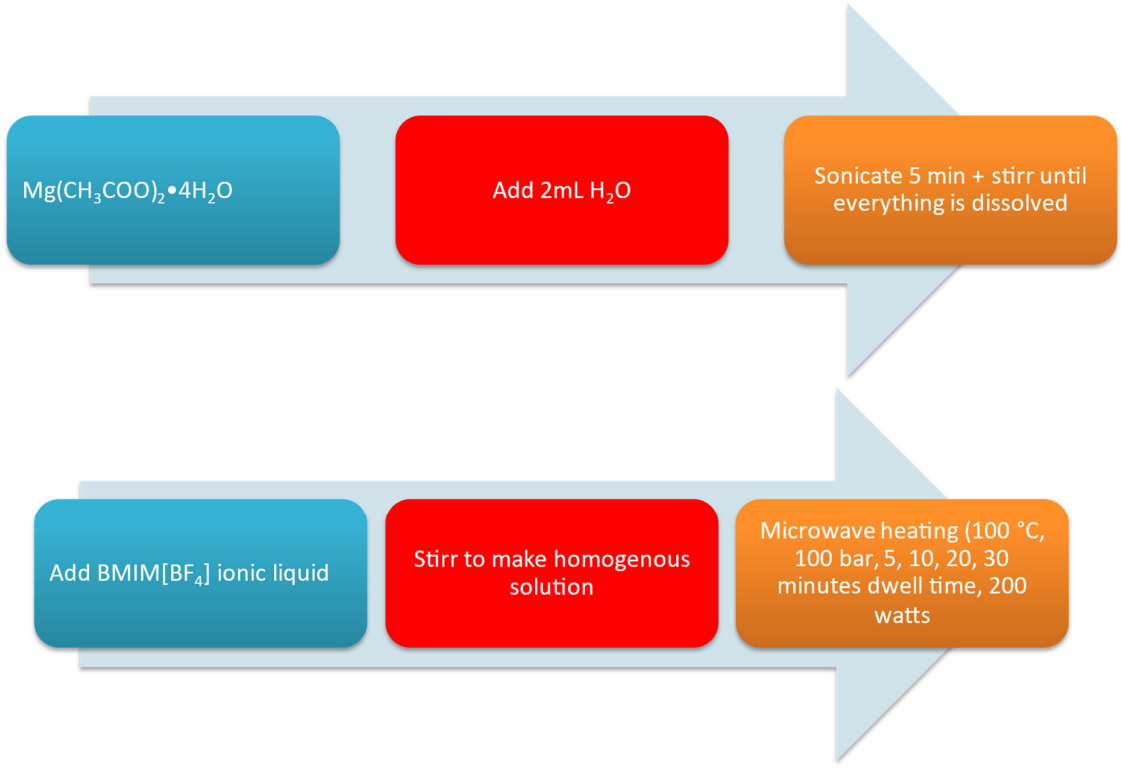

Figure 6.23: Synthesis steps for preparing MgF_2 nanowhiskers.

6.4.2 Synthesis of 5 µm MgF_2 beads

In a typical experiment to synthesize 5 µm MgF_2 beads, the following procedure was meticulously followed: Initially, 0.2340 g of $NaH_2PO_4 \cdot 2H_2O$ (A) and 0.3840 g of $Mg(NO_3)_2 \cdot 6H_2O$ (B) were accurately weighed separately in plastic or glass weighing boats, ensuring precise measurements as they significantly influence the size distribution of the resultant particles. From this point, all handling was conducted with gloves to maintain sample purity. Subsequently, 8.750 mL of Milli-Q water (D) was carefully pipetted into the Teflon liner (E) of the autoclave-hydrothermal reactor (from Hubei Hongshuang E-Commerce Co., Ltd China). Prior to use, D was filtered using a 0.2 µm filter (Merck, Darmstadt Germany) to remove any impurities, and the Teflon liner was pre-cleaned with filtered D to ensure it was dust-free. Following this, 1 mL of D was taken from E and added to the weighing boat containing A. The contents were gently stirred to partially dissolve A, which was then transferred into E. This process was repeated, ensuring all material from the weighing boat was thoroughly washed and transferred. A pre-cleaned magnetic stirrer was then added to E, covered, and stirred for 5 minutes at ambient conditions. The procedure was repeated for B, using the same D solution in E. B typically required an additional 2 to 3 minutes to dissolve completely, forming a clear solution. It is critical to avoid heating the solution during this stage to prevent premature nucleation of MgO, which could adversely affect the synthesis of MgF_2. Next, 6 mL of C was added to the resultant solution, which was stirred for 15 to 20 minutes at ambient conditions until a uniform cloudy solution formed, free from any visible particles. Heating the solution was avoided to prevent spontaneous nucleation and the formation of polydisperse particles. The Teflon liner (E) was then assembled with the autoclave reactor vessel (F), ensuring a complete seal. The assembled reactor was placed in an oven (Heraeus model VT5042 EK with nominal temperature capability of up to 250ºC, from Apeldoorn Netherlands) pre-set to 200°C and left undisturbed for 4 days. Post-reaction, the oven was turned off and allowed to cool to room temperature. The reaction mixture was immediately transferred to a centrifuge tube and centrifuged @ 6000 rpm for 5 minutes. The supernatant was decanted, and the precipitate was washed three times with ethanol and twice with water to remove any residual impurities. The particles were then dispersed in 1000 µL of Milli-Q water and stored in a dry environment. For obtaining a dry powder form, the wet solid was transferred

to a glass petri dish and dried in an oven at 60°C for 1 h. To examine the particle size and morphology, 20 µL of the particle suspension was mixed with 580 µL of Milli-Q water. A 10 µL drop of the resultant diluted suspension was placed on a SEM or TEM sample holder and left to dry overnight in a desiccator. This method ensured the reproducible synthesis of uniform 5 µm MgF_2 beads, suitable for subsequent morphological analysis and application.

6.4.3 FIB milling of MgF_2 beads

MgF_2 beads were shaped using FIB milling with a FEI Helios Nanolab 600, as illustrated in Figure 4.21. The diameter of the top face is controlled by the position of the FIB cut. To ensure a flat tip and prevent edge rounding from the Ga ion beam tail, the milling was executed at 30 kV with the smallest possible aperture to keep cutting times practical. Based on the wire tip diameter, the apertures chosen usually produced a beam current ranging from 0.92 to 2.8 nA. The experiment was done with support of *Dr. Steven Schellert* from *Micro- and Nanoanalytics Facility (MNaF) of University of Siegen.*

6.4.3 FESEM measurement of MgF_2 beads

Before conducting the FESEM analysis, the samples were sputtered with gold for 20 seconds to create a conductive surface, resulting in a gold layer approximately 3.0 ± 0.5 nm thick. The FESEM measurement was carried out using a Zeiss Ultra 55cv (FESEM, Zeiss, Oberkochen, Germany), equipped with an Inlens secondary electron detector. The measurements were performed at an operating voltage of 10 kV.

6.4.4 STEM measurement of MgF_2 beads

MgF_2 dispersions were pipetted (10 µL volume, concentration of 100 μgL^{-1}) onto a carbon-coated copper grid (Plano, 200 mesh) and left to dry overnight in a desiccator under a 0.1 mbar argon atmosphere. Physicochemical analyses of the MgF_2 samples were conducted with a FEI Talos F200X electron microscope (Thermo Fisher Scientific, Waltham) operating at 200 kV. The microscope featured a Super-X EDX detector, and a high-angle annular dark field (HAADF) detector was employed to enhance NP contrast in STEM mode.

Colors for atomic mapping were chosen arbitrarily based on the HAADF detector response for individual experiment. Hence, each STEM measurement resulted to a different color signal for each atom.

6.4.5 Quantitative phase imaging of MgF_2 beads with digital holographic microscopy

An inverted Nikon Ts2R microscope equipped with an attached DHM module and an automated microscope stage, based on concepts described previously,[274] was applied for bright-field imaging and quantitative phase imaging (QPI) of MgF_2 beads. The coherent light source for the recording of digital holograms was a fiber coupled solid state laser (Cobolt 06-DPL, λ=532 nm, Cobolt AB, Solna, Sweden). Digital off-axis holograms of the specimens were recorded with a complementary metal-oxide-semiconductor (CMOS) sensor (UI-3260CP-M-GL, IDS Imaging Development Systems GmbH, Obersulm, Germany) using a 20x objective lens (Nikon Plan 20x/0.4, Nikon, Japan). For each measurement, one bright-field image of the particles and 15 holograms were captured while the object illumination wave was modulated by an electrically focus tunable lens (ETL).[322] The reconstruction of quantitative phase images from digitally captured holograms was performed numerically as described with details before.[323] Quantitative phase images were reconstructed from the holograms as described above and subsequently averaged for reduction of coherence-induced image disturbances.[322] The resulting averaged quantitative phase images contain information about the phase shift delay induced by the monitored MgF_2 beads:

$$\Delta\varphi_{\mathrm{p}} = \frac{2\pi}{\lambda} d_{\mathrm{p}}\left(n_{\mathrm{p}} - n_{\mathrm{medium}}\right) \quad (4)$$

In Equation 4 n_{p} represents the integral refractive index of the MgF_2 beads, n_{medium} is the refractive index of the buffer medium and d_{p} is the particle thickness. Particle refractive indices and diameters were determined from averaged DHM QPI images as described with details in.[318]

6.4.6 Tomographic phase microscopy analysis of MgF_2 beads

The 3D refractive index distribution of the MgF_2 beads was obtained utilizing tomographic phase microscopy (TPM).[324] In TPM, different projections of the sample are recorded to achieve a plane selective refractive index (RI) reconstruction. Therefore, individual holographic images from the sample are acquired with laser light under different illumination angles. In this study TPM was performed using a commercial off-axis Mach–Zehnder interferometer-based instrument (HT-2H, Tomocube Inc., Daejeon, Republic of Korea). The laser light (λ=532 nm) that passed the sample was transmitted to the hologram recording device via a 60x objective lens (NA=0.8). TPM measurements were performed at room temperature as described before.[320] To achieved plane selective RI maps as well as to determine the refractive index, diameter, volume, surface area and the projected area of the analysed MgF_2 beads a commercial software was applied (TomoStudio 2.7.43, Tomocube, Inc., Daejeon, Republic of Korea).

Chapter 7 Functionalized nanoassemblies for future biomedical applications

7.1 Introduction

The field of nanotechnology has driven remarkable advancements in biomedical applications, particularly through the development of functionalized nanoassemblies.[325–328] These materials offer unique opportunities in diagnostics, drug delivery, and therapeutic interventions due to their customizable properties and multifunctional capabilities.[329–331] In this Chapter, the focus is laid on the functionalization of MgF_2 beads, initially synthesized and characterized in Chapter 6, to further enhance their photoluminescent properties and extend their biomedical applicability. The motivation behind doping MgF_2 beads with trivalent lanthanides such as Tb^{3+} and Eu^{3+} lies in their ability to impart distinctive and tunable photoluminescent properties, which are crucial for advanced imaging and sensing applications.[103] Additionally, coating these beads with polymer brushes, specifically poly(diethylene glycol methyl ether methacrylate)-*block*-poly(acrylic acid) (PDEGMA-*block*-PAA), aims to improve their biocompatibility,[332] stability,[333] and responsiveness to environmental stimuli,[334] thus enhancing their overall functionality in biomedical contexts.

MgF_2 beads doped with Tb^{3+} and Eu^{3+} ions exhibit distinctive photoluminescent properties, when subjected to UV illumination.[107] The unique electronic configurations of trivalent lanthanides like Tb^{3+} and Eu^{3+} contribute to their remarkable luminescent properties *(see Chapter 3)*. For instance, Tb^{3+} ions are known for their green luminescence,[232] while Eu^{3+} ions emit red light.[171] This versatility allows for the design of materials with specific emission characteristics tailored to various applications. Relevant literature highlights the significance of lanthanide-doped fluorides in biomedical applications.[171,233] For example, MgF_2 doped with Tb^{3+} has been studied for its potential in bioimaging due to its strong green luminescence under UV excitation.[335] Similarly, Eu^{3+}-doped MgF_2 has been investigated for its red luminescence, which can be utilized in multiplexed imaging techniques where different emission colors are required.[61] Beyond MgF_2, similar crystal structures such as calcium fluoride (CaF_2) and strontium fluoride (SrF_2) have

also been explored.[171] CaF_2 doped with lanthanides like Tb^{3+} and Eu^{3+} has shown promising results as luminescent biomarkers.[336,337] SrF_2, when doped with lanthanides, exhibits strong luminescence and has been utilized in various optical applications.[171,233]

To further extend the functionality of MgF_2 beads, this Chapter explores their modification with polymer brushes. Specifically, the functionalization with PDEGMA-*block*-PAA brushes synthesized via Activators Regenerated by Electron Transfer Atom Transfer Radical Polymerization (ARGET-ATRP) is investigated. This synthesis involves a three-step process: the initial formation of a layer of MUBiB, followed by the polymerization of DEGMA to yield polymer PDEGMA brushes, and culminating in the polymerization of a terminal block of PAA. This precise polymerization technique ensures a controlled brush architecture,[338] thereby enhancing the stability and functionality of MgF_2 beads.

Coating particles with PDEGMA-*block*-PAA polymer brushes offers several distinct advantages.[339] PDEGMA is known for its temperature-responsive behavior, which can be exploited for controlled drug release.[334,340] This property allows the polymer to undergo a reversible phase transition in response to temperature changes, making it highly suitable for applications, where drug release can be triggered by localized heating. On the other hand, PAA provides pH-responsive characteristics, enabling the polymer to swell or collapse depending on the pH of the surrounding environment.[341] This dual responsiveness to both temperature and pH renders the PDEGMA-*block*-PAA system highly versatile for various biomedical applications, including targeted drug delivery, where the polymer can release therapeutic agents in response to specific physiological conditions.[334,339]

Polymer brushes have been used to functionalize NPs for targeted drug delivery, enhancing the particles' stability and dispersibility in biological fluids.[332,333] In one study, poly(*N*-isopropylacrylamide) (PNIPAM) brushes were grafted onto gold nanoparticles to create a temperature-responsive drug delivery system.[342,343] This system exhibited controlled release of drugs at specific temperatures, demonstrating the potential of polymer brushes in creating smart drug delivery systems. Similarly, poly(ethylene glycol) (PEG) brushes have been widely used to functionalize various NPs, improving their biocompatibility and circulation time in the bloodstream.[344]

PEGylation, the process of attaching PEG chains to particles, effectively reduces protein adsorption and immune recognition, enhancing the efficacy of nanoparticle-based therapies.[345] Moreover, literature underscores that such polymer brushes significantly enhance biocompatibility and mitigate nonspecific protein adsorption, making them ideal for biomedical device coatings.[334,339,341,343,346] The biocompatible nature of these coatings reduces the likelihood of adverse immune responses, while their resistance to protein adsorption minimizes fouling and enhances the functionality of the coated devices. Additionally, the protective polymer layer can improve the stability and dispersibility of the MgF_2 beads in biological environments, further extending their practical applications.[333]

To comprehensively analyze the growth and stability of these polymer brushes on MgF_2 beads, an array of characterization techniques was employed. Field Emission Scanning Electron Microscopy (FESEM), Scanning Transmission Electron Microscopy with Energy Dispersive X-ray Spectroscopy (STEM-EDX), Thermogravimetric Analysis (TGA), and X-ray Photoelectron Spectroscopy (XPS) were utilized to provide detailed insights into the structural and chemical attributes of the polymer-functionalized MgF_2 beads. These analyses ensure the robustness and reliability of the modified beads for future biomedical applications.

Furthermore, the antibacterial efficacy of MgF_2 nanowhiskers (ranging between 50 nm and 200 nm ± 20 nm) was evaluated against *Escherichia coli* Mach 1 $T1^R$. This study aims to benchmark the antibacterial performance of the modified MgF_2 beads against commercially available MgF_2, thereby underscoring their potential as antibacterial agents in biomedical contexts.[347]

7.2 Results and discussion

7.2.1 Luminescent micro-sized beads by doping of MgF_2 with Eu^{3+} and Tb^{3+}

$MgF_2:Eu^{3+}$ and $MgF_2:Tb^{3+}$ beads were prepared using a 0.13 M solution of $Mg(NO_3)_2•6H_2O$ and $NaH_2PO_4•2H_2O$ in 8.750 mL of Milli-Q water. The stoichiometry was adjusted by adding 10% of $Eu(NO_3)_3•2H_2O$ or $Tb(NO_3)_3•2H_2O$ to the mixture, followed by the careful addition of HCl to dissolve any precipitated phosphate salt. The resulting pH was readjusted to 6.5 or 7 using a pH 10 buffer solution. This precursor solution underwent a hydrothermal process at 200°C for 4 days in a sealed autoclave. Post-reaction, the mixture was cooled to room temperature, centrifuged @ 6000 rpm for 5 minutes, and subjected to sequential washes with ethanol and water to remove residual reactants.

Figure 7.1 shows FESEM images of MgF_2:10%Eu^{3+} and MgF_2:10%Tb^{3+} beads (5.0 µm ± 0.3 µm) and photos of the beads as dry powder illuminated under UV light. The red and green emission is due to the Eu^{3+} and Tb^{3+} dopants, respectively.

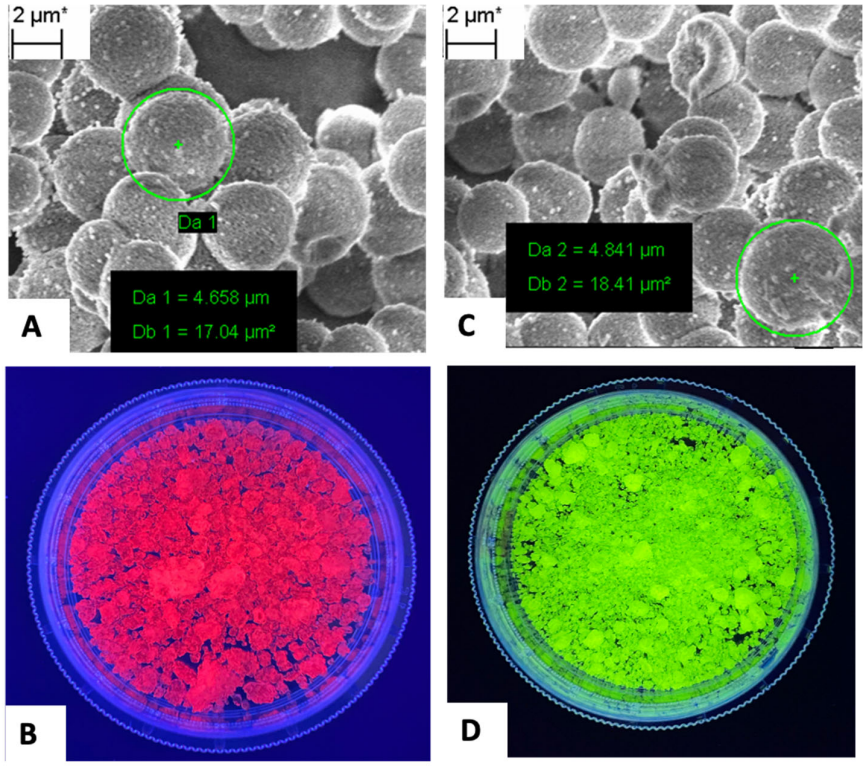

Figure 7.1: A) FESEM image of MgF_2:10%Eu^{3+}; B) Photograph of dry powder of MgF_2:10%Eu^{3+} as seen under UV illumination with λ_{exc} = 250 nm; C) FESEM image of MgF_2: 10% Tb^{3+}; D) Photograph of dry powder of MgF_2: 10% Tb^{3+}as seen under UV illumination with λ_{exc} = 350 nm.

Figure 7.2 shows an emission spectrum of MgF_2:10%Tb^{3+} measured at 350 nm (28570 cm^{-1}) excitation wavelength. A strong emission peak at 544 nm (18380 cm^{-1}) is detected, which is attributed to Tb^{3+} emission. Tb^{3+} ions partially substitute Mg^{2+} sites in MgF_2.[107,335] However, Mg^{2+} is smaller than Tb^{3+}, which causes charge imbalance and lattice distortion due to multiple site occupation.[348]

At a lower excitation wavelength of 350 nm, strong emission at 488 nm, 544 nm, 584 nm and 620 nm are detected, which correspond to $^5D_4 \rightarrow {}^7F_6$, $^5D_4 \rightarrow {}^7F_5$, $^5D_4 \rightarrow {}^7F_4$ and $^5D_4 \rightarrow {}^7F_3$ transitions of Tb^{3+}.[107] For related compounds (CaF_2 and SrF_2), Tb^{3+} emission has been reported by co-doping with Ce^{3+} to excite Tb^{3+} at higher energy (250 nm).[233]

However, detected excitation spectra *(see Figure 7.3)* show a strong broad band between 250 nm – 270 nm and weak bands between 300 nm – 400 nm. The bands correspond to low spin (LS) and high spin states (HS), respectively.[349] The magnetic dipole transition i.e., $^5D_4 \rightarrow {}^7F_5$ that possesses $\Delta J = \pm 1$, is the strongest transition. Thus from the literature corresponding transitions have been reported for SrF_2,[233] but not MgF_2:10%Tb^{3+}.

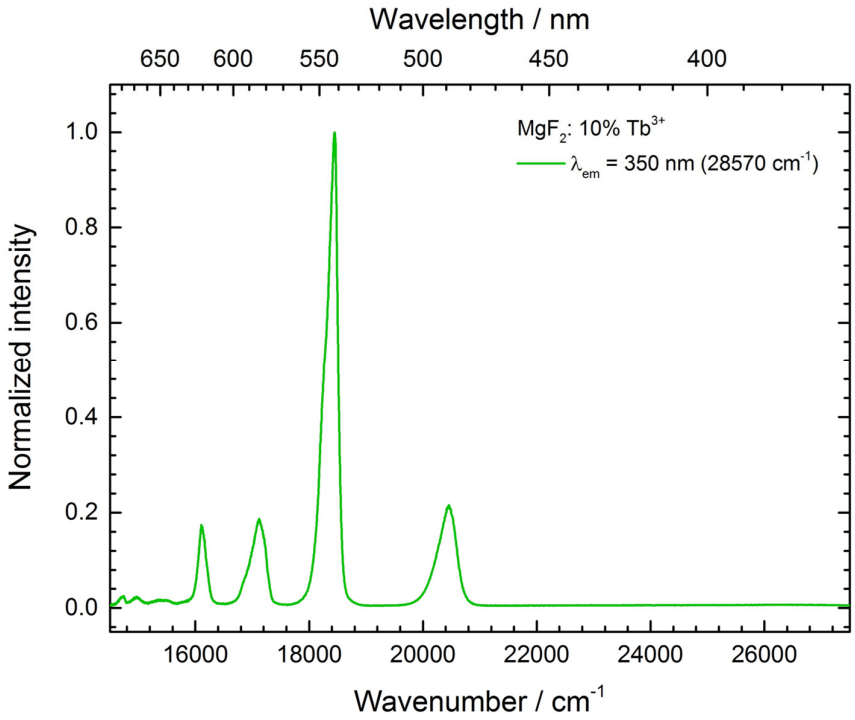

Figure 7.2: Emission spectrum of MgF_2:10%Tb^{3+} for λ_{exc} = 350 nm.

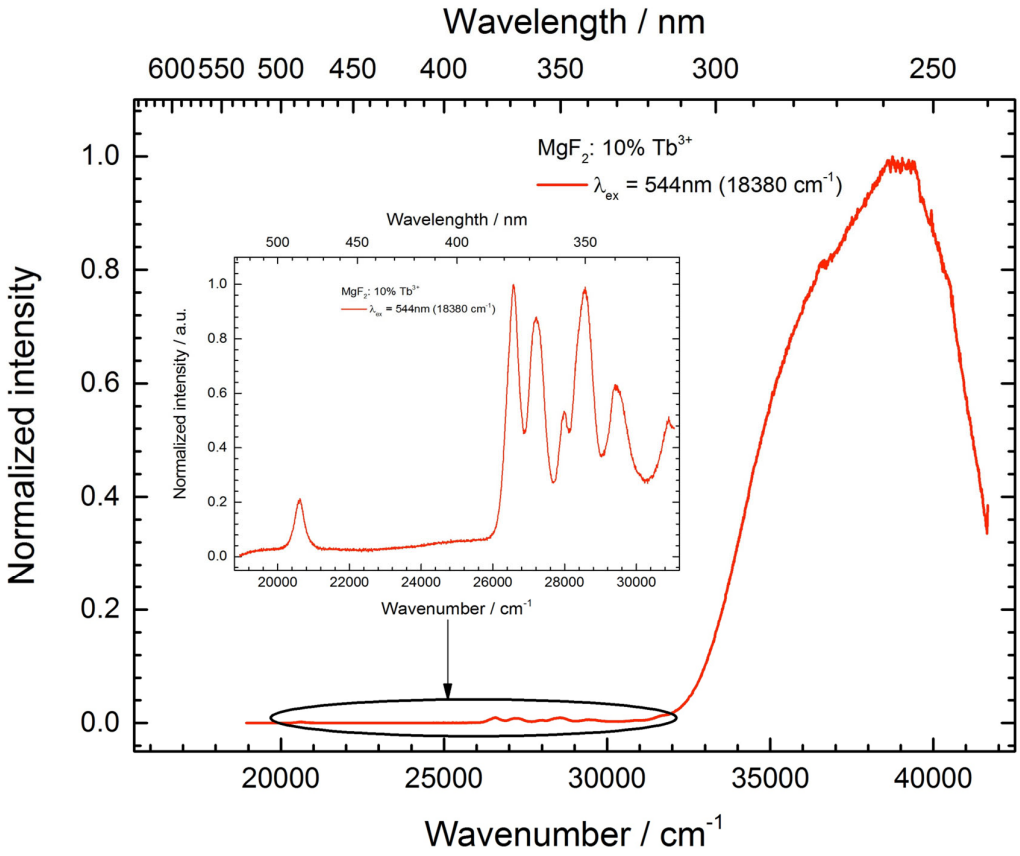

Figure 7.3: Excitation spectrum of MgF_2:10%Tb^{3+} for λ_{exc} = 544 nm. Inset shows a close-up spectrum between 32000 cm^{-1} and 22500 cm^{-1}.

Figure 7.4 shows the emission and excitation spectra of MgF_2:10%Eu^{3+} beads. The excitation spectra were measured at different emission wavelengths to understand the occurrence of red luminescence. The most visible emission bands (262 nm and 389 nm) are taken to probe the emission of Eu^{3+}. A charge transfer band (300 nm – 350 nm) was detected.[107] Ju et al., reported similar results but for BaFCl nanocrystals.[350] Their study indicated that distortion occurred due to Eu^{3+} occupying a Ba^{2+} site with a coordination number of 6. This substitution likely caused a change in the local environment and lattice parameters, which is consistent with the observed distortion of Mg^{2+} site.[350] The emission spectra detected at an excitation wavelength of 389 nm exhibits strong f-f transitions with bright red emission typically known for Eu^{3+}.[171]

When MgF_2:10%Eu^{3+} sample was excited with 262 nm, a broad emission was observed between 15300 cm^{-1} and 21500 cm^{-1} *(see Figure 7.5)*. The broad emission observed in the MgF_2:10%Eu^{3+} spectrum, is indicative of multiple overlapping electronic transitions and significant phonon interactions.[9,351] The $4f^6$ electronic configuration of Eu^{3+} ions permits numerous transitions, which overlap and result in broad emission bands.[236] Phonon coupling within the solid MgF_2 matrix further broadens the spectrum as electronic states interact with lattice vibrations.[352]

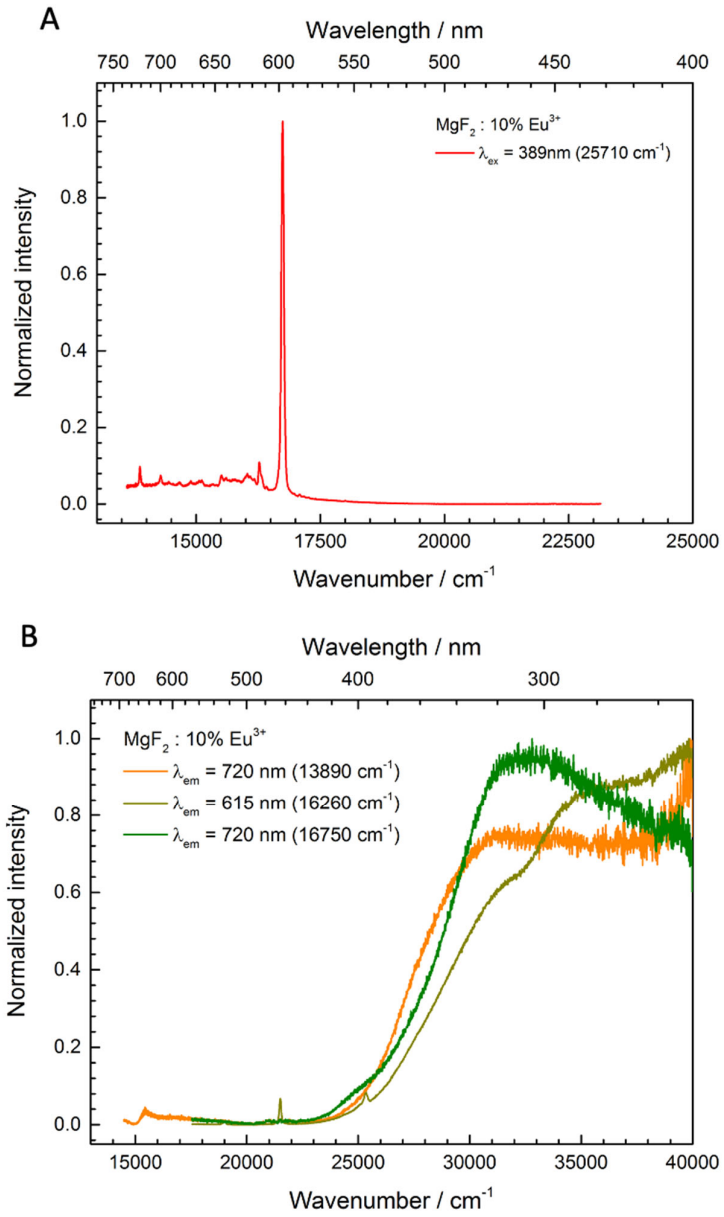

Figure 7.4: Emission (A) and excitation (B) spectra of MgF_2:10%Eu^{3+}. Excitation spectra measured at 597 nm, 615 nm and 720 nm.

The local environment around Eu^{3+} ions, influenced by crystal field effects, varies, particularly when Eu^{3+} occupies sites with differing symmetries or distortions.[107] This inhomogeneous broadening arises from Eu^{3+} ions occupying diverse lattice sites, each with slightly different local environments.[351] At higher doping concentrations, such as 10% Eu^{3+}, interactions between Eu^{3+} ions, including cross-relaxation processes, contribute to the broadening of the emission spectrum.[107]

In contrast, excitation at 389 nm leads to a sharp emission peak at approximately 16260 cm^{-1} (615 nm). This is an indication of electronic transitions, typically also associated with f-f transitions of Eu^{3+}.[9] Excitation at 262 nm apparently populates higher energy states and triggers charge transfer bands. Hence, broad emission due to multiple relaxation pathways is observed. Excitation at 389 nm populates specific energy levels within the Eu^{3+} ions, resulting in sharp emission bands with minimal phonon interaction.[353]

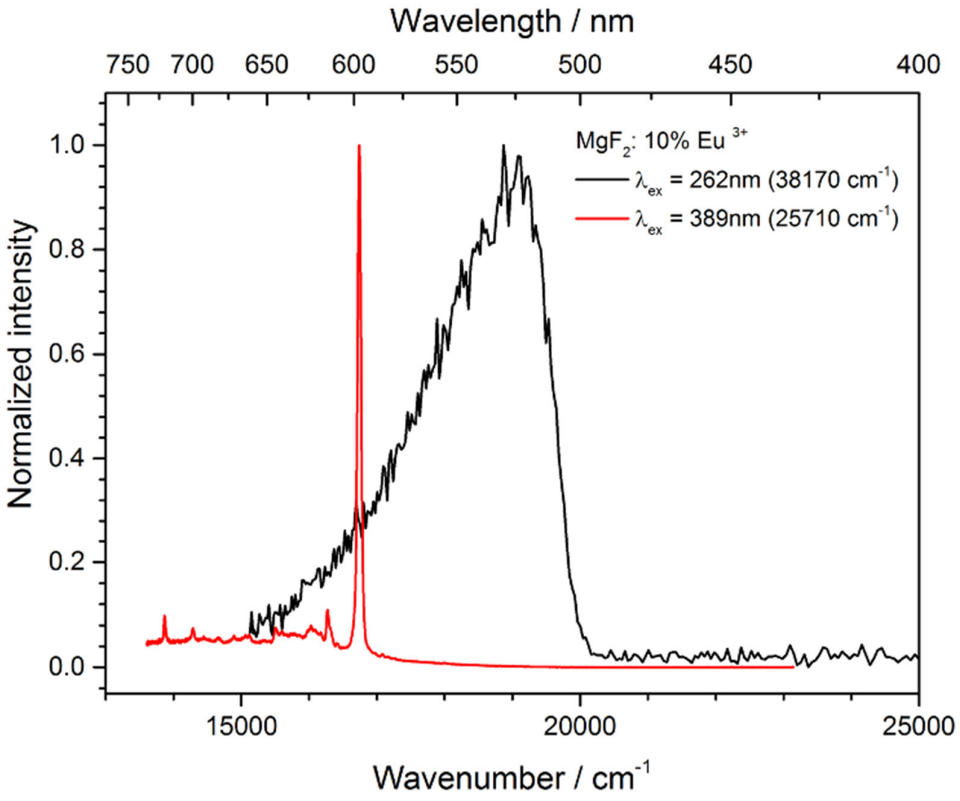

Figure 7.5: Emission spectra of MgF_2:10%Eu^{3+} excited at 262 nm and 389 nm.

7.2.2 Stabilization of MgF_2 beads with PDEGMA and PAA polymer brushes

This section details the preparation and characterization of MgF_2 beads coated with PDEGMA and PDEGMA-*b*-PAA polymer brushes using ARGET-ATRP. The use of PDEGMA and PAA in the preparation of polymer brushes on MgF_2 beads takes advantage of their hydrophilicity, responsiveness to environmental stimuli (temperature and pH), and functional versatility.[339,340] Initially, a layer of ω-mercaptoundecyl bromoisobutyrate (MUBiB) was formed on the MgF_2 beads *(see Figure 7.6)*. This was followed by the synthesis of PDEGMA brushes, using the bromoisobutyrate moiety as initiator for the polymerization of di(ethylene glycol) methyl ether methacrylate (DEGMA). Prior to the reaction, the DEGMA monomer was purified by removing the stabilizer using Al_2O_3 column chromatography. The purified DEGMA was then mixed with a copper-based catalyst, a ligand (e.g., PMDETA), and a suitable solvent (mixture of Milli-Q water and methanol) under argon atmosphere. This reaction mixture was added to the MUBiB-coated beads that were dispersed in the mixture of Milli-Q water and methanol. Then, polymerization was carried out to form PDEGMA brushes on the beads. Subsequently, the PDEGMA brushes were extended using AA to obtain PDEGMA-PAA block copolymer brushes.

The resulting polymer-decorated beads were characterized with STEM-EDX to visualize structural properties, TGA to determine the amount of polymer grafted onto the beads, and XPS for detailed surface composition analysis. TGA provided insights into the organic content and grafting density of the polymer layer, while XPS confirmed the presence and chemical state of the elements on the surface, verifying the successful attachment of the initiator and subsequent polymer layers.

Detailed STEM-EDX analyses were done after each step i.e., MgF_2 beads, MgF_2@MUBiB, MgF_2@PDEGMA and MgF_2@PDEGMA-*b*- PAA. Figure 7.7 shows the STEM-EDX data of MgF_2@PDEGMA beads. Due to the hollow spherical structures of MgF_2 beads, MUBiB penetrates the cavities within the beads. Thus, the layer formation not only take place at the beads outer surface, but also likely also inside the particles.

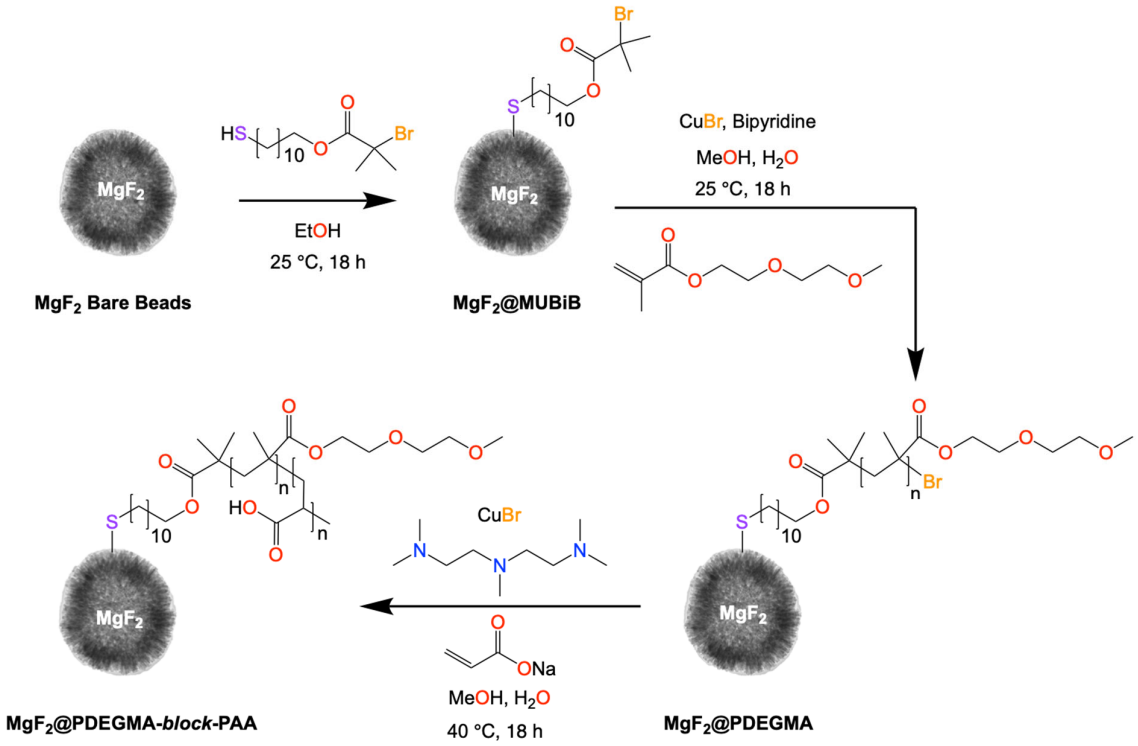

Figure 7.6: Synthesis of PDEGMA-*b*-PAA polymer brushes via ARGET-ATRP on MgF_2 beads.

The bright field STEM image (top left) clearly reveals the spherical morphology of the MgF_2 beads, indicating successful synthesis. In the C elemental map (top center), the green distribution signifies the presence of the PDEGMA polymer coating. This uniform carbon signal suggests an effective and consistent coating of PDEGMA on the surface of the MgF_2 beads, indicative of a successful polymerization process.

The Mg elemental map (top right), shown in magenta, highlights the core MgF_2 structure, confirming that the integrity of the MgF_2 beads was maintained throughout the synthesis steps. The overlay of F and Mg in the combined elemental map (bottom left) further supports this observation, with orange and magenta signals demonstrating a homogeneous distribution of MgF_2 within the beads.

The distinct F map (bottom center) reveals a consistent F signal across the beads, supporting the structural evidence and uniform composition of MgF_2 even after surface modifications. Moreover, the presence of Br in the elemental map (bottom right), represented by the blue distribution, indicates the successful incorporation of the MUBiB molecule into the MgF_2 beads. This is substantiated by the S map (bottom middle), where the yellow signal further validates the effective functionalization of the beads with MUBiB.

Collectively, these elemental mapping provide compelling evidence of the successful functionalization of MgF_2 beads with MUBiB, followed by the polymerization of PDEGMA. The uniform distribution of C, Br, and S signals across the beads affirms that the functionalization and polymerization processes occurred not only on the surface but also within the internal cavities of the MgF_2 beads. During the first minutes (≤ 5 minutes) of measurement, the beads appeared darkened, when observed in STEM. An intense carbon signal was detected in each bead. However, after long measurement time (20 minutes) the electron beam degrades part of the carbon and a ring is observed in the center of each bead.

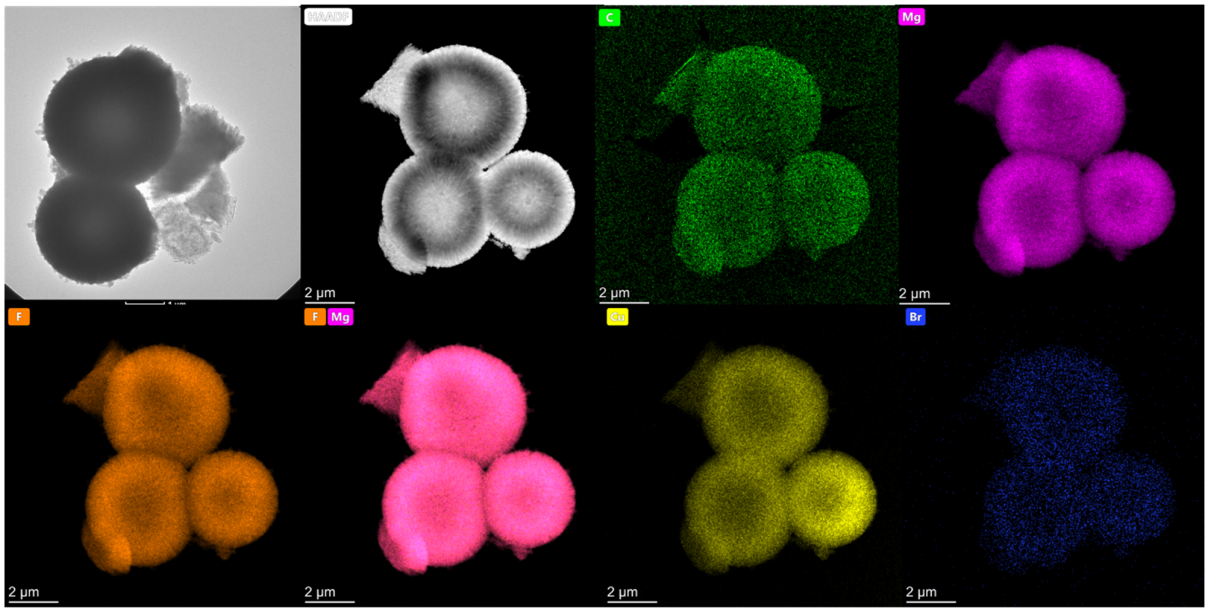

Figure 7.7: STEM – EDX visualization of MgF_2@PDEGMA beads done at 200 kV measured within 20 minutes.

Figure 7.8 shows STEM-EDX of MgF_2 not coated with PDEGMA-*b*-PAA polymer brushes. In comparison to Figure 7.7, rings due to long irradiation time are barely noted. The F-Kα (0.677 keV) signal is more intense than the signal of Mg-Kα (1.253 keV). However, the C-Kα (0.277 keV) signal due to the carbon film from the TEM grid is not clearly visible, because it is almost overlapping with F-Kα signal. Cu-Kα (8.040 keV) and Cu-Kβ (8.904 keV) are detected due to the Cu on the TEM grid. The signal at 1.74 keV is attributed to Si-Kα, which emanates from the detector made of Si-crystal.

It was challenging to distinguish between MgF_2@MUBiB, MgF_2@PDEGMA and MgF_2@PDEGMA-*b*-PAA due to the chemical similarity high signals of carbon. Furthermore, the contrast in the C intensity on the beads and in the background is detected at the same energy (0.277 keV) and also cannot be differentiated via STEM-EDX.

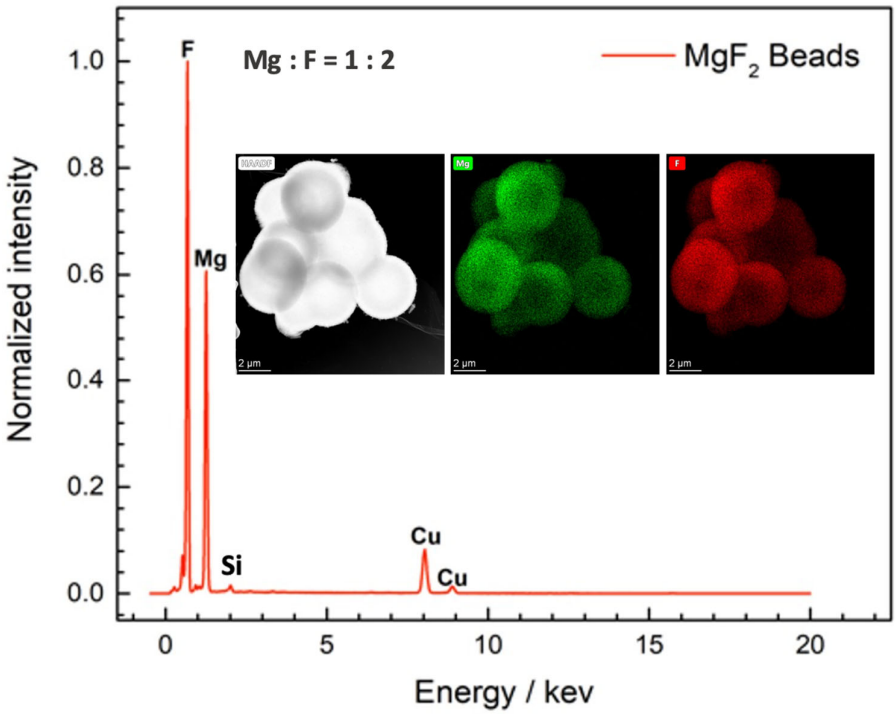

Figure 7.8: STEM – EDX analysis of 5 µm MgF_2 beads prepared in an autoclave at 200°C and for 4 days. Inset – atomic mapping using HAADF detector – scale bar represents 2 µm (green – Mg signal, red – F signal and grey – MgF_2 beads). Measurement time 5 minutes.

To further investigate how much polymer was attached to the MgF_2 beads, TGA was done in nitrogen atmosphere. TGA measurements were conducted by Alexander Kleimann from PC I group and data analysis done by the author of this Thesis. The TGA plot of neat MgF_2 beads shows only a very slight mass change at temperatures above 1000 K. Hence the beads are stable over the entire temperature range *(c.f. Appendix XII–Figure 9.49)*. However, the TGA results of MgF_2@MUBiB *(c.f. Appendix XII– Figure 9.50)*, show a slight decrease of sample mass over a larger temperature range (around 450 K to 750 K).

The weight is quite stable for a while but from 900 K, the weight decreases gradually. While the weight loss above 900 K was also noted in bare MgF_2, the initial weight loss from 450 K to 750 K can be speculated to originate from MUBiB or PDEGMA-*b*-PAA.

The TGA experiments did not provide adequate information for determining the extent of polymer attachment to the MgF_2 beads, as the weight loss observed was inconclusive in differentiating between the polymer and the MgF_2. Consequently, XPS was employed to gain more precise insights into the surface composition of the samples. XPS measurements were conducted by Kawaljit Kaur from MNaF facility and data analysis done by the author of this Thesis.

The XPS analysis depicted in Figure 7.9 provides a comprehensive characterization of the MgF_2@PDEGMA-*b*-PAA beads at each stage of polymerization, offering insights into both theoretical and experimental compositions. The survey spectra *(refer to Figures 7.9A-C)* reveal distinct peaks corresponding to Mg 2s, C 1s, and F 1s, indicative of successful polymerization steps.

Specifically, the initial survey spectrum of MgF_2@MUBiB *(see Figure 7.9A)* confirms the foundational MUBiB layer's coverage. The observed peaks at Mg 2s, C 1s, and F 1s are consistent with theoretical expectations, indicating successful formation of the base polymer layer.[354]

The survey spectrum for MgF_2@PDEGMA *(see Figure 7.9B)* resembles that of MgF_2@MUBiB, with additional changes in peak intensities and positions. This suggests the successful grafting of the PDEGMA layer onto the MgF_2@MUBiB beads. The presence of distinct Mg 2s, C 1s, and F 1s peaks, along with changes in their intensities, indicates an increased thickness and coverage of the polymer brush. For MgF_2@PDEGMA-*b*-PAA *(see Figure 7.9C)*, the survey spectrum shows further shifts and changes in peak intensities compared to the previous stages. These variations suggest the successful addition of the PAA layer, further increasing the polymer brush's thickness.

The high-resolution C 1s spectra *(refer to Figures 7.9D-F)* provide detailed insights into the chemical environment changes throughout the polymerization process. For MgF_2@MUBiB *(see Figure 7.9D)*, the high-resolution C 1s spectrum reveals peaks attributed to carbon in C–C/H (285.0 eV), C–O (288.0 eV), and O–C=O (291.2

eV).[346] Comparing these signals with the literature shows that the measured signals are shifted to higher binding energies compared to reported values (C–O: 287.3 eV, O–C=O: 289.3 eV).[346,355]

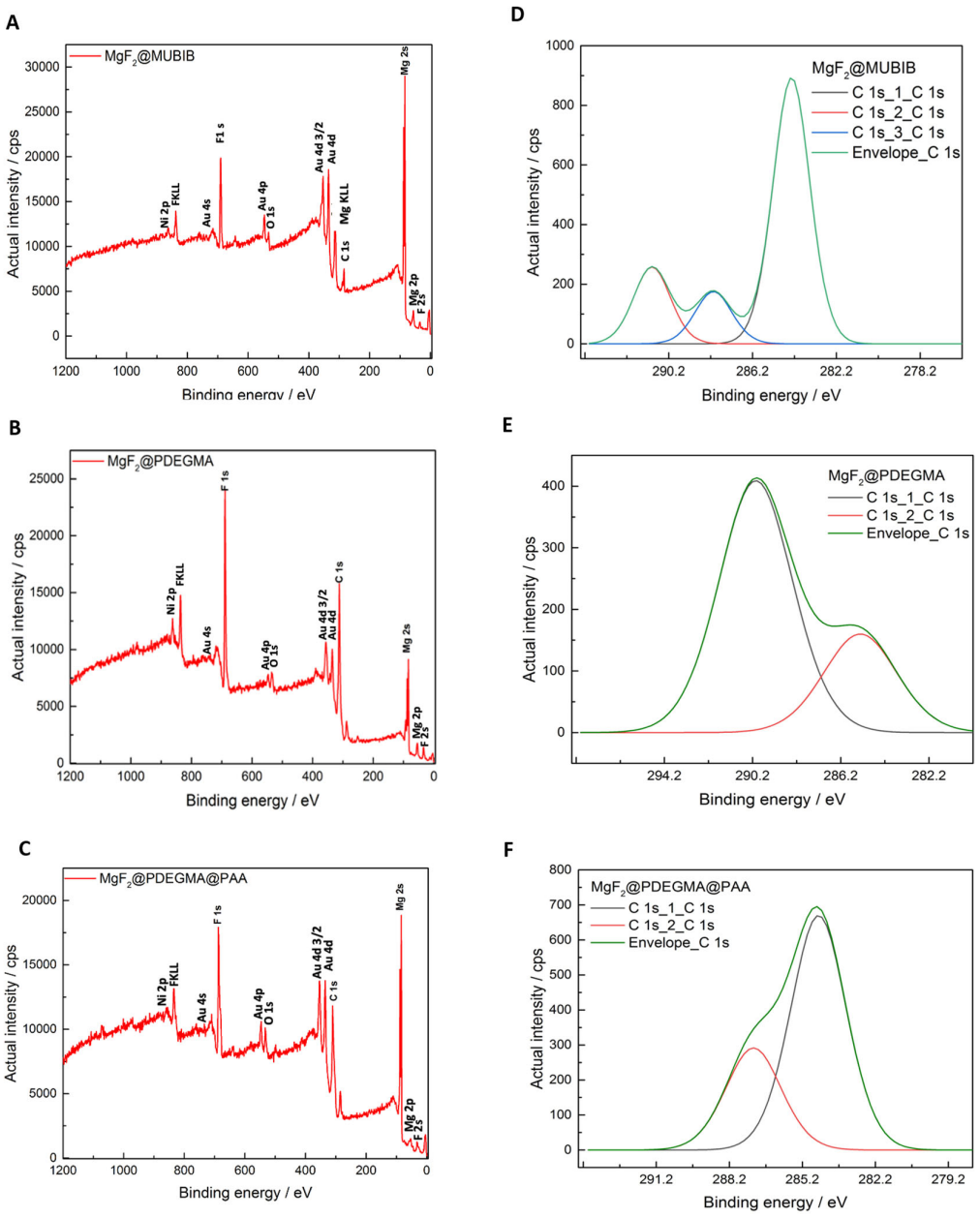

Figure 7.9: XPS analysis showing survey (A-C) and high-resolution (D-F) C1s spectra after each polymerization step to form MgF_2@PDEGMA-*b*-PAA beads.

For MgF_2@PDEGMA *(see Figure 7.9E)*, the high-resolution C 1s spectrum shows significant differences compared to MgF_2@MUBiB. The spectrum was deconvoluted

into signals for C–C/H (285.0 eV) and O–C=O (290.0 eV). Additionally, C–O carbons at 287.3 eV, emanating from the glycol functionalities in PDEGMA, were detected. These observations align well with theoretical expectations and literature values, confirming the successful grafting of the PDEGMA layer.[334,339,346]

The high-resolution C 1s spectrum for MgF_2@PDEGMA-*b*-PAA *(see Figure 7.9F)* was deconvoluted into signals for C–C/H (285.0 eV) and C–O (287.3 eV).

In conclusion, the XPS analysis provides both qualitative and quantitative confirmation of the theoretical compositions, closely matching the experimental data at each polymerization stage. This systematic approach ensures a thorough understanding of the polymerization process.

7.2.3 Antibacterial studies of magnesium fluoride nanowhiskers with *Escherichia coli*

In this experiment, MgF_2 nanowhiskers were selected for investigation with *E. coli* Mach 1 $T1^R$ due to their high surface-to-volume ratio compared to larger MgF_2 beads, which are composed of assembled nanowhiskers. The bacterial activity was compared to locally purchased MgF_2 from Alfa Aeser, Germany. *E. coli* Mach 1 $T1^R$ are fast growing strains and are visible within 8 h of incubation. To culture *E. coli* Mach 1 $T1^R$, a single colony was inoculated into fresh LB medium and incubated for 16 h at 37°C with shaking at 200 rpm. The optical density (OD) of the bacterial suspension was subsequently measured and adjusted to 0.5 by diluting 1 mL of bacterial suspension with PBS. The acceptable range for OD was between 0.2 and 0.8.[356] If the recorded OD was less than 0.2, the bacteria were allowed to grow for a few more hours. Conversely, if the OD exceeded 0.8, the overnight culture solution was diluted to bring it within the acceptable range. The optical density was monitored after 5 and 10 h for both samples (microwave and Alfa Aesar). According to the obtained results *(c.f. figure 7.10)*, microwave sample has a delayed growth compared to the purchased bulk sample. The colony-forming units (CFUs) per mL were determined by placing 50 µL of the diluted suspension on LB agar and incubating for 24 h. Additionally, a 10^{-6} dilution was prepared, with 10 µL aliquots placed in a 96-well plate containing LB medium, followed by incubation and measurement over a 16-h period.

Figure 7.11 shows the growth curves of *E. coli* Mach 1 $T1^R$ with different concentrations of MgF_2 samples. The growth curves are monitored and compared to a standard sample without added MgF_2. Furthermore, to rule out any interference due to contamination of MgF_2 samples; pure LB medium, LB & microwave and LB & Alfa Aesar samples were also simultaneously investigated. In Figure 7.11 panel A, no growth of bacteria was observed in the samples of MgF_2 dispersed in only LB medium. In addition, the blank (LB medium) also shows no growth of bacteria. These observations suggest medium no contamination in the LB medium. The growth curves of *E. coli* Mach 1 $T1^R$, depicted in Figure 7.11, elucidate the significant impact of MgF_2 on bacterial proliferation. Panel A provides a comparative analysis of *E. coli* growth in LB media alone and in the presence of MgF_2 sourced from Alfa Aesar and microwave synthesis at a concentration of 3.1 mg/mL.

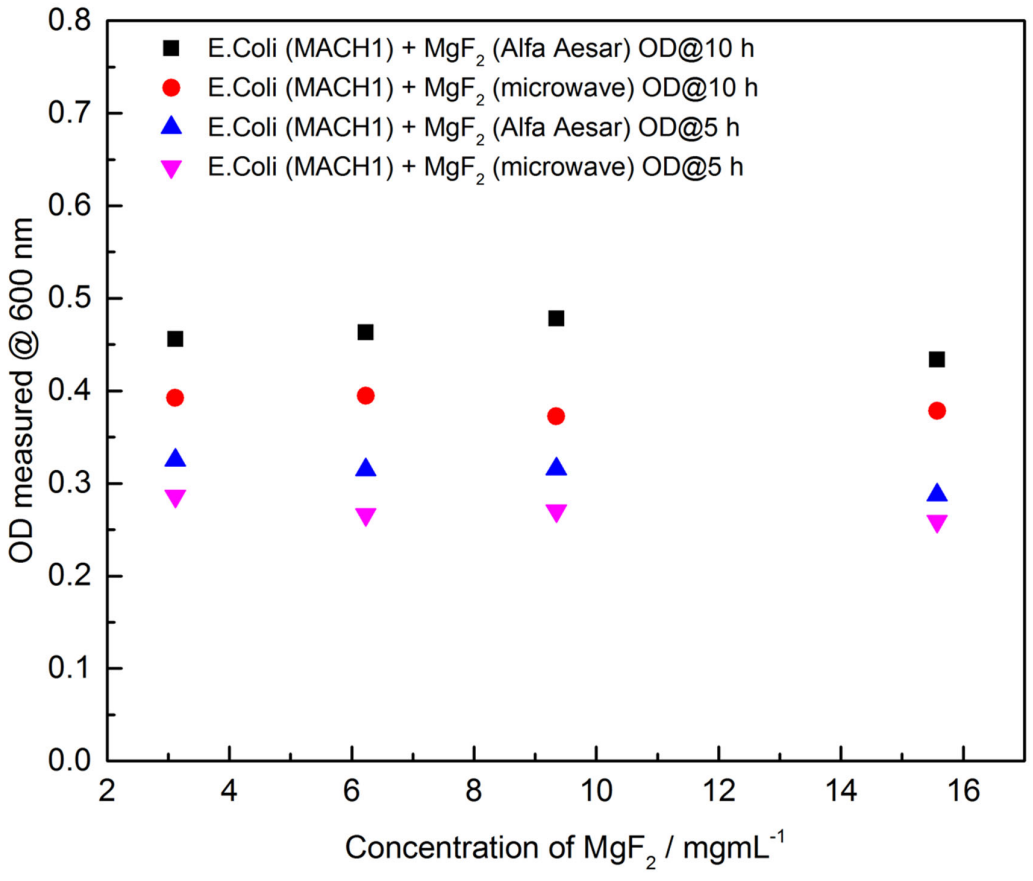

Figure 7.10: Plot of OD measured at 600 nm versus concentration of MgF_2 ($mgmL^{-1}$).

The results demonstrate that *E. coli* exhibits no growth in LB media alone, while the addition of MgF_2 markedly enhances bacterial proliferation, with Alfa Aesar MgF_2 showing superior efficacy compared to its microwave-synthesized counterpart. The anomalously increase in OD values for blank (LB only) observed in the first 2 h in the first panel of Figure 7.11, where no growth is anticipated, can be attributed to instrumental errors, such as baseline calibration issues or spectrophotometer drift.[357]

Furthermore, the presence of MgF_2 itself may also play a role, as incomplete dissolution can lead to precipitate formation or colloids that scatter light, thus increasing OD values.[358,359] Chemical interactions between MgF_2 and LB media components might form colored complexes or other species with absorbance at 600 nm, falsely elevating OD measurements. Background absorbance from LB media or MgF_2 solutions might also contribute to the observed discrepancies.[357]

Further analysis in Panel B, examining a higher concentration of 6.2 mg/mL, reveals robust growth with both sources of MgF_2, though the Alfa Aesar variant again slightly outperforms. This trend persists in Panel C, where at a concentration of 9.4 mg/mL, *E. coli* demonstrates significantly better growth with Alfa Aesar MgF_2 than with the microwave-synthesized form, highlighting a clearer distinction at this level. Lastly, Panel D explores the effects at 15.6 mg/mL, showing substantial growth enhancement with both sources, but with Alfa Aesar MgF_2 maintaining a slight edge. These findings suggest growth is slowest in the sample prepared via microwave. In fact, growth in Alfa Aesar sample is delayed compared to the standard sample (without MgF_2) and is attributed to its bulky nature that also hinders absorbance and not necessarily attributed to antibacterial activity. The sample with 9.4 mg/mL of MgF_2 nanowhiskers had more delayed growth effects.

Hence, 9.4 mg/mL concentration of MgF_2 nanowhiskers sample depicts the best concentration for antibacterial activity among the four tested concentrations. As for the Alfa Aesar samples, an increase in concentration shows no influence or appreciable changes. Even if the starting bacteria solution is further diluted to 10^{-5}, Alfa Aesar sample does not hinder growth of *E. coli* Mach 1 $T1^R$ *(c.f. Appendix XI–Figures 9.47 and 9.48)*. Lellouche et al., made similar observations with MgF_2 aggregated NPs.[347]

In contrast to previous bacterial studies of MgF_2,[347,360] the results in this work prove that MgF_2 prepared via microwave (nanowhiskers) without HF have antibacterial activity. Furthermore, the reported literature results were investigated in biofilms. In contrast, this work focusses on understanding the effect of the MgF_2 on the growth and CFU of *E. coli* Mach 1 $T1^R$. Figure 7.12 shows that the colony forming units (mL) is hindered by increase in concentration of MgF_2 nanowhiskers. If CFU values are plotted against concentration, a good fit for the decay curve (adj R^2 = 0.94553) is obtained *(c.f Appendix X–Figure 9.41)*.

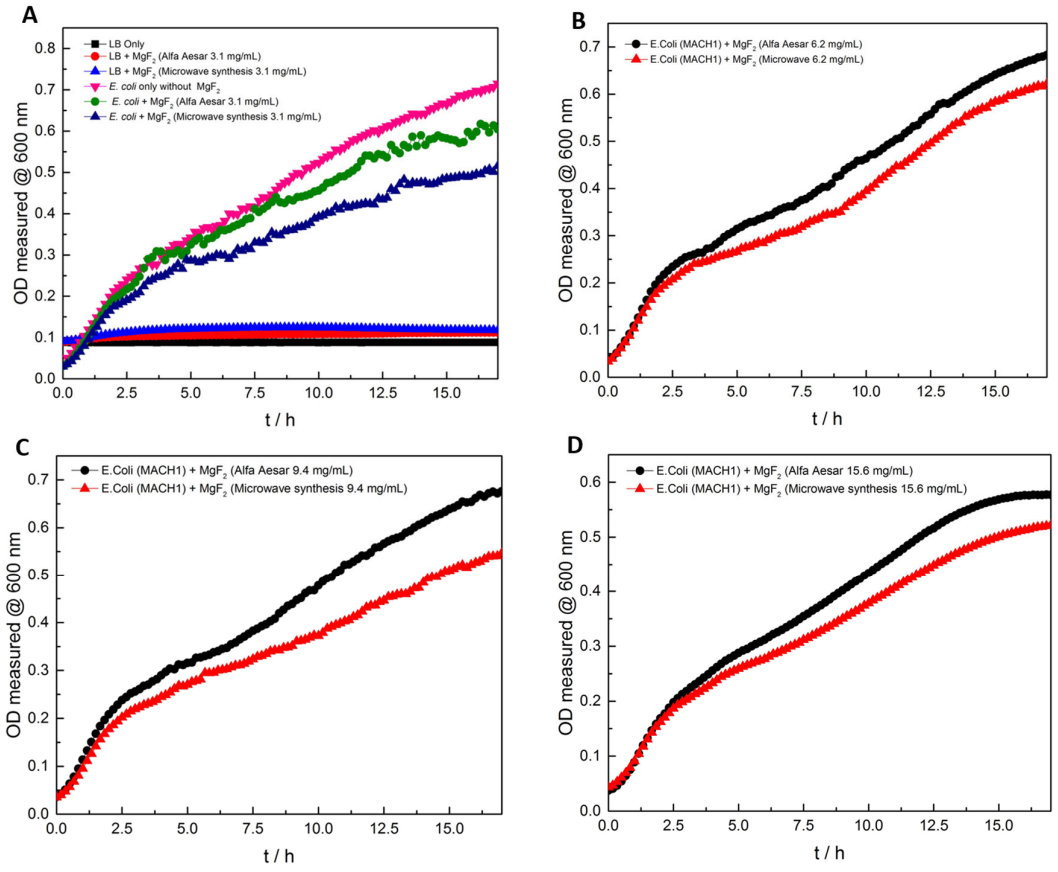

Figure 7.11: Growth curves of *E. coli* Mach 1 $T1^R$ for different concentration of microwave and Alfa Aesar MgF_2 ($mgmL^{-1}$) incubated up to 16 h. (A) Growth in LB media alone and with 3.1 mg/mL MgF_2 from Alfa Aesar and microwave synthesis, showing the significant enhancement of bacterial growth with MgF_2 addition. (B) Growth with 6.2 mg/mL MgF_2, illustrating a slight advantage of Alfa Aesar MgF_2 over microwave synthesized MgF_2. (C) Growth with 9.4 mg/mL MgF_2, highlighting the clearer distinction in growth enhancement by Alfa Aesar MgF_2. (D) Growth with 15.6 mg/mL MgF_2, demonstrating substantial growth with both sources, with a slight edge for Alfa Aesar MgF_2.

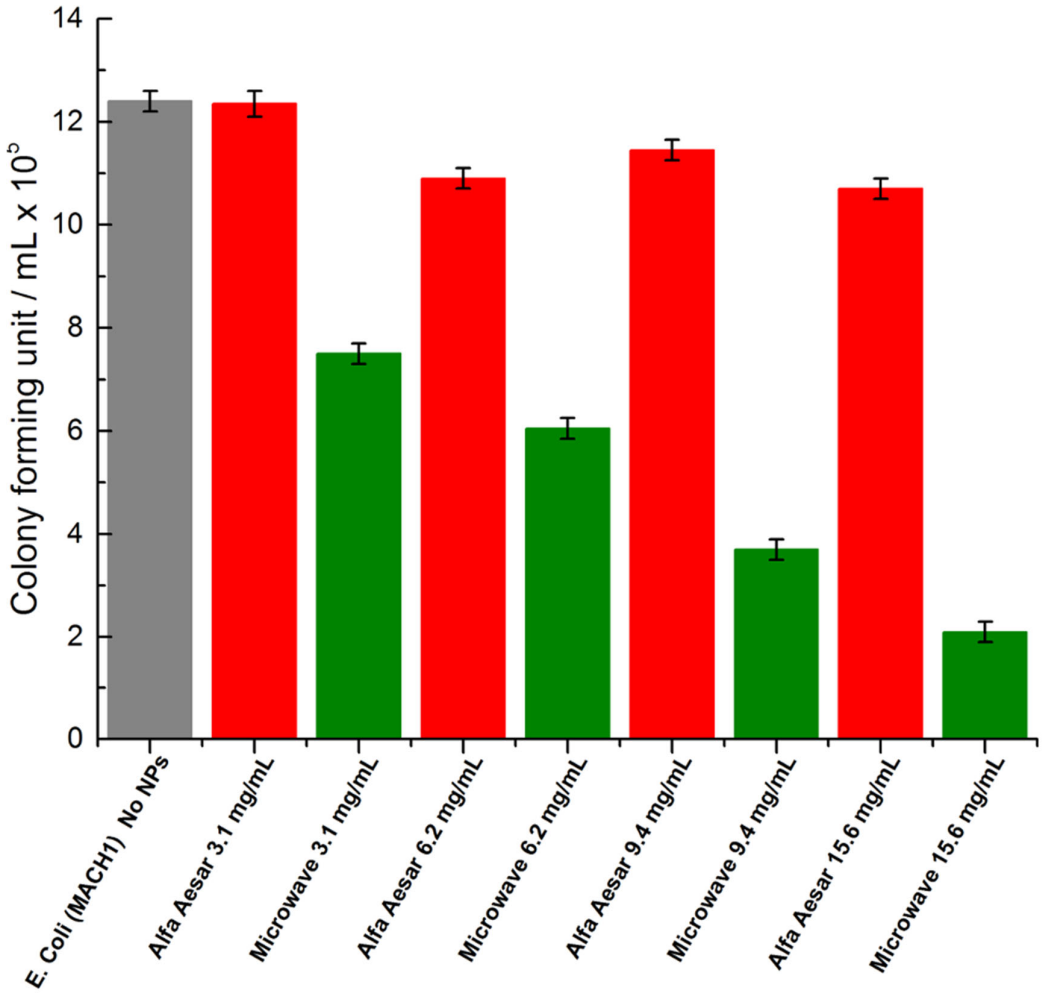

Figure 7.12: Influence of microwave and Alfa Aesar MgF_2 ($mgmL^{-1}$) samples on CFU (mL).

7.3 Conclusion

In this Chapter, the functionalization of MgF_2 beads was investigated to enhance their potential for future biomedical applications. Initially, MgF_2 beads were doped with Eu^{3+} and Tb^{3+} ions to obtain photoluminescent beads. The doped beads exhibited strong green and red emissions under UV illumination, corresponding to the emission Tb^{3+} and Eu^{3+} ions, respectively.

Subsequently, to improve the colloidal stability that is against agglomeration in aqueous media and functionality in terms of surface modification of MgF_2 beads, they were modified with polymer brushes. Brush synthesis was successfully synthesized using ARGET-ATRP, beginning with the formation of a self-assembled monolayer (SAM) of MUBiB on the substrate (MgF_2). This SAM facilitated the controlled polymerization of PDEGMA brushes, utilizing the ARGET-ATRP technique for precise growth regulation and resulting in densely packed PDEGMA brushes. Following this, PAA was grafted onto the PDEGMA brushes, creating a mixed brush architecture. The MgF_2 coated PDEGMA-*b*-PAA beads characterization via FESEM, STEM-EDX, TGA, and XPS confirmed successful modification. STEM-EDX analysis indicated the presence polymer brushes both on the surface and within the beads' hollow structures. XPS analyses provided further validation through surface chemistry insights, respectively.

The antibacterial efficacy of MgF_2 nanowhiskers that constitute the beads was assessed against *E. coli* Mach 1 $T1^R$, demonstrating slight activity compared to commercially available MgF_2. Synthesized via microwave, the nanowhiskers displayed antibacterial properties attributed to their higher surface area to volume ratio, facilitating enhanced interaction with bacterial cells and resulting in physical disruption and growth inhibition. At a concentration of 9.4 mg/mL, MgF_2 nanowhiskers showed antibacterial activity, significantly reducing bacterial growth and colony-forming units.

7.4 Materials and methods

BMIM[BF_4] (99%) purchased from io-li-tech, Heilbron Germany. $TbNO_3)_3$•$6H_2O$ (99.999%), $CeCl_3$•$7H_2O$ (99.999%), NaH_2PO_4•$2H_2O$ (99.9%), $Mg(NO_3)_2$•$6H_2O$ (99.97%), MgF_2 (99%) from Alfa Aesar, Germany. $EuCl_3$•xH_2O (99.99%) Reacton Germany. $Eu(NO_3)_3$•xH_2O (99.9%), ChemPur Germany. Ethanol denatured (90%), ethanol anhydrous (99+%), Alfa Aesar Germany. ≥99.9% Di(ethylene glycol) methyl ether methacrylate, Merck KGaA, Darmstadt, Germany. Aluminum oxide (90 neutral, Activity 1), MACHEREY-NAGEL GmbH & Co. KG, Düren, Germany. L-ascorbic acid (99%), Merck KGaA, Darmstadt, Germany. ≥99.9% Copper(II) chloride dihydrate (pure), AppliChem GmbH, Darmstadt, Germany. ≥99.9% Methanol, Thermo Fisher GmbH, Kandel, Germany. 99.9% 2,2'-bipyridyl,*N,N,N',N'',N''*-pentamethyldiethylenetriamine from Sigma Aldrich, 99.9% sodium acrylate from Merck KGaA, Darmstadt, Germany. Dulbecco's phosphate saline buffer (PBS) (10×, without Mg^{2+} and Ca^{2+}) from Lonza Switzerland.NIH 3T3 cell lines were obtained from Dr. Jürgen Schnekenburger (Biomedical Technology Center of the Medical Faculty Münster, Germany). *E. coli* W (ATCC9637) derivative Mach1 (T1 Phage-resistant, chemical competent, purchased from Invitrogen from Prof. Toby Jenkins (Department of Chemistry University of Bath, UK). Milli-Q water (resistivity of 18.2 MΩ cm), from a Millipore Direct Q8 system, (Millipore Advantage A10 system, Schwalbach, Germany) with a Millimark Express 40 as filter (Merck, Germany).

7.4.1 Preparation of MgF_2:10%Tb^{3+} and MgF_2:10%Eu^{3+} beads

To dope with Eu^{3+} / Tb^{3+}, after preparation of 0.13M of $Mg(NO_3)_2$•$6H_2O$ and NaH_2PO_4•$2H_2O$ in 8.750 mL of Milli-Q water *(refer to procedure outlined in 6.4.1)*, adjust the stoichiometry of $Mg(NO_3)_2$•$6H_2O$ using $Eu(NO_3)_3$•$2H_2O$ or $Tb(NO_3)_3$•$2H_2O$, by adding 10 % of Eu^{3+} / Tb^{3+}. Add few drops of HCl dropwise until the precipitated phosphate salt is dissolved. Readjust the pH to 6.5 or 7 by adding few drops of buffer pH 10. The other remaining steps are done as outlined in 6.4.1.

7.4.2 Preparation of MgF_2 beads coated with PDEGMA and PAA polymer brushes via ARGET-ATRP

A layer of *ω*-mercaptoundecyl bromoisobutyrate was attached to the surface as an anchor before polymer brushes were grafted. A (MUBiB, 10 mM, 2 ml) stock solution was diluted with pure ethanol (18 ml) to get the MUBiB (1 mM) solution that was used for the monolayer assembly. To generate the layer on the MgF_2 beads the prepared MUBiB (1 mM, 4 ml) was mixed with the solution of the beads (4 ml). This mixture was slowly stirred overnight. After stirring, the mixture was centrifuged (5 min, 5000 rpm) and the sediment dispersed in Milli-Q water (1 ml).

7.4.2.1 Synthesis of PDEGMA brushes

The stabilizer in di(ethylene glycol) methyl ether methacrylate (DEGMA) was removed by passing the monomer solution through a column of Al_2O_3. A solution of L-ascorbic acid (0.4M) was prepared by solving L-ascorbic acid (177.3 mg) in Milli-Q water (2.517 ml). A solution of CuBr (0.04 M) was prepared by dissolving CuBr dihydrate (37.5 mg) in Milli-Q water (5.499 ml). 25 mg of 2,2'-bipyridyl was added to a mixture of Milli-Q water (9.6 ml) and methanol (10.0 ml). The mixture is flushed with argon and stirred for 15 minutes. To the mixture, DEGMA monomer (3.5 ml) and a CuBr (0.2 ml, 0.04M) solution were added and stirred for 10 minutes under constant argon flow. A solution of ascorbic acid (0.2 ml, 0.4 M) was finally added to the mixture followed by stirring (5 min). The mixture was transferred into a reaction chamber containing the beads coated with MUBiB monolayer. The polymerization was performed for 1 h, constantly flushed with an argon stream. To stop polymerization, the mixture was centrifuged three times (5 min, 5000 rpm) interchangeably with Milli-Q water. The resulting polymerized beads are further redispersed in 1 mL Milli-Q water.

7.4.2.2 Synthesis of PDEGMA, PAA block copolymer brushes

PMDETA (*N,N,N',N'',N''*-pentamethyldiethylenetriamine, 0.35 ml) was introduced to a mixture of Milli-Q water (11.25 ml) and methanol (3.75 ml). The mixture was stirred (10 min) and flushed with argon. Followed by addition of sodium acrylate (NaA, 2.15 g). The mixture was stirred (20 min) under argon atmosphere. To increase the solubility of NaA the temperature was slightly increased with a warm

water bath (~40°C). Copper(I) bromide (0.15 g) was added and the mixture stirred for 2 min under an argon atmosphere. The mixture was transferred to a reaction chamber containing the particles already functionalized with MUBiB and PDEGMA and the polymerization was performed overnight. To stop polymerization, the mixture was centrifuged three times (5 min, 5000 rpm) interchangeably with ethanol and Milli-Q water mixture (70% EtOH). The resulting polymerized beads are further redispersed in 1 mL Milli-Q water.

7.4.2.3 TGA Measurements

Thermogravimetric analysis was done by analyzer Q500 v6.7 (TA Instruments, New Castle, DE, USA), purged with nitrogen gas at 40 mL/min. The dried beads were placed in a platinum pan and the temperature was ramped from 50°C up at a rate of 20°C/min to a maximum temperature of 800°C.

7.4.2.4 XPS Measurements

The beads were spin coated on a gold substrate 2 times for 30 sec, at 1200 rpm. Resulting samples were placed in a petri dish and left overnight to dry at room temperature. XPS was done with a photoelectron/ESCA spectrometer (SSX-100 S-probe, Surface Science Instruments, Mountain View, CA, USA) with 200 W of Al Kα X-ray radiation. Survey spectra were recorded from 0 to 1200 eV with a resolution of 1 eV. The carbon high-resolution scans were conducted with a pass energy of 20 eV and 0.1 eV resolution. XPS spectra was analysed using the Casa XPS processing software (version 2.3.16 PR 1.6).

7.4.3 *In-vitro* bacteria study

Figure 5.4a shows a pictorial experimental procedure for the in-vitro bacteria study. One colony of *E. coli* MACH 1 $T1^R$ was looped from LB agar plate and mixed with fresh sterilized LB medium in a 15 mL falcon tube. The falcon tube was placed in in a shaking incubator for 16 h at 37°C and 200 rpm. After 16 h, the OD of the bacterial suspension was determined using a UV spectrophotometer (Helios Epsilon, Thermo Scientific) by measuring absorbance of the suspension at 600 nm. The measured OD is adjusted to read absorbance 0.5 by diluting with fresh medium *(c.f. figure 5.4.2a)*.

50 µL of each diluted suspension was placed on freshly prepared LB agar plate and incubated for 24 h at 37°C for the determination of the colony-forming unit (CFU) in the bacterial suspension. In a separate experiment, 10 µL of the 10^{-6} dilution factor bacterial suspension was pipetted in a 96 well plate and topped up with 90 µL LB medium. The 96 well plate was put in a plate reader and measurement run for 16 h at 37°C. Resulting bacteria suspension were removed and further diluted as done in the previous process. 40 µL from each suspension was placed on a LB agar plate and CFU calculated after 24 h incubation at 37°C. The whole experiment was repeated with 10 µL of different concentration (3.1 mg/mL, 6.2 mg/mL, 9.4 mg/mL and

15.6 mg/mL) of MgF_2 prepared via microwave and readily purchased sample from Alfa Aesar. 6 wells in the 96 well plate was used for each sample and the experiment done 6 times totaling 36 measured points for each sample.

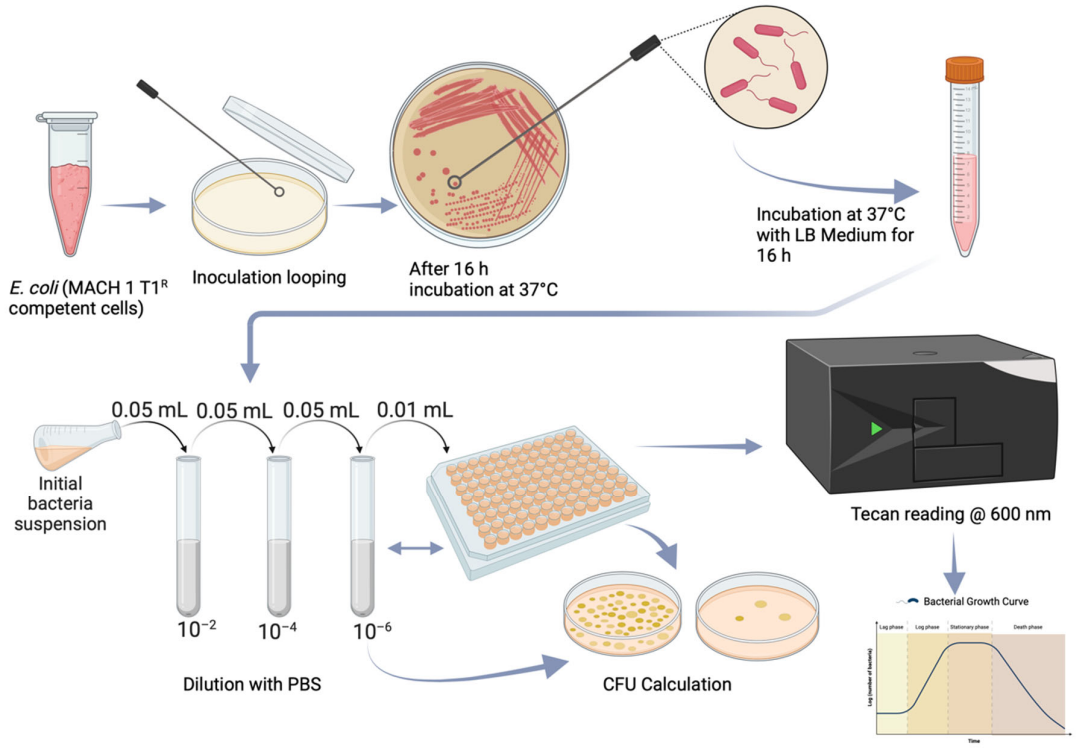

Figure 7.13: Schematic of bacteria experiment using *E. coli* MACH 1 $T1^R$ cells (created in BioRender app).

Chapter 8 Conclusion and Outlook

This Thesis has explored the synthesis and potential biomedical applications of photoluminescent nanomaterials. The research covers multiple aspects of nanomaterial development, starting with various synthetic methods utilizing room temperature ionic liquids. It further examines modifications in size and morphology, surface functionalization with hydrogels and polymer brushes, and evaluations of toxicity and photoluminescence characteristics.

In the first part of the Thesis, the synthesis and characterization of multifunctional lanthanide-doped luminescent NPs and CSNPs, such as LaF_3:$Ce^{3+}Tb^{3+}$, TiO_2@SiO_2@LaF_3:$Ce^{3+}Tb^{3+}$, and $KSmF_4$:Ln^{3+} (Ln = Ce, Tb, and Eu) was achieved. The research then advanced to the development of hybrid sodium alginate hydrogel-lanthanide doped luminescent NP systems. Integrating LaF_3:$Ce^{3+}Tb^{3+}$ NPs into sodium alginate hydrogels crosslinked with Eu^{3+} ions resulted in materials with enhanced mechanical strength and luminescent properties.

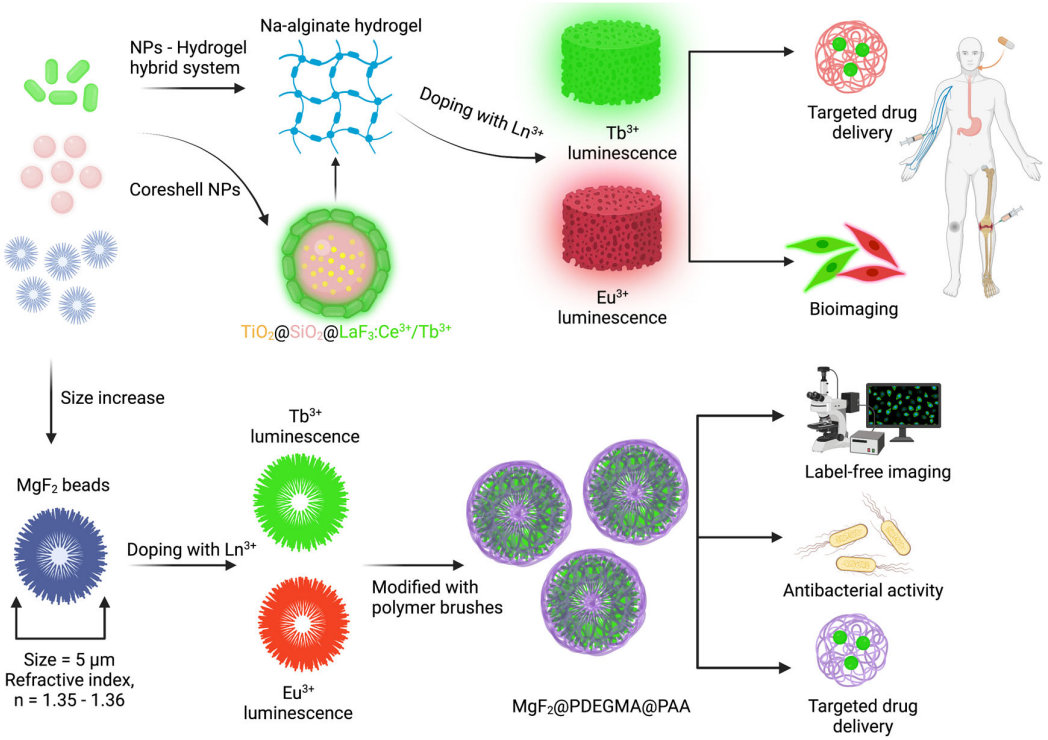

Figure 8: Schematic of NPs and MPs preparation, modification and possible future applications in biomedicine (created in BioRender app).

Further, this Thesis investigated the synthesis of spherical micrometer-sized MgF_2 beads for digital holography. Through various synthetic methods, including microwave heating, solvothermal, and hydrothermal techniques, the hydrothermal autoclave synthesis route was found to be most effective, yielding monodispersed MgF_2 beads of the desired size (5 µm ± 0.2 µm) and purity (> 99 %). These beads are well-suited for label-free quantitative *in vitro* live cell imaging.

The final part of the Thesis was focused on functionalizing these MgF_2 beads to enhance their potential biomedical applications. Doping the beads with Eu^{3+} and Tb^{3+} ions imparted strong photoluminescent properties, while surface modification with polymer brushes improved their colloidal stability and biocompatibility. The antibacterial efficacy of MgF_2 nanowhiskers against *E. coli* was also assessed, with results suggesting moderate antibacterial activity.

The results reported in this Thesis hint at promising avenues for future research. The optical properties of lanthanide-doped NPs and their integration into complex bioimaging and sensing platforms hold significant potential for enhancing diagnostic tools. Further studies should explore selected *in vivo* applications and the development of targeted imaging agents. Hydrogel-based therapeutics, particularly the biocompatible hydrogel-NP hybrid systems developed in this Thesis, provide valuable insights into how the photoluminescence of NPs can be modulated by the hydrogel's characteristics. The energy transfer from NP to the lanthanide crosslinker or vice versa offers a foundational understanding of how luminescence efficiency is regulated during hydrogel degradation. This should be further exploited using known drugs to investigate bioimaging at targeted drug delivery sections in cells and tissues. Future research should investigate the controlled release mechanisms of these hydrogels and their efficacy in delivering therapeutic agents *in vivo*.

In addition, basic DHM experiments with MgF_2 beads offer future perspectives to further develop label-free standards. DHM holds potential for high-throughput drug screening and toxicity testing, eliminating the need for labels or dyes, which simplifies and accelerates biomedical research. Its applications in studying disease mechanisms, cellular responses to treatments, and real-time monitoring of cellular interactions are expanding.

Furthermore, the integration of DHM into clinical diagnostics promises non-invasive, real-time monitoring of patient-derived cells, potentially revolutionizing diagnostic approaches and patient care.

The antibacterial properties of MgF_2 nanowhiskers should also be further investigated. Future studies should explore the mechanisms of action, optimize concentrations for maximum efficacy, test these materials against a broader range of bacterial strains and also investigate whether the different shapes of MgF_2 beads play a role in antibacterial activity.

In conclusion, the research conducted in this Thesis provides a foundation for developing refined multifunctional photoluminescent nanomaterials. The insights gained and methodologies developed offer valuable guidance for future work, thereby contributing in the long run to advancements in nanomaterials and ultimately medical diagnostics and therapeutics.

References

(1) Pallares, R. M.; Abergel, R. J. Transforming Lanthanide and Actinide Chemistry with Nanoparticles. *Nanoscale* **2020**, *12* (3), 1339–1348. https://doi.org/10.1039/C9NR09175K.

(2) Dong, H.; Du, S.-R.; Zheng, X.-Y.; Lyu, G.-M.; Sun, L.-D.; Li, L.-D.; Zhang, P.-Z.; Zhang, C.; Yan, C.-H. Lanthanide Nanoparticles: From Design toward Bioimaging and Therapy. *Chem. Rev.* **2015**, *115* (19), 10725–10815. https://doi.org/10.1021/acs.chemrev.5b00091.

(3) Kostelnik, T. I.; Orvig, C. Radioactive Main Group and Rare Earth Metals for Imaging and Therapy. *Chem. Rev.* **2019**, *119* (2), 902–956. https://doi.org/10.1021/acs.chemrev.8b00294.

(4) Ma, Q.; Wang, J.; Li, Z.; Lv, X.; Liang, L.; Yuan, Q. Recent Progress in Time-Resolved Biosensing and Bioimaging Based on Lanthanide-Doped Nanoparticles. *Small* **2019**, *15* (32), 1–22. https://doi.org/10.1002/smll.201804969.

(5) *Lanthanide Metal-Organic Frameworks*; Cheng, P., Ed.; Structure and Bonding; Springer Berlin Heidelberg: Berlin, Heidelberg, 2015; Vol. 163. https://doi.org/10.1007/978-3-662-45773-3.

(6) Li, X.; Chen, H.; Kirillov, A. M.; Xie, Y.; Shan, C.; Wang, B.; Shi, C.; Tang, Y. A Paper-Based Lanthanide Smart Device for Acid–Base Vapour Detection, Anti-Counterfeiting and Logic Operations. *Inorg. Chem. Front.* **2016**, *3* (8), 1014–1020. https://doi.org/10.1039/C6QI00164E.

(7) Hasegawa, Y.; Kitagawa, Y.; Nakanishi, T. Effective Photosensitized, Electrosensitized, and Mechanosensitized Luminescence of Lanthanide Complexes. *NPG Asia Mater.* **2018**, *10* (4), 52–70. https://doi.org/10.1038/s41427-018-0012-y.

(8) Zhou, J.; Leaño, J. L.; Liu, Z.; Jin, D.; Wong, K.; Liu, R.; Bünzli, J. G. Impact of Lanthanide Nanomaterials on Photonic Devices and Smart Applications. *Small* **2018**, *14* (40), 1–29. https://doi.org/10.1002/smll.201801882.

(9) Dieke, G. H.; Crosswhite, H. M. The Spectra of the Doubly and Triply Ionized Rare Earths. *Appl. Opt.* **1963**, *2* (7), 675–686. https://doi.org/10.1364/AO.2.000675.

(10) Kagan, H. B. Introduction: Frontiers in Lanthanide Chemistry. *Chem. Rev.* **2002**, *102* (6), 1805–1806. https://doi.org/10.1021/cr020014i.

(11) Mikhalyova, E. A.; Pavlishchuk, V. V. Modern Approaches to the Tuning of the Lanthanide(3+) Coordination Compound Luminescent Characteristics: A Review. *Theor. Exp. Chem.* **2019**, *55* (5), 293–315. https://doi.org/10.1007/s11237-019-09622-5.

(12) Bünzli, J.-C. G. Review: Lanthanide Coordination Chemistry: From Old Concepts to Coordination Polymers. *J. Coord. Chem.* **2014**, *67* (23), 3706–3733. https://doi.org/10.1080/00958972.2014.957201.

(13) Cotruvo, J. A. The Chemistry of Lanthanides in Biology: Recent Discoveries, Emerging Principles, and Technological Applications. *ACS Cent. Sci.* **2019**, *5* (9), 1496–1506. https://doi.org/10.1021/acscentsci.9b00642.

(14) Prajapati, K.; Prajapati, P.; Brahmbhatt, M.; Vora, J. A Review: Lanthanide Complexes and Their Biological Importance. Res. J. Life Sci. Bioinform. Pharm. Chem. Sci. **2018**, *12* (3), 45-67. https://doi.org/10.26479/2018.0405.56.

(15) Thoniyot, P.; Tan, M. J.; Karim, A. A.; Young, D. J.; Loh, X. J. Nanoparticle-Hydrogel Composites: Concept, Design, and Applications of These Promising, Multi-Functional Materials. *Adv. Sci.* **2015**, *2* (1), 1–13. https://doi.org/10.1002/advs.201400010.

(16) Thévenaz, D. C.; Monnier, C. A.; Balog, S.; Fiore, G. L. Luminescent Nanoparticles with Lanthanide-Containing Poly(ethylene glycol)–Poly(ε-caprolactone) Block Copolymers. *Biomacromolecules* **2014**, *15* (11), 3994–4001. https://doi.org/10.1021/bm501058n.

(17) Chen, P.; Li, Q.; Grindy, S.; Holten-Andersen, N. White-Light-Emitting Lanthanide Metallogels with Tunable Luminescence and Reversible Stimuli-Responsive Properties. *J. Am. Chem. Soc.* **2015**, *137* (36), 11590–11593. https://doi.org/10.1021/jacs.5b07394.

(18) Kim, H.; Young Chang, J. White Light Emission from a Mixed Organogel of Lanthanide(III)-Containing Organogelators. *RSC Adv* **2013**, *3* (6), 1774–1780. https://doi.org/10.1039/C2RA22908K.

(19) Kotova, O.; Daly, R.; dos Santos, C. M. G.; Boese, M.; Kruger, P. E.; Boland, J. J.; Gunnlaugsson, T. Europium-Directed Self-Assembly of a Luminescent Supramolecular Gel from a Tripodal Terpyridine-Based Ligand. *Angew. Chem. Int. Ed.* **2012**, *51* (29), 7208–7212. https://doi.org/10.1002/anie.201201506.

(20) Wang, M. X.; Yang, C. H.; Liu, Z. Q.; Zhou, J.; Xu, F.; Suo, Z.; Yang, J. H.; Chen, Y. M. Tough Photoluminescent Hydrogels Doped with Lanthanide. *Macromol. Rapid Commun.* **2015**, *36* (5), 465–471. https://doi.org/10.1002/marc.201400630.

(21) Martínez-Calvo, M.; Kotova, O.; Möbius, M. E.; Bell, A. P.; McCabe, T.; Boland, J. J.; Gunnlaugsson, T. Healable Luminescent Self-Assembly Supramolecular Metallogels Possessing Lanthanide (Eu/Tb) Dependent Rheological and Morphological Properties. *J. Am. Chem. Soc.* **2015**, *137* (5), 1983–1992. https://doi.org/10.1021/ja511799n.

(22) Chang, C.; Peng, J.; Zhang, L.; Pang, D.-W. Strongly Fluorescent Hydrogels with Quantum Dots Embedded in Cellulose Matrices. *J. Mater. Chem.* **2009**, *19* (41), 7771–7776. https://doi.org/10.1039/b908835k.

(23) Hu, X.-H.; Liu, J.-D.; Du, X.-Y.; Cheng, R.; Li, Q.; Chen, S. A Facile Synthesis of Self-Healing Hydrogels toward Flexible Quantum Dot-Based Luminescent Solar Concentrators and White LEDs. *J. Mater. Chem. C* **2019**, *7* (35), 10988–10995. https://doi.org/10.1039/C9TC03215K.

(24) Truskewycz, A.; Beker, S.; Ball, A. S.; Cole, I. Photoluminescence Measurements of Carbon Quantum Dots within Three-Dimensional Hydrogel Matrices Using a High Throughput 96 Well Plate Method. *MethodsX* **2019**, *6*, 437–441. https://doi.org/10.1016/j.mex.2019.02.014.

(25) Zhang, L.; Jean, S. R.; Ahmed, S.; Aldridge, P. M.; Li, X.; Fan, F.; Sargent, E. H.; Kelley, S. O. Multifunctional Quantum Dot DNA Hydrogels. *Nat. Commun.* **2017**, *8* (1), 1–9. https://doi.org/10.1038/s41467-017-00298-w.

(26) Shen, K.-H.; Lu, C.-H.; Kuo, C.-Y.; Li, B.-Y.; Yeh, Y.-C. Smart near Infrared-Responsive Nanocomposite Hydrogels for Therapeutics and Diagnostics. *J. Mater. Chem. B* **2021**, 9 (35), 7100–7116. https://doi.org/10.1039/D1TB00980J.

(27) Christadore, L.; Grinstaff, M.; Schaus, S. Fluorescent Dendritic Micro-Hydrogels: Synthesis, Analysis and Use in Single-Cell Detection. *Molecules* **2018**, *23* (4), 1–10. https://doi.org/10.3390/molecules23040936.

(28) Zhang, C.; Li, Y.; Xue, X.; Chu, P.; Liu, C.; Yang, K.; Jiang, Y.; Chen, W.-Q.; Zou, G.; Liang, X.-J. A Smart pH-Switchable Luminescent Hydrogel. *Chem. Commun.* **2015**, *51* (20), 4168–4171. https://doi.org/10.1039/C4CC09861G.

(29) Li, Z.; Chen, H.; Li, B.; Xie, Y.; Gong, X.; Liu, X.; Li, H.; Zhao, Y. Photoresponsive Luminescent Polymeric Hydrogels for Reversible Information Encryption and Decryption. *Adv. Sci.* **2019**, *6* (21), 1–7 https://doi.org/10.1002/advs.201901529.

(30) Pandey, P. K.; Preeti; Rawat, K.; Prasad, T.; Bohidar, H. B. Multifunctional, Fluorescent DNA-Derived Carbon Dots for Biomedical Applications: Bioimaging, Luminescent DNA Hydrogels, and Dopamine Detection. *J. Mater. Chem. B* **2020**, *8* (6), 1277–1289. https://doi.org/10.1039/C9TB01863H.

(31) Xie, S.; Ren, B.; Gong, G.; Zhang, D.; Chen, Y.; Xu, L.; Zhang, C.; Xu, J.; Zheng, J. Lanthanide-Doped Upconversion Nanoparticle-Cross-Linked Double-Network Hydrogels with Strong Bulk/Interfacial Toughness and Tunable Full-Color Fluorescence for Bioimaging and Biosensing. *ACS Appl. Nano Mater.* **2020**, *3* (3), 2774–2786. https://doi.org/10.1021/acsanm.0c00105.

(32) Park, H.-I.; Park, S.-Y. Smart Fluorescent Hydrogel Glucose Biosensing Microdroplets with Dual-Mode Fluorescence Quenching and Size Reduction. *ACS Appl. Mater. Interfaces* **2018**, *10* (36), 30172–30179. https://doi.org/10.1021/acsami.8b10768.

(33) Wang, Y.; Liang, Z.; Su, Z.; Zhang, K.; Ren, J.; Sun, R.; Wang, X. All-Biomass Fluorescent Hydrogels Based on Biomass Carbon Dots and Alginate/Nanocellulose for Biosensing. *ACS Appl. Bio Mater.* **2018**, *1* (5), 1398–1407. https://doi.org/10.1021/acsabm.8b00348.

(34) Song, H.; Zhang, Y.; Wang, S.; Huang, K.; Luo, Y.; Zhang, W.; Xu, W. Label-Free Polygonal-Plate Fluorescent-Hydrogel Biosensor for Ultrasensitive microRNA Detection. *Sens. Actuators B Chem.* **2020**, *306* (127554), 1–10. https://doi.org/10.1016/j.snb.2019.127554.

(35) Qasemi, S.; Ghaemy, M. Highly Sensitive and Strongly Fluorescent Gum Tragacanth Based Superabsorbent Hydrogel as a New Biosensor for Glucose Optical Detection. *J. Mater. Chem. C* **2020**, *8* (12), 4148–4156. https://doi.org/10.1039/C9TC07014A.

(36) Wang, X.; Wolfbeis, O. S.; Meier, R. J. Luminescent Probes and Sensors for Temperature. *Chem. Soc. Rev.* **2013**, *42* (19), 7834–7869. https://doi.org/10.1039/c3cs60102a.

(37) Wang, T.; Li, P.; Li, H. Color-Tunable Luminescence of Organoclay-Based Hybrid Materials Showing Potential Applications in White LED and Thermosensors. *ACS Appl. Mater. Interfaces* **2014**, *6* (15), 12915–12921. https://doi.org/10.1021/am5028555.

(38) Kang, X.; Cheng, Z.; Yang, D.; Ma, P.; Shang, M.; Peng, C.; Dai, Y.; Lin, J. Design and Synthesis of Multifunctional Drug Carriers Based on Luminescent Rattle-Type Mesoporous Silica Microspheres with a Thermosensitive Hydrogel as a Controlled Switch. *Adv. Funct. Mater.* **2012**, *22* (7), 1470–1481. https://doi.org/10.1002/adfm.201102746.

(39) McCoy, C. P.; Stomeo, F.; Plush, S. E.; Gunnlaugsson, T. Soft Matter pH Sensing: From Luminescent Lanthanide pH Switches in Solution to Sensing in Hydrogels. *Chem. Mater.* **2006**, *18* (18), 4336–4343. https://doi.org/10.1021/cm060603v.

(40) Sun, L.-N.; Peng, H.; Stich, M. I. J.; Achatz, D.; Wolfbeis, O. S. pH Sensor Based on Upconverting Luminescent Lanthanide Nanorods. *Chem. Commun.* **2009**, *33* (24), 5000–5002. https://doi.org/10.1039/b907822c.

(41) Kharlampieva, E.; Kozlovskaya, V.; Zavgorodnya, O.; Lilly, G. D.; Kotov, N. A.; Tsukruk, V. V. pH-Responsive Photoluminescent LbL Hydrogels with Confined Quantum Dots. *Soft Matter* **2010**, *6* (4), 800–807. https://doi.org/10.1039/B917845G.

(42) Ye, W.; Zhu, L.; Xia, S.; Zhang, X. Dual pH-/Temperature-Responsive and Fluorescent Hydrogel for Controlled Drug Delivery. *J. Polym. Eng.* **2018**, *38* (4), 371–379. https://doi.org/10.1515/polyeng-2016-0228.

(43) Dong, X.; Wei, C.; Chen, H.; Qin, J.; Liang, J.; Kong, D.; Liu, T.; Lv, F. Real-Time Imaging Tracking of a Dual Fluorescent Drug Delivery System Based on Zinc Phthalocyanine-Incorporated Hydrogel. *ACS Biomater. Sci. Eng.* **2016**, *2* (11), 2001–2010. https://doi.org/10.1021/acsbiomaterials.6b00403.

(44) Sershen, S. R.; Westcott, S. L.; Halas, N. J.; West, J. L. Independent Optically Addressable Nanoparticle-Polymer Optomechanical Composites. *Appl. Phys. Lett.* **2002**, *80* (24), 4609–4611. https://doi.org/10.1063/1.1481536.

(45) Wang, D.; Tan, Y.; Xu, H.; Wang, X.; Yu, L.; Xiao, Z.; Wang, J.; Xu, S. A Tough and Fluorescent Dual Nanocomposite Hydrogel Based on SiO_2@TiO_2 Core-Shell Nanoparticles. *Appl. Surf. Sci.* **2019**, *467–468* (2019), 588–595. https://doi.org/10.1016/j.apsusc.2018.10.208.

(46) Vimala, K.; Samba Sivudu, K.; Murali Mohan, Y.; Sreedhar, B.; Mohana Raju, K. Controlled Silver Nanoparticles Synthesis in Semi-Hydrogel Networks of Poly(Acrylamide) and Carbohydrates: A Rational Methodology for Antibacterial Application. *Carbohydr. Polym.* **2009**, *75* (3), 463–471. https://doi.org/10.1016/j.carbpol.2008.08.009.

(47) *Lanthanide Luminescence: Photophysical, Analytical and Biological Aspects*; Hänninen, P., Härmä, H., Eds.; Springer Series on Fluorescence; Springer Berlin Heidelberg: Berlin, Heidelberg, 2011; Vol. 7. https://doi.org/10.1007/978-3-642-21023-5.

(48) de Bettencourt-Dias, A. Book Review of Lanthanide Luminescence: Photophysical, Analytical, and Biological Aspects. *J. Am. Chem. Soc.* **2011**, *133* (48), 19566–19566. https://doi.org/10.1021/ja210402p.

(49) Nicholas, H. M.; Mills, D. P. Lanthanides: Divalent Organometallic Chemistry. In *Encyclopedia of Inorganic and Bioinorganic Chemistry*; Scott, R. A., Ed.; John Wiley & Sons, Ltd: Chichester, UK, 2017; pp 1–10. https://doi.org/10.1002/9781119951438.eibc2453.

(50) Bochkarev, M. N. Molecular Compounds of “New” Divalent Lanthanides. *Coord. Chem. Rev.* **2004**, *248* (9–10), 835–851. https://doi.org/10.1016/j.ccr.2004.04.004.

(51) Suta, M.; Wickleder, C. Synthesis, Spectroscopic Properties and Applications of Divalent Lanthanides Apart from Eu^{2+}. *J. Lumin.* **2019**, *210*, 210–238. https://doi.org/10.1016/j.jlumin.2019.02.031.

(52) da Silva, F. F.; de Menezes, F. L.; da Luz, L. L.; Alves, S. Supramolecular Luminescent Hydrogels Based on β-Amino Acid and Lanthanide Ions Obtained by Self-Assembled Hydrothermal Reactions. *New J Chem* **2014**, *38* (3), 893–896. https://doi.org/10.1039/C3NJ01560B.

(53) Nesmerak, K. Lanthanide/Actinide Toxicity. In *Encyclopedia of Metalloproteins*; Kretsinger, R. H., Uversky, V. N., Permyakov, E. A., Eds.; Springer New York: New York, NY, 2013; pp 1098–1103. https://doi.org/10.1007/978-1-4614-1533-6_151.

(54) Pałasz, A.; Czekaj, P. Toxicological and Cytophysiological Aspects of Lanthanides Action. *Acta Biochim. Pol.* **2000**, *47* (4), 1107–1114. https://doi.org/10.18388/abp.2000_3963.

(55) Ma, Q.; Zhang, M.; Yao, C.; Du, Y.; Yang, D. Supramolecular Hydrogel with Luminescence Tunablility and Responsiveness Based on Co-Doped Lanthanide and Deoxyguanosine Complex. *Chem. Eng. J.* **2020**, *394* (124894), 1–9. https://doi.org/10.1016/j.cej.2020.124894.

(56) Zhou, B.; Guo, J.; Yang, C.; Kong, L. Upconversion-Luminescent Hydrogel Optical Probe for in Situ Dopamine Monitoring. *Photonics Res.* **2020**, *8* (11), 1800–1807. https://doi.org/10.1364/PRJ.403223.

(57) Gulzar, A.; Xu, J.; Yang, P.; He, F.; Xu, L. Upconversion Processes: Versatile Biological Applications and Biosafety. *Nanoscale* **2017**, *9* (34), 12248–12282. https://doi.org/10.1039/C7NR01836C.

(58) Mohanty, S.; Lederer, M.; Premcheska, S.; Rijckaert, H.; De Buysser, K.; Bruneel, E.; Skirtach, A.; Van Hecke, K.; Kaczmarek, A. M. Exploring the Potential of Lanthanide-Doped Oxyfluoride Materials for Bright Green Upconversion and Their Promising Applications towards Temperature Sensing and Drug Delivery. *J. Mater. Chem. C* **2024**, *31* (12) 11785–11802. https://doi.org/10.1039/D4TC01740D.

(59) Zhu, L.; Liu, S.; Hui, Y.; Zou, B.; Cao, X. Synthesis and Fluorescence Properties of LaF_3: Tb^{3+} Phosphors via Ultrasonic-Assisted Ionic Liquid Method. *Nano* **2014**, *9* (07), 1450082–9. https://doi.org/10.1142/S1793292014500829.

(60) Zhang, C.; Chen, J.; Zhou, Y.; Li, D. Ionic Liquid-Based “All-in-One” Synthesis and Photoluminescence Properties of Lanthanide Fluorides. *J. Phys. Chem. C* **2008**, *112* (27), 10083–10088. https://doi.org/10.1021/jp802083q.

(61) Richter, K.; Lorbeer, C.; Mudring, A.-V. A Novel Approach to Prepare Optically Active Ion Doped Luminescent Materials via Electron Beam Evaporation into Ionic Liquids. *Chem. Commun.* **2015**, *51* (1), 114–117. https://doi.org/10.1039/C4CC05817H.

(62) Li, C.; Ma, P.; Yang, P.; Xu, Z.; Li, G.; Yang, D.; Peng, C.; Lin, J. Fine Structural and Morphological Control of Rare Earth Fluorides REF_3 (RE = La–Lu, Y) Nano/Microcrystals: Microwave-Assisted Ionic Liquid Synthesis, Magnetic and Luminescent Properties. *CrystEngComm* **2011**, *13* (3), 1003–1013. https://doi.org/10.1039/C0CE00186D.

(63) Guricová, M.; Pinc, J.; Malinčik, J.; Rak, J.; Kuchař, M.; Bartůněk, V. Rare Earth Nanofluorides: Synthesis Using Ionic Liquids. *Rev. Inorg. Chem.* **2019**, *39* (2), 77–90. https://doi.org/10.1515/revic-2018-0016.

(64) Krossing, I.; Slattery, J. M.; Daguenet, C.; Dyson, P. J.; Oleinikova, A.; Weingärtner, H. Why Are Ionic Liquids Liquid? A Simple Explanation Based on Lattice and Solvation Energies. *J. Am. Chem. Soc.* **2006**, *128* (41), 13427–13434. https://doi.org/10.1021/ja0619612.

(65) Ding, Y.-S.; Zha, M.; Zhang, J.; Wang, S.-S. Synthesis, Characterization and Properties of Geminal Imidazolium Ionic Liquids. *Colloids Surf. Physicochem. Eng. Asp.* **2007**, *298* (3), 201–205. https://doi.org/10.1016/j.colsurfa.2006.10.063.

(66) Huddleston, J. G.; Visser, A. E.; Reichert, W. M.; Willauer, H. D.; Broker, G. A.; Rogers, R. D. Characterization and Comparison of Hydrophilic and Hydrophobic Room Temperature Ionic Liquids Incorporating the Imidazolium Cation. *Green Chem.* **2001**, *3* (4), 156–164. https://doi.org/10.1039/b103275p.

(67) Seddon, K. R. Ionic Liquids for Clean Technology. *J. Chem. Technol. Biotechnol.* **1997**, *68* (4), 351–356. https://doi.org/10.1002/(SICI)1097-4660(199704)68:4<351::AID-JCTB613>3.0.CO;2-4.

(68) Blesic, M.; Marques, M. H.; Plechkova, N. V.; Seddon, K. R.; Rebelo, L. P. N.; Lopes, A. Self-Aggregation of Ionic Liquids: Micelle Formation in Aqueous Solution. *Green Chem.* **2007**, *9* (5), 481–490. https://doi.org/10.1039/b615406a.

(69) Mellein, B. R.; Aki, S. N. V. K.; Ladewski, R. L.; Brennecke, J. F Solvatochromic Studies of Ionic Liquid/Organic Mixtures. *J. Phys. Chem. B* **2007**, *111* (1), 131–138. https://doi.org/10.1021/jp0653353.

(70) Lunstroot, K.; Baeten, L.; Nockemann, P.; Martens, J.; Verlooy, P.; Ye, X.; Görller-Walrand, C.; Binnemans, K.; Driesen, K. Luminescence of LaF_3 :Ln^{3+} Nanocrystal Dispersions in Ionic Liquids. *J. Phys. Chem. C* **2009**, *113* (31), 13532–13538. https://doi.org/10.1021/jp9015118.

(71) Bartůněk, V.; Jakeš, V.; Král, V.; Rak, J. Lanthanum Trifluoride Nanoparticles Prepared Using Ionic Liquids. *J. Fluor. Chem.* **2012**, *135*, 358–361. https://doi.org/10.1016/j.jfluchem.2011.09.003.

(72) Xu, J.-S.; Zhu, Y.-J. Microwave-Assisted Ionic Liquid Solvothermal Rapid Synthesis of Hollow Microspheres of Alkaline Earth Metal Fluorides (MF_2, M = Mg, Ca, Sr). *CrystEngComm* **2012**, *14* (8), 2630–2634. https://doi.org/10.1039/C2CE06619J.

(73) Weber, M. J. Probabilities for Radiative and Nonradiative Decay of Er^{3+} in LaF_3. *Phys. Rev.* **1967**, *157* (2), 262–272. https://doi.org/10.1103/PhysRev.157.262.

(74) Zhou, J.; Wu, Z.; Zhang, Z.; Liu, W.; Dang, H. Study on an Antiwear and Extreme Pressure Additive of Surface Coated LaF3 Nanoparticles in Liquid Paraffin. *Wear* **2001**, *249* (5–6), 333–337. https://doi.org/10.1016/S0043-1648(00)00547-0.

(75) Stouwdam, J. W.; van Veggel, F. C. J. M. Near-Infrared Emission of Redispersible Er^{3+}, Nd^{3+}, and Ho^{3+} Doped LaF_3 Nanoparticles. *Nano Lett.* **2002**, *2* (7), 733–737. https://doi.org/10.1021/nl025562q.

(76) Liu, Y.; Chen, W.; Wang, S.; Joly, A. G.; Westcott, S.; Woo, B. K. X-Ray Luminescence of LaF_3:Tb^{3+} and LaF_3:Ce^{3+},Tb^{3+} Water-Soluble Nanoparticles. *J. Appl. Phys.* **2008**, *103* (6), 1–7. https://doi.org/10.1063/1.2890148.

(77) Liu, Y.; Chen, W.; Wang, S.; Joly, A. G. Investigation of Water-Soluble X-Ray Luminescence Nanoparticles for Photodynamic Activation. *Appl. Phys. Lett.* **2008**, *92* (4), 1–3. https://doi.org/10.1063/1.2835701.

(78) Mi, C.-C.; Tian, Z.; Han, B.; Mao, C.; Xu, S. Microwave-Assisted One-Pot Synthesis of Water-Soluble Rare-Earth Doped Fluoride Luminescent Nanoparticles with Tunable Colors. *J. Alloys Compd.* **2012**, *525*, 154–158. https://doi.org/10.1016/j.jallcom.2012.02.095.

(79) Hebecker, Ch. Neue ternäre Fluoride der Lanthaniden vom Typ $KMeF_4$. *Naturwissenschaften* **1973**, *60* (11), 518–519. https://doi.org/10.1007/BF00603258.

(80) Zhang, F.; Li, J.; Shan, J.; Xu, L.; Zhao, D. Shape, Size, and Phase-Controlled Rare-Earth Fluoride Nanocrystals with Optical Up-Conversion Properties. *Chem. Eur. J.* **2009**, *15* (41), 11010–11019. https://doi.org/10.1002/chem.200900861.

(81) Cao, C.; Yang, H. K.; Chung, J. W.; Moon, B. K.; Choi, B. C.; Jeong, J. H.; Kim, K. H. Hydrothermal Synthesis and Optical Properties of Eu^{3+} Doped $NaREF_4$ (RE=Y, Gd), LnF_3 (Ln=Y, La), and $YF_3 \cdot 1.5NH_3$ Micro/Nanocrystals. *Mater. Res. Bull.* **2011**, *46* (10), 1553–1559. https://doi.org/10.1016/j.materresbull.2011.06.026.

(82) Xu, Z.; Li, C.; Yang, P.; Zhang, C.; Huang, S.; Lin, J. Rare Earth Fluorides Nanowires/Nanorods Derived from Hydroxides: Hydrothermal Synthesis and Luminescence Properties. *Cryst. Growth Des.* **2009**, *9* (11), 4752–4758. https://doi.org/10.1021/cg900604j.

(83) Fedorov, P. P.; Mayakova, M. N.; Kuznetsov, S. V.; Voronov, V. V.; Ermakov, R. P.; Samarina, K. S.; Popov, A. I.; Osiko, V. V. Co-Precipitation of Yttrium and Barium Fluorides from Aqueous Solutions. *Mater. Res. Bull.* **2012**, *47* (7), 1794–1799. https://doi.org/10.1016/j.materresbull.2012.03.027.

(84) Zhou, X.; Wang, Z.; Li, S.; Shan, S.; Wang, X. Formation and Luminescence of Sodium Rare Earth Fluoride Nanocrystals in the Presence of Chelators. *J. Nanosci. Nanotechnol.* **2010**, *10* (3), 2193–2202. https://doi.org/10.1166/jnn.2010.2134.

(85) Wang, F.; Deng, R.; Liu, X. Preparation of Core-Shell $NaGdF_4$ Nanoparticles Doped with Luminescent Lanthanide Ions to Be Used as Upconversion-Based Probes. *Nat. Protoc.* **2014**, *9* (7), 1634–1644. https://doi.org/10.1038/nprot.2014.111.

(86) Yu, Y.; Zhihuai, S.; Chen, S.; Bian, C.; Chen, W.; Xue, G. Facile Synthesis of Polyaniline−Sodium Alginate Nanofibers. *Langmuir* **2006**, *22* (8), 3899–3905. https://doi.org/10.1021/la051911v.

(87) Sepand, M. R.; Ranjbar, S.; Kempson, I. M.; Akbariani, M.; Muganda, W. C. A.; Müller, M.; Ghahremani, M. H.; Raoufi, M. Targeting Non-Apoptotic Cell Death in Cancer Treatment by Nanomaterials: Recent Advances and Future Outlook. *Nanomedicine Nanotechnol. Biol. Med.* **2020**, *29* (102243), 1–20. https://doi.org/10.1016/j.nano.2020.102243.

(88) Gmeiner, W. H.; Ghosh, S. Nanotechnology for Cancer Treatment. *Nanotechnol. Rev.* **2014**, *3* (2), 111-122. https://doi.org/10.1515/ntrev-2013-0013.

(89) Caracciolo, G.; Vali, H.; Moore, A.; Mahmoudi, M. Challenges in Molecular Diagnostic Research in Cancer Nanotechnology. *Nano Today* **2019**, *27* (5), 6–10. https://doi.org/10.1016/j.nantod.2019.06.001.

(90) Ghosh Chaudhuri, R.; Paria, S. Core/Shell Nanoparticles: Classes, Properties, Synthesis Mechanisms, Characterization, and Applications. *Chem. Rev.* **2012**, *112* (4), 2373–2433. https://doi.org/10.1021/cr100449n.

(91) Paściak, A.; Pilch-Wróbel, A.; Marciniak, Ł.; Schuck, P. J.; Bednarkiewicz, A. Standardization of Methodology of Light-to-Heat Conversion Efficiency Determination for Colloidal Nanoheaters. *ACS Appl. Mater. Interfaces* **2021**, *13* (37), 44556–44567. https://doi.org/10.1021/acsami.1c12409.

(92) Wysokińska, E.; Cichos, J.; Zioło, E.; Bednarkiewicz, A.; Strządała, L.; Karbowiak, M.; Hreniak, D.; Kałas, W. Cytotoxic Interactions of Bare and Coated $NaGdF_4:Yb^{3+}:Er^{3+}$ Nanoparticles with Macrophage and Fibroblast Cells. *Toxicol. In Vitro* **2016**, *32*, (2), 16–25. https://doi.org/10.1016/j.tiv.2015.11.021.

(93) Whitesides, G. M. Soft Robotics. *Angew. Chem. Int. Ed.* **2018**, *57* (16), 4258–4273. https://doi.org/10.1002/anie.201800907.

(94) Williams, D. F. Challenges With the Development of Biomaterials for Sustainable Tissue Engineering. *Front. Bioeng. Biotechnol.* **2019**, *7* (127), 1–10. https://doi.org/10.3389/fbioe.2019.00127.

(95) Adams, F.; Barbante, C. Spectroscopic Imaging. In *Comprehensive Analytical Chemistry*; Elsevier, 2015; Vol. 69, pp 339–384. https://doi.org/10.1016/B978-0-444-63439-9.00009-8.

(96) Alford, R.; Simpson, H. M.; Duberman, J.; Hill, G. C.; Ogawa, M.; Regino, C.; Kobayashi, H.; Choyke, P. L. Toxicity of Organic Fluorophores Used in Molecular Imaging: Literature Review. *Mol. Imaging* **2009**, *8* (6), 341–354. https://doi.org/10.2310/7290.2009.00031.

(97) Mehwish, N.; Dou, X.; Zhao, Y.; Feng, C.-L. Supramolecular Fluorescent Hydrogelators as Bio-Imaging Probes. *Mater. Horiz.* **2019**, *6* (1), 14–44. https://doi.org/10.1039/C8MH01130C.

(98) Zuo, Y.; Gou, Z.; Zhang, Y.; Yang, T.; Lin, W. Thermally Responsive Materials for Bioimaging. *Chem. Asian J.* **2019**, *14* (1), 67–75. https://doi.org/10.1002/asia.201801305.

(99) Wickleder, M. 2.1 Halides of Trivalent Lanthanides. In *Rare Earth Chemistry*; Pöttgen, R., Jüstel, T., Strassert, C. A., Eds.; De Gruyter, 2020; pp 99–116. https://doi.org/10.1515/9783110654929-009.

(100) Wells, A. F. *Structural Inorganic Chemistry*, Fifth edition.; Oxford classic texts in the physical sciences; Clarendon Press: Oxford, 2012.

(101) Le, Q. M.; Tran, T. H.; Nguyen, T. H.; Hoang, T. K.; Nguyen, T. B.; Do, K. T.; Tran, K. A.; Nguyen, D. H.; Le, T. L.; Nguyen, T. Q.; Dang, M. D.; Thu Nguyen, N. A.; Nguyen, V. M. Development of a Fluorescent Label Tool Based on Lanthanide Nanophosphors for Viral Biomedical Application. *Adv. Nat. Sci. Nanosci. Nanotechnol.* **2012**, *3* (3), 035003–35004. https://doi.org/10.1088/2043-6262/3/3/035003.

(102) Demchenko, A. P. Photobleaching of Organic Fluorophores: Quantitative Characterization, Mechanisms, Protection. *Methods Appl. Fluoresc.* **2020**, *8* (2), 022001–024001. https://doi.org/10.1088/2050-6120/ab7365.

(103) Cho, U.; Chen, J. K. Lanthanide-Based Optical Probes of Biological Systems. *Cell Chem. Biol.* **2020**, *27* (8), 921–936. https://doi.org/10.1016/j.chembiol.2020.07.009.

(104) Vogler, A.; Kunkely, H. Excited State Properties of Lanthanide Complexes: Beyond Ff States. *Inorganica Chim. Acta* **2006**, *359* (12), 4130–4138. https://doi.org/10.1016/j.ica.2006.05.025.

(105) Barraza, R.; Allen, M. Lanthanide Luminescence in Visible-Light-Promoted Photochemical Reactions. *Molecules* **2020**, *25* (17), 1–20. https://doi.org/10.3390/molecules25173892.

(106) Dorenbos, P. F d Transition Energies of Divalent Lanthanides in Inorganic Compounds. *J. Phys. Condens. Matter* **2003**, *15* (3), 575–594. https://doi.org/10.1088/0953-8984/15/3/322.

(107) Dorenbos, P. Systematic Behaviour in Trivalent Lanthanide Charge Transfer Energies. *J. Phys. Condens. Matter* **2003**, *15* (49), 8417–8434. https://doi.org/10.1088/0953-8984/15/49/018.

(108) Bünzli, J. G. Rising Stars in Science and Technology: Luminescent Lanthanide Materials. *Eur. J. Inorg. Chem.* **2017**, *2017* (44), 5058–5063. https://doi.org/10.1002/ejic.201701201.

(109) Dong, H.; Du, S.-R.; Zheng, X.-Y.; Lyu, G.-M.; Sun, L.-D.; Li, L.-D.; Zhang, P.-Z.; Zhang, C.; Yan, C.-H. Lanthanide Nanoparticles: From Design toward Bioimaging and Therapy. *Chem. Rev.* **2015**, *115* (19), 10725–10815. https://doi.org/10.1021/acs.chemrev.5b00091.

(110) Hifumi, H.; Yamaoka, S.; Tanimoto, A.; Citterio, D.; Suzuki, K. Gadolinium-Based Hybrid Nanoparticles as a Positive MR Contrast Agent. *J. Am. Chem. Soc.* **2006**, *128* (47), 15090–15091. https://doi.org/10.1021/ja066442d.

(111) Korsvik, C.; Patil, S.; Seal, S.; Self, W. T. Superoxide Dismutase Mimetic Properties Exhibited by Vacancy Engineered Ceria Nanoparticles. *Chem. Commun.* **2007**, *10* (13), 1056–1058. https://doi.org/10.1039/b615134e.

(112) Liu, S.; An, Z.; Zhou, B. Optical Multiplexing of Upconversion in Nanoparticles towards Emerging Applications. *Chem. Eng. J.* **2023**, *452* (139649), 1–18. https://doi.org/10.1016/j.cej.2022.139649.

(113) Zhao, H.; Shu, G.; Zhu, J.; Fu, Y.; Gu, Z.; Yang, D. Persistent Luminescent Metal-Organic Frameworks with Long-Lasting near Infrared Emission for Tumor Site Activated Imaging and Drug Delivery. *Biomaterials* **2019**, *217* (119332), 1–8. https://doi.org/10.1016/j.biomaterials.2019.119332.

(114) Zhao, H.; Liu, C.; Gu, Z.; Dong, L.; Li, F.; Yao, C.; Yang, D. Persistent Luminescent Nanoparticles Containing Hydrogels for Targeted, Sustained, and Autofluorescence-Free Tumor Metastasis Imaging. *Nano Lett.* **2020**, *20* (1), 252–260. https://doi.org/10.1021/acs.nanolett.9b03755.

(115) Dieke, G. H.; Crosswhite, H. M. The Spectra of the Doubly and Triply Ionized Rare Earths. *Appl. Opt.* **1963**, *2* (7), 675–686. https://doi.org/10.1364/AO.2.000675.

(116) Ma, Q.; Wang, J.; Li, Z.; Lv, X.; Liang, L.; Yuan, Q. Recent Progress in Time-Resolved Biosensing and Bioimaging Based on Lanthanide-Doped Nanoparticles. *Small* **2019**, *15* (32), 1–22. https://doi.org/10.1002/smll.201804969.

(117) Ferro-Flores, G.; Ancira-Cortez, A.; Ocampo-García, B.; Meléndez-Alafort, L. Molecularly Targeted Lanthanide Nanoparticles for Cancer Theranostic Applications. *Nanomaterials* **2024**, *14* (3), 1–25. https://doi.org/10.3390/nano14030296.

(118) Li, S.; Wei, J.; Yao, Q.; Song, X.; Xie, J.; Yang, H. Emerging Ultrasmall Luminescent Nanoprobes for *in Vivo* Bioimaging. *Chem. Soc. Rev.* **2023**, *52* (5), 1672–1696. https://doi.org/10.1039/D2CS00497F.

(119) Cardoso Dos Santos, M.; Runser, A.; Bartenlian, H.; Nonat, A. M.; Charbonnière, L. J.; Klymchenko, A. S.; Hildebrandt, N.; Reisch, A. Lanthanide-Complex-Loaded Polymer Nanoparticles for Background-Free Single-Particle and Live-Cell Imaging. *Chem. Mater.* **2019**, *31* (11), 4034–4041. https://doi.org/10.1021/acs.chemmater.9b00576.

(120) Ferro-Flores, G.; Ancira-Cortez, A.; Ocampo-García, B.; Meléndez-Alafort, L. Molecularly Targeted Lanthanide NPs for Cancer Theranostic Applications. *Nanomaterials* **2024**, *14* (3), 1–25. https://doi.org/10.3390/nano14030296.

(121) Zhang, Q.; O'Brien, S.; Grimm, J. Biomedical Applications of Lanthanide Nanomaterials, for Imaging, Sensing and Therapy. *Nanotheranostics* **2022**, *6* (2), 184–194. https://doi.org/10.7150/ntno.65530.

(122) Xu, W.; Kattel, K.; Park, J. Y.; Chang, Y.; Kim, T. J.; Lee, G. H. Paramagnetic Nanoparticle T1 and T2 MRI Contrast Agents. *Phys. Chem. Chem. Phys.* **2012**, *14* (37), 12687–12700. https://doi.org/10.1039/c2cp41357d.

(123) Narmani, A.; Farhood, B.; Haghi-Aminjan, H.; Mortezazadeh, T.; Aliasgharzadeh, A.; Mohseni, M.; Najafi, M.; Abbasi, H. Gadolinium Nanoparticles as Diagnostic and Therapeutic Agents: Their Delivery Systems in Magnetic Resonance Imaging and Neutron Capture Therapy. *J. Drug Deliv. Sci. Technol.* **2018**, *44*, 457–466. https://doi.org/10.1016/j.jddst.2018.01.011.

(124) Debroye, E.; Parac-Vogt, T. N. Towards Polymetallic Lanthanide Complexes as Dual Contrast Agents for Magnetic Resonance and Optical Imaging. *Chem Soc Rev* **2014**, *43* (23), 8178–8192. https://doi.org/10.1039/C4CS00201F.

(125) Caravan, P. Strategies for Increasing the Sensitivity of Gadolinium Based MRI Contrast Agents. *Chem. Soc. Rev.* **2006**, *35* (6), 512–523. https://doi.org/10.1039/b510982p.

(126) Sun, L.-D.; Wang, Y.-F.; Yan, C.-H. Paradigms and Challenges for Bioapplication of Rare Earth Upconversion Luminescent Nanoparticles: Small Size and Tunable Emission/Excitation Spectra. *Acc. Chem. Res.* **2014**, *47* (4), 1001–1009. https://doi.org/10.1021/ar400218t.

(127) Wang, F.; Liu, X. Recent Advances in the Chemistry of Lanthanide-Doped Upconversion Nanocrystals. *Chem. Soc. Rev.* **2009**, *38* (4), 976–989. https://doi.org/10.1039/b809132n.

(128) Osuchowski, M.; Osuchowski, F.; Latos, W.; Kawczyk-Krupka, A. The Use of Upconversion Nanoparticles in Prostate Cancer Photodynamic Therapy. *Life* **2021**, *11* (4), 1–11. https://doi.org/10.3390/life11040360.

(129) Heckert, E. G.; Karakoti, A. S.; Seal, S.; Self, W. T. The Role of Cerium Redox State in the SOD Mimetic Activity of Nanoceria. *Biomaterials* **2008**, *29* (18), 2705–2709. https://doi.org/10.1016/j.biomaterials.2008.03.014.

(130) Pirmohamed, T.; Dowding, J. M.; Singh, S.; Wasserman, B.; Heckert, E.; Karakoti, A. S.; King, J. E. S.; Seal, S.; Self, W. T. Nanoceria Exhibit Redox State-Dependent Catalase Mimetic Activity. *Chem. Commun.* **2010**, *46* (16), 2736–2738. https://doi.org/10.1039/b922024k.

(131) Lee, S. S.; Song, W.; Cho, M.; Puppala, H. L.; Nguyen, P.; Zhu, H.; Segatori, L.; Colvin, V. L. Antioxidant Properties of Cerium Oxide Nanocrystals as a Function of Nanocrystal Diameter and Surface Coating. *ACS Nano* **2013**, *7* (11), 9693–9703. https://doi.org/10.1021/nn4026806.

(132) Jiao, X.; Song, H.; Zhao, H.; Bai, W.; Zhang, L.; Lv, Y. Well-Redispersed Ceria Nanoparticles: Promising Peroxidase Mimetics for H_2O_2 and Glucose Detection. *Anal. Methods* **2012**, *4* (10), 3261–3267. https://doi.org/10.1039/c2ay25511a.

(133) Asati, A.; Santra, S.; Kaittanis, C.; Nath, S.; Perez, J. M. Oxidase-Like Activity of Polymer-Coated Cerium Oxide Nanoparticles. *Angew. Chem. Int. Ed.* **2009**, *48* (13), 2308–2312. https://doi.org/10.1002/anie.200805279.

(134) Rzigalinski, B. A.; Meehan, K.; Davis, R. M.; Xu, Y.; Miles, W. C.; Cohen, C. A. Radical Nanomedicine. *Nanomed.* **2006**, *1* (4), 399–412. https://doi.org/10.2217/17435889.1.4.399.

(135) Estevez, A. Y.; Erlichman, J. S. The Potential of Cerium Oxide Nanoparticles (Nanoceria) for Neurodegenerative Disease Therapy. *Nanomed.* **2014**, *9* (10), 1437–1440. https://doi.org/10.2217/nnm.14.87.

(136) Ganesana, M.; Erlichman, J. S.; Andreescu, S. Real-Time Monitoring of Superoxide Accumulation and Antioxidant Activity in a Brain Slice Model Using an Electrochemical Cytochrome c Biosensor. *Free Radic. Biol. Med.* **2012**, *53* (12), 2240–2249. https://doi.org/10.1016/j.freeradbiomed.2012.10.540.

(137) Das, S.; Dowding, J. M.; Klump, K. E.; McGinnis, J. F.; Self, W.; Seal, S. Cerium Oxide Nanoparticles: Applications and Prospects in Nanomedicine. *Nanomed.* **2013**, *8* (9), 1483–1508. https://doi.org/10.2217/nnm.13.133.

(138) Maldiney, T.; Bessière, A.; Seguin, J.; Teston, E.; Sharma, S. K.; Viana, B.; Bos, A. J. J.; Dorenbos, P.; Bessodes, M.; Gourier, D.; Scherman, D.; Richard, C. The in Vivo Activation of Persistent Nanophosphors for Optical Imaging of Vascularization, Tumours and Grafted Cells. *Nat. Mater.* **2014**, *13* (4), 418–426. https://doi.org/10.1038/nmat3908.

(139) le Masne de Chermont, Q.; Chaneac, C.; Seguin, J.; Pelle, F.; Maitrejean, S.; Jolivet, J.-P.; Gourier, D.; Bessodes, M.; Scherman, D. Nanoprobes with Near-Infrared Persistent Luminescence for in Vivo Imaging. *Proc. Natl. Acad. Sci.* **2007**, *104* (22), 9266–9271. https://doi.org/10.1073/pnas.0702427104.

(140) Abdukayum, A.; Chen, J.-T.; Zhao, Q.; Yan, X.-P. Functional Near Infrared-Emitting Cr^{3+} /Pr^{3+} Co-Doped Zinc Gallogermanate Persistent Luminescent Nanoparticles with Superlong Afterglow for *in Vivo* Targeted Bioimaging. *J. Am. Chem. Soc.* **2013**, *135* (38), 14125–14133. https://doi.org/10.1021/ja404243v.

(141) Pan, Z.; Lu, Y.-Y.; Liu, F. Sunlight-Activated Long-Persistent Luminescence in the near-Infrared from Cr^{3+}-Doped Zinc Gallogermanates. *Nat. Mater.* **2012**, *11* (1), 58–63. https://doi.org/10.1038/nmat3173.

(142) Li, Z.; Zhang, Y.; Wu, X.; Huang, L.; Li, D.; Fan, W.; Han, G. Direct Aqueous-Phase Synthesis of Sub-10 Nm “Luminous Pearls” with Enhanced *in Vivo* Renewable Near-Infrared Persistent Luminescence. *J. Am. Chem. Soc.* **2015**, *137* (16), 5304–5307. https://doi.org/10.1021/jacs.5b00872.

(143) Wu, S.-Q.; Chi, C.-W.; Yang, C.-X.; Yan, X.-P. Penetrating Peptide-Bioconjugated Persistent Nanophosphors for Long-Term Tracking of Adipose-Derived Stem Cells with Superior Signal-to-Noise Ratio. *Anal. Chem.* **2016**, *88* (7), 4114–4121. https://doi.org/10.1021/acs.analchem.6b00449.

(144) Sun, S.-K.; Wu, J.-C.; Wang, H.; Zhou, L.; Zhang, C.; Cheng, R.; Kan, D.; Zhang, X.; Yu, C. Turning Solid into Gel for High-Efficient Persistent Luminescence-Sensitized Photodynamic Therapy. *Biomaterials* **2019**, *218*, 1–10. https://doi.org/10.1016/j.biomaterials.2019.119328.

(145) Li, Z.; Chen, X.; Huang, Z.; Zhou, J.; Liu, R.; Lv, Y. Multiplex Nucleic Acid Assay of SARS-CoV-2 via a Lanthanide Nanoparticle-Tagging Strategy. *Anal. Chem.* **2021**, *93* (37), 12714–12722. https://doi.org/10.1021/acs.analchem.1c02657.

(146) Zhang, S.; Liu, R.; Xing, Z.; Zhang, S.; Zhang, X. Multiplex miRNA Assay Using Lanthanide-Tagged Probes and the Duplex-Specific Nuclease Amplification Strategy. *Chem. Commun.* **2016**, *52* (99), 14310–14313. https://doi.org/10.1039/C6CC08334J.

(147) Liu, R.; Zhang, S.; Wei, C.; Xing, Z.; Zhang, S.; Zhang, X. Metal Stable Isotope Tagging: Renaissance of Radioimmunoassay for Multiplex and Absolute Quantification of Biomolecules. *Acc. Chem. Res.* **2016**, *49* (5), 775–783. https://doi.org/10.1021/acs.accounts.5b00509.

(148) Steinhoff, B.; Müller, J.; Mozhayeva, D.; Spelz, B. T. F.; Engelhard, C.; Butz, B.; Schönherr, H. Investigation of the Fate of Silver and Titanium Dioxide Nanoparticles in Model Wastewater Effluents via Selected Area Electron Diffraction. *Environ. Sci. Technol.* **2020**, *54* (14), 8681–8689. https://doi.org/10.1021/acs.est.9b07840.

(149) Liu, Y.; Meng, H.; Konst, S.; Sarmiento, R.; Rajachar, R.; Lee, B. P. Injectable Dopamine-Modified Poly(Ethylene Glycol) Nanocomposite Hydrogel with Enhanced Adhesive Property and Bioactivity. *ACS Appl. Mater. Interfaces* **2014**, *6* (19), 16982–16992. https://doi.org/10.1021/am504566v.

(150) Skelton, S.; Bostwick, M.; O'Connor, K.; Konst, S.; Casey, S.; Lee, B. P. Biomimetic Adhesive Containing Nanocomposite Hydrogel with Enhanced Materials Properties. *Soft Matter* **2013**, *9* (14), 3825–3833. https://doi.org/10.1039/c3sm27352k.

(151) Marcelo, G.; López-González, M.; Mendicuti, F.; Tarazona, M. P.; Valiente, M. Poly(*N*-Isopropylacrylamide)/Gold Hybrid Hydrogels Prepared by Catechol Redox Chemistry. Characterization and Smart Tunable Catalytic Activity. *Macromolecules* **2014**, *47* (17), 6028–6036. https://doi.org/10.1021/ma501214k.

(152) Ravi, N.; Aliyar, H. A.; Hamilton, P. D. Hydrogel Nanocomposite as a Synthetic Intra-Ocular Lens Capable of Accommodation. *Macromol. Symp.* **2005**, *227* (1), 191–202. https://doi.org/10.1002/masy.200550919.

(153) Weissman, J. M.; Sunkara, H. B.; Tse, A. S.; Asher, S. A. Thermally Switchable Periodicities and Diffraction from Mesoscopically Ordered Materials. *Science* **1996**, *274* (5289), 959–963. https://doi.org/10.1126/science.274.5289.959.

(154) Holtz, J. H.; Asher, S. A. Polymerized Colloidal Crystal Hydrogel Films as Intelligent Chemical Sensing Materials. *Nature* **1997**, *389* (6653), 829–832. https://doi.org/10.1038/39834.

(155) Xia, Y.; Yang, P.; Sun, Y.; Wu, Y.; Mayers, B.; Gates, B.; Yin, Y.; Kim, F.; Yan, H. One-Dimensional Nanostructures: Synthesis, Characterization, and Applications. *Adv. Mater.* **2003**, *15* (5), 353–389. https://doi.org/10.1002/adma.200390087.

(156) Sershen, S. R.; Westcott, S. L.; Halas, N. J.; West, J. L. Temperature-Sensitive Polymer-Nanoshell Composites for Photothermally Modulated Drug Delivery. *J. Biomed. Mater. Res.* **2000**, *51* (3), 293–298. https://doi.org/10.1002/1097-4636(20000905)51:3<293AID-JBM1>3.0CO;2-T.

(157) Liu, M.; Ishida, Y.; Ebina, Y.; Sasaki, T.; Aida, T. Photolatently Modulable Hydrogels Using Unilamellar Titania Nanosheets as Photocatalytic Crosslinkers. *Nat. Commun.* **2013**, *4* (1), 1–7. https://doi.org/10.1038/ncomms3029.

(158) Pardo-Yissar, V.; Gabai, R.; Shipway, A. N.; Bourenko, T.; Willner, I. Gold Nanoparticle/Hydrogel Composites with Solvent-Switchable Electronic Properties. *Adv. Mater.* **2001**, *13* (17), 1320–1323. https://doi.org/10.1002/1521-4095(200109)13:17<1320::AID-ADMA1320>3.0.CO;2-8.

(159) Souza, G. R.; Christianson, D. R.; Staquicini, F. I.; Ozawa, M. G.; Snyder, E. Y.; Sidman, R. L.; Miller, J. H.; Arap, W.; Pasqualini, R. Networks of Gold Nanoparticles and Bacteriophage as Biological Sensors and Cell-Targeting Agents. *Proc. Natl. Acad. Sci.* **2006**, *103* (5), 1215–1220. https://doi.org/10.1073/pnas.0509739103.

(160) Skardal, A.; Zhang, J.; McCoard, L.; Oottamasathien, S.; Prestwich, G. D. Dynamically Crosslinked Gold Nanoparticle - Hyaluronan Hydrogels. *Adv. Mater.* **2010**, *22* (42), 4736–4740. https://doi.org/10.1002/adma.201001436.

(161) Zhang, D.; Yang, J.; Bao, S.; Wu, Q.; Wang, Q. Semiconductor Nanoparticle-Based Hydrogels Prepared via Self-Initiated Polymerization under Sunlight, Even Visible Light. *Sci. Rep.* **2013**, *3* (1), 1–7. https://doi.org/10.1038/srep01399.

(162) Wu, H.; Yu, G.; Pan, L.; Liu, N.; McDowell, M. T.; Bao, Z.; Cui, Y. Stable Li-Ion Battery Anodes by in-Situ Polymerization of Conducting Hydrogel to Conformally Coat Silicon Nanoparticles. *Nat. Commun.* **2013**, *4* (1), 1–6. https://doi.org/10.1038/ncomms2941.

(163) Campos, E.; Branquinho, J.; Carreira, A. S.; Carvalho, A.; Coimbra, P.; Ferreira, P.; Gil, M. H. Designing Polymeric Microparticles for Biomedical and Industrial Applications. *Eur. Polym. J.* **2013**, *49* (8), 2005–2021. https://doi.org/10.1016/j.eurpolymj.2013.04.033.

(164) Nandiyanto, A. B. D.; Iskandar, F.; Ogi, T.; Okuyama, K. Nanometer to Submicrometer Magnesium Fluoride Particles with Controllable Morphology. *Langmuir* **2010**, *26* (14), 12260–12266. https://doi.org/10.1021/la101194w.

(165) Sevonkaev, I.; Matijević, E. Formation of Magnesium Fluoride Particles of Different Morphologies. *Langmuir* **2009**, *25* (18), 10534–10539. https://doi.org/10.1021/la901307t.

(166) Noack, J.; Emmerling, F.; Kirmse, H.; Kemnitz, E. Sols of Nanosized Magnesium Fluoride: Formation and Stabilisation of Nanoparticles. *J. Mater. Chem.* **2011**, *21* (38), 15015–15021. https://doi.org/10.1039/C1JM11943E.

(167) Scheurell, K.; Noack, J.; König, R.; Hegmann, J.; Jahn, R.; Hofmann, Th.; Löbmann, P.; Lintner, B.; Garcia-Juan, P.; Eicher, J.; Kemnitz, E. Optimisation of a Sol–Gel Synthesis Route for the Preparation of MgF_2 Particles for a Large Scale Coating Process. *Dalton Trans.* **2015**, *44* (45), 19501–19508. https://doi.org/10.1039/C5DT02196K.

(168) Kemnitz, E. Fluorolytic Sol-Gel Processes. In *Handbook of Sol-Gel Science and Technology*; Klein, L., Aparicio, M., Jitianu, A., Eds.; Springer International Publishing: Cham, 2016; pp 1–41. https://doi.org/10.1007/978-3-319-19454-7_114-1.

(169) Lellouche, J.; Friedman, A.; Lahmi, R.; Gedanken, A.; Banin, E. *Antibiofilm surface functionalization of catheters by magnesium fluoride nanoparticles*. *Int. J. Nanomedicine*. https://doi.org/10.2147/IJN.S26770.

(170) Qin, T.; Zhang, P.; Qin, W. A Novel Method to Synthesize Low-Cost Magnesium Fluoride Spheres from Seawater. *Ceram. Int.* **2017**, *43* (16), 14481–14483. https://doi.org/10.1016/j.ceramint.2017.06.145.

(171) Cortelletti, P.; Pedroni, M.; Boschi, F.; Pin, S.; Ghigna, P.; Canton, P.; Vetrone, F.; Speghini, A. Luminescence of Eu^{3+} Activated CaF_2 and SrF_2 Nanoparticles: Effect of the Particle Size and Codoping with Alkaline Ions. *Cryst. Growth Des.* **2018**, *18* (2), 686–694. https://doi.org/10.1021/acs.cgd.7b01050.

(172) Wang, J.; Shen, L.; He, Z.; Hu, J.; Cai, Z.; Zheng, P.; Hu, B. Spatial and Temporal Distribution of Nitrite-Dependent Anaerobic Methane-Oxidizing Bacteria in an Intertidal Zone of the East China Sea. *Appl. Microbiol. Biotechnol.* **2017**, *101* (21), 8007–8014. https://doi.org/10.1007/s00253-017-8521-0.

(173) Wang, D.; Hou, P.; Zhang, L.; Xie, N.; Yang, P.; Cheng, X. Photocatalytic Activities and Chemically-Bonded Mechanism of SiO_2@ TiO_2 Nanocomposites Coated Cement-Based Materials. *Mater. Res. Bull.* **2018**, *102*, (6), 262–268. https://doi.org/10.1016/j.materresbull.2018.02.013.

(174) Horn, M.; Schwerdtfeger, C. F.; Meagher, E. P. Refinement of the Structure of Anatase at Several Temperatures*. *Z. Für Krist.* **1972**, *136* (3–4), 273–281. https://doi.org/10.1524/zkri.1972.136.3-4.273.

(175) Holder, C. F.; Schaak, R. E. Tutorial on Powder X-Ray Diffraction for Characterizing Nanoscale Materials. *ACS Nano* **2019**, *13* (7), 7359–7365. https://doi.org/10.1021/acsnano.9b05157.

(176) Cullity, B. D.; Stock, S. R. *Elements of X-Ray Diffraction*, 3. ed., internat. ed.; Pearson/Prentice Hall: Upper Saddle River, NJ, 2001.

(177) *Powder Diffraction: Theory and Practice*; Dinnebier, R. E., Billinge, S. J. L., Eds.; Royal Society of Chemistry: Cambridge, 2008. https://doi.org/10.1039/9781847558237.

(178) *Diffraction Analysis of the Microstructure of Materials*; Mittemeijer, E. J., Scardi, P., Eds.; Hull, R., Osgood, R. M., Parisi, J., Warlimont, H., Series Eds.; Springer Series in Materials Science; Springer Berlin Heidelberg: Berlin, Heidelberg, 2004; Vol. 68. https://doi.org/10.1007/978-3-662-06723-9.

(179) Mittemeijer, E. J.; Welzel, U. The “State of the Art” of the Diffraction Analysis of Crystallite Size and Lattice Strain. *J. Cryst.* **2008**, *223* (9), 552–560. https://doi.org/10.1524/zkri.2008.1213.

(180) Balzar, D.; Audebrand, N.; Daymond, M. R.; Fitch, A.; Hewat, A.; Langford, J. I.; Le Bail, A.; Louër, D.; Masson, O.; McCowan, C. N.; Popa, N. C.; Stephens, P. W.; Toby, B. H. Size–Strain Line-Broadening Analysis of the Ceria Round-Robin Sample. *J. Appl. Crystallogr.* **2004**, *37* (6), 911–924. https://doi.org/10.1107/S0021889804022551.

(181) Stöber, W.; Fink, A.; Bohn, E. Controlled Growth of Monodisperse Silica Spheres in the Micron Size Range. *J. Colloid Interface Sci.* **1968**, *26* (1), 62–69. https://doi.org/10.1016/0021-9797(68)90272-5.

(182) Rosales, A.; Esquivel, K. SiO2@TiO2 Composite Synthesis and Its Hydrophobic Applications: A Review. *Catalysts* **2020**, *10* (2), 171–188. https://doi.org/10.3390/catal10020171.

(183) Feng, X.; Zhang, S.; Lou, X. Controlling Silica Coating Thickness on TiO_2 Nanoparticles for Effective Photodynamic Therapy. *Colloids Surf. B Biointerfaces* **2013**, *107* (7), 220–226. https://doi.org/10.1016/j.colsurfb.2013.02.007.

(184) Pudovkin, M. S.; Koryakovtseva, D. A.; Lukinova, E. V.; Korableva, S. L.; Khusnutdinova, R. Sh.; Kiiamov, A. G.; Nizamutdinov, A. S.; Semashko, V. V. Characterization of Pr-Doped LaF_3 Nanoparticles Synthesized by Different Variations of Coprecipitation Method. *J. Nanomater.* **2019**, *2019*, 1–17. https://doi.org/10.1155/2019/7549325.

(185) Shen, H.; Wang, F.; Fan, X.; Wang, M. Synthesis of LaF_3:Yb^{3+}, Ln^{3+} Nanoparticles with Improved Upconversion Luminescence. *J. Exp. Nanosci.* **2007**, *2* (4), 303–311. https://doi.org/10.1080/17458080701724943.

(186) Dewan, M.; Kumar, A.; Saxena, A.; De, A.; Mozumdar, S. Using Hydrophilic Ionic Liquid, $[BMIM]BF_4$ – Ethylene Glycol System as a Novel Media for the Rapid Synthesis of Copper Nanoparticles. *PLoS ONE* **2012**, *7* (1), 1–5. https://doi.org/10.1371/journal.pone.0029131.

(187) Zalkin, A.; Templeton, D. H.; Hopkins, T. E. The Atomic Parameters in the Lanthanum Trifluoride Structure. *Inorg. Chem.* **1966**, *5* (8), 1466–1468. https://doi.org/10.1021/ic50042a047.

(188) Xie, Z.-L.; Feng, M.-L.; Tan, B.; Huang, X.-Y. The Multifunctional Roles of the Ionic Liquid $[BMIM][BF_4]$ in the Creation of Cadmium Metal–Organic Frameworks. *CrystEngComm* **2012**, *14* (15), 4894–4901. https://doi.org/10.1039/c2ce25169h.

(189) León, A.; Reuquen, P.; Garín, C.; Segura, R.; Vargas, P.; Zapata, P.; Orihuela, P. FTIR and Raman Characterization of TiO_2 Nanoparticles Coated with Polyethylene Glycol as Carrier for 2-Methoxyestradiol. *Appl. Sci.* **2017**, *7* (49), 1–9. https://doi.org/10.3390/app7010049.

(190) Samitier, J.; Marco, S.; Ruiz, O.; Morante, J. R.; Esteve-Tinto, J.; Bausells, J. Analysis by FT-IR Spectroscopy of SiO_2-Polycrystalline Structures Used in Micromechanics: Stress Measurements. *Sens. Actuators Phys.* **1992**, *32* (1–3), 347–353. https://doi.org/10.1016/0924-4247(92)80010-Z.

(191) Murashkevich, A. N.; Lavitskaya, A. S.; Barannikova, T. I.; Zharskii, I. M. Infrared Absorption Spectra and Structure of TiO_2-SiO_2 Composites. *J. Appl. Spectrosc.* **2008**, *75* (5), 730–734. https://doi.org/10.1007/s10812-008-9097-3.

(192) Kai, C.; Chao, G.; Bo, P.; Wei, W. The Influence of SiO_2 Shell on Fluorescent Properties of LaF_3:Nd^{3+}/SiO_2 Core/Shell Nanoparticles. *J. Nanomater.* **2010**, *2010*, 1–5. https://doi.org/10.1155/2010/238792.

(193) Wu, C.-Y.; Tu, K.-J.; Deng, J.-P.; Lo, Y.-S.; Wu, C.-H. Markedly Enhanced Surface Hydroxyl Groups of TiO_2 Nanoparticles with Superior Water-Dispersibility for Photocatalysis. *Materials* **2017**, *10* (5), 566–581. https://doi.org/10.3390/ma10050566.

(194) Chen, Y.; Zou, C.; Mastalerz, M.; Hu, S.; Gasaway, C.; Tao, X. Applications of Micro-Fourier Transform Infrared Spectroscopy (FTIR) in the Geological Sciences—A Review. *Int. J. Mol. Sci.* **2015**, *16* (12), 30223–30250. https://doi.org/10.3390/ijms161226227.

(195) Yan, W.; Liu, D.; Tan, D.; Yuan, P.; Chen, M. FTIR Spectroscopy Study of the Structure Changes of Palygorskite under Heating. *Spectrochim. Acta. A. Mol. Biomol. Spectrosc.* **2012**, *97*, 1052–1057. https://doi.org/10.1016/j.saa.2012.07.085.

(196) Nakamoto, K. *Infrared and Raman Spectra of Inorganic and Coordination Compounds*, 3d ed.; Wiley: New York, 1978.

(197) Chien, H.-W.; Huang, C.-H.; Yang, C.-H.; Wang, T.-L. Synthesis, Optical Properties, and Sensing Applications of LaF_3:Yb^{3+}/Er^{3+}/Ho^{3+}/Tm^{3+} Upconversion Nanoparticles. *Nanomaterials* **2020**, *10* (12), 2477–2498. https://doi.org/10.3390/nano10122477.

(198) Sakatani, Y.; Grosso, D.; Nicole, L.; Boissière, C.; De A. A. Soler-Illia, G. J.; Sanchez, C. Optimised Photocatalytic Activity of Grid-like Mesoporous TiO_2 Films: Effect of Crystallinity, Pore Size Distribution, and Pore Accessibility. *J Mater Chem* **2006**, *16* (1), 77–82. https://doi.org/10.1039/B512824M.

(199) Li, D.; Song, H.; Meng, X.; Shen, T.; Sun, J.; Han, W.; Wang, X. Effects of Particle Size on the Structure and Photocatalytic Performance by Alkali-Treated TiO_2. *Nano* **2020**, *10* (3), 546–560. https://doi.org/10.3390/nano10030546.

(200) Budnyk, A.; Damin, A.; Bordiga, S.; Zecchina, A. Synthesis and Characterization of High-Surface-Area Silica–Titania Monoliths. *J. Phys. Chem. C* **2012**, *116* (18), 10064–10072. https://doi.org/10.1021/jp3012798.

(201) Jadhav, S. V.; Nikam, D. S.; Khot, V. M.; Thorat, N. D.; Phadatare, M. R.; Ningthoujam, R. S.; Salunkhe, A. B.; Pawar, S. H. Studies on Colloidal Stability of PVP-Coated LSMO Nanoparticles for Magnetic Fluid Hyperthermia. *New J. Chem.* **2013**, *37* (10), 3121–3130. https://doi.org/10.1039/c3nj00554b.

(202) Lu, G.; Li, S.; Guo, Z.; Farha, O. K.; Hauser, B. G.; Qi, X.; Wang, Y.; Wang, X.; Han, S.; Liu, X.; DuChene, J. S.; Zhang, H.; Zhang, Q.; Chen, X.; Ma, J.; Loo, S. C. J.; Wei, W. D.; Yang, Y.; Hupp, J. T.; Huo, F. Imparting Functionality to a Metal–Organic Framework Material by Controlled Nanoparticle Encapsulation. *Nat. Chem.* **2012**, *4* (4), 310–316. https://doi.org/10.1038/nchem.1272.

(203) Koczkur, K. M.; Mourdikoudis, S.; Polavarapu, L.; Skrabalak, S. E. Polyvinylpyrrolidone (PVP) in Nanoparticle Synthesis. *Dalton Trans.* **2015**, *44* (41), 17883–17905. https://doi.org/10.1039/C5DT02964C.

(204) Kedia, A.; Senthil Kumar, P. Precursor-Driven Nucleation and Growth Kinetics of Gold Nanostars. *J. Phys. Chem. C* **2012**, *116* (2), 1679–1686. https://doi.org/10.1021/jp2063518.

(205) Bahadory, M. Synthesis of Noble Metal Nanoparticles, Drexler University, USA, 2008.

(206) Graf, C.; Dembski, S.; Hofmann, A.; Rühl, E. A General Method for the Controlled Embedding of Nanoparticles in Silica Colloids. *Langmuir* **2006**, *22* (13), 5604–5610. https://doi.org/10.1021/la060136w.

(207) Filippov, S. K.; Khusnutdinov, R.; Murmiliuk, A.; Inam, W.; Zakharova, L. Ya.; Zhang, H.; Khutoryanskiy, V. V. Dynamic Light Scattering and Transmission Electron Microscopy in Drug Delivery: A Roadmap for Correct Characterization of Nanoparticles and Interpretation of Results. *Mater. Horiz.* **2023**, *10* (12), 5354–5370. https://doi.org/10.1039/D3MH00717K.

(208) Si, R.; Zhang, Y.-W.; You, L.-P.; Yan, C.-H. Self-Organized Monolayer of Nanosized Ceria Colloids Stabilized by Poly(Vinylpyrrolidone). *J. Phys. Chem. B* **2006**, *110* (12), 5994–6000. https://doi.org/10.1021/jp057501x.

(209) Kyrychenko, A.; Korsun, O. M.; Gubin, I. I.; Kovalenko, S. M.; Kalugin, O. N. Atomistic Simulations of Coating of Silver Nanoparticles with Poly(Vinylpyrrolidone) Oligomers: Effect of Oligomer Chain Length. *J. Phys. Chem. C* **2015**, *119* (14), 7888–7899. https://doi.org/10.1021/jp510369a.

(210) Li, F.; Li, C.; Liu, X.; Bai, T.; Dong, W.; Zhang, X.; Shi, Z.; Feng, S. Microwave-Assisted Synthesis and up–down Conversion Luminescent Properties of Multicolor Hydrophilic LaF_3:Ln^{3+} Nanocrystals. *Dalton Trans* **2013**, *42* (6), 2015–2022. https://doi.org/10.1039/C2DT32295A.

(211) González Mancebo, D.; Becerro, A. I.; Corral, A.; Moros, M.; Balcerzyk, M.; Fuente, J. M. de la; Ocaña, M. Enhancing Luminescence and X-Ray Absorption Capacity of Eu^{3+}:LaF_3 Nanoparticles by Bi^{3+} Codoping. *ACS Omega* **2019**, *4* (1), 765–774. https://doi.org/10.1021/acsomega.8b03160.

(212) Wang, Y.; Wang, Y.; Huang, C.; Chen, T.; Wu, J. Ultra-Weak Chemiluminescence Enhanced by Cerium-Doped LaF_3 Nanoparticles: A Potential Nitrite Analysis Method. *Front. Chem.* **2020**, *8*, 639–648. https://doi.org/10.3389/fchem.2020.00639.

(213) Duan, Y.; Yu, Y.; Wang, L.; Zhao, S. Dual-Emission LaF_3:Tb@DPA-Eu Nanoparticles as a Ratiometric Fluorescence Probe for the Detection of Marbofloxacin. *Microchem. J.* **2021**, *168*, 106469–106476. https://doi.org/10.1016/j.microc.2021.106469.

(214) Rocha, U.; Upendra Kumar, K.; Jacinto, C.; Ramiro, J.; Caamaño, A. J.; García Solé, J.; Jaque, D. Nd^{3+} Doped LaF_3 Nanoparticles as Self-Monitored Photo-Thermal Agents. *Appl. Phys. Lett.* **2014**, *104* (5), 053703–053708. https://doi.org/10.1063/1.4862968.

(215) González-Mancebo, D.; Becerro, A. I.; Calderón-Olvera, R. M.; Cantelar, E.; Corral, A.; Balcerzyk, M.; de la Fuente, J. M.; Ocaña, M. Neodymium Doped Lanthanide Fluoride Nanoparticles as Contrast Agents for Luminescent Bioimaging and X-Ray Computed Tomography. *Bol. Soc. Esp. Cerámica Vidr.* **2021**, *61* (7), S40–S49. https://doi.org/10.1016/j.bsecv.2021.07.004.

(216) Gaurkhede, S. G. Microwave Synthesis and Studies Room Temperature Optical Properties of LaF_3:Ce^{3+}, Pr^{3+}, Nd^{3+} Nanocrystals. *Nanosyst. Phys. Chem. Math.* **2020**, *11* (1), 117–122. https://doi.org/10.17586/2220-8054-2020-11-1-117-122.

(217) Wang, C.; Chen, S.-H. Factors Influencing Particle Agglomeration during Solid-State Sintering. *Acta Mech. Sin.* **2012**, *28* (3), 711–719. https://doi.org/10.1007/s10409-012-0029-3.

(218) Grover, I. S.; Prajapat, R. C.; Singh, S.; Pal, B. SiO_2-Coated Pure Anatase TiO_2 Catalysts for Enhanced Photo-Oxidation of Naphthalene and Anthracene. *Particuology* **2017**, *34*, 156–161. https://doi.org/10.1016/j.partic.2017.03.001.

(219) Williams, D. B.; Carter, C. B. *Transmission Electron Microscopy: A Textbook for Materials Science*, 2nd ed.; Springer: New York, 2008.

(220) *Energy Table for EDS Analysis*. Energy Table for EDS Analysis. https://www.unamur.be/services/microscopie/sme-documents/Energy-20table-20for-20EDS-20analysis-1.pdf (accessed 2019-09-26).

(221) *JEOL Ltd.* https://www.jeol.co.jp/en/ (accessed 2022-05-27).

(222) Saf'yanov, Yu. N.; Belov, N. V.; Kuz'min, E. A.; Bochkova, R. I. Application of Method of Rhombus to Interpreting the Crystal Structure of KSmF4. *Doklady Akademii Nauk SSSR* **1973**. *212* (1), 96–98.

(223) Fleischer, T.; Hoppe, R. Neues Über Fluoride A[CoF_4] Mit A = Li-Cs Sowie Über $CsFeF_4$ / News on Fluorides A[CoF_4] with A = Li-Cs and on $CsFeF_4$. *J. Nat. Res. B* **1982**, *37* (9), 1132–1136. https://doi.org/10.1515/znb-1982-0908.

(224) Branca, M.; Ibrahim, M.; Ciuculescu, D.; Philippot, K.; Amiens, C. Water Transfer of Hydrophobic Nanoparticles: Principles and Methods. In *Handbook of Nanoparticles*; Aliofkhazraei, M., Ed.; Springer International Publishing: Cham, 2014; pp 1–26. https://doi.org/10.1007/978-3-319-13188-7_29-1.

(225) You, F.; Wang, Y.; Lin, J.; Tao, Y. Hydrothermal Synthesis and Luminescence Properties of $NaGdF_4$:Eu. *J. Alloys Compd.* **2002**, *343* (1–2), 151–155. https://doi.org/10.1016/S0925-8388(02)00203-7.

(226) Wang, F.; Zhang, Y.; Fan, X.; Wang, M. Facile Synthesis of Water-Soluble LaF_3:Ln^{3+} Nanocrystals. *J. Mater. Chem.* **2006**, *16* (11), 1031–1034. https://doi.org/10.1039/b518262j.

(227) Wang, L.; Li, P.; Li, Y. Down- and Up-Conversion Luminescent Nanorods. *Adv. Mater.* **2007**, *19* (20), 3304–3307. https://doi.org/10.1002/adma.200700144.

(228) Wang, Z. L.; Quan, Z. W.; Jia, P. Y.; Lin, C. K.; Luo, Y.; Chen, Y.; Fang, J.; Zhou, W.; O'Connor, C. J.; Lin, J. A Facile Synthesis and Photoluminescent Properties of Redispersible CeF_3, CeF_3:Tb^{3+}, and CeF_3:Tb^{3+}/LaF_3 (Core/Shell) Nanoparticles. *Chem. Mater.* **2006**, *18* (8), 2030–2037. https://doi.org/10.1021/cm052360x.

(229) Wang, L.; Li, Y. $Na(Y_{1.5}Na_{0.5})F_6$ Single-Crystal Nanorods as Multicolor Luminescent Materials. *Nano Lett.* **2006**, *6* (8), 1645–1649. https://doi.org/10.1021/nl060684u.

(230) Carnall, W. T.; Goodman, G. L.; Rajnak, K.; Rana, R. S. A Systematic Analysis of the Spectra of the Lanthanides Doped into Single Crystal LaF_3. *J. Chem. Phys.* **1989**, *90* (7), 3443–3457. https://doi.org/10.1063/1.455853.

(231) Zhao, D.; Xue, Y.-L.; Zhang, S.-R.; Shi, L.-Y.; Liu, B.-Z.; Fan, Y.-P.; Yao, Q.-X.; Dai, S.-J. Non-Concentration Quenching, Good Thermal Stability and High Quantum Efficiency of $K_5Y(P_2O_7)_2:Eu^{3+}/Tb^{3+}$ Phosphors with a Novel Two-Dimensional Layer Structure. *J. Mater. Chem. C* **2019**, *7* (45), 14264–14274. https://doi.org/10.1039/C9TC04977K.

(232) Zhang, H.; Chen, Y.; Zhu, X.; Liu, K.; Zhou, H.; Yao, Y.; Sun, X. Energy Transfer Mechanism of $Ce^{3+} \rightarrow Tb^{3+} \rightarrow Eu^{3+}$ in $Ba_9Y_2Si_6O_{24}$. *Opt. Mater.* **2020**, *104*, 1–5. https://doi.org/10.1016/j.optmat.2020.109958.

(233) Chatti, M.; Sarkar, S.; Mahalingam, V. Glutathione-Modified Ultrasmall Ce^{3+} and Tb^{3+}-Doped SrF_2 Nanocrystals for Fluorescent Determination of Hg(II) and Pb(II) Ions. *Microchim. Acta* **2016**, *183* (1), 133–140. https://doi.org/10.1007/s00604-015-1610-9.

(234) Chen, P.; Li, Q.; Grindy, S.; Holten-Andersen, N. White-Light-Emitting Lanthanide Metallogels with Tunable Luminescence and Reversible Stimuli-Responsive Properties. *J. Am. Chem. Soc.* **2015**, *137* (36), 11590–11593. https://doi.org/10.1021/jacs.5b07394.

(235) Ansari, A. A.; Majeed Khan, M. A. $LnPO_4:Eu^{3+}$ Nanoparticles: Role of Host Lattices on Physiochemical and Luminescent Properties. *J. King Saud Univ. - Sci.* **2024**, *36* (2), 103042. https://doi.org/10.1016/j.jksus.2023.103042.

(236) Feinle, A.; Lavoie-Cardinal, F.; Akbarzadeh, J.; Peterlik, H.; Adlung, M.; Wickleder, C.; Hüsing, N. Novel Sol–Gel Precursors for Thin Mesoporous Eu^{3+} Doped Silica Coatings as Efficient Luminescent Materials. *Chem. Mater.* **2012**, *24* (19), 3674–3683. https://doi.org/10.1021/cm300996j.

(237) Pallotti, D. K.; Passoni, L.; Maddalena, P.; Di Fonzo, F.; Lettieri, S. Photoluminescence Mechanisms in Anatase and Rutile TiO_2. *J. Phys. Chem. C* **2017**, *121* (16), 9011–9021. https://doi.org/10.1021/acs.jpcc.7b00321.

(238) Grzyb, T.; Runowski, M.; Dąbrowska, K.; Giersig, M.; Lis, S. Structural, Spectroscopic and Cytotoxicity Studies of $TbF_3@CeF_3$ and $TbF_3@CeF_3@SiO_2$ Nanocrystals. *J. Nanoparticle Res.* **2013**, *15* (10), 1–15. https://doi.org/10.1007/s11051-013-1958-x.

(239) Toyozawa, Y. Phonon Structures in the Spectra of Solids. *J. Lumin.* **1970**, *1–2*, 732–746. https://doi.org/10.1016/0022-2313(70)90086-4.

(240) Toyozawa, Y. Dynamics of Excitons in Deformable Lattice. *J. Lumin.* **1981**, *24–25* (1), 23–30. https://doi.org/10.1016/0022-2313(81)90212-X.

(241) Toyozawa, Y. Elementary Processes in Luminescence. *J. Lumin.* **1976**, *12–13*, 13–21. https://doi.org/10.1016/0022-2313(76)90061-2.

(242) ICSD. ICSD Karlsruhe. https://icsd.fiz-karlsruhe.de/search/basic.

(243) Horiba Scientific. Horiba Scientific FlouroMax4. https://www.horiba.com/fileadmin/uploads/Scientific/Downloads/UserArea/Fluorescence/Manuals/FluoroMax4_4P_Manual_USB.pdf.

(244) OriginPro. https://www.originlab.com.

(245) Thoniyot, P.; Tan, M. J.; Karim, A. A.; Young, D. J.; Loh, X. J. Nanoparticle-Hydrogel Composites: Concept, Design, and Applications of These Promising, Multi-Functional Materials. *Adv. Sci.* **2015**, *2* (1400010), 1–13. https://doi.org/10.1002/advs.201400010.

(246) Fertah, M.; Belfkira, A.; Dahmane, E. M.; Taourirte, M.; Brouillette, F. Extraction and Characterization of Sodium Alginate from Moroccan Laminaria Digitata Brown Seaweed. *Arab. J. Chem.* **2017**, *10*, S3707–S3714. https://doi.org/10.1016/j.arabjc.2014.05.003.

(247) Zhang, Z.; Zhu, H.; Xu, Q.; Liu, F.; Zhu, A.; Kou, J. Hybrid Luminescent Alginate Hydrogels Containing Lanthanide with Potential for Acetone Sensing. *New J. Chem.* **2019**, *43* (33), 13205–13211. https://doi.org/10.1039/C9NJ01522A.

(248) Augst, A. D.; Kong, H. J.; Mooney, D. J. Alginate Hydrogels as Biomaterials. *Macromol. Biosci.* **2006**, *6* (8), 623–633. https://doi.org/10.1002/mabi.200600069.

(249) Rowley, J. A.; Madlambayan, G.; Mooney, D. J. Alginate Hydrogels as Synthetic Extracellular Matrix Materials. *Biomaterials* **1999**, *20* (1), 45–53. https://doi.org/10.1016/S0142-9612(98)00107-0.

(250) Das, D.; Pham, H. T. T.; Lee, S.; Noh, I. Fabrication of Alginate-Based Stimuli-Responsive, Non-Cytotoxic, Terpolymric Semi-IPN Hydrogel as a Carrier for Controlled Release of Bovine Albumin Serum and 5-Amino Salicylic Acid. *Mater. Sci. Eng. C* **2019**, *98*, 42–53. https://doi.org/10.1016/j.msec.2018.12.127.

(251) Śliwka, L.; Wiktorska, K.; Suchocki, P.; Milczarek, M.; Mielczarek, S.; Lubelska, K.; Cierpiał, T.; Łyżwa, P.; Kiełbasiński, P.; Jaromin, A.; Flis, A.; Chilmonczyk, Z. The Comparison of MTT and CVS Assays for the Assessment of Anticancer Agent Interactions. *PLOS ONE* **2016**, *11* (5), 1–17. https://doi.org/10.1371/journal.pone.0155772.

(252) Joris, F.; Manshian, B. B.; Peynshaert, K.; De Smedt, S. C.; Braeckmans, K.; Soenen, S. J. Assessing Nanoparticle Toxicity in Cell-Based Assays: Influence of Cell Culture Parameters and Optimized Models for Bridging the in Vitro–in Vivo Gap. *Chem. Soc. Rev.* **2013**, *42* (21), 8339–8359. https://doi.org/10.1039/c3cs60145e.

(253) Martin, A.; Sarkar, A. In Vitro Toxicity Testing of Nanomaterials. In *Cell Culture*; Ali Mehanna, R., Ed.; IntechOpen, 2019. https://doi.org/10.5772/intechopen.80818.

(254) *Vybrant® MTT Cell Proliferation Assay Kit - DE*. //www.thermofisher.com/de/de/home/references/protocols/cell-culture/mtt-assay-protocol/vybrant-mtt-cell-proliferation-assay-kit.html (accessed 2021-01-11).

(255) Kamiloglu, S.; Sari, G.; Ozdal, T.; Capanoglu, E. Guidelines for Cell Viability Assays. *Food Front.* **2020**, *1* (3), 332–349. https://doi.org/10.1002/fft2.44.

(256) Vanhaecke, F. The Use of Internal Standards in ICP-MS. *Talanta* **1992**, *39* (7), 737–742. https://doi.org/10.1016/0039-9140(92)80088-U.

(257) Jayakumar, R.; Sudheesh Kumar, P.; Mohandas, A.; Lakshmanan, V.-K.; Biswas, R. Exploration of Alginate Hydrogel/Nano Zinc Oxide Composite Bandages for Infected Wounds. *Int. J. Nanomedicine* **2015**, 53–66. https://doi.org/10.2147/IJN.S79981.

(258) Zhang, M.; Qiao, X.; Han, W.; Jiang, T.; Liu, F.; Zhao, X. Alginate-Chitosan Oligosaccharide-ZnO Composite Hydrogel for Accelerating Wound Healing. *Carbohydr. Polym.* **2021**, *266* (118100), 1–9. https://doi.org/10.1016/j.carbpol.2021.118100.

(259) Harper, B. A.; Barbut, S.; Lim, L.; Marcone, M. F. Effect of Various Gelling Cations on the Physical Properties of “Wet” Alginate Films. *J. Food Sci.* **2014**, *79* (4), E562-E567. https://doi.org/10.1111/1750-3841.12376.

(260) Middleman, S. Rheology: Principles, Measurements, and Applications by C. Macosko, VCH Publishers, 1994, 550pp. *AIChE J.* **1995**, *41* (10), 2344–2344. https://doi.org/10.1002/aic.690411025.

(261) Adibnia, V.; Hill, R. J. Viscoelasticity of Near-Critical Silica-Polyacrylamide Hydrogel Nanocomposites. *Polymer* **2017**, *112*, 457–465. https://doi.org/10.1016/j.polymer.2017.01.013.

(262) Grosskopf, A. K.; Saouaf, O. A.; Lopez Hernandez, H.; Appel, E. A. Gelation and Yielding Behavior of Polymer–Nanoparticle Hydrogels. *J. Polym. Sci.* **2021**, *59* (22), 2854–2866. https://doi.org/10.1002/pol.20210652.

(263) Agrawal, A.; Yu, H.-Y.; Sagar, A.; Choudhury, S.; Archer, L. A. Molecular Origins of Temperature-Induced Jamming in Self-Suspended Hairy Nanoparticles. *Macromolecules* **2016**, *49* (22), 8738–8747. https://doi.org/10.1021/acs.macromol.6b01280.

(264) Yu, A. C.; Smith, A. A. A.; Appel, E. A. Structural Considerations for Physical Hydrogels Based on Polymer–Nanoparticle Interactions. *Mol. Syst. Des. Eng.* **2020**, *5* (1), 401–407. https://doi.org/10.1039/C9ME00120D.

(265) Donley, G. J.; Singh, P. K.; Shetty, A.; Rogers, S. A. Elucidating the G″ Overshoot in Soft Materials with a Yield Transition via a Time-Resolved Experimental Strain Decomposition. *Proc. Natl. Acad. Sci.* **2020**, *117* (36), 21945–21952. https://doi.org/10.1073/pnas.2003869117.

(266) Leibiger, C.; Kosyakova, N.; Mkrtchyan, H.; Glei, M.; Trifonov, V.; Liehr, T. First Molecular Cytogenetic High Resolution Characterization of the NIH 3T3 Cell Line by Murine Multicolor Banding. *J. Histochem. Cytochem.* **2013**, *61* (4), 306–312. https://doi.org/10.1369/0022155413476868.

(267) Gershman, H.; Rosen, J. J. Cell Adhesion and Cell Surface Topography in Aggregates of 3T3 and SV40-Virus-Transformed 3T3 Cells. Visualization of Interior Cells by Scanning Electron Microscopy. *J. Cell Biol.* **1978**, *76* (3), 639–651. https://doi.org/10.1083/jcb.76.3.639.

(268) Sambale, F.; Stahl, F.; Rüdinger, F.; Seliktar, D.; Kasper, C.; Bahnemann, D.; Scheper, T. Iterative Cellular Screening System for Nanoparticle Safety Testing. *J. Nanomater.* **2015**, *2015*, 1–16. https://doi.org/10.1155/2015/691069.

(269) Song, Q.; Schönherr, H. Control of Orientation, Formation of Ordered Structures, and Self-Sorting of Surface-Functionalized Microcubes at the Air–Water Interface. *Langmuir* **2019**, *35* (20), 6742–6751. https://doi.org/10.1021/acs.langmuir.9b00792.

(270) Gonzalez-Fernandez T, Tenorio AJ, Campbell KT, Silva EA, Leach JK. Alginate-Based Bioinks for 3D Bioprinting and Fabrication of Anatomically Accurate Bone Grafts. *Tissue Eng Part A*. **2021,** *27* (17-18) 1168-1181. https://doi: 10.1089/ten.TEA.2020.0305.

(271) Carneiro Neto, A. N.; Moura, R. T.; Carlos, L. D.; Malta, O. L.; Sanadar, M.; Melchior, A.; Kraka, E.; Ruggieri, S.; Bettinelli, M.; Piccinelli, F. Dynamics of the Energy Transfer Process in Eu(III) Complexes Containing Polydentate Ligands Based on Pyridine, Quinoline, and Isoquinoline as Chromophoric Antennae. *Inorg. Chem.* **2022**, *61* (41), 16333–16346. https://doi.org/10.1021/acs.inorgchem.2c02330.

(272) Lilge, I.; Jiang, S.; Schönherr, H. Long-Term Stable Poly(Acrylamide) Brush Modified Transparent Microwells for Cell Attachment Studies in 3D. *Macromol. Biosci.* **2017**, *17* (5), 1–11. https://doi.org/10.1002/mabi.201600451.

(273) Song, Q.; Steuber, M.; Druzhinin, S. I.; Schönherr, H. Tailored Combinatorial Microcompartments through the Self-Organization of Microobjects: Assembly, Characterization, and Cell Studies. *Angew. Chem. Int. Ed.* **2019**, *58* (16), 5246–5250. https://doi.org/10.1002/anie.201814076.

(274) Kemper, B.; Bauwens, A.; Bettenworth, D.; Götte, M.; Greve, B.; Kastl, L.; Ketelhut, S.; Lenz, P.; Mues, S.; Schnekenburger, J.; Vollmer, A. Label-Free Quantitative In Vitro Live Cell Imaging with Digital Holographic Microscopy; Bioanalytical Reviews; Springer Berlin Heidelberg: Berlin, Heidelberg, 2019. https://doi.org/10.1007/11663_2019_6.

(275) *The Molecular Probes Handbook: A Guide to Fluorescent Probes and Labeling Technologies*, 11. ed.; Johnson, I., Ed.; Life Technologies Corp: Carlsbad, California, 2010.

(276) Monici, M. Cell and Tissue Autofluorescence Research and Diagnostic Applications. In *Biotechnology Annual Review*; Elsevier, 2005; Vol. 11, pp 227–256. https://doi.org/10.1016/S1387-2656(05)11007-2.

(277) Chang, C.; Sud, D.; Mycek, M. Fluorescence Lifetime Imaging Microscopy. In *Methods in Cell Biology*; Elsevier, 2007; Vol. 81, pp 495–524. https://doi.org/10.1016/S0091-679X(06)81024-1.

(278) Kroll, A.; Dierker, C.; Rommel, C.; Hahn, D.; Wohlleben, W.; Schulze-Isfort, C.; Göbbert, C.; Voetz, M.; Hardinghaus, F.; Schnekenburger, J. Cytotoxicity Screening of 23 Engineered Nanomaterials Using a Test Matrix of Ten Cell Lines and Three Different Assays. *Part. Fibre Toxicol.* **2011**, *8* (1), 1–19. https://doi.org/10.1186/1743-8977-8-9.

(279) Shimomura, O. The Discovery of Aequorin and Green Fluorescent Protein. *J. Microsc.* **2005**, *217* (1), 3–15. https://doi.org/10.1111/j.0022-2720.2005.01441.x.

(280) Felgner, P. L.; Gadek, T. R.; Holm, M.; Roman, R.; Chan, H. W.; Wenz, M.; Northrop, J. P.; Ringold, G. M.; Danielsen, M. Lipofection: A Highly Efficient, Lipid-Mediated DNA-Transfection Procedure. *Proc. Natl. Acad. Sci.* **1987**, *84* (21), 7413–7417. https://doi.org/10.1073/pnas.84.21.7413.

(281) Tsampoula, X.; Taguchi, K.; Čižmár, T.; Garces-Chavez, V.; Ma, N.; Mohanty, S.; Mohanty, K.; Gunn-Moore, F.; Dholakia, K. Fibre Based Cellular Transfection. *Opt. Express* **2008**, *16* (21), 17000–17007. https://doi.org/10.1364/OE.16.017007.

(282) Shaked, N. T.; Boppart, S. A.; Wang, L. V.; Popp, J. Label-Free Biomedical Optical Imaging. *Nat. Photonics* **2023**, *17* (12), 1031–1041. https://doi.org/10.1038/s41566-023-01299-6.

(283) Zernike, F. How I Discovered Phase Contrast. *Science* **1955**, *121* (3141), 345–349. https://doi.org/10.1126/science.121.3141.345.

(284) Marquet, P.; Rappaz, B.; Magistretti, P. J.; Cuche, E.; Emery, Y.; Colomb, T.; Depeursinge, C. Digital Holographic Microscopy: A Noninvasive Contrast Imaging Technique Allowing Quantitative Visualization of Living Cells with Subwavelength Axial Accuracy. *Opt. Lett.* **2005**, *30* (5), 468–470. https://doi.org/10.1364/OL.30.000468.

(285) Girshovitz, P.; Shaked, N. T. Generalized Cell Morphological Parameters Based on Interferometric Phase Microscopy and Their Application to Cell Life Cycle Characterization. *Biomed. Opt. Express* **2012**, *3* (8), 1757–1773. https://doi.org/10.1364/BOE.3.001757.

(286) Park, Y.; Depeursinge, C.; Popescu, G. Quantitative Phase Imaging in Biomedicine. *Nat. Photonics* **2018**, *12* (10), 578–589. https://doi.org/10.1038/s41566-018-0253-x.

(287) Poon, T.-C.; Poon, T.-C. *Digital Holography and Three-Dimensional Display: Principles and Applications*; Springer: New York London, 2006.

(288) *Handbook of Biomedical Optics*; CRC PRESS: S.l., 2020.

(289) Joo, C.; Akkin, T.; Cense, B.; Park, B. H.; De Boer, J. F. Spectral-Domain Optical Coherence Phase Microscopy for Quantitative Phase-Contrast Imaging. *Opt. Lett.* **2005**, *30* (16), 2131–2133. https://doi.org/10.1364/OL.30.002131.

(290) Choma, M. A.; Ellerbee, A. K.; Yang, C.; Creazzo, T. L.; Izatt, J. A. Spectral-Domain Phase Microscopy. *Opt. Lett.* **2005**, *30* (10), 1162–1164. https://doi.org/10.1364/OL.30.001162.

(291) Kemper, B.; Illy, E. Digital Holographic Microscopy: Requirements of Lasers for a Novel Label-free Cytometry Tool. *PhotonicsViews* **2020**, *17* (1), 32–35. https://doi.org/10.1002/phvs.202000007.

(292) Zhang, Q.; Zhong, L.; Tang, P.; Yuan, Y.; Liu, S.; Tian, J.; Lu, X. Quantitative Refractive Index Distribution of Single Cell by Combining Phase-Shifting Interferometry and AFM Imaging. *Sci. Rep.* **2017**, *7* (1), 2532–2542. https://doi.org/10.1038/s41598-017-02797-8.

(293) Gul, B.; Ashraf, S.; Khan, S.; Nisar, H.; Ahmad, I. Cell Refractive Index: Models, Insights, Applications and Future Perspectives. *Photodiagnosis Photodyn. Ther.* **2021**, *33* (102096), 1–8. https://doi.org/10.1016/j.pdpdt.2020.102096.

(294) Silva, M. F.; Pimenta, S.; Rodrigues, J. A.; Freitas, J. R.; Ghaderi, M.; Goncalves, L. M.; De Graaf, G.; Wolffenbuttel, R. F.; Correia, J. H. Magnesium Fluoride as Low-Refractive Index Material for near-Ultraviolet Filters Applied to Optical Sensors. *Vacuum* **2020**, *181* (109673), 1–7. https://doi.org/10.1016/j.vacuum.2020.109673.

(295) Thanh, N. T. K.; Maclean, N.; Mahiddine, S. Mechanisms of Nucleation and Growth of Nanoparticles in Solution. *Chem. Rev.* **2014**, *114* (15), 7610–7630. https://doi.org/10.1021/cr400544s.

(296) Cai, S.; Li, Q.; Li, M.; Liu, C. Molecular Characteristics of [BMIM][BF4] Ionic Liquids and Water Mixtures on the Pt Surface. *J. Mol. Liq.* **2020**, *304* (112782), 1–6. https://doi.org/10.1016/j.molliq.2020.112782.

(297) Zheng, H.; Smith, R. K.; Jun, Y.; Kisielowski, C.; Dahmen, U.; Alivisatos, A. P. Observation of Single Colloidal Platinum Nanocrystal Growth Trajectories. *Science* **2009**, *324* (5932), 1309–1312. https://doi.org/10.1126/science.1172104.

(298) Niederberger, M.; Cölfen, H. Oriented Attachment and Mesocrystals: Non-Classical Crystallization Mechanisms Based on Nanoparticle Assembly. *Phys Chem Chem Phys* **2006**, *8* (28), 3271–3287. https://doi.org/10.1039/B604589H.

(299) Li, D.; Nielsen, M. H.; Lee, J. R. I.; Frandsen, C.; Banfield, J. F.; De Yoreo, J. J. Direction-Specific Interactions Control Crystal Growth by Oriented Attachment. *Science* **2012**, *336* (6084), 1014–1018. https://doi.org/10.1126/science.1219643.

(300) Peng, X.; Manna, L.; Yang, W.; Wickham, J.; Scher, E.; Kadavanich, A.; Alivisatos, A. P. Shape Control of CdSe Nanocrystals. *Nature* **2000**, *404* (6773), 59–61. https://doi.org/10.1038/35003535.

(301) Peng, Z. A.; Peng, X. Nearly Monodisperse and Shape-Controlled CdSe Nanocrystals via Alternative Routes: Nucleation and Growth. *J. Am. Chem. Soc.* **2002**, *124* (13), 3343–3353. https://doi.org/10.1021/ja0173167.

(302) Niederberger, M.; Pinna, N. *Metal Oxide Nanoparticles in Organic Solvents*; Engineering Materials and Processes; Springer London: London, 2009. https://doi.org/10.1007/978-1-84882-671-7.

(303) Wang, Y.; Gohari Bajestani, Z.; Lhoste, J.; Auguste, S.; Hémon-Ribaud, A.; Body, M.; Legein, C.; Maisonneuve, V.; Guiet, A.; Brunet, S. The Effects of Various Parameters of the Microwave-Assisted Solvothermal Synthesis on the Specific Surface Area and Catalytic Performance of MgF_2 Nanoparticles. *Mat.* **2020**, *13* (16), 3566–3583. https://doi.org/10.3390/ma13163566.

(304) Liu, C.; Du, Y.; Lü, C.; Chen, W. Growth and Patterns of Residually Stressed Core–Shell Soft Sphere. *Int. J. Non-Linear Mech.* **2020**, *127* (11), 1–7. https://doi.org/10.1016/j.ijnonlinmec.2020.103594.

(305) Curetti, N.; Merli, M.; Capella, S.; Benna, P.; Pavese, A. Low-Pressure Ferroelastic Phase Transition in Rutile-Type AX_2 Minerals: Cassiterite (SnO_2), Pyrolusite (MnO_2) and Sellaite (MgF_2). *Phys. Chem. Miner.* **2019**, *46* (10), 987–1002. https://doi.org/10.1007/s00269-019-01057-7.

(306) Bach, A.; Fischer, D.; Mu, X.; Sigle, W.; Van Aken, P. A.; Jansen, M. Structural Evolution of Magnesium Difluoride: From an Amorphous Deposit to a New Polymorph. *Inorg. Chem.* **2011**, *50* (4), 1563–1569. https://doi.org/10.1021/ic1021615.

(307) Liebich, B. W.; Nicollin, D. Refinement of the PbFCl Types BaFI, BaFBr and CaFCl. *Acta Crystallogr. B* **1977**, *33* (9), 2790–2794. https://doi.org/10.1107/S0567740877009480.

(308) Sasaki, S.; Fujino, K.; Takéuchi, Y. X-Ray Determination of Electron-Density Distributions in Oxides, MgO, MnO, CoO, and NiO, and Atomic Scattering Factors of Their Constituent Atoms. *Proc. Jpn. Acad. Ser. B* **1979**, *55* (2), 43–48. https://doi.org/10.2183/pjab.55.43.

(309) Baur, W. H. Über Die Verfeinerung Der Kristallstrukturbestimmung Einiger Vertreter Des Rutiltyps: TiO_2, SnO_2, GeO_2 Und MgF_2. *Acta Crystallogr.* **1956**, *9* (6), 515–520. https://doi.org/10.1107/S0365110X56001388.

(310) Baur, W. H. Rutile-Type Compounds. V. Refinement of MnO_2 and MgF_2. *Acta Crystallogr. B* **1976**, *32* (7), 2200–2204. https://doi.org/10.1107/S0567740876007371.

(311) Wevers, M. A. C.; Schön, J. C.; Jansen, M. Global Aspects of the Energy Landscape of Metastable Crystal Structures in Ionic Compounds. *J. Phys. Condens. Matter* **1999**, *11* (33), 6487–6499. https://doi.org/10.1088/0953-8984/11/33/316.

(312) Wevers, M. A. C.; Schön, J. C.; Jansen, M. Characteristic Regions on the Energy Landscape of MgF_2. *J. Phys. Math. Gen.* **2001**, *34* (19), 4041–4052. https://doi.org/10.1088/0305-4470/34/19/306.

(313) Zhang, X.; Li, L.; Yu, Y.; Zhang, Q.; Sun, N.; Mao, Z.; Zhang, D. High Pressure–Temperature Study of MgF_2, CaF_2, and BaF_2 by Raman Spectroscopy: Phase Transitions and Vibrational Properties of AF_2 Difluorides. *ACS Omega* **2024**, *9* (22), 23675–23687. https://doi.org/10.1021/acsomega.4c01347.

(314) Shannon, R. D.; Prewitt, C. T. Effective Ionic Radii in Oxides and Fluorides. *Acta Crystallogr. B* **1969**, *25* (5), 925–946. https://doi.org/10.1107/S0567740869003220.

(315) Duncanson, A.; Stevenson, R. W. H. Some Properties of Magnesium Fluoride Crystallized from the Melt. *Proc. Phys. Soc.* **1958**, *72* (6), 1001–1006. https://doi.org/10.1088/0370-1328/72/6/308.

(316) Zhao, M.; Yao, X.; Zhu, Y. F.; Jiang, Q. Effect of the Interface Energy on the Pressure-Induced Superheating of Metallic Nanoparticles Embedded in a Matrix. *Scr. Mater.* **2018**, *142*, 23–27. https://doi.org/10.1016/j.scriptamat.2017.07.009.

(317) Velox Software. https://assets.thermofisher.com/TFS-Assets/MSD/Datasheets/velox-datasheet.pdf.

(318) Steike, D. R.; Hessler, M.; Korsching, E.; Lehmann, F.; Schmidt, C.; Ertmer, C.; Schnekenburger, J.; Eich, H. T.; Kemper, B.; Greve, B. Digital Holographic Microscopy for Label-Free Detection of Leukocyte Alternations Associated with Perioperative Inflammation after Cardiac Surgery. *Cells* **2022**, *11* (4), 755. https://doi.org/10.3390/cells11040755.

(319) Kastl, L.; Isbach, M.; Dirksen, D.; Schnekenburger, J.; Kemper, B. Quantitative Phase Imaging for Cell Culture Quality Control. *Cytometry A* **2017**, *91* (5), 470–481. https://doi.org/10.1002/cyto.a.23082.

(320) Baczewska, M.; Eder, K.; Ketelhut, S.; Kemper, B.; Kujawińska, M. Refractive Index Changes of Cells and Cellular Compartments Upon Paraformaldehyde Fixation Acquired by Tomographic Phase Microscopy. *Cytometry A* **2021**, *99* (4), 388–398. https://doi.org/10.1002/cyto.a.24229.

(321) Bokemeyer, A.; Buskermolen, J.; Ketelhut, S.; Tepasse, P.-R.; Vollenberg, R.; Trebicka, J.; Schmidt, H. H.; Vieth, M.; Bettenworth, D.; Kemper, B. Quantitative Phase Imaging Using Digital Holographic Microscopy to Assess the Degree of Intestinal Inflammation in Patients with Ulcerative Colitis. *J. Clin. Med.* **2023**, *12* (12), 1–16. https://doi.org/10.3390/jcm12124067.

(322) Kemper, B.; Barroso, Á.; Eder, K.; Marzi, A.; Ritz, S.; Schnekenburger, J.; Ketelhut, S. Reduction of the Influence of Parasitic Interferences and Coherence Induced Disturbances in Digital Holography-Based Quantitative Phase Microscopy by Modulation of the Object Illumination with an Electrically Focus Tunable Lens. In *Quantitative Phase Imaging VII*; Popescu, G., Park, Y., Liu, Y., Eds.; SPIE: Online Only, United States, 2021; p 20. https://doi.org/10.1117/12.2577807.

(323) Min, J.; Yfao, B.; Ketelhut, S.; Engwer, C.; Greve, B.; Kemper, B. Simple and Fast Spectral Domain Algorithm for Quantitative Phase Imaging of Living Cells with Digital Holographic Microscopy. *Opt. Lett.* **2017**, *42* (2), 227–230. https://doi.org/10.1364/OL.42.000227.

(324) Balasubramani, V.; Kuś, A.; Tu, H.-Y.; Cheng, C.-J.; Baczewska, M.; Krauze, W.; Kujawińska, M. Holographic Tomography: Techniques and Biomedical Applications. *Appl. Opt.* **2021**, *60* (10), B65–B80. https://doi.org/10.1364/AO.416902.

(325) *Surface Design: Applications in Bioscience and Nanotechnology*; Förch, R., Schönherr, H., Jenkins, A. T. A., Eds.; Wiley-VCH: Weinheim, 2009.

(326) Diez-Pascual, A. M.; Rahdar, A. Functional Nanomaterials in Biomedicine: Current Uses and Potential Applications. *ChemMedChem* **2022**, *17* (16), 1–15. https://doi.org/10.1002/cmdc.202200142.

(327) De Crozals, G.; Bonnet, R.; Farre, C.; Chaix, C. Nanoparticles with Multiple Properties for Biomedical Applications: A Strategic Guide. *Nano Today* **2016**, *11* (4), 435–463. https://doi.org/10.1016/j.nantod.2016.07.002.

(328) Doll, T. A. P. F.; Raman, S.; Dey, R.; Burkhard, P. Nanoscale Assemblies and Their Biomedical Applications. *J. R. Soc. Interface* **2013**, *10* (80), 20120740. https://doi.org/10.1098/rsif.2012.0740.

(329) Hong, E. J.; Choi, D. G.; Shim, M. S. Targeted and Effective Photodynamic Therapy for Cancer Using Functionalized Nanomaterials. *Acta Pharm. Sin. B* **2016**, *6* (4), 297–307. https://doi.org/10.1016/j.apsb.2016.01.007.

(330) Rahdar, A.; Hajinezhad, M. R.; Hamishekar, H.; Ghamkhari, A.; Kyzas, G. Z. Copolymer/Graphene Oxide Nanocomposites as Potential Anticancer Agents. *Polym. Bull.* **2021**, *78* (9), 4877–4898. https://doi.org/10.1007/s00289-020-03354-6.

(331) Patra, J. K.; Das, G.; Fraceto, L. F.; Campos, E. V. R.; Rodriguez-Torres, M. D. P.; Acosta-Torres, L. S.; Diaz-Torres, L. A.; Grillo, R.; Swamy, M. K.; Sharma, S.; Habtemariam, S.; Shin, H.-S. Nano Based Drug Delivery Systems: Recent Developments and Future Prospects. *J. Nanobiotechnology* **2018**, *16* (1), 71. https://doi.org/10.1186/s12951-018-0392-8.

(332) Pavón, C.; Benetti, E. M.; Lorandi, F. Polymer Brushes on Nanoparticles for Controlling the Interaction with Protein-Rich Physiological Media. *Langmuir* **2024**, *40* (23), 11843–11857. https://doi.org/10.1021/acs.langmuir.4c00956.

(333) Pradhan, S. S.; Saha, S. Advances in Design and Applications of Polymer Brush Modified Anisotropic Particles. *Adv. Colloid Interface Sci.* **2022**, *300* (102580), 1–40. https://doi.org/10.1016/j.cis.2021.102580.

(334) Choi, H.; Schulte, A.; Müller, M.; Park, M.; Jo, S.; Schönherr, H. Drug Release from Thermo-Responsive Polymer Brush Coatings to Control Bacterial Colonization and Biofilm Growth on Titanium Implants. *Adv. Healthc. Mater.* **2021**, *10* (2100069), 1–12. https://doi.org/10.1002/adhm.202100069.

(335) Cai, C.; Li, L.; Li, P.; Li, T.; Peng, D.; Yang, Y. Mechanoluminescence Ratiometric Thermometry via MgF_2:Tb^{3+}. *Opt. Lett.* **2022**, *47* (23), 6293–6296. https://doi.org/10.1364/OL.476530.

(336) Sasidharan, S.; Jayasree, A.; Fazal, S.; Koyakutty, M.; Nair, S. V.; Menon, D. Ambient Temperature Synthesis of Citrate Stabilized and Biofunctionalized, Fluorescent Calcium Fluoridenanocrystals for Targeted Labeling of Cancer Cells. *Biomater Sci* **2013**, *1* (3), 294–305. https://doi.org/10.1039/C2BM00127F.

(337) Kar, N.; Koppisetti, H. V. S. R. M.; Mahalingam, V. Selective Detection of Iron (III) Using Salicylic Acid Capped Tb^{3+}-Doped CaF_2 Colloidal Nanoparticles. *J. Indian Chem. Soc.* **2022**, *99* (6), 100452. https://doi.org/10.1016/j.jics.2022.100452.

(338) Flejszar, M.; Chmielarz, P. Surface-Initiated Atom Transfer Radical Polymerization for the Preparation of Well-Defined Organic–Inorganic Hybrid Nanomaterials. *Materials* **2019**, *12* (18), 1–28. https://doi.org/10.3390/ma12183030.

(339) Lilge, I.; Steuber, M.; Tranchida, D.; Sperotto, E.; Schönherr, H. Tailored (Bio)Interfaces via Surface Initiated Polymerization: Control of Grafting Density and New Responsive Diblock Copolymer Brushes. *Macromol. Symp.* **2013**, *328* (1), 64–72. https://doi.org/10.1002/masy.201350607.

(340) Lilge, I.; Schönherr, H. Synthesis and Characterization of Well-Defined Ligand-Terminated Block Copolymer Brushes for Multifunctional Biointerfaces. *Polymer* **2016**, *98* (31), 409–420. https://doi.org/10.1016/j.polymer.2016.03.031.

(341) Chiang, E. N.; Dong, R.; Ober, C. K.; Baird, B. A. Cellular Responses to Patterned Poly(Acrylic Acid) Brushes. *Langmuir* **2011**, *27* (11), 7016–7023. https://doi.org/10.1021/la200093e.

(342) Jones, S. T.; Walsh-Korb, Z.; Barrow, S. J.; Henderson, S. L.; Del Barrio, J.; Scherman, O. A. The Importance of Excess Poly(*N*-Isopropylacrylamide) for the Aggregation of Poly(*N*-Isopropylacrylamide)-Coated Gold Nanoparticles. *ACS Nano* **2016**, *10* (3), 3158–3165. https://doi.org/10.1021/acsnano.5b04083.

(343) Aqil, A.; Qiu, H.; Greisch, J.-F.; Jérôme, R.; De Pauw, E.; Jérôme, C. Coating of Gold Nanoparticles by Thermosensitive Poly(*N*-Isopropylacrylamide) End-Capped by Biotin. *Polymer* **2008**, *49* (5), 1145–1153. https://doi.org/10.1016/j.polymer.2007.12.033.

(344) Rahme, K.; Dagher, N. Chemistry Routes for Copolymer Synthesis Containing PEG for Targeting, Imaging, and Drug Delivery Purposes. *Pharmaceutics* **2019**, *11* (7), 1–23. https://doi.org/10.3390/pharmaceutics11070327.

(345) Li, M.; Jiang, S.; Simon, J.; Paßlick, D.; Frey, M.-L.; Wagner, M.; Mailänder, V.; Crespy, D.; Landfester, K. Brush Conformation of Polyethylene Glycol Determines the Stealth Effect of Nanocarriers in the Low Protein Adsorption Regime. *Nano Lett.* **2021**, *21* (4), 1591–1598. https://doi.org/10.1021/acs.nanolett.0c03756.

(346) Lilge, I.; Schönherr, H. Control of Cell Attachment and Spreading on Poly(Acrylamide) Brushes with Varied Grafting Density. *Langmuir* **2016**, *32* (3), 838–847. https://doi.org/10.1021/acs.langmuir.5b04168.

(347) Lellouche, J.; Friedman, A.; Lellouche, J.-P.; Gedanken, A.; Banin, E. Improved Antibacterial and Antibiofilm Activity of Magnesium Fluoride Nanoparticles Obtained by Water-Based Ultrasound Chemistry. *Nanomedicine Nanotechnol. Biol. Med.* **2012**, *8* (5), 702–711. https://doi.org/10.1016/j.nano.2011.09.002.

(348) El Bahi, R.; Dammak, M.; Donner, W.; Njeh, A. Charge Compensation Assisted Enhancement of Photoluminescence in (Li^{+}, Mg^{2+}, Sr^{2+}) Doped $CaTiO_3$: Eu/Dy/xGd for WLEDs Applications. *J. Lumin.* **2021**, *237*, 118176. https://doi.org/10.1016/j.jlumin.2021.118176.

(349) Ning, L.; Mak, C. S. K.; Tanner, P. A. High-Spin and Low-Spin f − d Transitions of Tb^{3+} in Elpasolite Hosts. *Phys. Rev. B* **2005**, *72* (8), 085127. https://doi.org/10.1103/PhysRevB.72.085127.

(350) Ju, Q.; Liu, Y.; Li, R.; Liu, L.; Luo, W.; Chen, X. Optical Spectroscopy of Eu^{3+}-Doped BaFCl Nanocrystals. *J. Phys. Chem. C* **2009**, *113* (6), 2309–2315. https://doi.org/10.1021/jp809233p.

(351) Ellens, A.; Andres, H.; Ter Heerdt, M. L. H.; Wegh, R. T.; Meijerink, A.; Blasse, G. Spectral-Line-Broadening Study of the Trivalent Lanthanide-Ion Series.II. The Variation of the Electron-Phonon Coupling Strength through the Series. *Phys. Rev. B* **1997**, *55* (1), 180–186. https://doi.org/10.1103/PhysRevB.55.180.

(352) Suta, M.; Wickleder, C. Synthesis, Spectroscopic Properties and Applications of Divalent Lanthanides Apart from Eu^{2+}. *J. Lumin.* **2019**. https://doi.org/10.1016/j.jlumin.2019.02.031.

(353) Dorenbos, P. The 5d Level Positions of the Trivalent Lanthanides in Inorganic Compounds. *J. Lumin.* **2000**, *91* (3–4), 155–176. https://doi.org/10.1016/S0022-2313(00)00229-5.

(354) Su, K.; He, Q.; Zhang, J.; Ren, Z.; Chen, J.; Li, J.; Wang, H.; Zhang, J.; Hao, Y. The Heterointerface Characterization of BaF_2 or MgF_2 on the Hydrogenated Diamond by X-Ray Photoelectron Spectroscopy. *Mater. Sci. Semicond. Process.* **2024**, *179*, 1–6. https://doi.org/10.1016/j.mssp.2024.108516.

(355) Jiang, S.; Lyu, B.; Müller, M.; Wesner, D.; Schönherr, H. Thickness-Encoded Micropatterns in One-Component Thermoresponsive Polymer Brushes for Culture and Triggered Release of Pancreatic Tumor Cell Monolayers and Spheroids. *Langmuir* **2018**, *34* (48), 14670–14677. https://doi.org/10.1021/acs.langmuir.8b03040.

(356) Volkmer, B.; Heinemann, M. Condition-Dependent Cell Volume and Concentration of Escherichia Coli to Facilitate Data Conversion for Systems Biology Modeling. *PLoS ONE* **2011**, *6* (7), 1–6. https://doi.org/10.1371/journal.pone.0023126.

(357) Beal, J.; Farny, N. G.; Haddock-Angelli, T.; Selvarajah, V.; Baldwin, G. S.; Buckley-Taylor, R.; Gershater, M.; Kiga, D.; Marken, J.; Sanchania, V.; Sison, A.; Workman, C. T.; iGEM Interlab Study Contributors; Aachen; Pehlivan, M.; Roige, B. B.; Aalto-Helsinki; Aarnio, T.; Kivisto, S.; Koski, J.; Lehtonen, L.; Pezzutto, D.; Rautanen, P.; AHUT_China; Bian, W.; Hu, Z.; Liu, Z.; Liu, Z.; Ma, L.; Pan, L.; Qin, Z.; Wang, H.; Wang, X.; Xu, H.; Xu, X.; Aix-Marseille; El Moubayed, Y.; ASTWS-China; Dong, S.; Fang, C.; He, H.; He, H.; Huang, F.; Shi, R.; Tang, C.; Tang, C.; Xu, S.; Yan, C.; Athens; Bartzoka, N.; Kanata, E.; Kapsokefalou, M.; Katopodi, X.-L.; Kostadima, E.; Kostopoulos, I. V.; Kotzastratis, S.; Koutelidakis, A. E.; Krokos, V.; Litsa, M.; Ntekas, I.; Spatharas, P.; Tsitsilonis, O. E.; Zerva, A.; Austin_LASA; Annem, V.; Cone, E.; Elias, N.; Gupta, S.; Lam, K.; Tutuianu, A.; Austin_UTexas; Mishler, D. M.; Toro, B.; Baltimore_BioCrew; Akinfenwa, A.; Burns, F.; Herbert, H.; Jones, M.; Laun, S.; Morrison, S.; Smith, Z.; BCU; Peng, Z.; Ziwei, Z.; BFSUICC-China; Deng, R.; Huang, Y.; Li, T.; Ma, Y.; Shen, Z.; Wang, C.; Wang, Y.; Zhao, T.; BGIC-Global; Lang, Y.; Liang, Y.; Wang, X.; Wu, Y.; BGU_Israel; Aizik, D.; Angel, S.; Farhi, E.; Keidar, N.; Oser, E.; Pasi, M.; Bielefeld-CeBiTec; Kalinowski, J.; Otto, M.; Ruhnau, J.; Bilkent-UNAMBG; Cubukcu, H.; Hoskan, M. A.; Senyuz, I.; BioIQS-Barcelona; Chi, J.; Sauter, A. P.; Simona, M. F.; BioMarvel; Byun, S.; Cho, S.; Kim, G.; Lee, Y.; Lim, S.; Yang, H.; BIT; Xin, T.;

Yaxi, Z.; Zhao, P.; BIT-China; Han, W.; He, F.; He, Y.; Li, N.; Luo, X.; BJRS_China; Boxuan, C.; Jiaqi, H.; Liangjian, Y.; Wanji, L.; Xinguang, C.; Xinyu, L.; BNDS_CHINA; Wu, Z.; Xi, Y.; Yang, X.; Yang, Y.; Yang, Z.; Zhang, Y.; Zhou, Y.; BNU-China; Peng, Y.; Yadi, L.; Yang, S.; Yuanxu, J.; Zhang, K.; BOKU-Vienna; Abraham, D.; Heger, T.; BostonU; Leach, C.; Lorch, K.; Luo, L.; British_Columbia; Gaudi, A.; Ho, A.; Huang, M.; Kim, C.; Kugathasan, L.; Lam, K.; Pan, C.; Qi, A.; Yan, C.; Calgary; Schaaf, K.; Sillner, C.; Cardiff_Wales; Coates, R.; Elliott, H.; Heath, E.; McShane, E.; Parry, G.; Tariq, A.; Thomas, S.; CCU_Taiwan; Chen, C.-W.; Cheng, Y.-H.; Hsu, C.-W.; Liao, C.-H.; Liu, W.-T.; Tang, Y.-C.; Tang, Y.-H.; Yang, Z. E.; CDHSU-CHINA; Jian, L.; Li, C.; Lin, C.; Ran, G.; Run, Z.; Ting, W.; Yong, Z.; Yu, L.; Chalmers-Gothenburg; Lind, A. C.; Norberg, A.; Olmin, A.; Sjolin, J.; Torell, A.; Trivellin, C.; Zorrilla, F.; Vries, P. G. D.; CIEI-BJ; Cheng, H.; Peng, J.; Xiong, Z.; CMUQ; Altarawneh, D.; Amir, S. S.; Hassan, S.; Vincent, A.; CO_Mines; Costa, B.; Gallegos, I.; Hale, M.; Sonnier, M.; Whalen, K.; ColumbiaNYC; Elikan, M.; Kim, S.; You, J.; Cornell; Rambhatla, R.; Viswanathan, A.; CPU_CHINA; Tian, H.; Xu, H.; Zhang, W.; Zhou, S.; CSU_CHINA; Jiamiao, L.; Jiaqi, X.; CSU_Fort_Collins; Craw, D.; Goetz, M.; Rettedal, N.; Yarbrough, H.; Delgado-Ivy-Marin; Ahlgren, C.; Guadagnino, B.; Guenther, J.; Huynh, J.; DLUT_China; He, Z.; Liu, H.; Liu, Y.; Qu, M.; Song, L.; Yang, C.; Yang, J.; Yin, X.; Zhang, Y.; Zhou, J.; Zi, L.; DLUT_China_B; Jinyu, Z.; Kang, X.; Xilei, P.; Xue, H.; Xun, S.; DNHS_SanDiego; Babu, P.; Dogra, A.; Thokachichu, P.; DTU-Denmark; Faurdal, D.; Jensen, J. H.; Mejlsted, J.; Nielsen, L.; Rasmussen, T.; Duesseldorf; Denter, J.; Husnatter, K.; Longo, Y.; Ecuador; Luzuriaga, J. C.; Moncayo, E.; Moreira, N. T.; Tapia, J.; ECUST; Dingyue, T.; Jingjing, Z.; Wenhao, X.; Xinyu, T.; Xiujing, H.; Edinburgh_OG; DeKloe, J.; Edinburgh_UG; Astles, B.; Baronaite, U.; Grazulyte, I.; Emory; Hwang, M.; Pang, Y.; EPFL; Crone, M. A.; Hosseini, R.; Houmani, M.; Zadeh, D.; Zanotti, V.; ETH_Zurich; Baltensperger, O. A.; Bijman, E. Y.; Garulli, E.; Krusemann, J. L.; Martinelli, A.; Martinez, A.; Vornholt, T.; Evry_Paris-Saclay; Camille, M.; Paul, A.; Exeter; Browne, E.; Gilman, D. B. J.; Hewitt, A.; Hodson, S.; Holmedal, I.; Kennedy, F.; Sackey, J.; FAU_Erlangen; Beck, S.; Eidloth, F.; Imgold, M.; Matheis, A.; Meerbrei, T.; Ruscher, D.; Schaeftlein, M.; FJNU-China; Hanrong, Z.; Fudan; Wan, M.; Fudan-CHINA; Dai, L.; Jin, K.; Wang,

S.; Wang, X.; Wang, Y.; Wang, Y.; Wu, C.; Zhang, Z.; Zhou, Y.; GDSYZX; Xinyu, L.; Zirong, Z.; Georgia_State; Babar, R.; Brewer, M.; Clodomir, C.; Das Neves, L.; Iwuogo, A.; Jones, A.; Jones, C.; Kelly, J.; Kim, G.; Siemer, J.; Yadav, Y.; Gifu; Ikagawa, Y.; Isogai, T.; Niwa, R.; GO_Paris-Saclay; Aubry, C.; Briand, W.; Jacq, A.; Lautru, S.; Marta, B.; Maupu, C.; Ollessa-Daragon, X.; Papadopoulo, K.; Azad, M. S.; GreatBay_China; Kuangyi, W.; Xiu, Y.; Yang, C.; Groningen; Iyer, A.; Prins, R.; Yesley, P.; GZHS-United; Lichi, F.; Xuan, C. Z.; HAFS; Jo, K.; Park, M.; Park, S.; Yoo, H.; Hamburg; Burckhardt, N.; Daniels, L.; Klopprogge, B.; Kruger, D.; Meyfarth, O.-E.; Putthoff, L.; Wawrzyniak, D.; HBUT-China; Hu, X.; Wang, Y.; HebrewU; Badash, L.; Baichman-Kass, A.; Barshap, A.; Friedman, Y.; Milshtein, E.; Vardi, O.; HFLS_ZhejiangUnited; Dong, S.; Gu, Y.; Pei, Y.; Shi, R.; Yang, F.; Yang, J.; Zhu, X.; HK_HCY_LFC; Ching, L. K.; Ching, L. H.; Chun, N. T.; Hin, Y. M.; Hong, L. T.; Lam, C. W.; Lam, Y. C.; Matthew, C.; Ngo, C. T.; Shuan, Y.; Wan, C. T.; Yan, T. S.; Yee, C. Y.; Yu, T. C.; Yu, Y. W.; HKJS_S; Anson, C. T. H.; Choi, L. S.; Chun, C. M.; Hin, C. L.; Hin, W. C.; Ho, N. S.; Jay, L. C. Y.; Katherine, L. M. W.; Kin-ning, W. C.; Kiu, L. H.; Kong, C. C.; Wai, L. C.; Yan, Y. W.; Yeung, W. T.; Yin, L. K.; Hong_Kong_HKU; Grace, T. S. Y.; Joe, L. K. C.; Kenneth, N. T. C.; Shuan, C. M. Y.; Hong_Kong_HKUST; Aldo, F.; Pang, C. H.; So, K. P.; Wong, H. M.; Hong_Kong_JSS; Ching, L. T.; Ching, L. H.; Fung, I. N.; Fung, Y. S.; Hong, L. C.; Ning, H. O.; Sang, J. C. H.; Hong_Kong-CUHK; Elsa, Y. H. L.; Hei, C. Y.; Sing, L. H.; Wang, C. S.; HUBU-Wuhan; Gu, Y.; Rong, Z.; Song, H.; Wang, P.; Wang, Y.; HUST-China; Chen, Y.; Qiu, H.; Ren, H.; Xiao, Z.; HZAU-China; Heng, H.; Rao, X.; Tian, R.; ICT-Mumbai; Deb, S. S.; Kamble, Y. L.; Kumbhojkar, N.; Patel, B.; Prakash, S.; Reshamwala, S. M. S.; Taskar, P.; IISc-Bangalore; Gokul; Uday, A. B.; IISER-Bhopal-India; Basu, A.; Gandhi, R.; Khaimani, J.; Khenwar, A.; Raut, S.; Somvanshi, T.; IISER-Kolkata; Das, D.; Ghosh, S.; Rai, H.; IISER-Mohali; Anand, N. M.; Jainarayanan, A. K.; Kalson, P.; Liya, D. H.; Mishra, V.; Pai, S. S.; Pitaliya, M.; Rana, Y.; Yadav, R.; IIT_Delhi; Arora, N.; Arora, V.; Jain, S.; Patel, A.; Sharma, S.; Singh, P.; IIT_Kanpur; Goenka, A.; Jain, R.; Jha, A.; Kumar, A.; Soni, A.; IIT-Madras; Ananthakrishnan, S.; Devi, V.; Faidh, M.; Jayaraman, G.; Kittur, M. S.; Mahapatra, N. R.; Menon, S.; Muthukrishnan, A. B.; Kailash, B. P.; Sabuwala, B.; Shinde, M.; Venkatraghavan, S.;

Jiangnan_China; Liu, W.; Miao, Z.; Wang, T.; Wang, Y.; Zhang, S.; Jilin_China; Chai, R.; Ge, Y.; Hou, A.; Liu, F.; Liu, X.; Mao, J.; Wang, Z.; Yu, H.; Yuan, H.; Zhan, Y.; JMU_Wuerzburg; Ries, A.; Wolfbeisz, C.; KAIT_JAPAN; Kanaya, T.; Kawasaki, Y.; Maruo, T.; Mori, Y.; Satoh, T.; KCL_UK; Chau, A.; Chu, W. Y.; Markiv, A.; Marti, M. V.-H.; Medina, M. J. R.; Raju, D.; Sinha, S.; KUAS_Korea; Choi, Y.; Ryu, B. S.; Lambert_GA; Byagathvalli, G.; Kim, E.; Leiden; Crooijmans, M.; Waard, J. D.; Amstel, C. V.; Lethbridge; Demchuk, A.; Haight, T.; Kim, D. J.; Neda, A.; Roberts, L.; Saville, L.; Takeyasu, R.; Tobin, D.; Lethbridge_HS; Akbary, M.; Avileli, R.; He, K.; Pageni, A.; Saville, L.; Silva, D. D.; De Silva, N.; Turton, K.; Wu, M.; Zhang, A.; Lubbock_TTU; Chavez, B.; Garavito, P.; Latham, M.; Ptak, J.; Tharp, D.; Lund; Izzati, N.; Jonsson, M.; Labecka, N.; Palo, S.; Macquarie_Australia; Beale, R.; Logel, D.; Mellou, A.-E.; Myers, K.; Madrid-OLM; Alonso, A.; Cifuentes, R. H.; Clemente, B. S.; Gonzalo, G. S.; Hernandez, I. M.; Hernandez, L. A.; Lombardero, F. J. Q.; Marquina, D.; Rodriguez, G. F.; Smet, I. A.; Manchester; Butterfield, T.; Deshmukh-Reeves, E.; Gogineni, N.; Hemmings, S.; Kabbara, I.; Norvaisaite, I.; Smith, R.; Marburg; Bauersachs, D.; Daniel, B.; Inckemann, R.; Seiffermann, A.; Stukenberg, D.; Weile, C.; McGill; Clerc, V.; Ha, J.; Totten, S.; McMaster; Chang, T.; Jimenez, C.; Maddiboina, D.; METU_HS_Ankara; Acar, B. L.; Elcin, E.; Inanc, T.; Kantas, G.; Kayihan, C.; Secen, M.; Suer, G.; Ucan, K.; Unal, T.; Michigan; Fischer, M.; Jasti, N.; Stewart, T.; MichiganState; Caldwell, S.; Lee, J.; Schultz, J.; Mingdao; Chang, T.-C.; Chen, P.-H.; Cheng, Y.-H.; Hsu, Y.-H.; Yeh, C.; Minnesota; Ding, Z.; Li, Z.; Lockwood, S.; Quinn, K.; Montpellier; Carrillo, L.; Heintze, M.; Meneu, L.; Peras, M.; Yehouessi, T.; Munich; Eilers, K.; Falgenhauer, E.; Kiu, W. H.; Mayer, J.; Mueller, J.; Von Schoenberg, S.; Schwarz, D.; Tunaj, B.; Nanjing-China; Hu, Z.; Huang, Y.; Li, Y.; NAU-CHINA; Fang, C.; Liu, J.; Liu, Y.; Wu, Y.; Xu, S.; Yuan, L.; NAWI_Graz; Edelmayer, M.; Hiesinger, M.; Hofer, S.; Krainer, B.; Oswald, A.; Strasser, D.; Zimmermann, A.; NCHU_Taichung; Chen, Y.-C.; NCTU_Formosa; Chan, Y.-Y.; Chang, Y.-C.; Deng, N. R.; Ku, C.-Y.; Lee, M.-Z.; NEU_China_A; Li, H.; Liu, Z.; Song, G.; Xiang, Y.; Yan, H.; NEU_China_B; Huanying, H.; Qiaochu, J.; Shengjuan, J.; Yujie, P.; Newcastle; Burridge, M.; Standforth, K.; Went, S.; NJU-China; Chenxi, L.; Han, W.; Qipeng, Z.; Yifan, L.; Yiming, Q.; Yutong, P.;

NKU_CHINA; Kou, S.; Luan, L.; Northwestern; Akova, U.; Fitzgerald, L.; Ikwuagwu, B.; Johnson, M.; Kurian, J.; Throsberg, C.; Nottingham; Allen, L.; Humphreys, C.; Partridge, D.; Whittle, M.; Zilinskaite, N.; NPU-China; Lee, M.; Lin, W.; Ma, Y.; Wang, K.; NTHU_Formosa; Cheng, H.; Chi, S.; Chuang, Y.-C.; Huang, R.; Ko, L.; Lin, Y.-C.; NTHU_Taiwan; Tsai, Y.-Y.; Wang, C.-C.; Yu, K.-C.; NTNU_Trondheim; Burud, H. N.; Chen, C.; Haralsvik, A. K.; Marinovic, A.; Pedersen, H. H.; Sande, A.; Solvang, V.; NTU-Singapore; Ming, S. K.; Praditya, A.; NU_Kazakhstan; Abduraimova, A.; Meirkhanova, A.; Mukhanova, A.; Mulikova, T.; NUDT_CHINA; Gou, Y.; Lu, C.; Ma, J.; Zhu, C.; NUS_Singapore-A; Aaron, L. C. Y.; Iyer, T. S.; Jiacheng, W.; Lim, Y. P.; Lin, B. T. X.; Ramzeen, A.; Yong, N. L. B. A. O.; NUS_Singapore-Sci; Chua, Y. T. S.; Fong, Y. D.; He, M.; Tan, L. Y.; NWU-China; Jiahe, Z.; Mingge, L.; Nianlong, L.; Yueyi, L.; Yuhan, C.; NYMU-Taipei; Chang, A.; Chen, C.-C.; Chou, R.; Clapper, J.; Lai, E.; Lin, Y.; Wang, K.; Yang, J.; NYU_Abu_Dhabi; Anwar, M.; Chehade, I.; Hariyani, I.; Hau, S.; Isaac, A.; Karpauskaite, L.; Magzoub, M.; Obaji, D.; Song, Y. R.; Yun, Y.; OUC-China; Sun, K.; Zhang, Y.; Oxford; Beard, E.; Crosby, L. C.; Delalez, N.; Karshenas, A.; Kozhevnikov, A.; Kryukova, J.; Saini, K.; Stocks, J.; Sudarshan, B.; Taylor, M.; Wadhams, G.; Windo, J.; Paris_Bettencourt; Ameziane, A.; Bhatt, D.; Casas, A.; Levrier, A.; Santos, A.; Sia, N. E. M.; Wintermute, E.; Pasteur_Paris; Dejoux, A.; Gopaul, D.; Guerassimoff, L.; Jaoui, S.; Madelenat, M.; Petracchini, S.; Peking; Cai, F.; Jianzhao, Y.; Shuyu, S.; Tairan, L.; Xin, L.; Yongjie, L.; Zhecheng, H.; Pittsburgh; Becker, E.; Greenwald, M.; Hu, V.; Pavelek, T.; Pinto, E.; Wei, Z.; Purdue; Burgland, Z.; Chan, J.; Dejoie, J.; Fitzgerald, K.; Hartley, Z.; Rasheed, M.; Schacht, M.; Queens_Canada; Gahagan, M.; Kelly, E.; Krauss, E.; RDFZ-China; Cao, Y.; Shen, Y.; Wang, X.; Xu, H.; Zhang, J.; REC-CHENNAI; Chandramouli, P.; Ashwin F, A. J.; Jayaraman, S.; Jude, M. S.; Kumar, V.; Lekshmi, H.; Preetha, R.; Rashid, K.; Deepak Kumar, S.; Mohan Kumar, B. S.; Rheda_Bielefeld; Barrat, L. M.; Dissmann, J.-S.; Kalinowski, J.; Otto, M.; Ruhnau, J.; Stuhlweissenburg, F.; Ueding, E.; RHIT; Bohner, A.; Clark, B.; Deibel, E.; Klaas, L.; Pate, K.; Weber, E.; Rice; Cohen, K.; Guseva, A.; King, S.; Yoon, S.; Ruia-Mumbai; Ambre, S.; Bhowmick, S.; Pange, N.; Parab, K.; Patel, V.; Patil, M.; Rajurkar, A.; Rege, M.; Sawant, M.; Sawant, S.; Vaidya, A.; SBS_SH_112144; Ji, P.; Luo, F.; Ma, G.; Xu, X.; Yin, J.; Zhou, Y.;

Zhu, K.; SCAU-China; Huang, Y.; Huang, Y.; Li, J.; Li, X.; Wang, H.; Wang, K.; Wang, W.; Zhang, X.; Zou, J.; SCU-China; Bao, M.; Kang, H.; Liu, X.; Tao, Y.; Wang, Z.; Yang, F.; Zhang, T.; Zhong, Y.; SCUT_ChinaB; Liu, J.; Liu, J.; Ma, L.; Niu, X.; Qian, L.; Wang, L.; Yan, Q.; Zhao, N.; SCUT-ChinaA; Chen, W.; Zhou, Y.; SDU-CHINA; Chen, J.; SFLS_Shenzhen; Hao, J.; HuaYue, Z.; Li, P.; Pei, Y.; Qu, J.; Wang, R.; Wang, X.; Wu, K.; Wu, Y.; Xiang, M.; Yang, L.; Yang, Z.; Zhaoting, L.; ShanghaiTech; Fu, W.; Li, Z.; Tang, W.; Zhang, K.; SHSBNU_China; Li, H.; Shao, X.; Yang, C.; Zeng, Y.; Zhou, Y.; SHSID_China; Dong, S.; Jung, Y.; Li, S. R.; Li, T.; Yu, J.; SHSU_China; Dong, S.; Li, T.; Miao, X.; Wang, S.; SIAT-SCIE; Ding, Y.; Huang, J.; Li, Y.; Sun, T.; Tian, Q.; Wu, M.; Xing, J.; Xiong, X.; Yan, Y.; Yihang, Q.; Zhang, J.; Zhou, Y.; Zhou, Z.; SJTU-BioX-Shanghai; Chen, Z.; He, P.; Hong, Y.; Hsiao, C.-Y.; Liang, Z.; Liu, Z.; Ran, Y.; Sun, S.; Xia, R.; SKLMT-China; Dong, D.; Zhao, W.; SMMU-China; Hu, M.; Hu, S.; Shi, W.; Shulun; Yan, H.; Ye, Y.; SMS_Shenzhen; Hong, Y.; Pan, Y.; Song, Y.; Zhang, J.; Zhao, Y.; Sorbonne_U_Paris; Chater, D.; Foda, A.; Li, Y.; Saade, U.; Sayous, V.; SSHS-Shenzhen; Mo, Y.; Ren, W.; Zeng, C.; SSTi-SZGD; Cao, Y.; St_Andrews; Czekster, C.; Dunstan, I.; Powis, S.; Reaney, B.; Snaith, E.; Young, C.; Stanford; Frankel, E.; Glockner, E.; Justice, I.; Stanford-Brown-RISD; Murugan, S.; Penny, L.; Stockholm; Garcia, C.; Rentouli, S.; Stony_Brook; Aggarwal, P.; Budhan, S.; Chiang, W.; Kwasniak, D.; Ledalla, K.; Lee, M.; Lo, N.; Mullin, M.; Pan, L. Y.; Rakhimov, J.; Ruzic, R.; Shah, M.; Velikov, L.; Vincent, S.; Stuttgart; Horz, P.; Kuebler, N.; Notheisen, J.; SUIS_Shanghai; Doyle, D.; Gu, J.; Hu, W.; Yang, S.; SYSU-CHINA; Kehan, T.; Menghan, G.; Xiaowen, M.; SYSU-Software; Chen, Y.; Kang, Z.; Ni, H.; SZU-China; Chen, J.; He, L.; Luo, M.; Tang, J.; Tacoma_RAINmakers; Boyce, K.; Lee, J.; Martin, M.; Nguyen, J. V.; Wan, L.; Tartu_TUIT; Astapenka, A.; Badalli, T.; Borovko, I.; Chulkova, N.; Faustova, I.; Kolosova, A.; Loog, M.; Maljavin, A.; Matiyevskaya, F.; Tuzov, V.; TAS_Taipei; Chang, C.; Chou, R.; Clapper, J.; Ho, T.; Hsieh, Y. D.; Lai, E.; Tsai, L.; Wang, K.; Wu, J.; Tec-Chihuahua; Dominguez, V. I. P.; Fernandez, C. I. R.; Fierro, D. O.; Nunez, A. K. A.; Perez, J. P. R.; Rivera, M. L.; Trevizo, C. L. G.; Velasco, M. A. L.; Tec-Monterrey; Oropeza, C. J. C.; Mendoza, A. F. H.; Figueroa, J. A. J.; Leal, L. M.; Benavides, S. A. P.; Martinez, V. J. R.; Aguirre, A. L. R.; Alvarado, A. B.

S.; Solano, M. S. C.; Castillo, N. E. T.; Zamora, A. R.; Pena Thevenet, E. D. L.; TecCEM; Blas, K. S.; Huerta, A. L. T.; Resendiz, A. C.; TecMonterrey_GDL; Cruz, F.; Diaz, F.; Espinoza, D.; Figueroa, A. C.; Luque, A. C.; Portillo, R.; Senes, C.; Tamayo, D.; Del Toro, M.; Thessaloniki; Alexopoulos, I.; Giannopoulos, A. D.; Giannoula, Y.; Kyrpizidis, G.; Tongji_China; Xinyue, M.; Xirui, C.; Zhiwei, S.; Toronto; Adler, N.; Caballero, A.; Hamady, C.; Ibrahim, A.; Parmar, J.; Rastogi, T.; Yang, J.; Toulouse-INSA-UPS; Delhomme, J.; Henras, A.; Heux, S.; Romeo, Y.; Toanen, M.; Wagner, C.; Zanoni, P.; TU_Darmstadt; Lotz, T.; Nickels, E.; Suss, B.; Warzecha, H.; Zimmermann, J.; TU-Eindhoven; Dubuc, E.; Eijkens, B.; Keij, S.; Twisk, S.; Verhagen, M.; Oetelaar, M. V. D.; TUDelft; Armstrong, A.; Bennis, N.; Bouwmeester, S.; Buller, L.; Kohabir, K.; Leeuw, M. D.; Mangkusaputra, V.; Mattens, J.; Nijenhuis, J.; Paez, T.; Schmidtchen, L.; Voort, G. V. D.; TUST_China; Ge, G.; Haoran, X.; Xiaojin, L.; UAlberta; Agena, E.; Agena, E.; Bath, S.; Campbell, R.; Dalangin, R.; Kim, A.; Sauvageau, D.; Shkolnikov, I.; UC_Davis; Graves, D.; Lang, J.; Nieberding-Swanberg, J.; Rao, A.; Torres, A.; Yao, A.; UC_San_Diego; Abbas, A.; Luo, C.; UCAS-China; Zepeng, X.; Ziyi, Z.; UChicago; Chen, J.; Colgan, C.; Dvorkin, S.; Filzen, R.; Patel, V.; Scott, A.; Zulueta, P.; UChile_Biotec; Acosta, J.; Araya, L.; Chavez, F.; Farias, S.; Garrido, D.; Marcoleta, A.; Munoz, F.; Rivas, P.; UCL; Colant, N.; Fan, C.; Frank, S.; Gabrielli, J.; Handal, P.; Pinheiro, V.; Santamaria, S.; Withanage, S.; Xue, F.; UCLouvain; Gerard, A.; Lefevre, M.; Milano, F.; Oliveira, N. D. S.; Parmentier, M.; Rigon, L.; UConn; Chamiec-Case, E.; Chen, R.; Crowley, P.; Doyle, S.; Kadimi, S.; Vella, T.; UCopenhagen; Adulyanukosol, N.; Dusseaux, T. A.; Forman, V.; Hansen, C.; Kofoed, S.; Louis, S.; Lykkegaard, M. R.; Mancinotti, D.; Meyer, L.; Michelsen, S.; Raadam, M.; Rasmussen, V. S.; Thormar, E. A.; Uslu, A.; Leelahakorn, N.; UESTC-China; Ding, S.; Li, C.; Tan, H.; Xu, Y.; Yang, J.; UFlorida; Gamoneda, D.; Kantor, N.; Trujillo-Rodriguez, L.; Turner, M.; UGA; George, S.; McConnell, K.; Pollitt, C.; UI_Indonesia; Amin, I. F.; Ikhsan, M.; Japranata, V. V.; Laurentius, A.; Nurachman, L. A.; Pratama, M. I. A.; UiOslo_Norway; Dirven, Y.; Frohlich, L.; Linke, D.; Mertes, V.; Rolfsnes, R. R.; Saragliadis, A.; UIOWA; Castillo, S.; Chinnathambi, S.; Ellermeier, C.; Farrell, J.; Fassler, J.; Fuentes, E.; Ryan, S.; Sander, E.; UIUC_Illinois; Bott, A.; Healy, L.;

Karumanchi, P.; Ruzicka, A.; Wang, Z.; ULaval; Byatt, G.; Despres, P. C.; Dube, A.; Lemieux, P.; Echelard, F.; Lortie, L.-A.; Rouleau, F. D.; ULaVerne_Collab; Barrington, S.; Basulto, C.; Delgadillo, S.; Leon, K. D.; Madrid, M.; Meas, C.; Sabandal, A.; Sanchez, M. A.; Tsui, J.; Woodward, N.; UMaryland; Battina, R.; Boyer, J.; Cherupalla, A.; Chiang, J.; Heng, M.; Keating, C.; Liang, T.; Loke, C. K.; Premo, J.; Srinivasan, K.; Starkel, J.; Zheng, D.; UNebraska-Lincoln; Astorino, G.; Cott, R. V.; Guo, J.; Kortus, D.; Niu, W.; Unesp_Brazil; Freire, P. J. C.; Pedrolli, D. B.; Ribeiro, N. V.; Silva, B. F.; Vanini, N. V.; Mota, M. S. D.; Crispim, L. D. S.; UNSW_Australia; Chapman, T.; Gaitt, T.; Jones, M.; Watson, E.; UPF_CRG_Barcelona; Lopez-Grado, G.; Sans, L.; UPF_CRG_Barcelona; Brink, M.; Rajagopal, V.; Ramstrom, E.; US_AFRL_CarrollHS; Bete, A.; Camacho, Y.; Carter, J.; Davis, C.; Dong, J.; Ehrenworth, A.; Goodson, M.; Guptil, C.; Herrmann, M.; Hung, C.; Jesse, H.; Krabacher, R.; McDonald, D.; Menart, P.; O'Leary, T.; Polanka, L.; Poole, A.; Varaljay, V.; USMA-West_Point; Appel, A.; Cave, J.; Huuki, L.; McDonough, M.; Mills, C.; Mitropoulos, A.; Pruneski, J.; Wickiser, K.; USP-Brazil; Buson, F. X.; Flores, V.; Lima, G. M.; Rosa, C. G. T.; UST_Beijing; Bao, G.; Dong, H.; Luo, Z.; Peng, J.; USTC; An, Y.; Cheng, C.; Jiang, Z.; Kong, L.; Luo, C.; Luo, L.; Shi, Y.; Tang, E.; Wang, P.; Wang, Y.; Xu, G.; Yu, W.; Zhang, B.; Zhang, Q.; UT-Knoxville; Garcia, D.; Jiang, N.; Kristy, B.; Laurel, R.; Leitner, K.; Loeffler, F.; Ripp, S.; Street, M.; Utrecht; Amheine, K.; Bindt, F.; Boer, M.; Boxem, M.; Govers, J.; Jongkees, S.; Pattiradjawane, L.; Swart, P.; Tsang, H.; Graaf, F. D.; Ten Dam, M.; Heijningen, F. V.; Valencia_UPV; Boada, Y.; Vignoni, A.; Vilnius-Lithuania; Brasas, V.; Gaizauskaite, A.; Jakutis, G.; Jasiunas, S.; Juskaite, I.; Ritmejeris, J.; Vaitkus, D.; Venclovas, T.; Vitkute, K.; Yeliseyeva, H.; Zukauskaite, K.; Zvirblyte, J.; Vilnius-Lithuania-OG; Karpus, L.; Mazelis, I.; Rokaitis, I.; Virginia; Akingbesote, N. D.; Culfogienis, D.; Huang, W.; Park, K.; Warwick; Ahuja, J.; Corre, C.; Dhaliwal, G.; Evans, R.; Hill, K.; Holman, O.; Jaramillo, A.; Khalid, A.; Lawrence, J.; Mansfield, L.; O'Brien, J.; Ong, J.; Prakash, S.; Whiteside, J.; Washington; Anderson, K.; Chun, E.; Kim, G.; Nguyen, A.; Shola, C.; Toghani, D.; Wong, A.; Wong, J.; Yung, J.; WashU_StLouis; Johnson, E.; Lahad, D.; Nicholson, K.; Pedamallu, H.; Phelan, C.; Waterloo; Fikry, C.; Fulton, L.; Lassel, N.; Perera, D.; Robin, M.; Shaw, N.; Westminster_UK;

Bowman, K.; Coleman, S.; Emilov, K.; Gaspar, C.; Jenakendran, J.; Mubeen, S.; Obrvan, M.; Smith, C.; WHU-China; Bo, T.; Du Liaoqi; Tianyi, C.; Yuan, X.; Yue, Q.; William_and_Mary; Do, S.; Fang, X.; Jones, E.; Laury, J.; Liu, W.; Oliver, A.; Parr, L.; Saha, M.; Shen, C.; Son, T.; Urban, J.; Verma, Y.; Zhou, H.; Worldshaper-Wuhan; Dong, S.; Hao, Z.; Kuang, Y.; Liu, T.; Zhou, R.; WPI_Worcester; Arruda, B.; Farny, N.; Hao, M.; Pearce, C.; Rebello, A.; Sharma, A.; Sumner, K.; Sweet, B.; XJTLU-CHINA; Lin, J.; XJTU-China; Mengtao, D.; Peiyao, F.; Xinlei, F.; XMU-China; Cai, N.; Chen, J.; Fu, Y.; Hu, Y.; Qiang, Y.; Wang, Q.; Yang, R.; Yucheng, C.; Zheng, J.; Yale; Chang, K.; Gao, C.; Isaacs, F.; Li, K.; Moscoso, R.; Patel, J.; Telesz, L.; Tirad, A.; ZJU-China; Cao, Q.; Feng, X.; Lu, Y.; Zhang, X.; Zhou, X.; ZJUT-China; Sun, D.; Yuan, Z.; Zhou, J. Robust Estimation of Bacterial Cell Count from Optical Density. *Commun. Biol.* **2020**, *3* (1), 1–29. https://doi.org/10.1038/s42003-020-01127-5.

(358) Kinoshita, T.; Kiso, K.; Le, D. Q.; Shiigi, H.; Nagaoka, T. Light-Scattering Characteristics of Metal Nanoparticles on a Single Bacterial Cell. *Anal. Sci.* **2016**, *32* (3), 301–305. https://doi.org/10.2116/analsci.32.301.

(359) Sausset, R.; Krupova, Z.; Guédon, E.; Peron, S.; Grangier, A.; Petit, M.-A.; De Sordi, L.; De Paepe, M. Comparison of Interferometric Light Microscopy with Nanoparticle Tracking Analysis for the Study of Extracellular Vesicles and Bacteriophages. *J. Extracell. Biol.* **2023**, *2* (2), 1–17. https://doi.org/10.1002/jex2.75.

(360) Banin, E.; Alexandra Friedman; Roxanne Lahmi; Aharon Gedanken; Banin, E. Antibiofilm Surface Functionalization of Catheters by Magnesium Fluoride Nanoparticles. *Int. J. Nanomedicine* **2012**, 1175–1188. https://doi.org/10.2147/IJN.S26770.

Appendix

I TEM and STEM images of TiO_2@SiO_2 and LaF_3:$Ce^{3+}Tb^{3+}$ NPs.

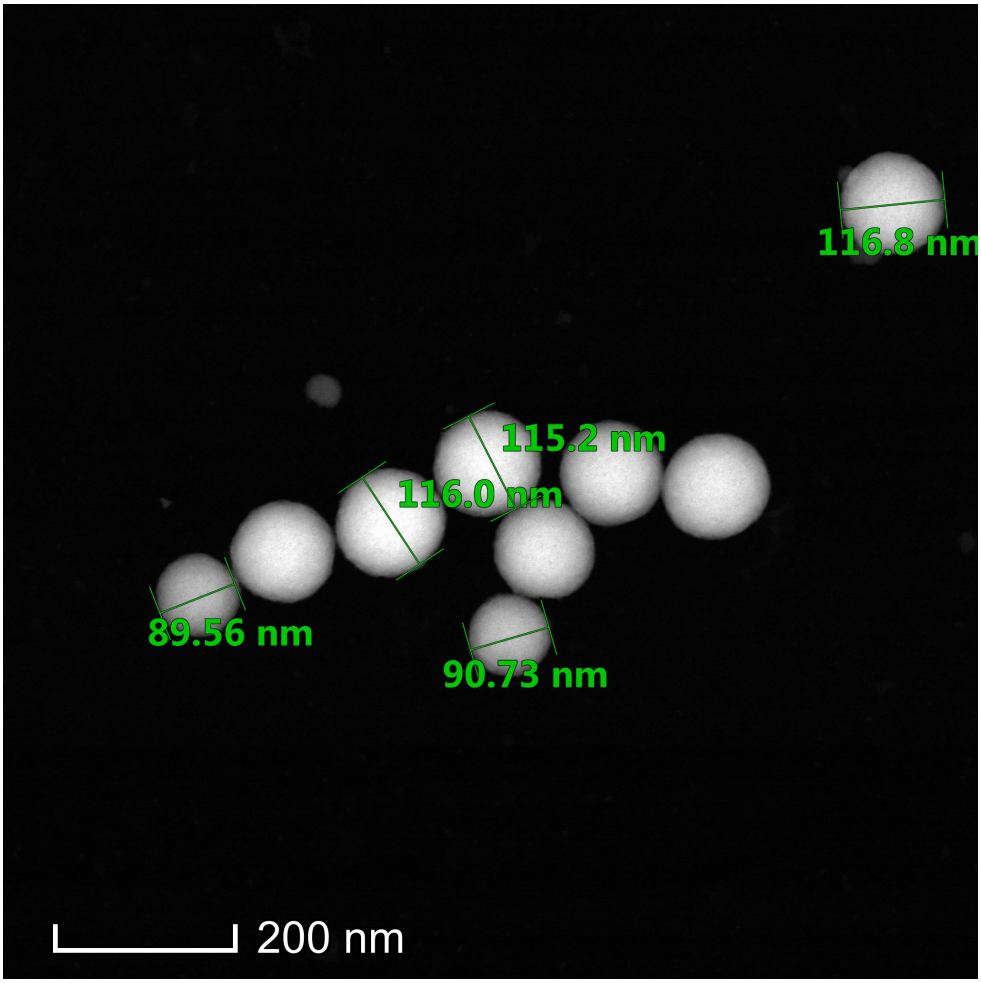

Figure 9.1: STEM images of TiO_2@SiO_2 NPs prepared via Stöber synthesis.

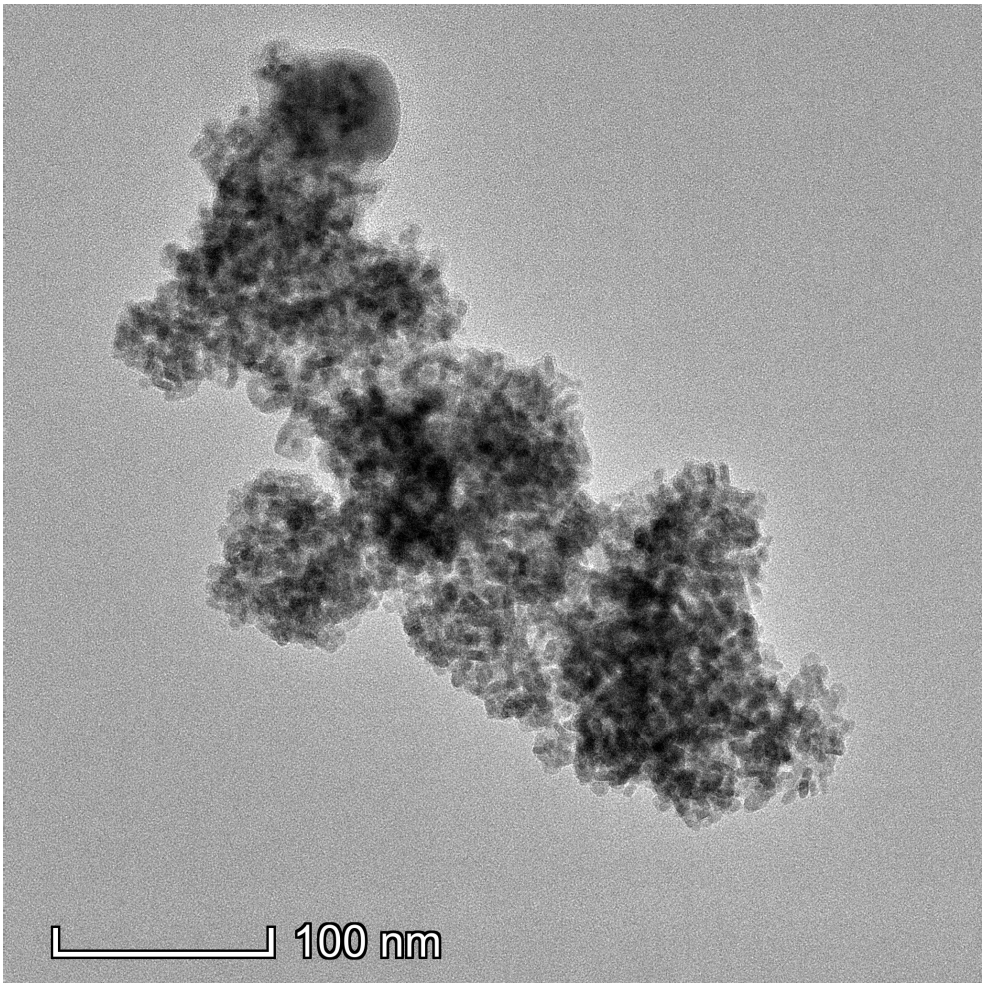

Figure 9.2: TEM images of highly crystalline LaF_3:$Ce^{3+}Tb^{3+}$ NPs prepared in 1:1 ratio of EG:PVP and dispersed in a suspension of Milli-Q water and 25 mmol PVP.

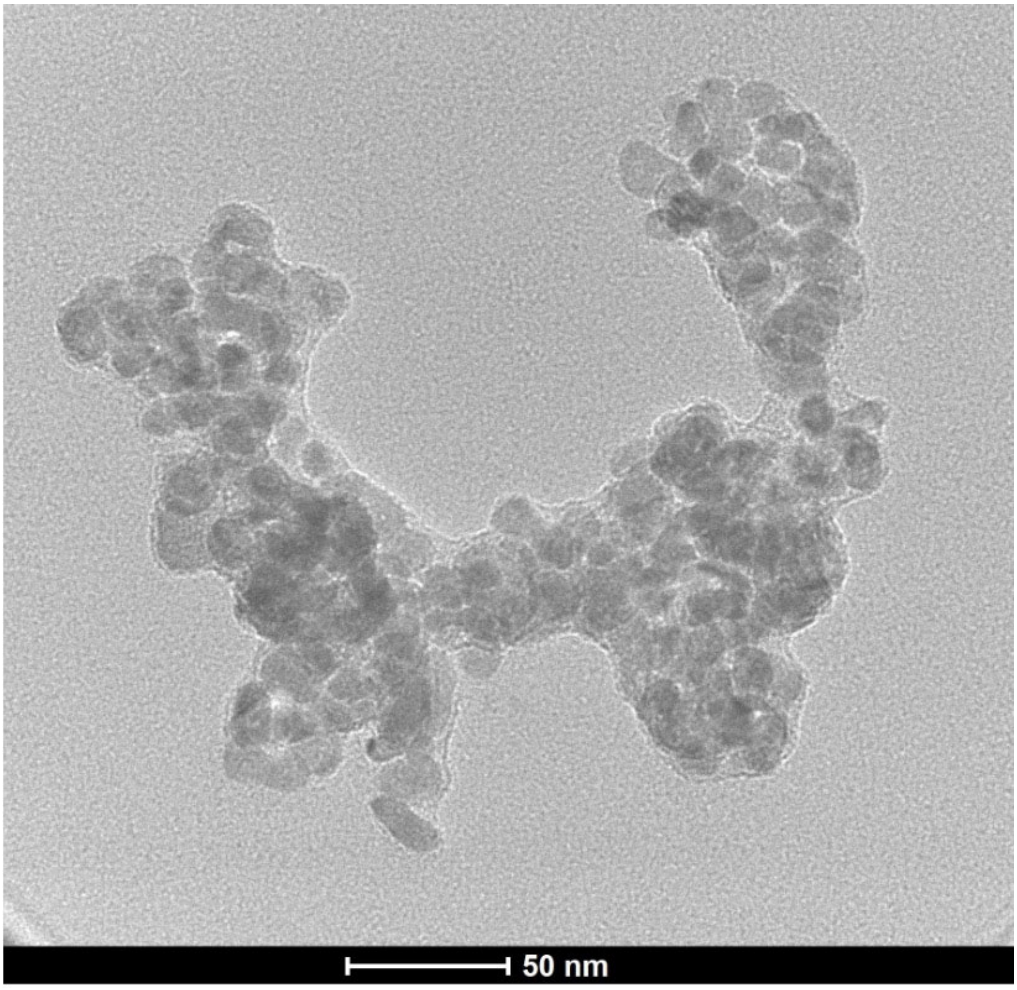

Figure 9.3: TEM images of highly crystalline $LaF_3:Ce^{3+}Tb^{3+}$ NPs prepared in 1:1 ratio of EG:PVP and dispersed in a suspension of Milli-Q water and 25 mmol PVP.

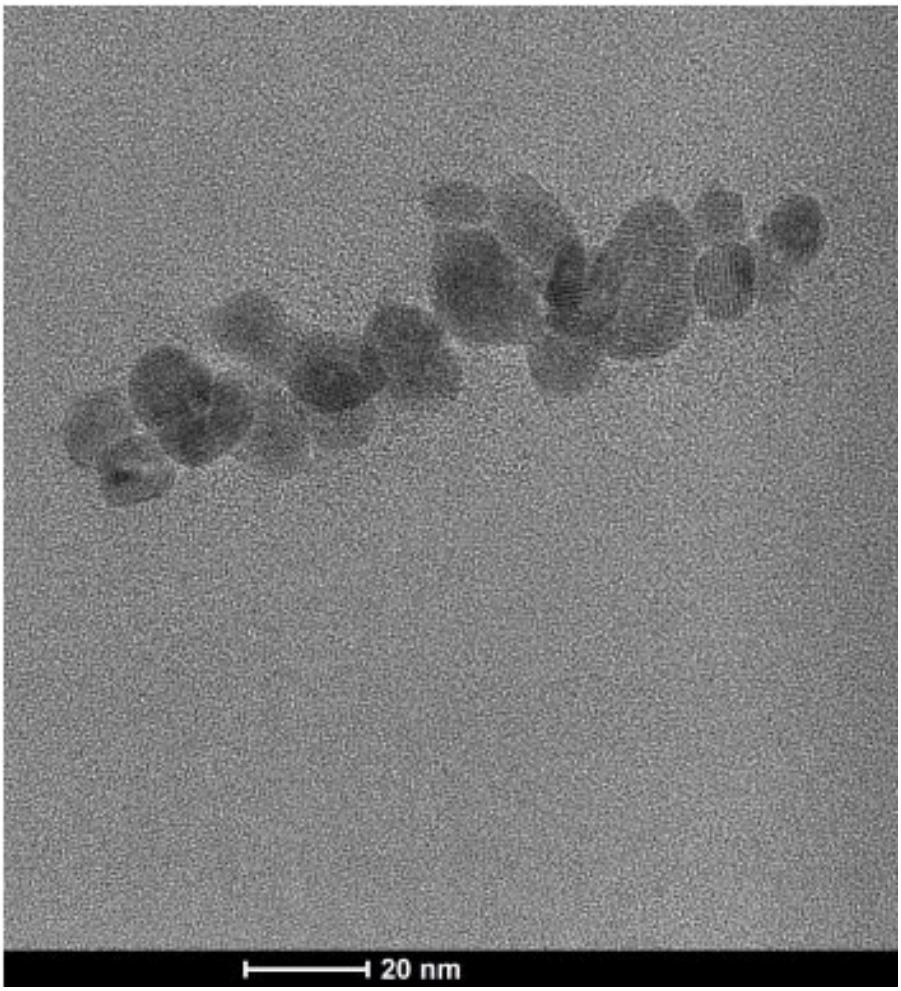

Figure 9.4: TEM images of highly crystalline $LaF_3:Ce^{3+}Tb^{3+}$ NPs prepared in 1:1 ratio of EG:PVP and dispersed in a suspension of Milli-Q water and 25 mmol PVP.

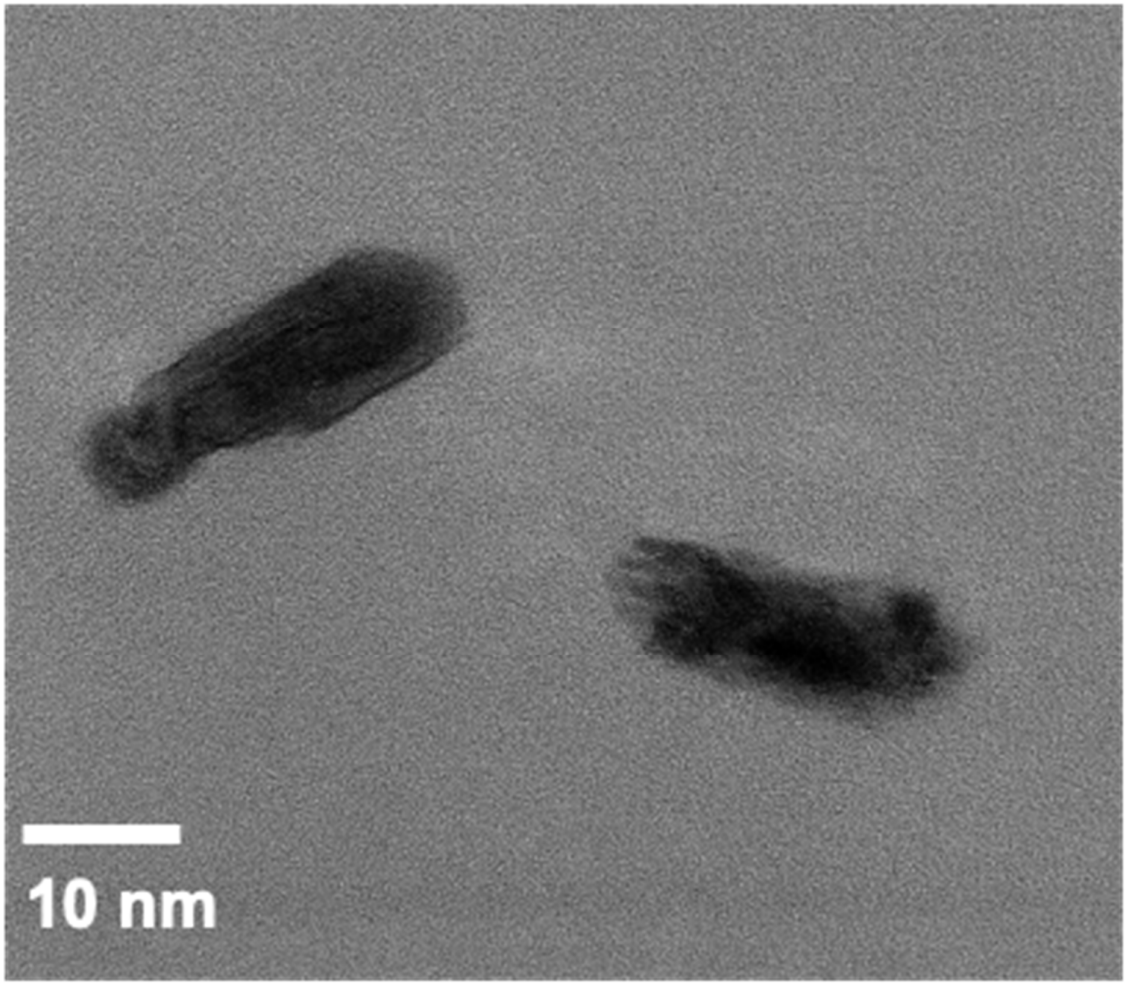

Figure 9.5: TEM images of highly crystalline LaF_3:$Ce^{3+}Tb^{3+}$ NPs prepared in 1:1 ratio of EG:PVP and dispersed in a suspension of Milli-Q water and 25 mmol PVP.

II Rheology plots of Eu^{3+} cross linked Na-alginate hydrogel–$LaF_3:Ce^{3+}Tb^{3+}$ NPs hybrid system.

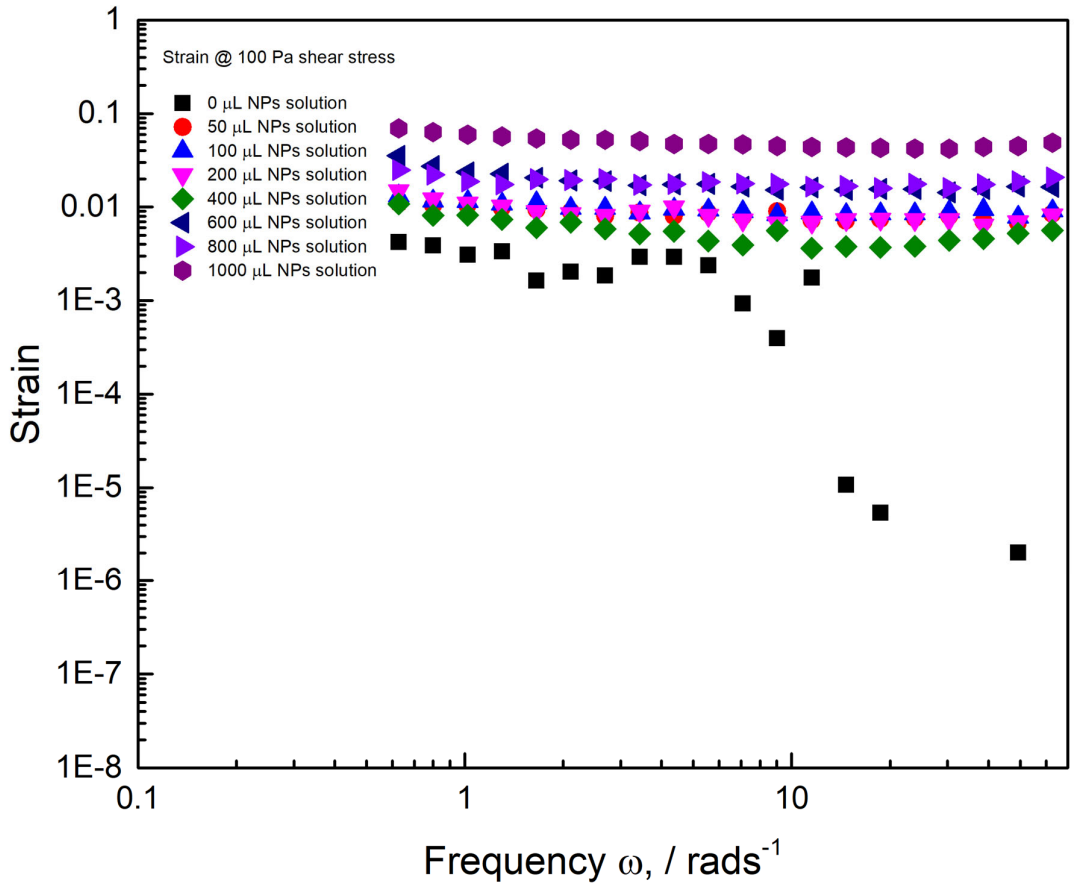

Figure 9.6: Frequency dependence of strain at 100 Pa shear stress for various volumes of NP solutions.

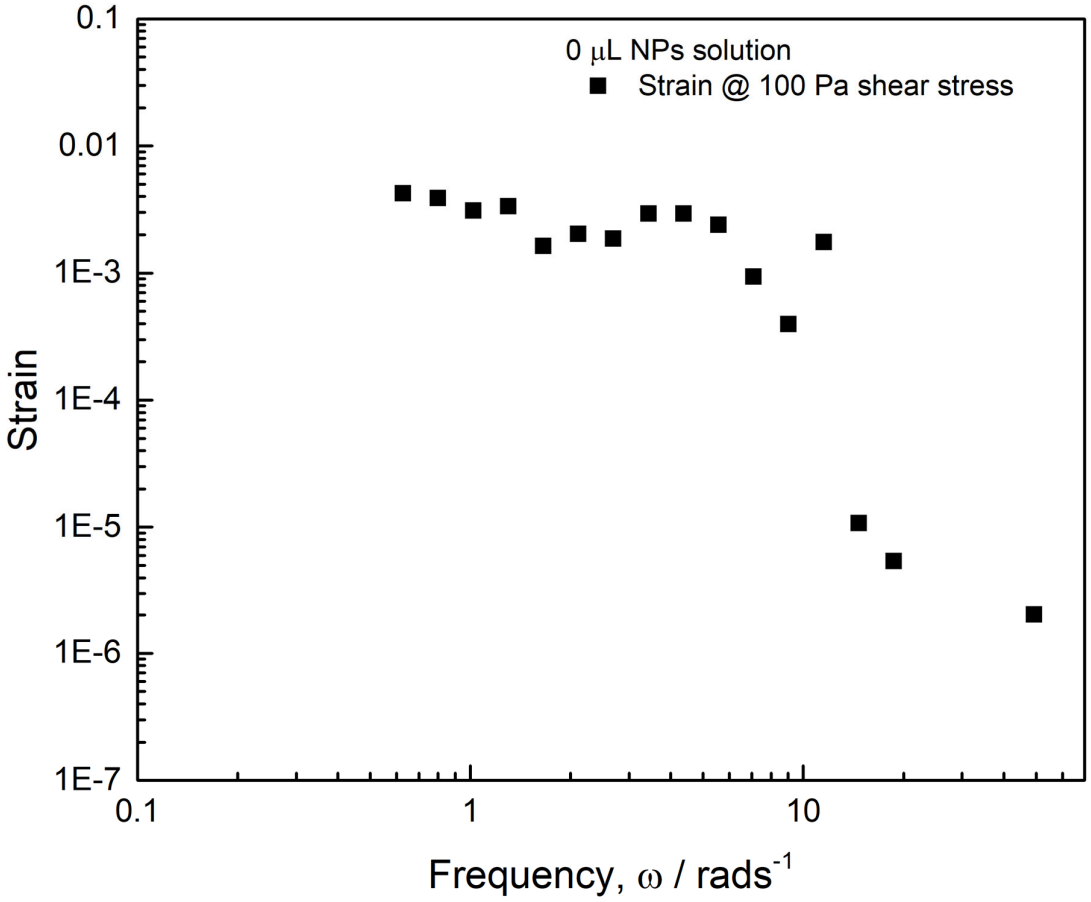

Figure 9.7: Frequency dependence of strain at 100 Pa shear stress for 0 μL volume (0 μg/L) of NP solution.

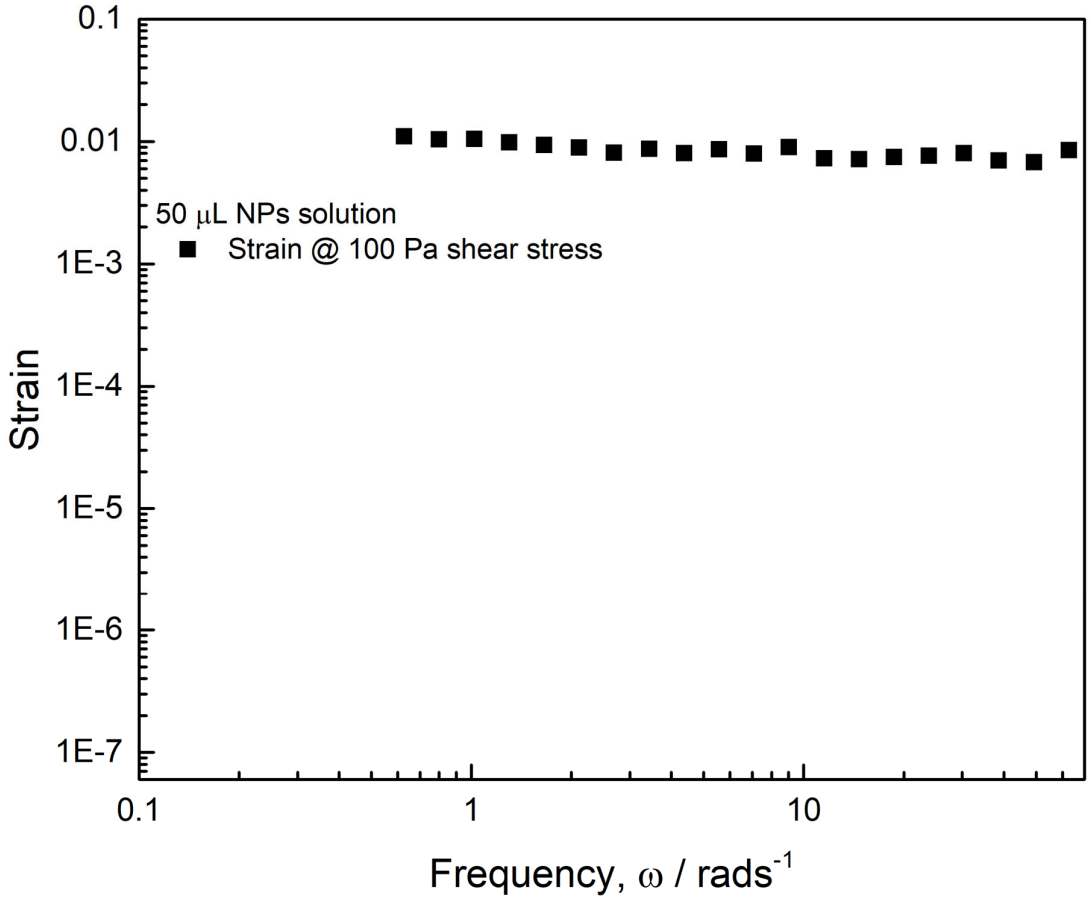

Figure 9.8: Frequency dependence of strain at 100 Pa shear stress for 50 µL volume (1.3 µg/L) of NP solution.

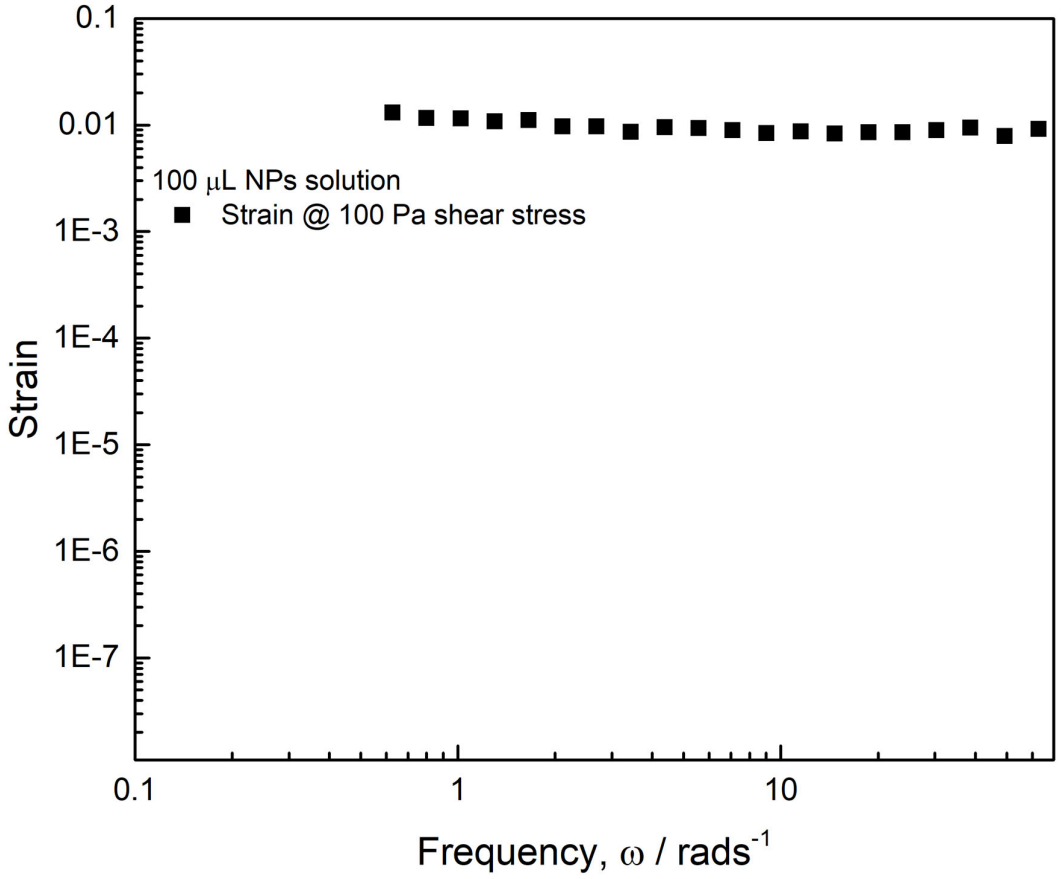

Figure 9.9: Frequency dependence of strain at 100 Pa shear stress for 100 µL volume (2.6 µg/L) of NP solution.

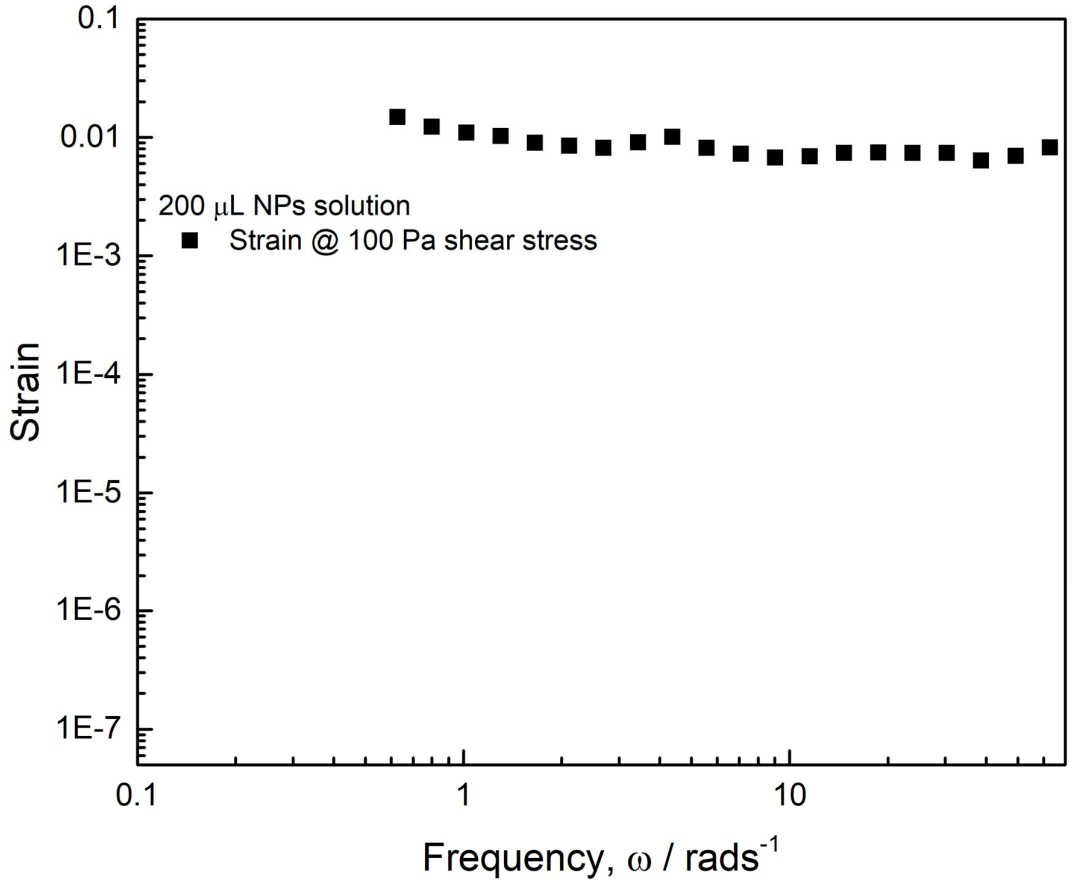

Figure 9.10: Frequency dependence of strain at 100 Pa shear stress for 200 µL volume (5.1 µg/L) of NP solution.

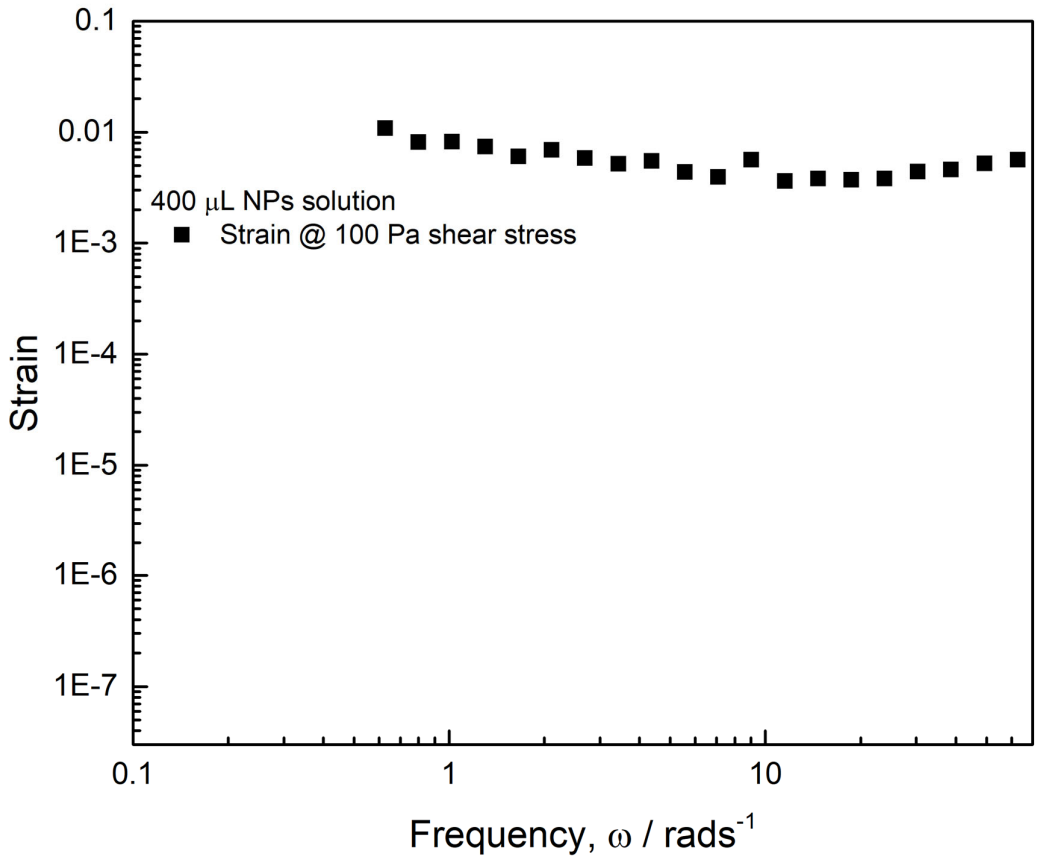

Figure 9.11: Frequency dependence of strain at 100 Pa shear stress for 400 µL volume (10.2 µg/L) of NP solution.

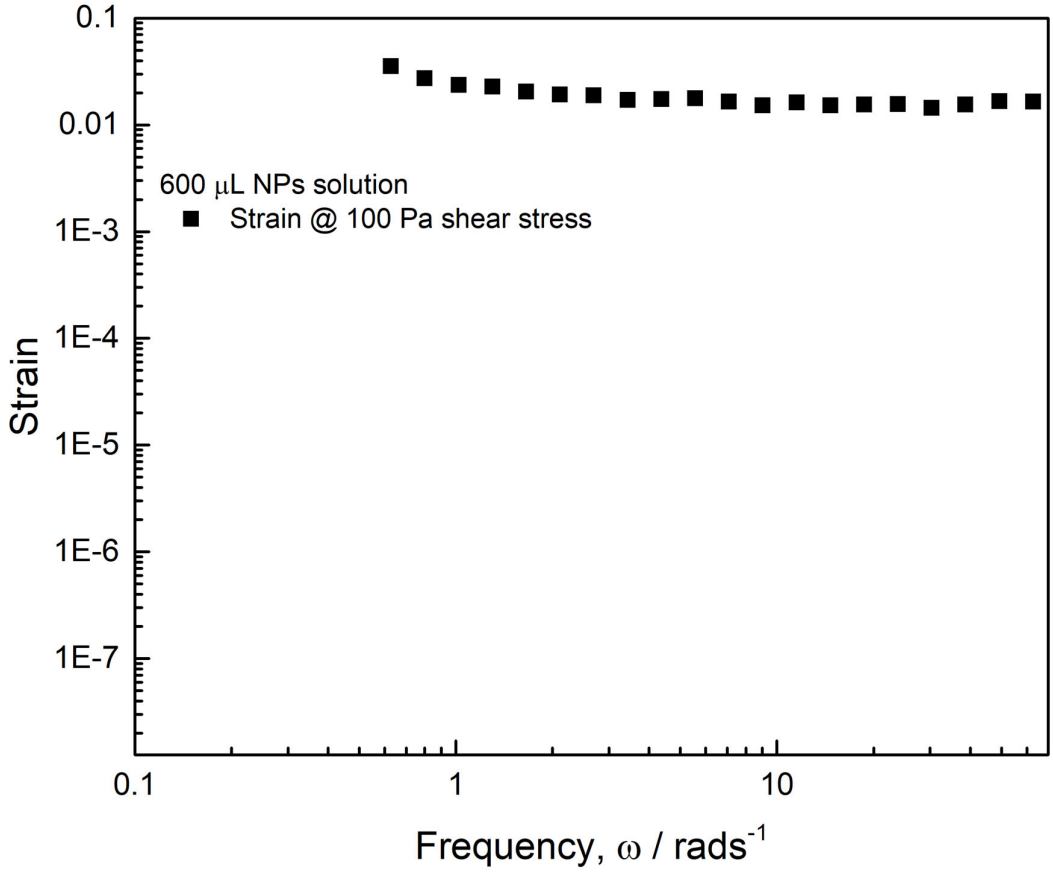

Figure 9.12: Frequency dependence of strain at 100 Pa shear stress for 600 µL volume (15.4 µg/L) of NP solution.

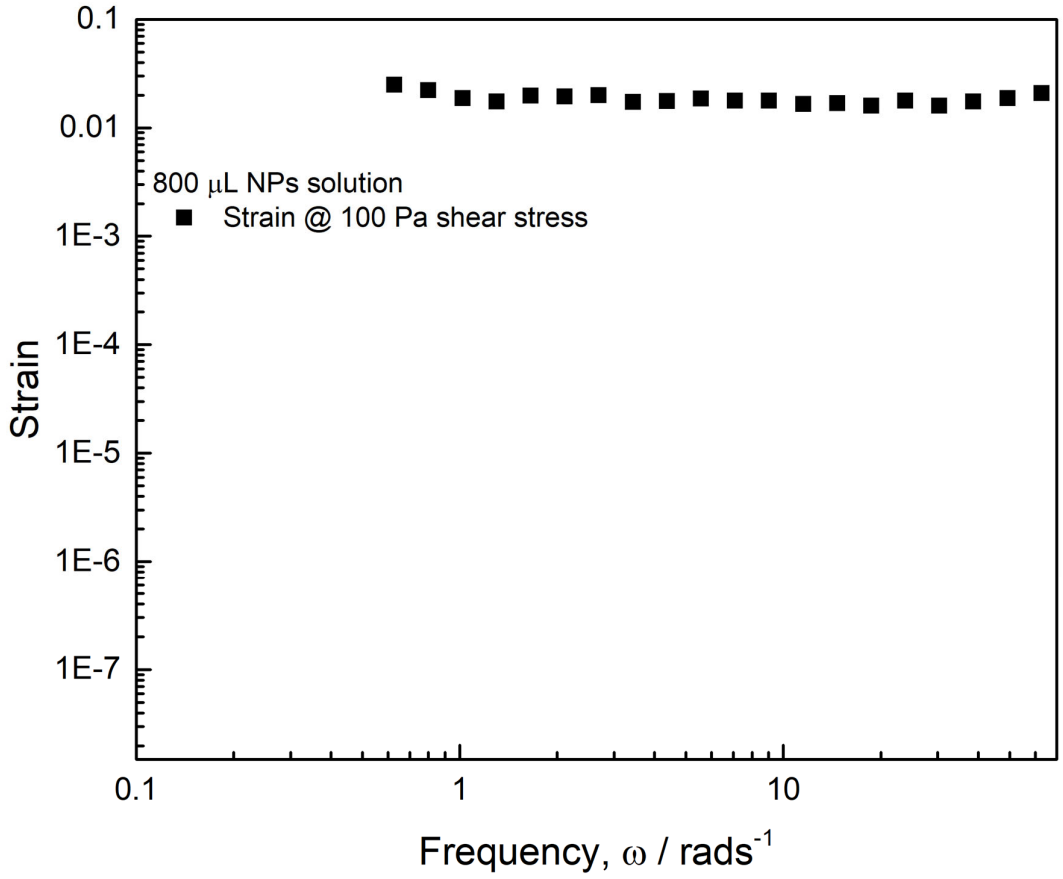

Figure 9.13: Frequency dependence of strain at 100 Pa shear stress for 800 µL volume (20.5 µg/L) of NP solution.

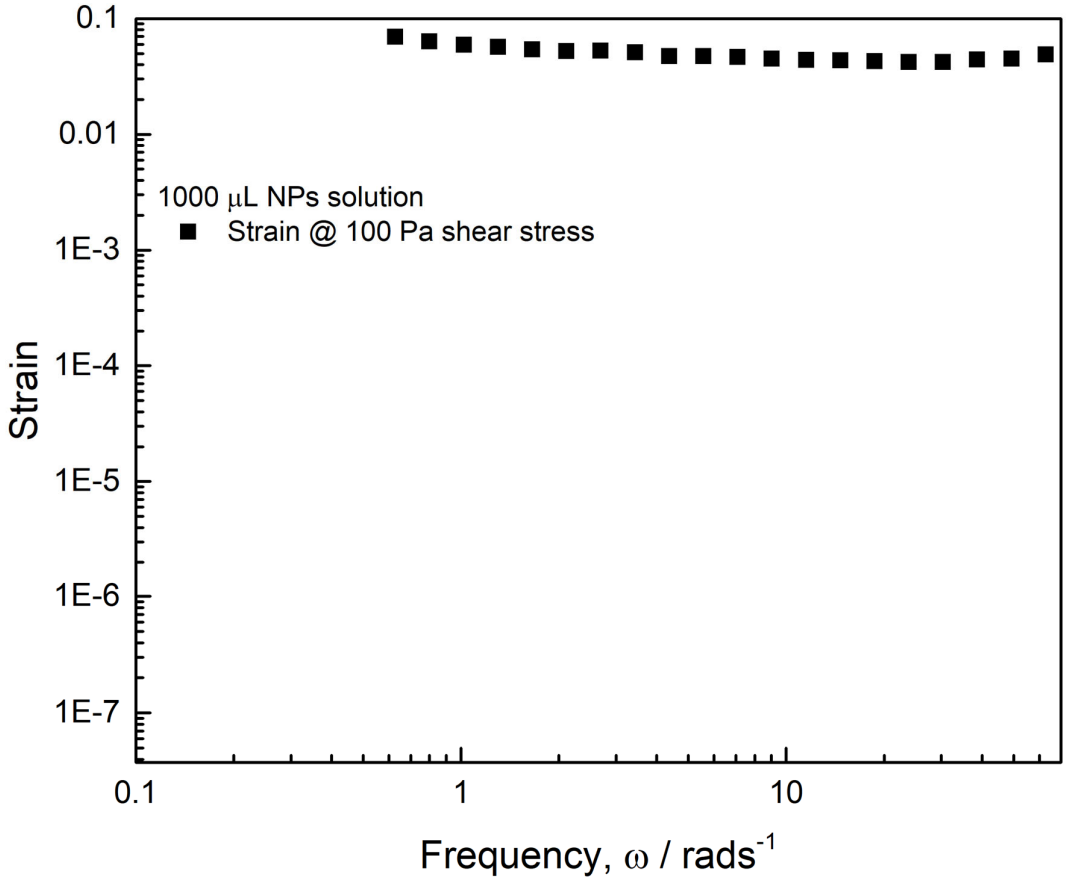

Figure 9.14: Frequency dependence of strain at 100 Pa shear stress for 1000 μL volume (25.6 μg/L) of NP solution.

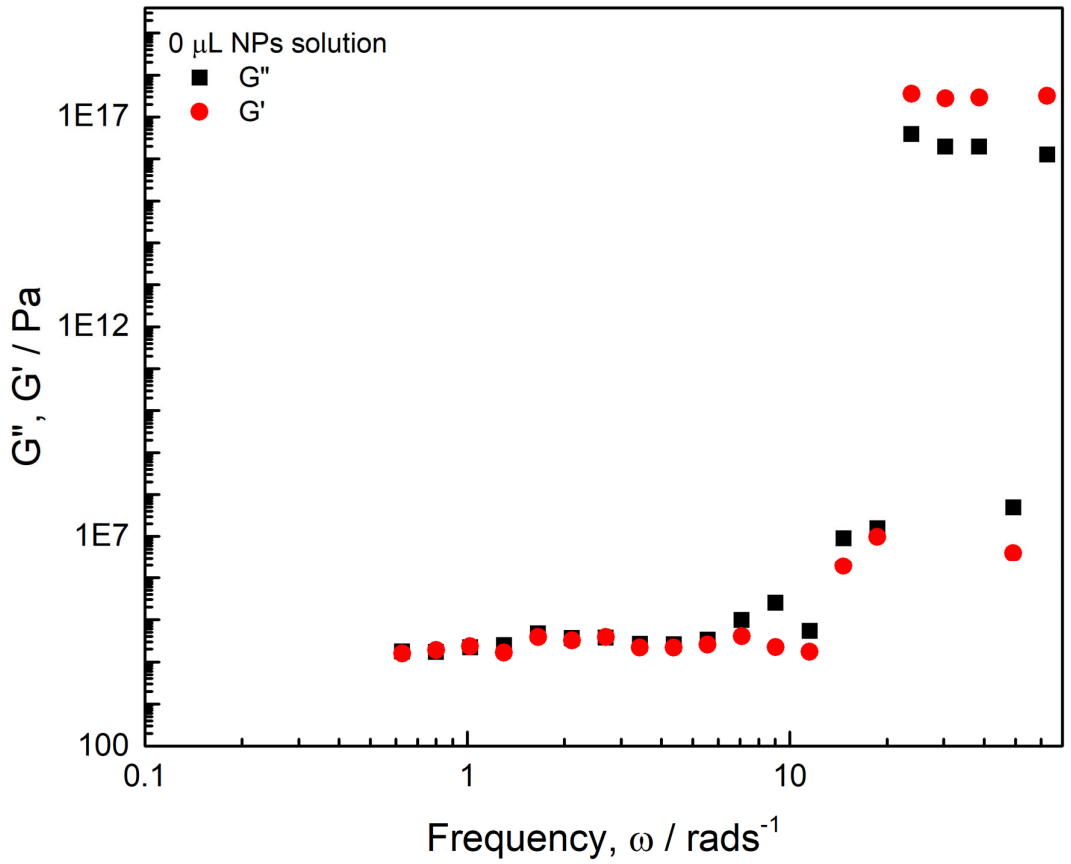

Figure 9.15: Frequency dependence of storage modulus (G') and loss modulus (G") for 0 µL NP solution (0 µg/L) under shear stress, illustrating viscoelastic behavior across a range of frequencies.

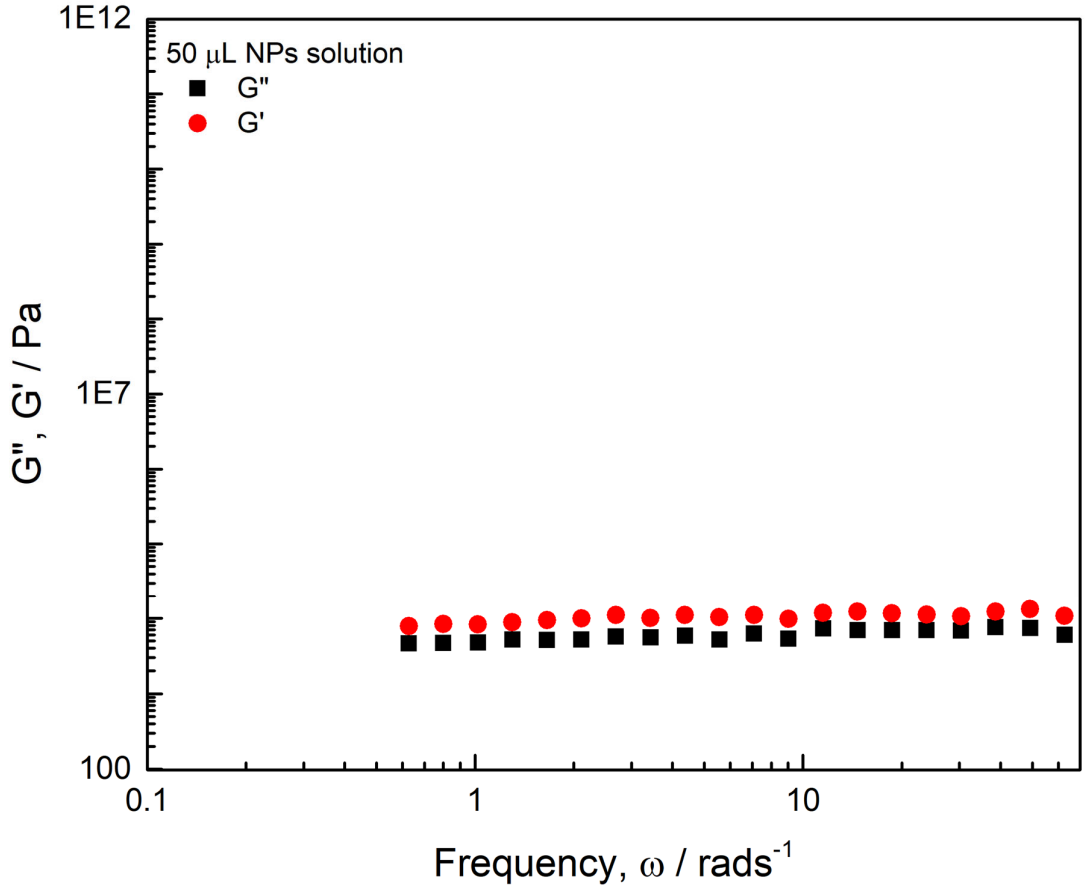

Figure 9.16: Frequency dependence of storage modulus (G') and loss modulus (G'') for 50 µL NP solution (1.3 µg/L) under shear stress, illustrating viscoelastic behavior across a range of frequencies.

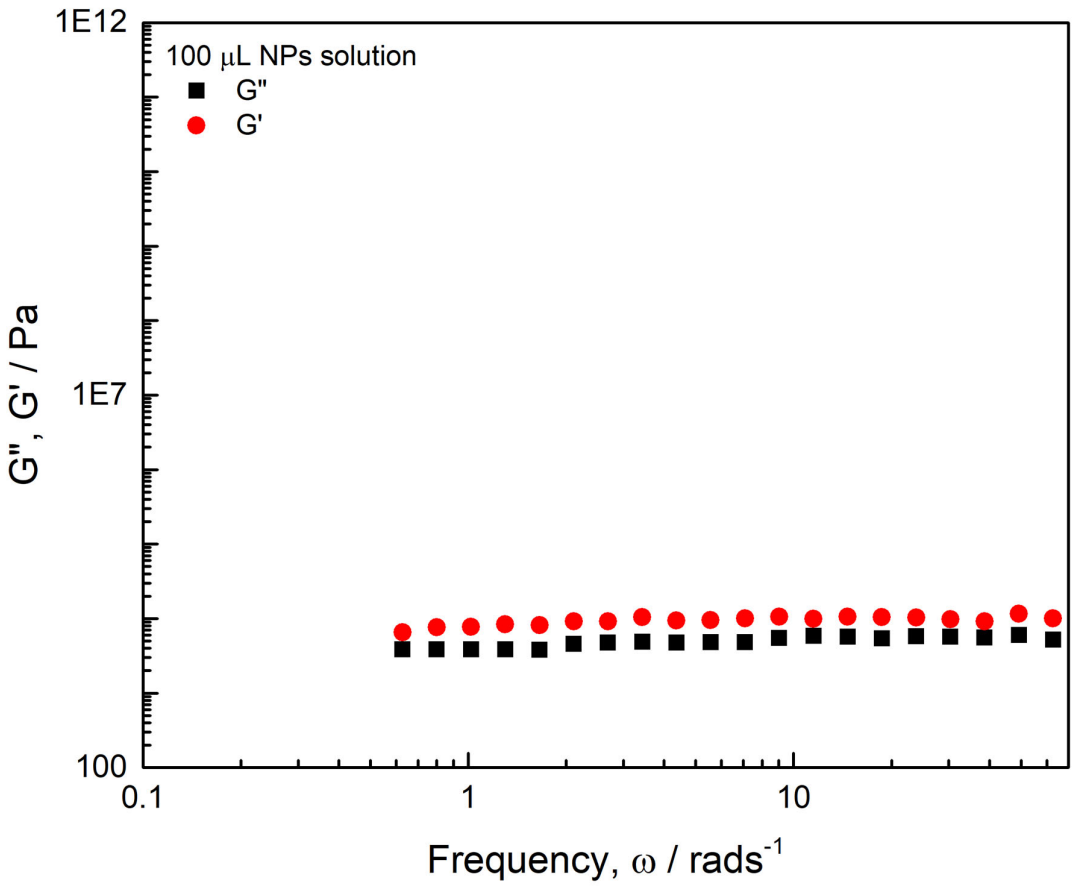

Figure 9.17: Frequency dependence of storage modulus (G') and loss modulus (G'') for 100 µL NP solution (2.6 µg/L) under shear stress, illustrating viscoelastic behavior across a range of frequencies.

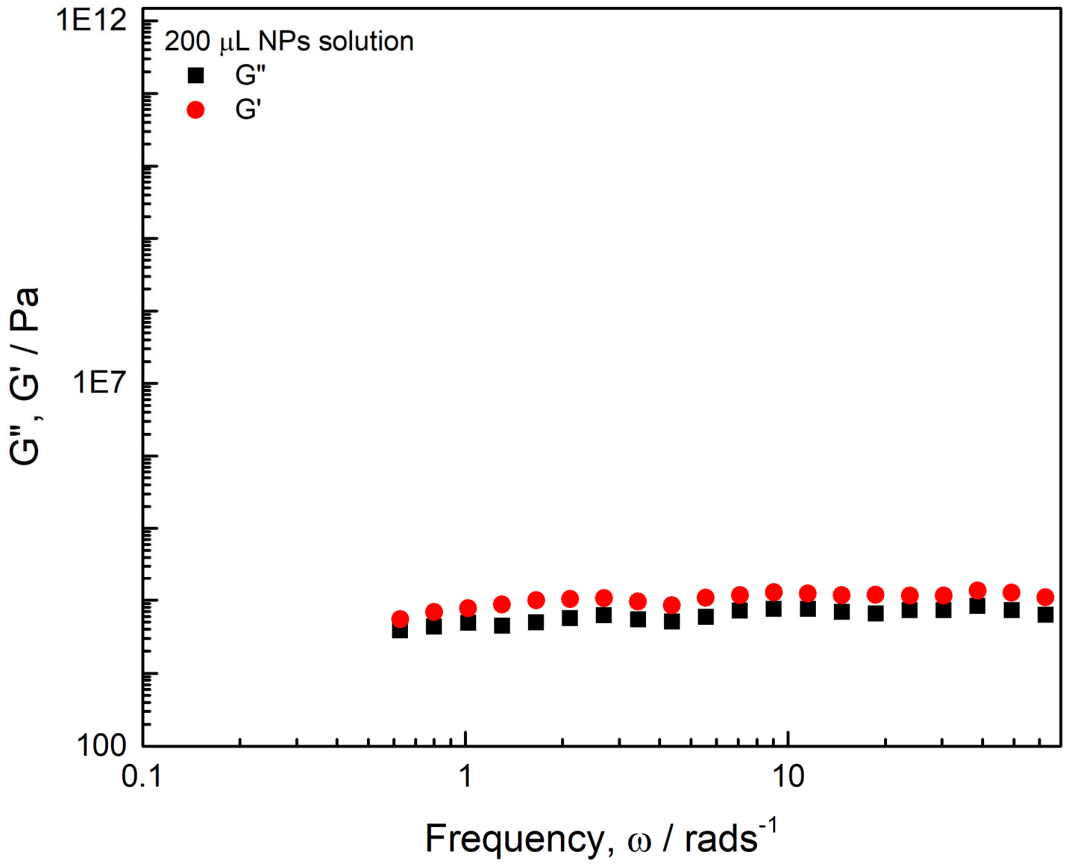

Figure 9.18: Frequency dependence of storage modulus (G') and loss modulus (G'') for 200 µL NP solution (5.1 µg/L) under shear stress, illustrating viscoelastic behavior across a range of frequencies.

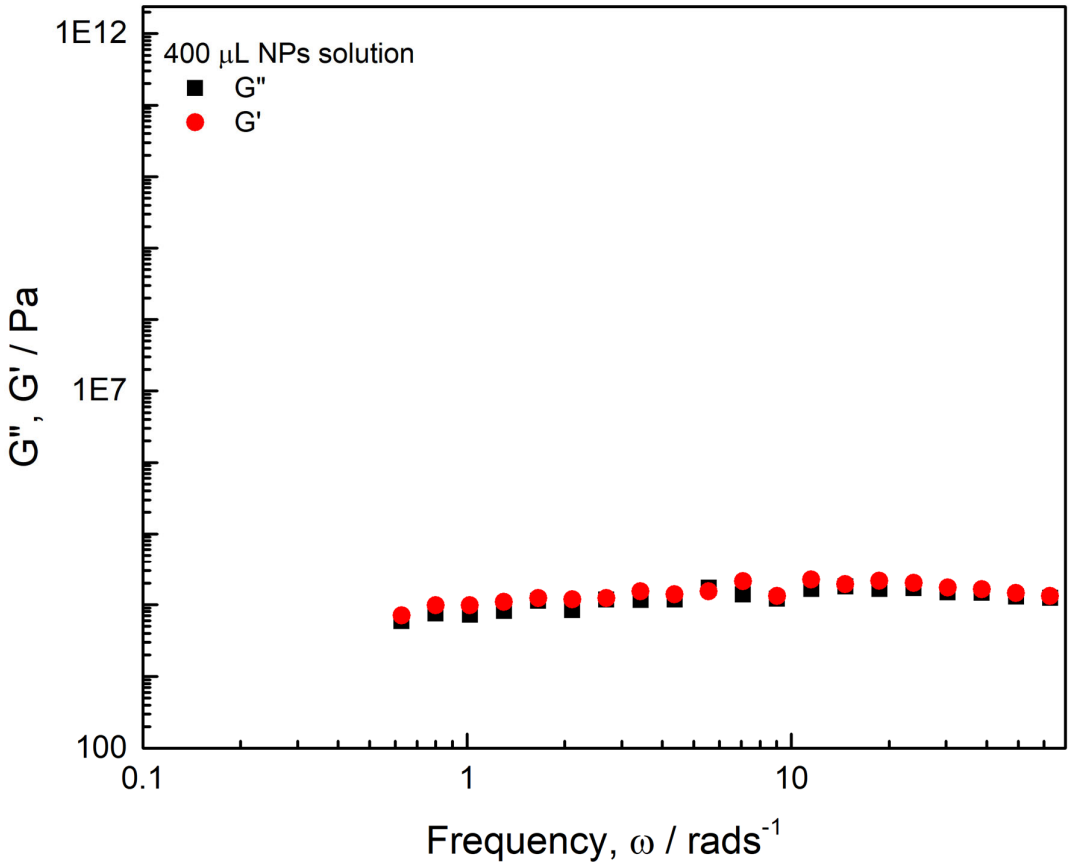

Figure 9.19: Frequency dependence of storage modulus (G') and loss modulus (G'') for 400 µL NP solution (10.2 µg/L) under shear stress, illustrating viscoelastic behavior across a range of frequencies.

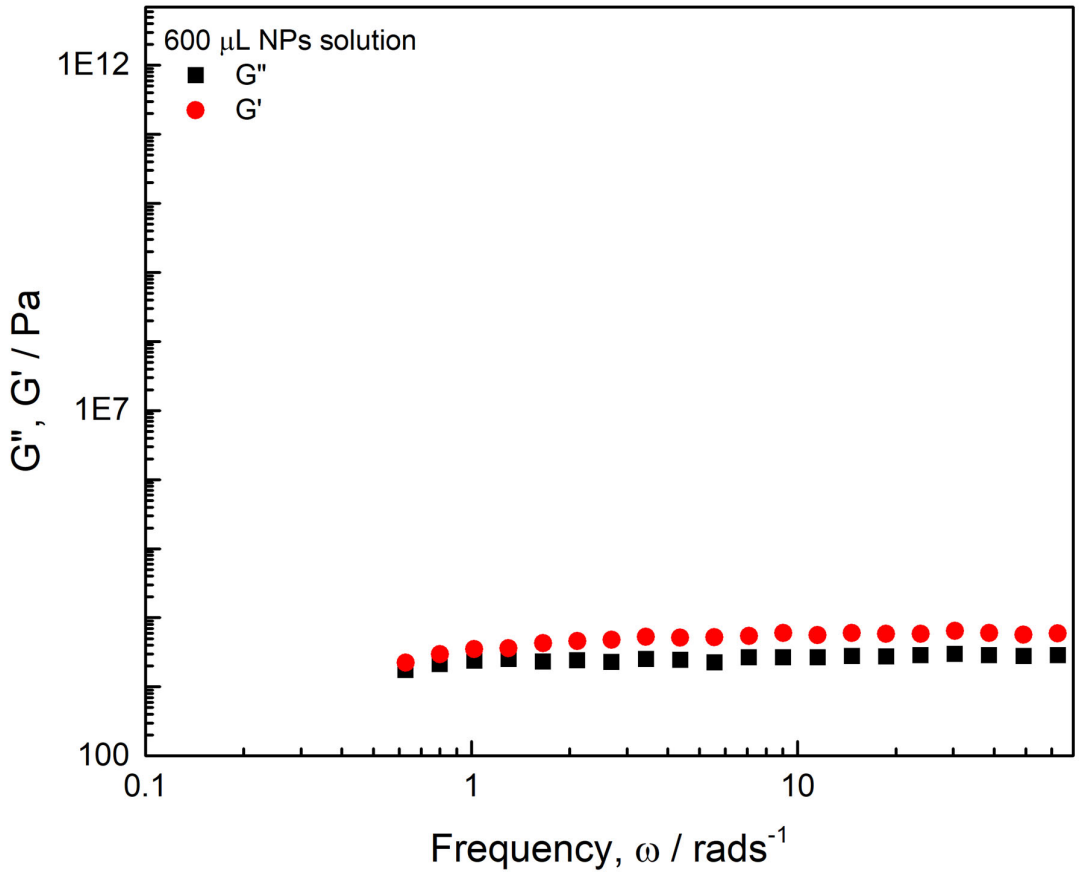

Figure 9.20: Frequency dependence of storage modulus (G') and loss modulus (G'') for 600 µL NP solution (15.4 µg/L) under shear stress, illustrating viscoelastic behavior across a range of frequencies.

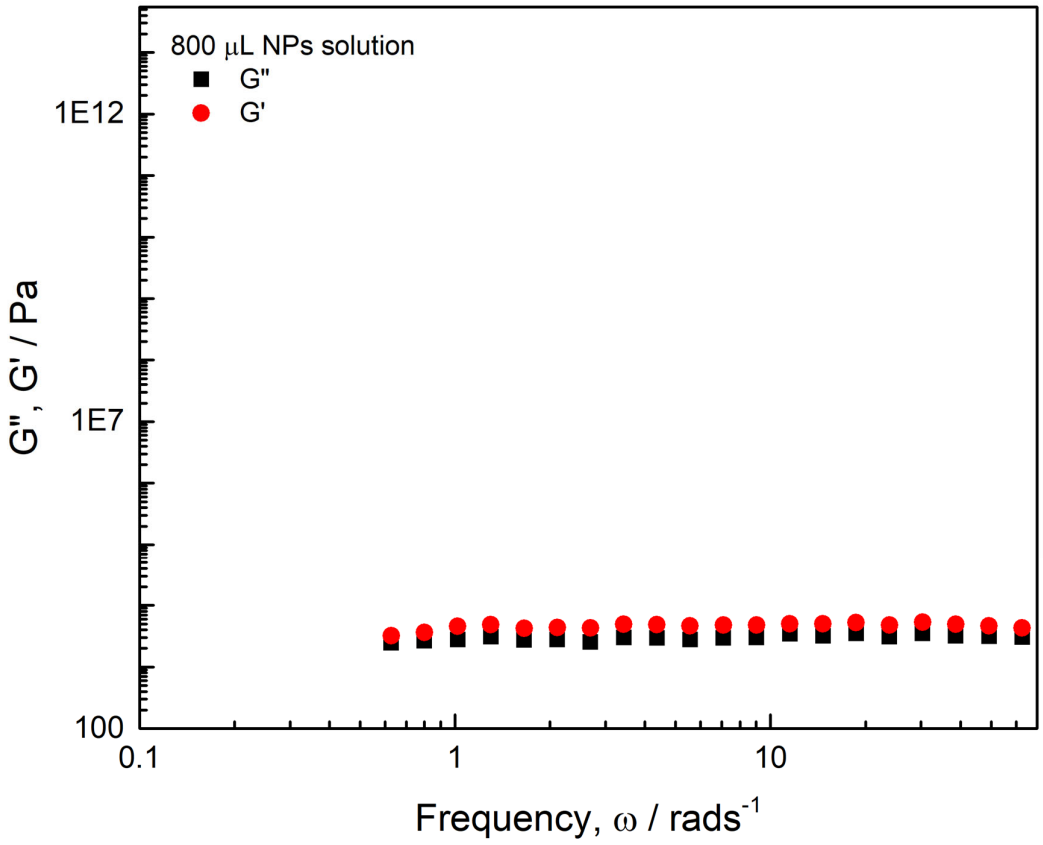

Figure 9.21: Frequency dependence of storage modulus (G') and loss modulus (G'') for 800 µL NP solution (20.5 µg/L) under shear stress, illustrating viscoelastic behavior across a range of frequencies.

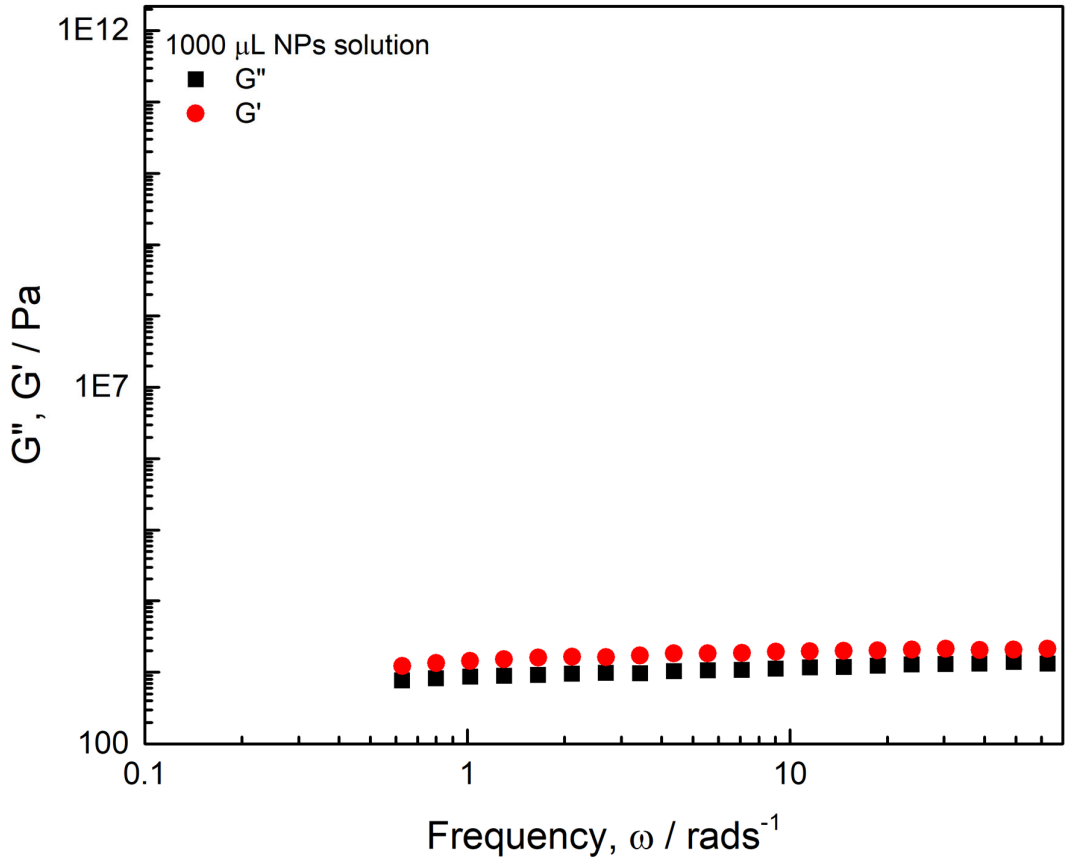

Figure 9.22: Frequency dependence of storage modulus (G') and loss modulus (G'') for 1000 µL NP solution (25.6 µg/L) under shear stress, illustrating viscoelastic behavior across a range of frequencies.

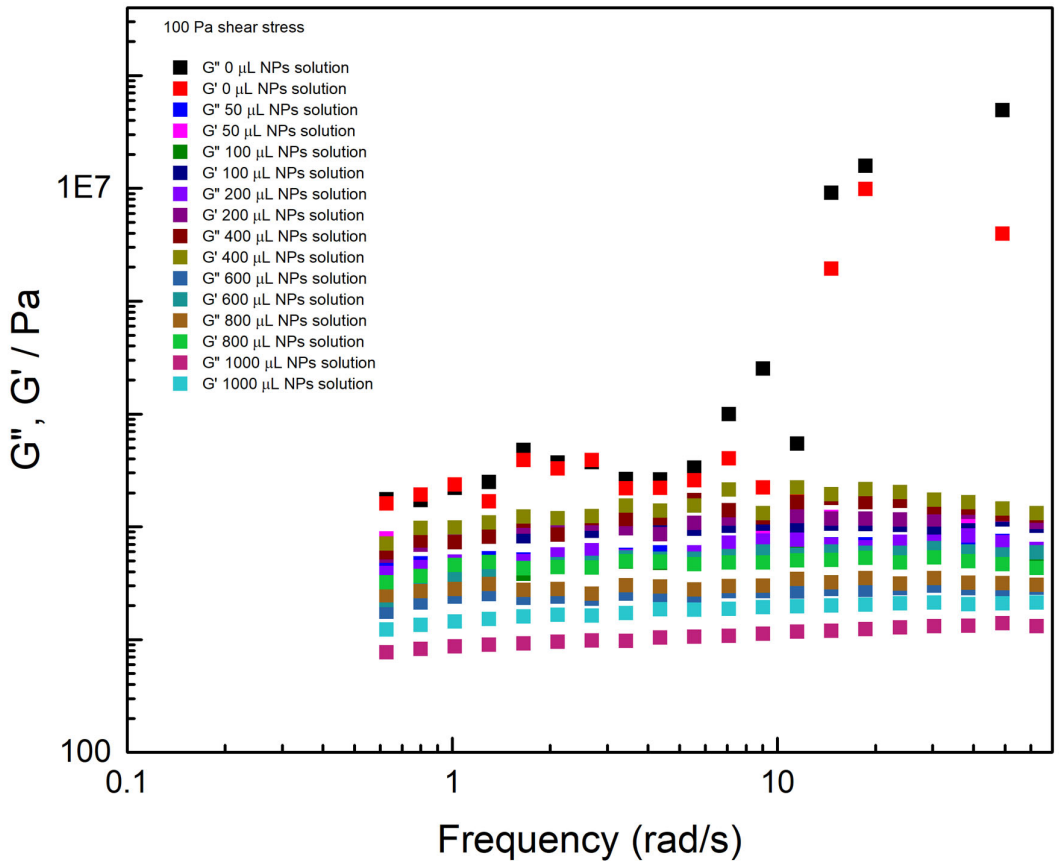

Figure 9.23: Frequency dependence of storage modulus (G') and loss modulus (G'') for various NP solutions under shear stress, illustrating viscoelastic behavior across a range of frequencies.

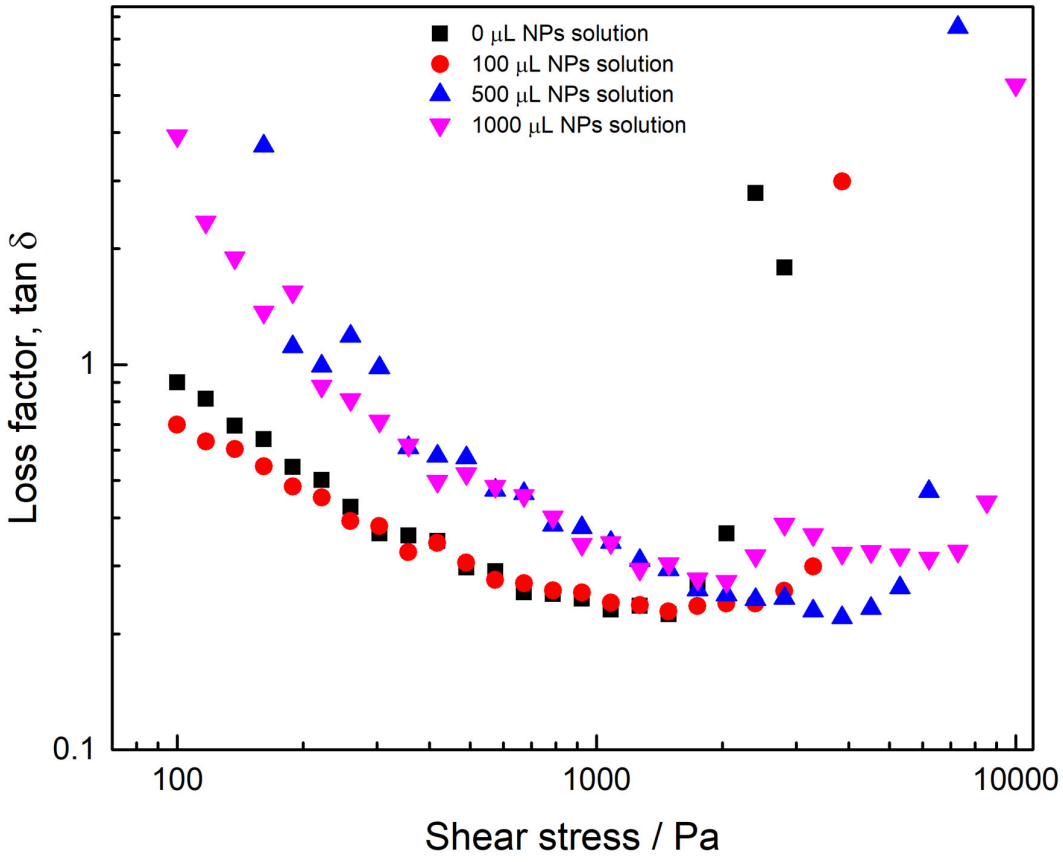

Figure 9.24: Dependence of loss factor (tan δ) on shear stress for various volumes of NP solutions, highlighting the influence of NP concentration on viscoelastic properties.

III SOP 1 – MTT assay (with & without NPs).

Prepared and modified by PC I S1 Lab (procedure for NPs modified by the author of this thesis).

A) Without NPs.

- seed cells: 40.000 cells/well (normal densities 5000 – 10.000 cells/well (96-well-plate) **28.000 – 56.000 cells/well (24-well-plate))**

standard curve: 80.000 / 40.000 / 20.000 / 10.000 / 5.000 / 2.500 cells per well and a negative control without cells (always perform as duplicates, better as triplicates and calculate the average value)

- let cells grow for 46-48 h.

- remove medium and replace it with 100 µl (96-well-plate) or **500 µl (24-well-plate)** fresh culture medium (*use DMEM medium **without** phenol red!)*

- add 10 µl (96) or **50 µl (24)** of 12 mM MTT stock solution to each well

- incubate at 37°C for 4 h.

*- remove all but 25 µl (96) or **125 µl (24)** of medium from the wells

- add 50 µl (96) or **250 µl (24)** of DMSO to each well and mix thoroughly with the pipette

- incubate at 37°C for 10 min

- mix each sample again and read absorbance at **540** nm

**alternative protocol:*

- add 100 µl (96) or **500 µl (24)** SDS-HCl to each well and mix thoroughly with the pipette

- incubate at 37°C for 4-18 h.

- mix each sample again and read absorbance at **570** nm

÷

100 mg MTT in 20 ml PBS (filter if you want to) and store aliquots at -20°C:

aliquot 1000 µl for 96-well-plate

1300 µl for 24-well-plate

aliquot 5000 µl DMSO for 96-well-plate

6500 µl DMSO for 24-well-plate

SDS-HCl: 1 g SDS in 10 ml 0,01M HCl

(or: 5 ml 20% SDS + 5 ml 0,02M HCl)

B) With NPs

- For the standard curve start with high cell concentration from 40000 cells/ well and above to get accurate results
- Sterilize the NPs in solution in the autoclave before use
- Use a different pipette tip for each individual well (the concentration of NPs sticking on the Eppendorf tips can influence the results especially for low concentration of cells.
- Only add the NPs after cell attachment (6 h). Adding NPs directly after seeding is not recommended since most cells will not get in contact with NPs. After some time, the NPs aggregate and drift away from the TCPS surface.
- Do not use the SDS procedure for NPs, recovering the NPs may be impossible if there is need to further investigate the NPs after MTT assay.
- Repeat the experiment at least 6 times but 8 is recommended and consider only 4 best fitting absorbance reading. In most cases, the NPs aggregates will interfere with absorbance reading.

IV SOP 2 – Live – dead staining

Prepared and modified by PC I S1 Lab.

Stock solutions:

- FDA (Fluorescein diacetate)
    - Dissolve 10mg in 1ml acetone
    - Store at -20°C – PI (Propidium Iodide)
    - Dissolve 2mg in 1ml PBS o Store at 4°C

Negative control (dead cells):

- remove medium
- wash with PBS
- add 0.5% Triton in PBS -> 10min at RT
- wash with PBS
- prepare serum free Media for the used cell type (no FBS / horse serum)
- work from now on with NITRIL gloves

Staining solution:

- serum free Media: 5ml – FDA (1mg/ml): 4µl – PI (2mg/ml): 50µl

(stored at -20°C) (stored at 4°C)

- remove medium
- wash with PBS: 2x
- add staining solution (each 1ml) -> 4-5min at RT, in the dark
- remove the staining solution
- wash with PBS
- leave them in PBS

Sealing samples (if they have to analyzed upside down) – Place a peace of Roti-SEAL in an eppi

- close it tight
- place it in a 50°C warm water bath until it is fluid
- use 1ml tip to seal a cover glass onto the glass slide and fix the sandwich to a microscope slide

Fluorescence microscopy

- Red: dead cells / Green: living cells

V SOP 3 – Cell freezing, defrosting and counting.

Prepared and modified by PC I S1 Lab.

Freezing:

- remove the medium
- wash with PBS (10 ml)
- add 2 ml Trypsin
→incubate 3-5min at 37°C

- collect the cells with 9 ml medium -> centrifuge (4min, 1200rpm)

- remove the excess medium
- add 1.5ml freezing-medium (80% FBS; 1.2ml+20% DMSO; 0.3ml) + 1.5ml Medium

- add 1ml per cryotube (label: name, cells, passage, date)
- place the cryotubes in a isopropanol box
- close the box (not completely, otherwise you will not be able to open it, when it is frozen)

→incubate at -80°C for <2 weeks -> store at -150°C for 1-10 years

Defrosting:

- place the cryotube in the water bath
- fill the flask with 15 ml medium
- use 1 ml warm medium and mix with the cells – transfer the 2 ml cell solution to the flask
- change the medium the next day

DMSO

- filtration with Nylon membranes 0.2 µm

Counting:

- remove the culture medium – wash with PBS (10 ml)
- add 2 ml trypsin

→incubate for 3-5 min at 37°C

- add 9 ml medium to the flask and mix it -> centrifuge (4 min, 1200 rpm)

- remove the excess of the medium (take care about the cell pallet) – add 1ml to the cell pallet

- prepare an Eppi with 90 µl of medium – add 10 µl cell solution

- use the Neubauer counting chamber and add 5 µl to each side

$$\frac{Z_1 + Z_2}{2} * 10^5 = X \ Zellen/_{ml} \tag{5}$$

N = number of cells per well

$$\left(\frac{1000yl}{X \ Zellen/_{ml}}\right) * N = n \tag{6}$$

- add 15 ml medium to the culture flask
- add the determined number of cells
- label the flask: name, cells, passage, date

VI MgF_2 SEM, TEM & XRD Images.

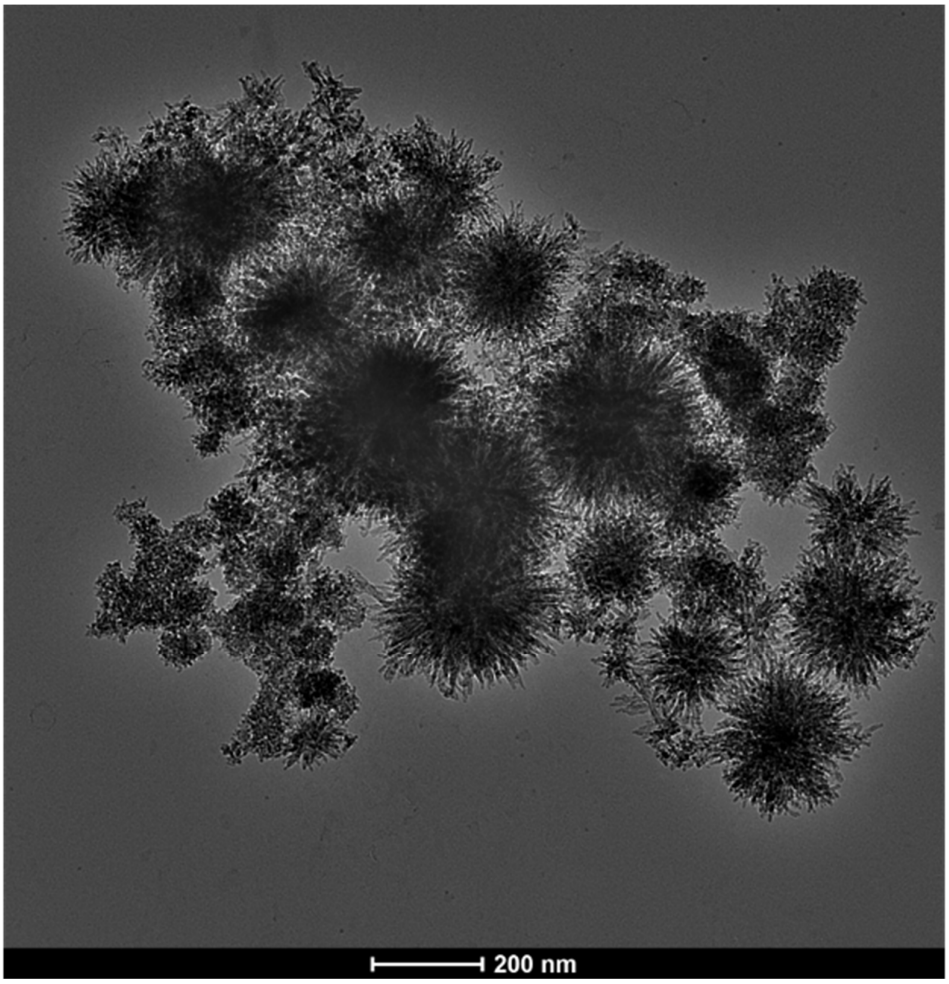

Figure 9.25: TEM images of MgF_2 spherulites prepared from $Mg(acet)_2$, $BMIM[BF_4]$ ionic liquid and Milli-Q H_2O via microwave synthesis (30 minutes dwell time, 100 bar, 100°C). Addition of Na_2HPO_4 to control nucleation fosters self-assembly of the nanowhiskers to form nano spherulites of about 150 nm.

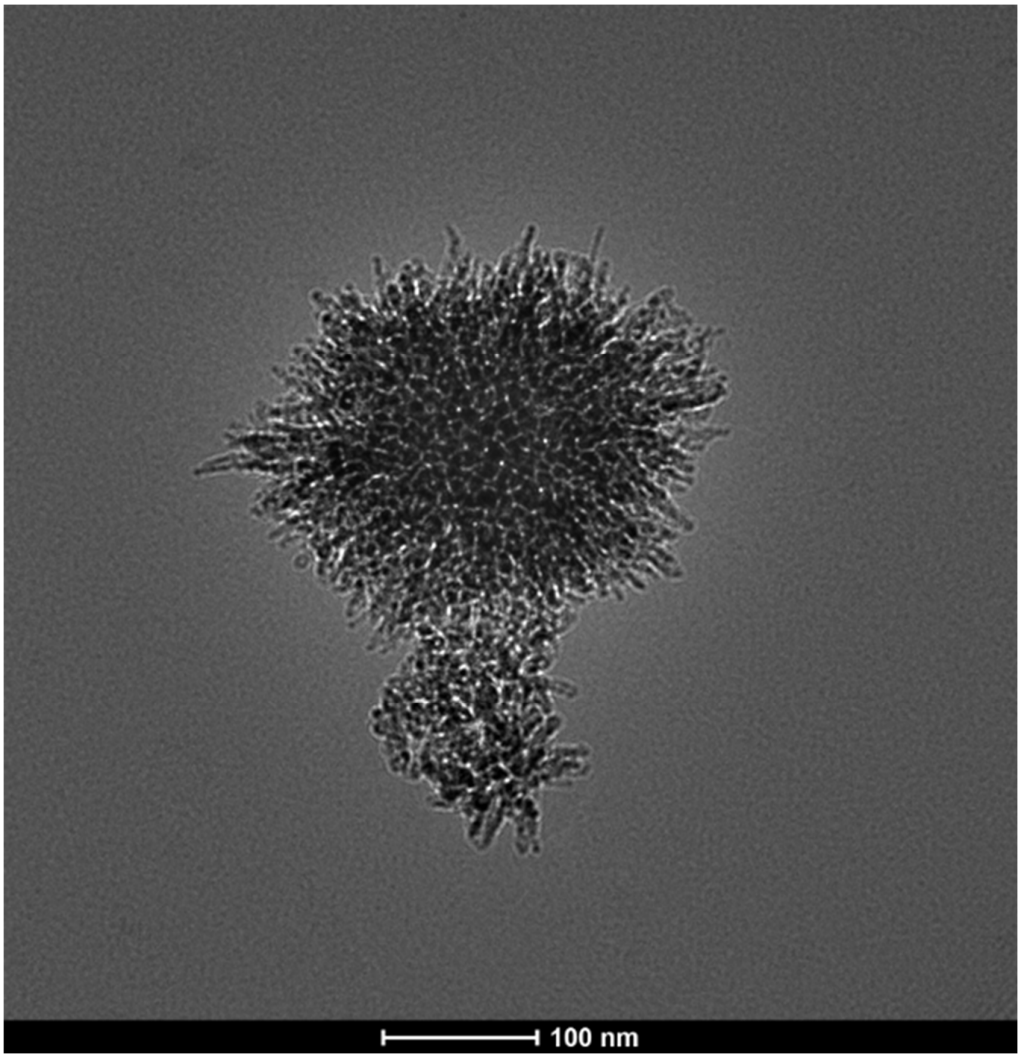

Figure 9.26: TEM images of MgF_2 spherulites prepared from $Mg(acet)_2$, $BMIM[BF_4]$ ionic liquid and Milli-Q H_2O via microwave synthesis (30 minutes dwell time, 100 bar, 100°C). Addition of Na_2HPO_4 to control nucleation fosters self-assembly of the nanowhiskers to form nano spherulites of about 150 nm.

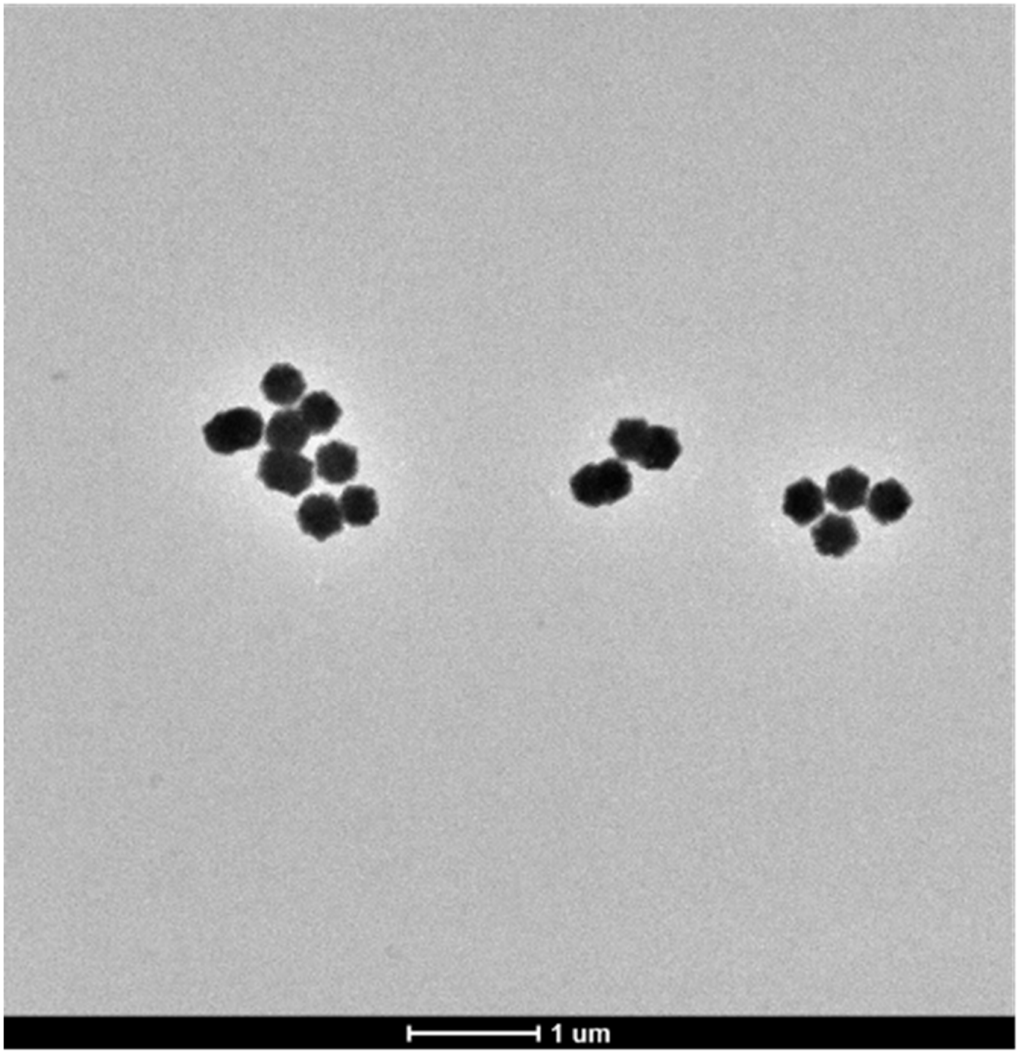

Figure 9.27: TEM images of MgF_2 nanospheres prepared from $Mg(NO_3)_2 \cdot 6H_2O$, BMIM[BF_4] ionic liquid, Milli-Q H_2O, Na_2HPO_4 via microwave synthesis (30 minutes dwell time, 100 bar, 150°C). Changing Mg source from acetate to nitrate leads to nanospheres instead of whiskers. However, the nanospheres look like petals arranged together. Monodisperse NPs 300 nm.

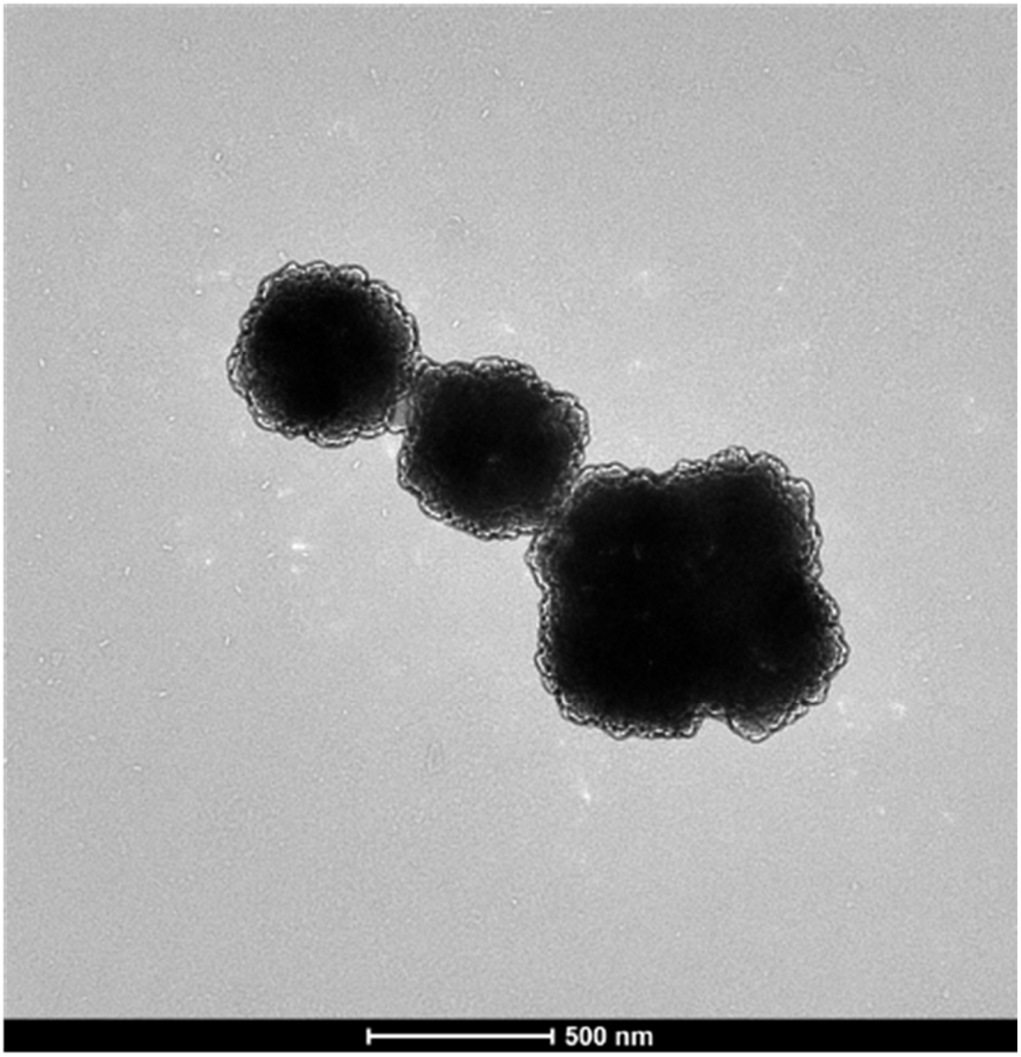

Figure 9.28: TEM images of MgF_2 nanospheres prepared from $Mg(NO_3)_2 \cdot 6H_2O$, BMIM[BF_4] ionic liquid, Milli-Q H_2O, Na_2HPO_4 via microwave synthesis (30 minutes dwell time, 100 bar, 150°C). Changing Mg source from acetate to nitrate leads to nanospheres instead of whiskers. However, the nanospheres look like petals arranged together. Monodisperse NPs 300 nm.

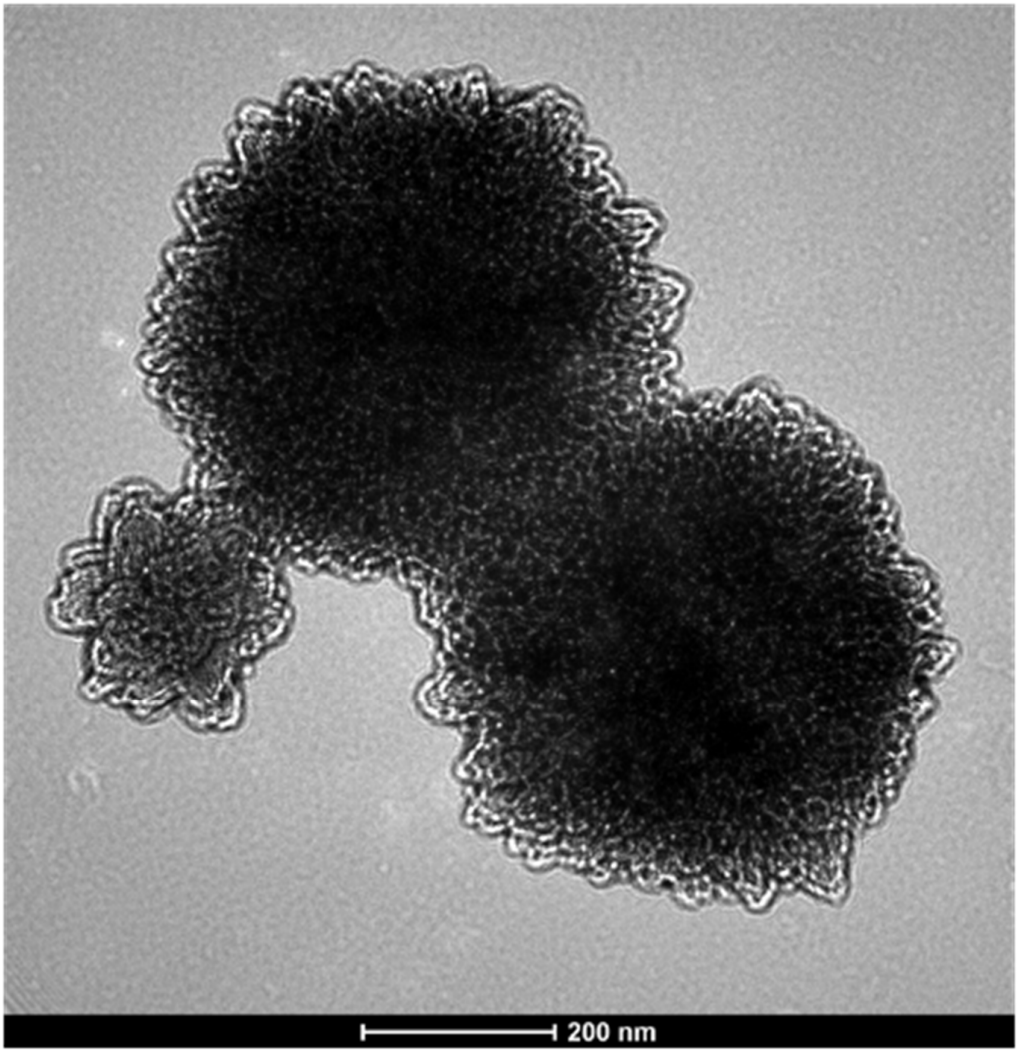

Figure 9.29: TEM images of MgF_2 nanofractals prepared from $Mg(NO_3)_2 \cdot 6H_2O$, BMIM[BF_4] ionic liquid, Milli-Q H_2O, Na_2HPO_4 via microwave synthesis (60 minutes dwell time, 100 bar, 150°C). Increase in dwell time to 60 minutes leads high crystallinity and more petals structures are visible.

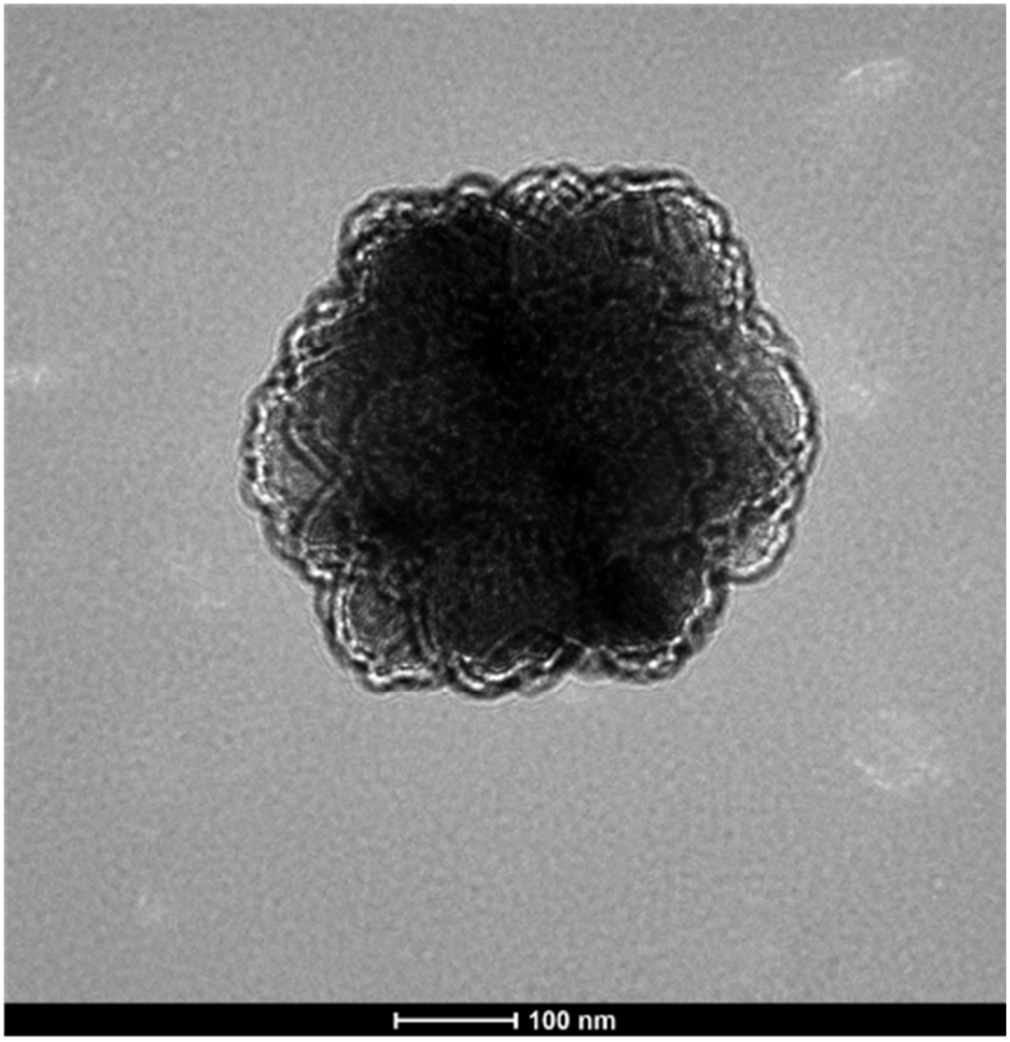

Figure 9.30: TEM images of MgF_2 nanofractals prepared from $Mg(NO_3)_2 \cdot 6H_2O$, BMIM[BF_4] ionic liquid, Milli-Q H_2O, Na_2HPO_4 via microwave synthesis (60 minutes dwell time, 100 bar, 150°C). Increase in dwell time to 60 minutes leads high crystallinity and more petals structures are visible.

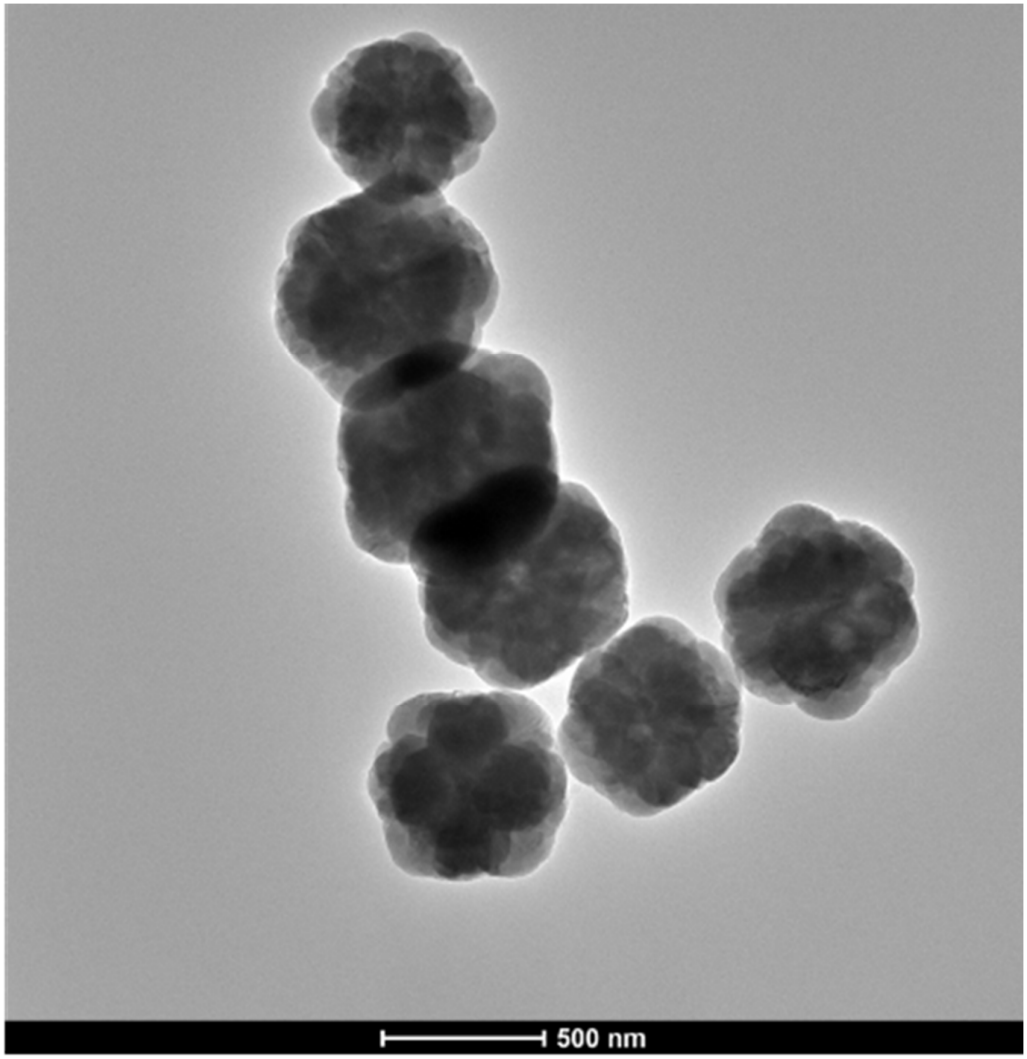

Figure 9.31: TEM images of MgF_2 beads prepared via autoclave hydrothermal setup with maximum pressure 3 Mpa instead of microwave synthesis at 90 minutes, the NPs size increases to 600 nm. The elongated petal structures are replaced with smooth curved edges.

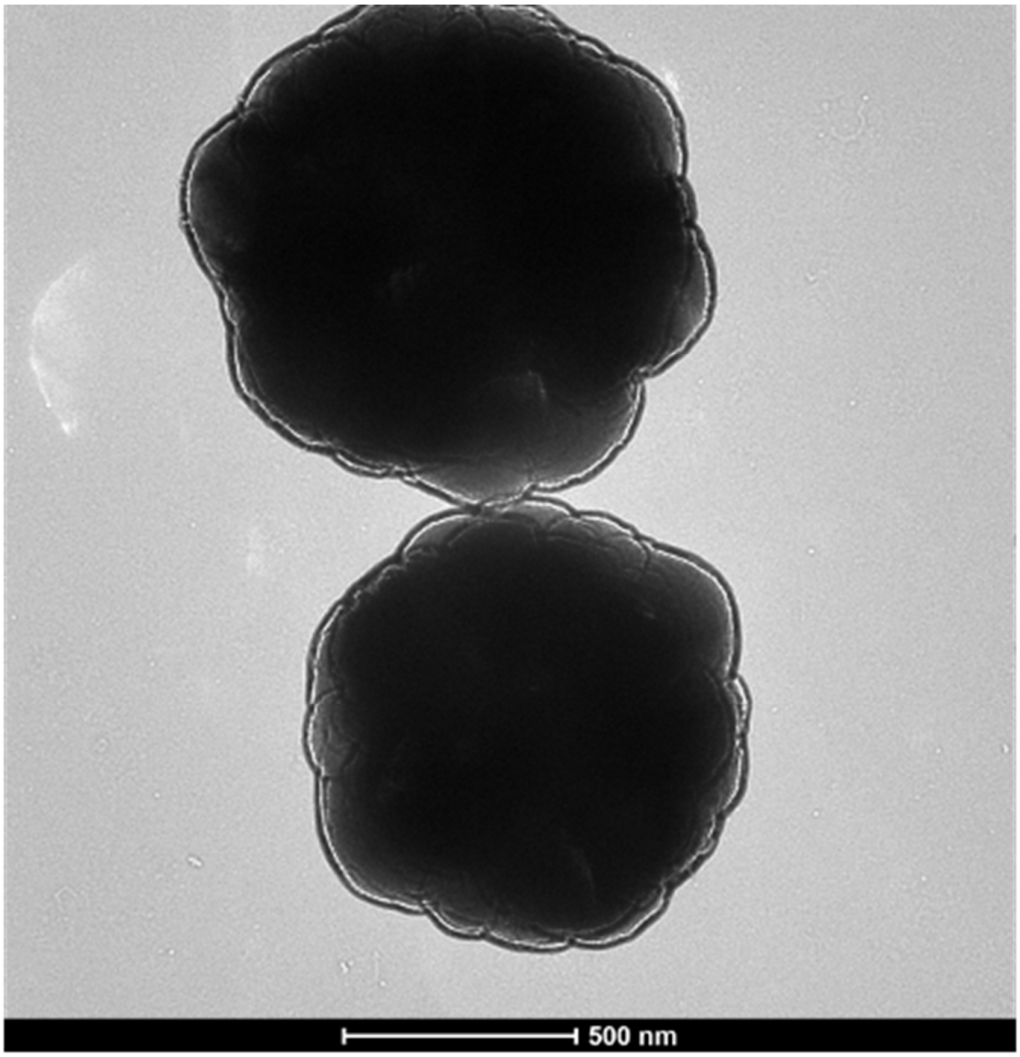

Figure 9.32: TEM images of MgF_2 beads prepared via autoclave hydrothermal setup with maximum pressure 3 Mpa instead of microwave synthesis at 90 minutes, the NPs size increases to 600 nm. The elongated petal structures are replaced with smooth curved edges.

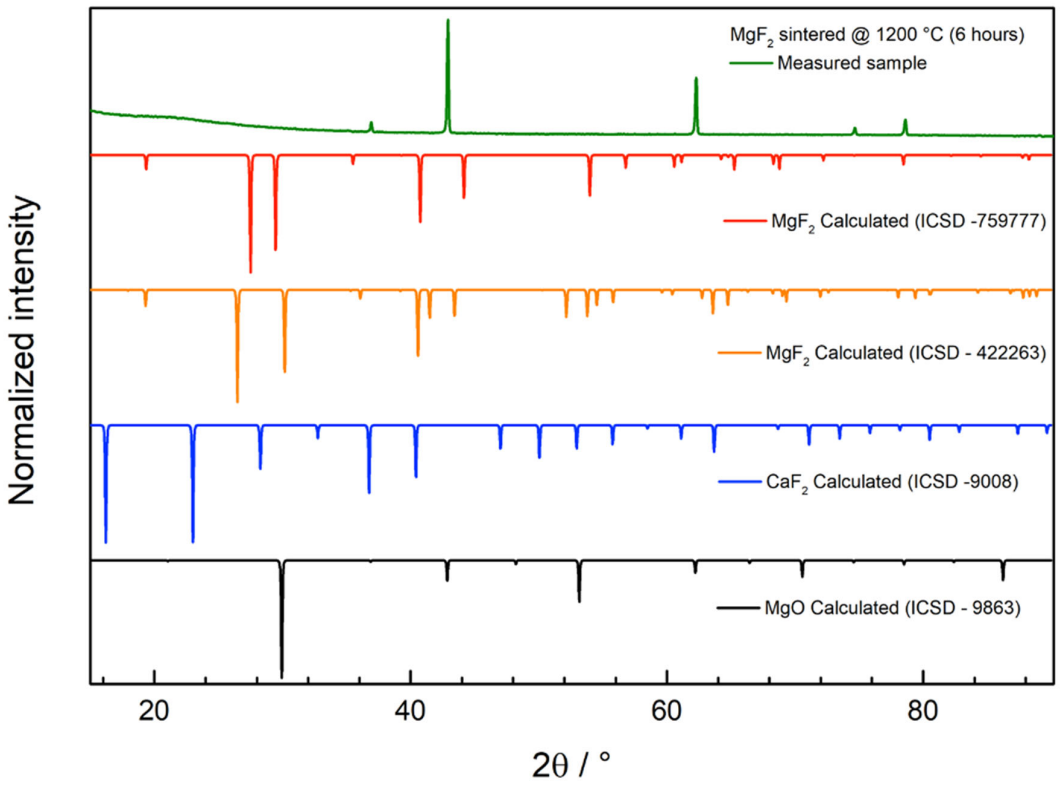

Figure 9.33: XRD of sintered MgF_2 beads at 1200°C for 6 h resulting in impurities that partially originate from oxyfluorides.

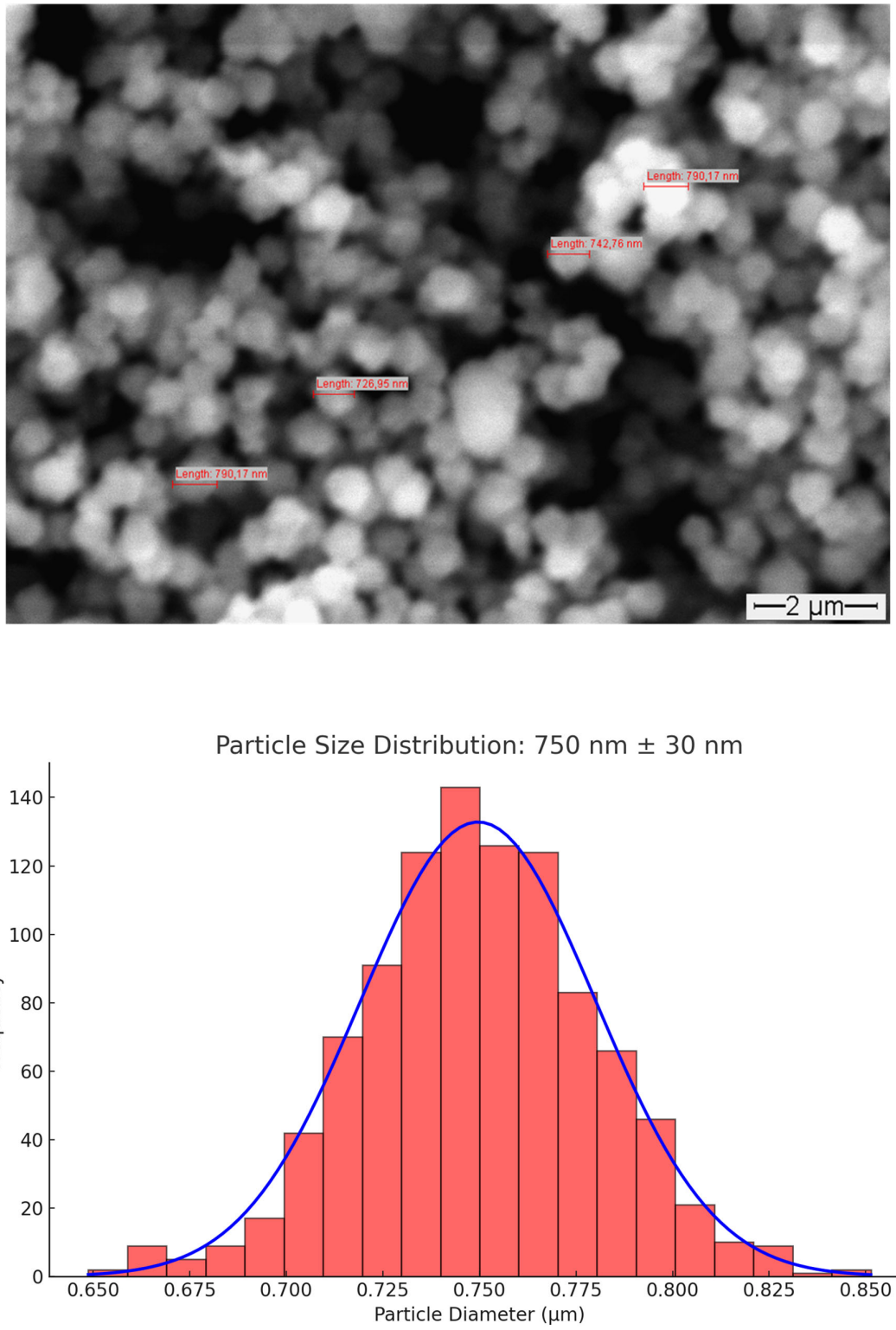

Figure 9.34: SEM image (top) after the 1st step of the synthesis of MgF_2 beads prepared via core shell synthesis using octadecene at 180°C for 24 h and (bottom) particle size distribution.

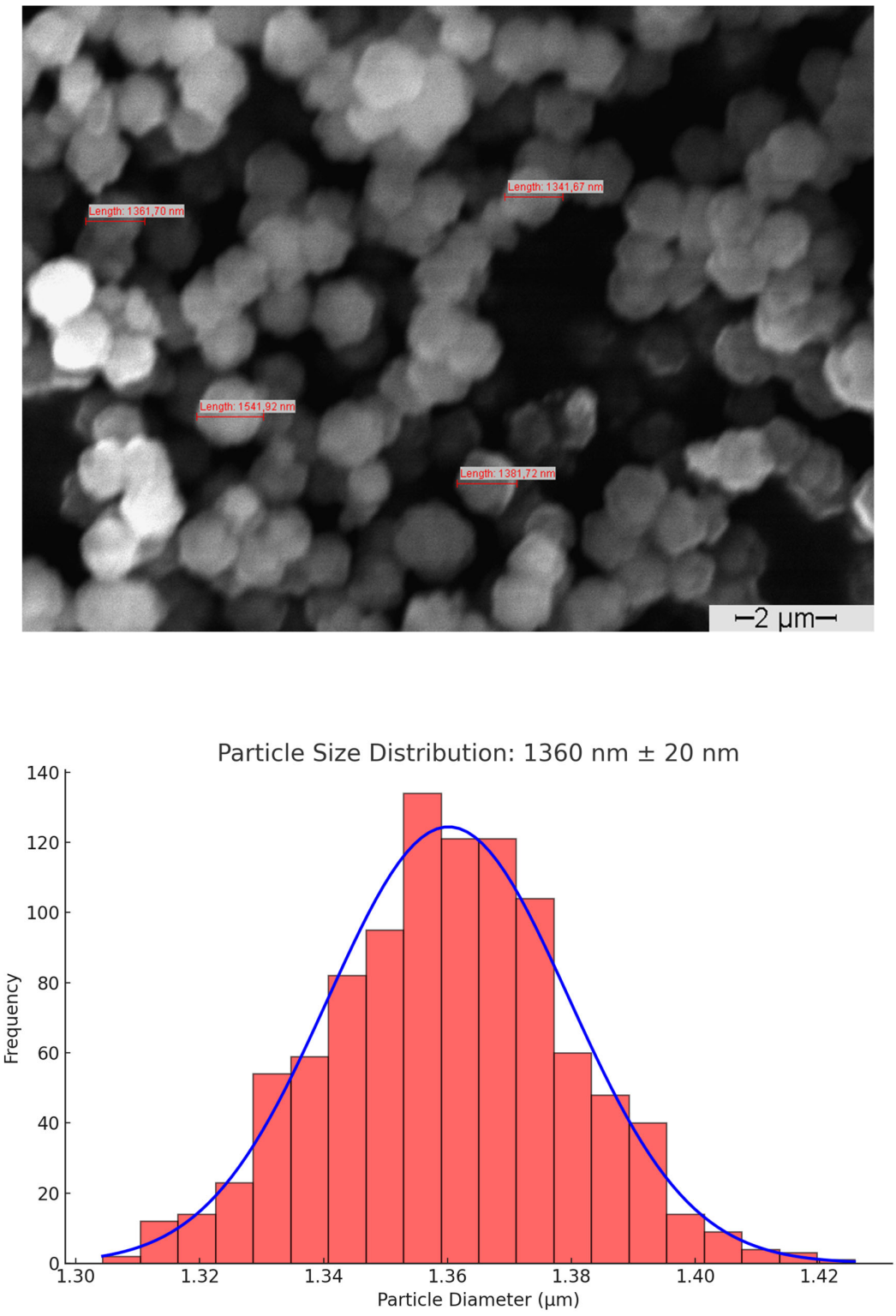

Figure 9.35: SEM image (top) after the 2nd step of the synthesis of MgF_2 beads prepared via core shell synthesis using octadecene at 180°C for 24 h and (bottom) particle size distribution.

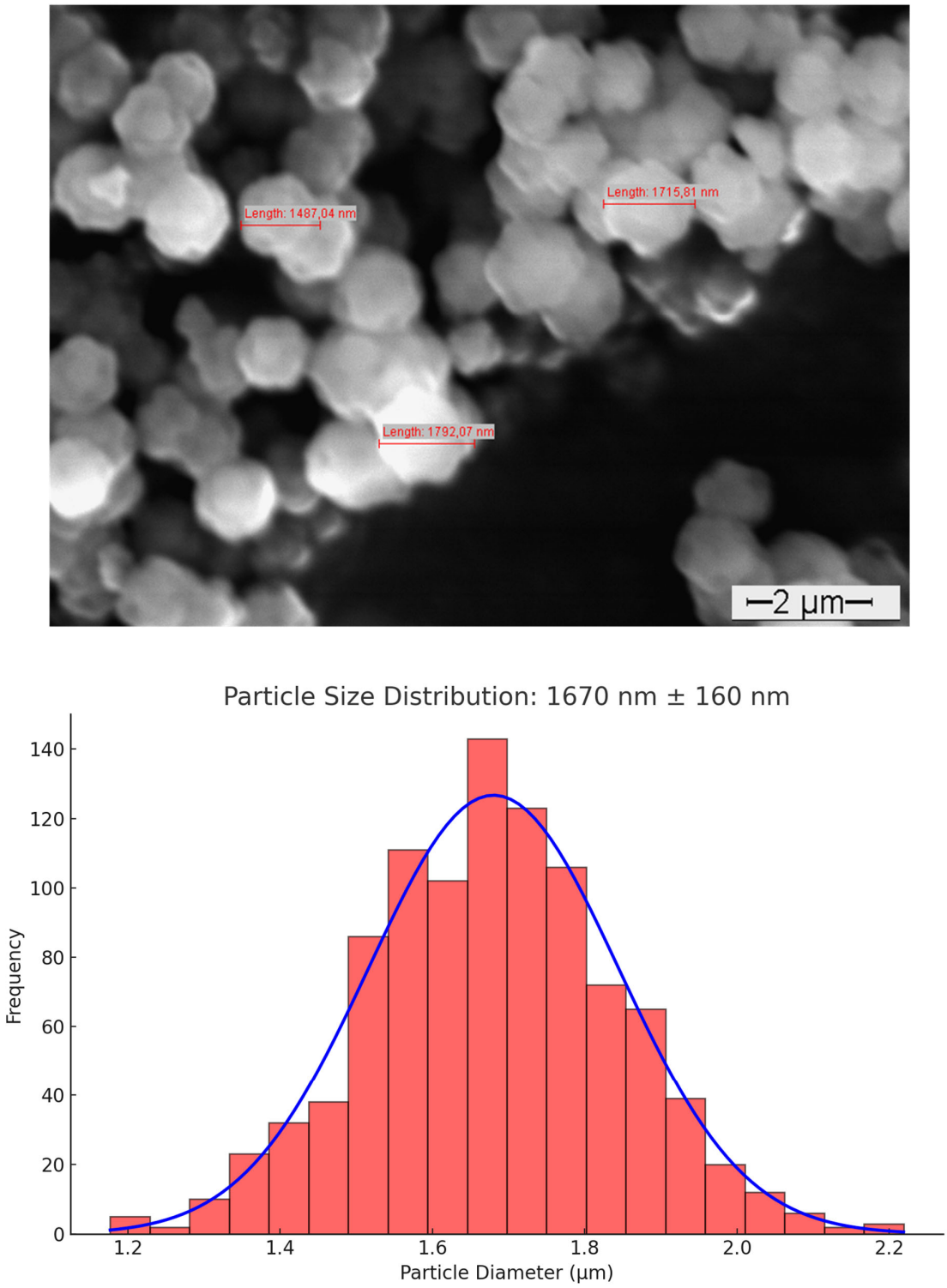

Figure 9.36: SEM image (top) after the 3rd step of the synthesis of MgF_2 beads prepared via core shell synthesis using octadecene at 180°C for 24 h and (bottom) particle size distribution.

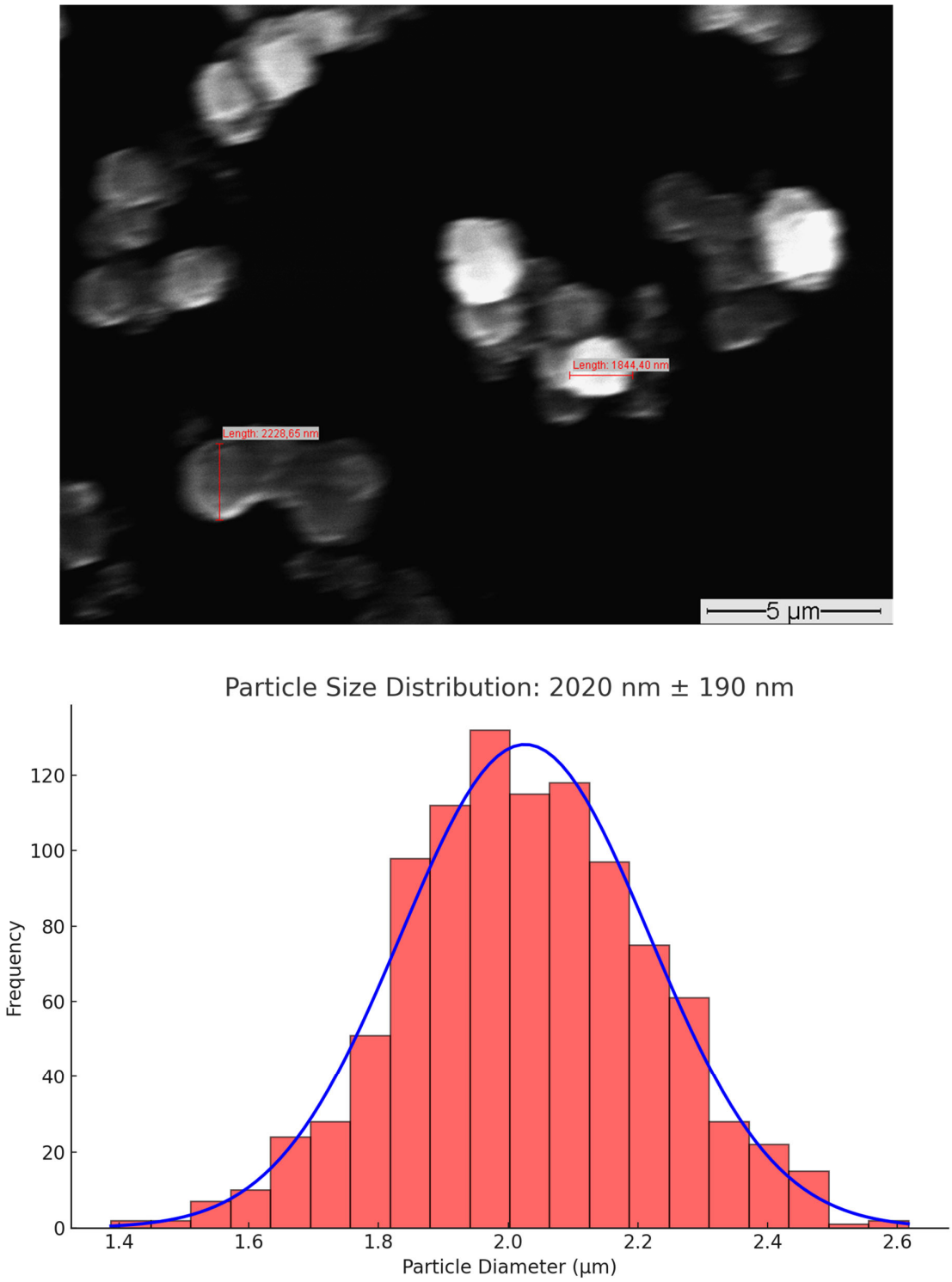

Figure 9.37: SEM image (top) after the 4th step of the synthesis of MgF_2 beads prepared via core shell synthesis using octadecene at 180°C for 24 h and (bottom) particle size distribution.

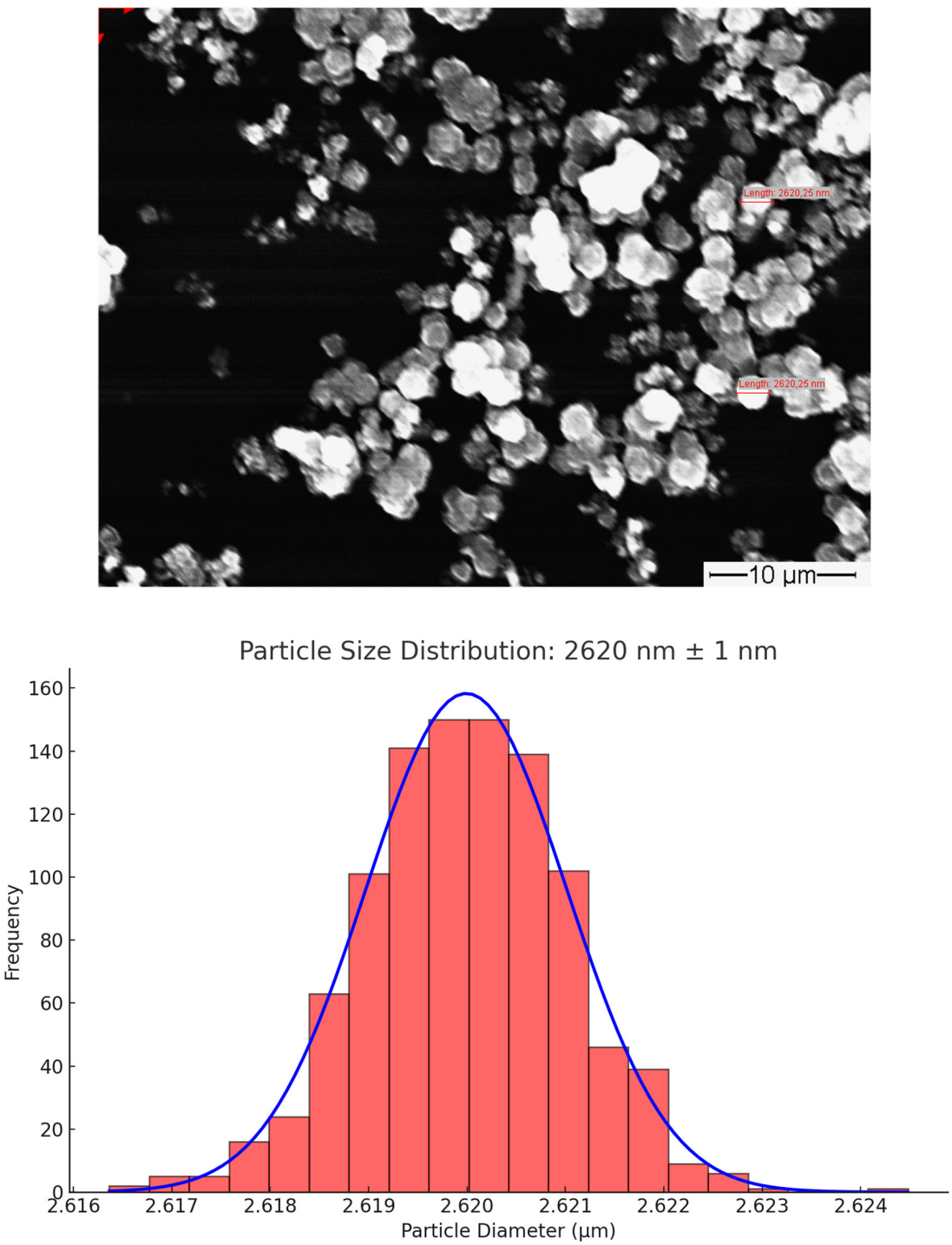

Figure 9.38: SEM image (top) after the 5th step of the synthesis of MgF_2 beads prepared via core shell synthesis using octadecene at 180°C for 24 h and (bottom) particle size distribution.

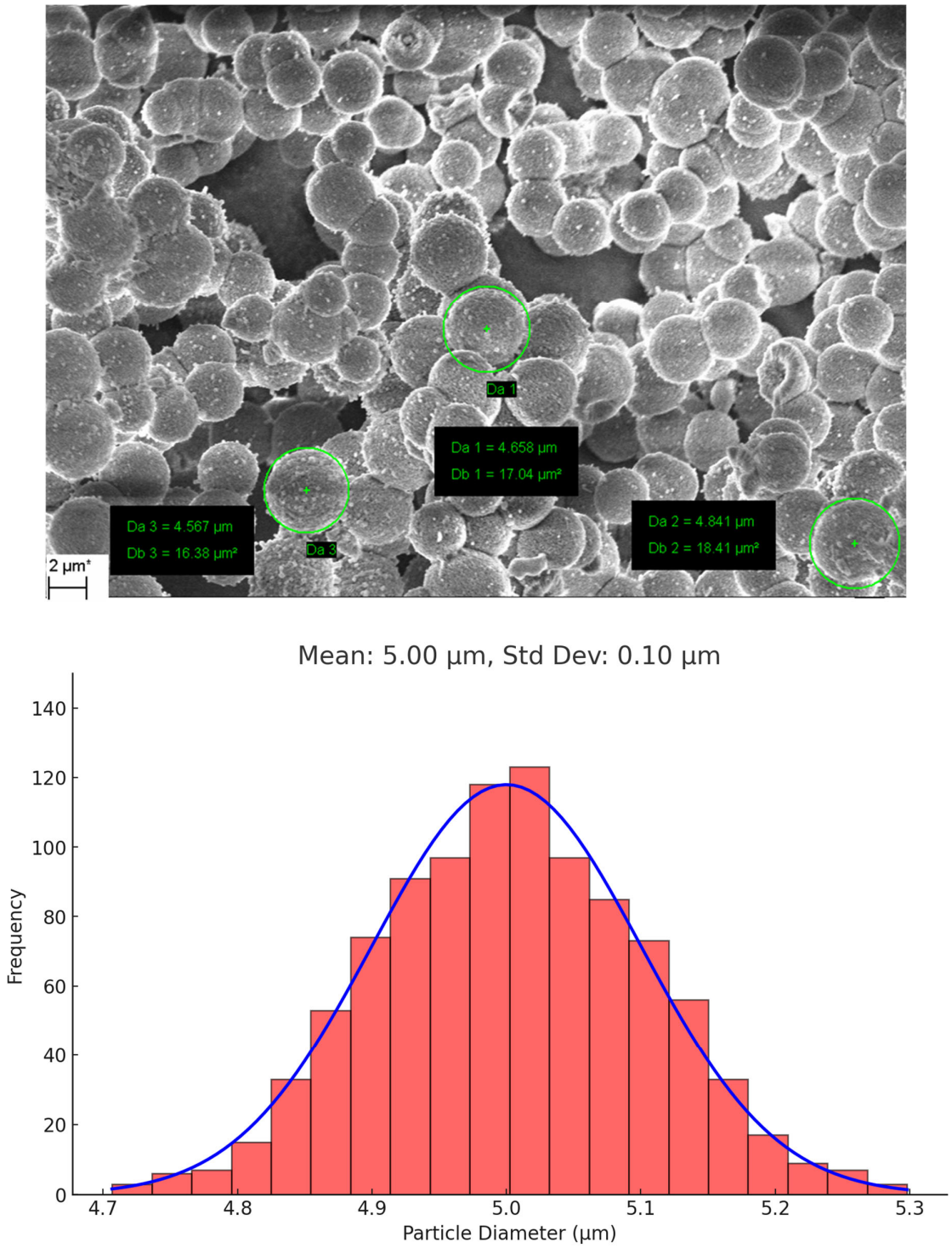

Figure 9.39: (Top) FESEM image of 5 µm MgF_2 beads prepared in an autoclave at 200°C and 30 bar for 4 days. (Bottom) – beads size distribution. The green circle shows the bead size and surface area in µm and μm^2 respectively.

VII SOP 4 – Bacteria culture *E. coli* MACH 1 T1^{R}.

Prepared and modified by PC I S1 & S2 Labs.

Overnight culture preparation and analysis

Preparation of LB-Agar Plates (with or without ampicillin)

1. Fill Duran bottles with LB Agar.
    - Perform at RT in cell lab or S2 lab
    - Corresponding amounts are written on the package, e.g. weigh 12.5 g LB media powder (Roth) in flask and make the volume up to 500 mL with Milli Q water.
2. Autoclave the agar (can be kept in fluid state in the incubator at 45°C).
3. Cool down the agar (~ 45-50°C, so that you can touch it) and add if needed a suitable amount of antibiotics
    - e.g. for 100 µg/ml Ampicillin: dilute the stock solution (100 mg/ml, aliquots in the – 20°C freezer (bacteria or cell lab)) 1/1000 in LB Agar. Mix.
4. Pour 15-20 mL (~ 0.5 cm height) agar in the prepared petri dishes (sterile petri dishes found in bacteria lab).
5. Let the agar harden under sterile conditions, leaving the lid slightly open to prevent condensation.
6. After hardening, store the agar plates in a sterile plastic bag in the fridge.

Preparation of overnight culture

1. Clean the work bench with Bacillol AF
2. Label 2 cell culture tubes with initials and date. On 1 write the bacteria name, and on the other write control.
3. Pipette 5 mL LB-media in each cell culture tube.
4. Pick 1 colony with a sterile loop from the culture plate and transfer it to the corresponding cell culture tube.
5. Shake the loop slightly.
6. Vortex the tube for a few seconds, without completely tightening the lid.
7. Place both tubes in the shaker at 200 rpm at the required temperature for 16 h -18 h.

8. After 16-18 h, remove the tubes.
    - A turbid solution indicates the growth of the bacteria.

Analysis of overnight culture (ONC)

Optical density (OD) measurements

1. Turn on the spectrophotometer 30 mins prior to measurement.
2. Fill a cuvette with 1 mL LB medium. This is the blank.
3. Fill a second cuvette with 1ml ONC solution.
4. Place the blank cuvette in the spectrophotometer.
5. Close the lid and press the blank button. After the measurement, take the cuvette out.
6. Place the ONC cuvette in the spectrophotometer.
7. Close the lid and record the OD.
    - An OD between 0.2 and 0.8 is acceptable.
    - If OD<0.2, leave the bacteria to grow for a few hours.
    - If OD>0.8, the ONC requires dilution.

Colony forming unit (CFU) analysis

For CFU counting, different concentrations of the overnight culture are made by serial dilution of the overnight culture with PBS:

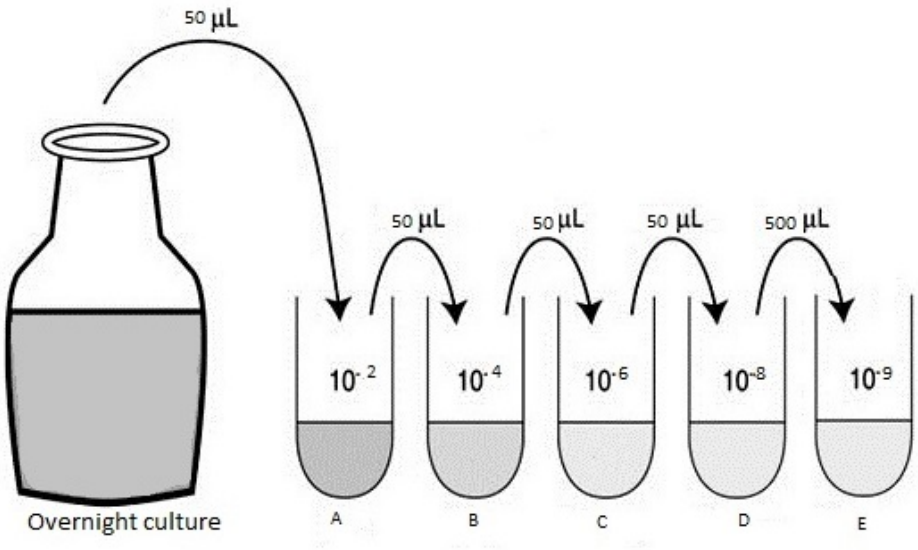

1. On the back of an LB agar plate, draw a cross to divide the plate into four equal parts.
2. Label the required number of tubes (red caps) with the dilution factor on the lid and on the side.
3. Fill all tubes with PBS. For 1 in 100 dilutions (can be performed at the higher concentrations), add 5 mL PBS. For 1 in 10 dilutions (necessary for lower concentrations), add 4.5 mL PBS.
4. Pipette 0.05 mL (i.e. 50 µL) initial bacteria suspension into the first tube. This is the 10^{-2} sample.
5. Discard of the pipette tip.
6. Vortex the sample.
7. Pipette 0.05 mL (i.e. 50 µL) of the 10^{-2} sample into the next tube. This is the 10^{-4} sample.
8. Discard of the pipette tip.
9. Vortex the sample.
10. Continue with 1 in 100 dilutions until required concentration is reached.
11. For a 1 in 10 dilution, take 0.5 mL (i.e. 500 µL) previous mixture and put it into 4.5 mL PBS.
12. Continue until required concentration reached.
13. Once the serial dilution is complete, the dilutions must be plated.
    a. For each dilution, take up 50 µL into a pipette, and dispense it onto a quarter of the labelled plate in 3 drops.
    b. For example, if the CFU is known to be around 10^{8}, plate 10^{-6}, 10^{-7}, 10^{-8}, 10^{-9}.
    c. It may be necessary to also plate pure PBS to check for sterility.
    d. For each dilution required, it should be plated twice, e.g.:

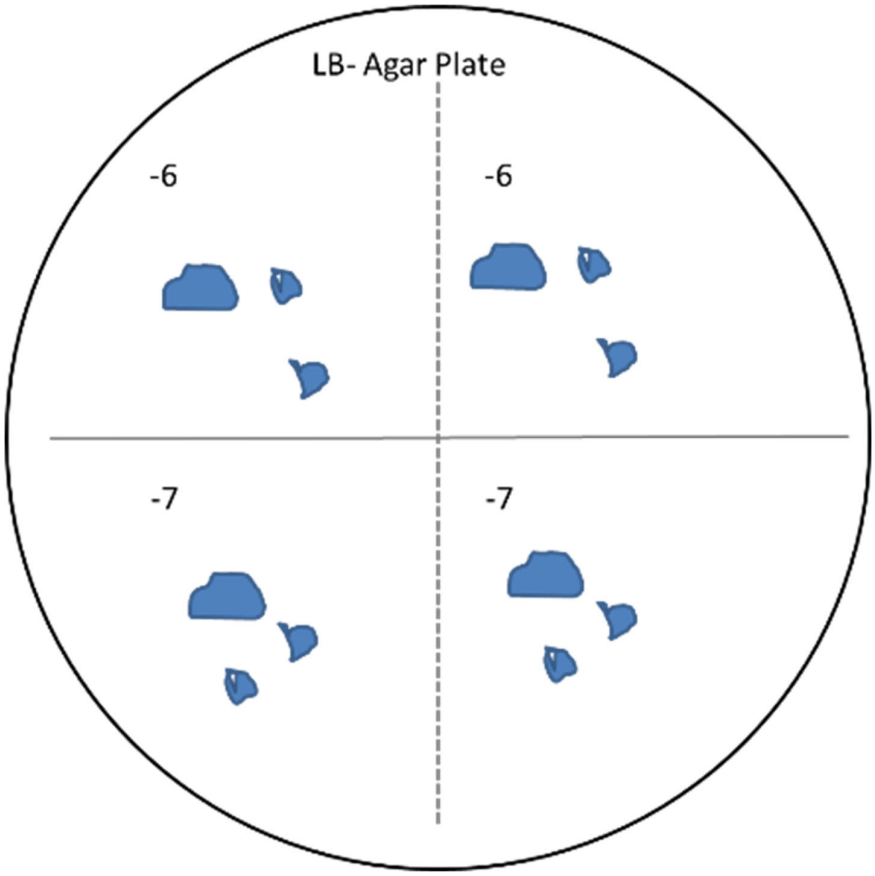

14. Incubate the plates at 37°C for 1 day (or *P.fluorescens* at 28°C for 2 days
15. After incubation, count the number of individual colonies in each quarter.
16. To calculate the CFU per mL: multiply the number of colonies by 20 (to convert from 50 µL to 1 mL) then multiply by the concentration

    E.g.: 32 individual colonies are counted at a concentration of 10^{-6}

    CFU = 32 x 20 x 10^{6} = 64 x 10^{8} / mL

VIII DHM microscope imaging.

Measurement done at BMTZ University of Münster.

The DHM microscope used enables:

- Bright field microscopy
- Quantitative phase contrast microscopy (QPI: Quantitative Phase Imaging)
- “Advanced QPI” by acquiring multiple QPI images under modulated illumination

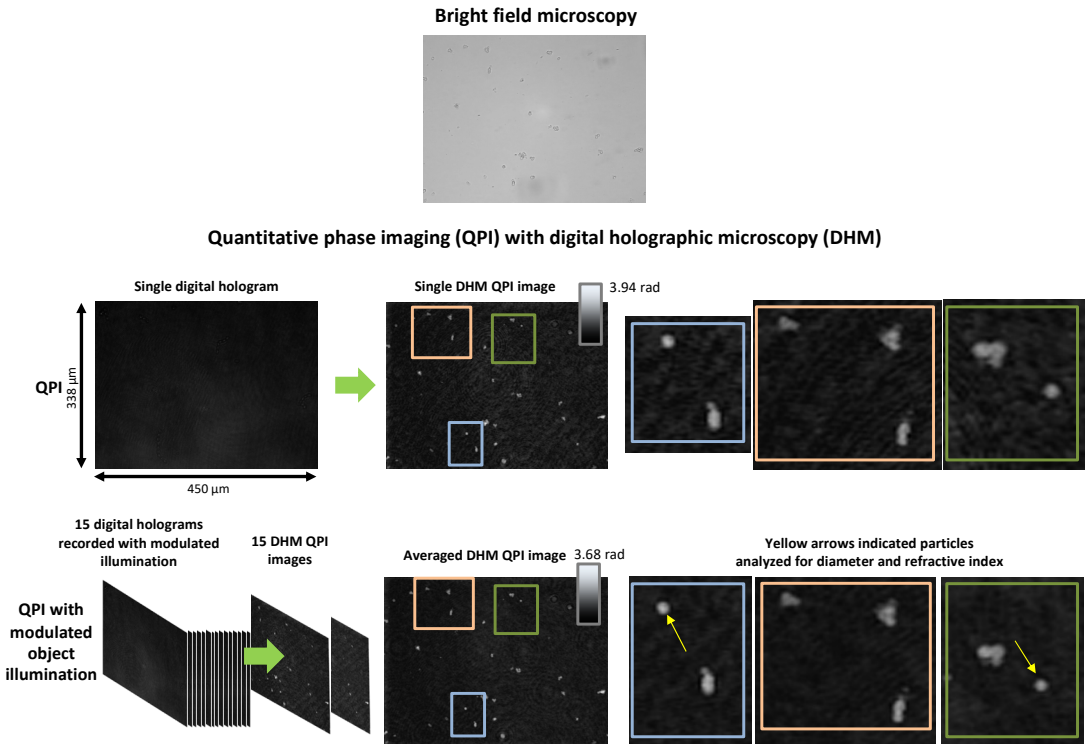

Figure: 9.40: Illustration of brightfield imaging and QPI, with DHM. For each measurement one bright-field image and N=15 digital off-axis holograms are captured while the object illumination is modulated in amplitude and phase by an electrically focus tunable lens. The reconstruction of QPI images was performed automated with a previously reported evaluation procedure. Reduction of coherence induced QPI image disturbances was achieved by subsequently averaging of the retrieved series of quantitative phase images.

IX MgF_2 beads Tomographic Phase Microscopy.

Measurement done at BMTZ University of Münster.

Refractive index 1.360 ± 0.004 (N=5), Diameter 5. 50365 µm (N=5)

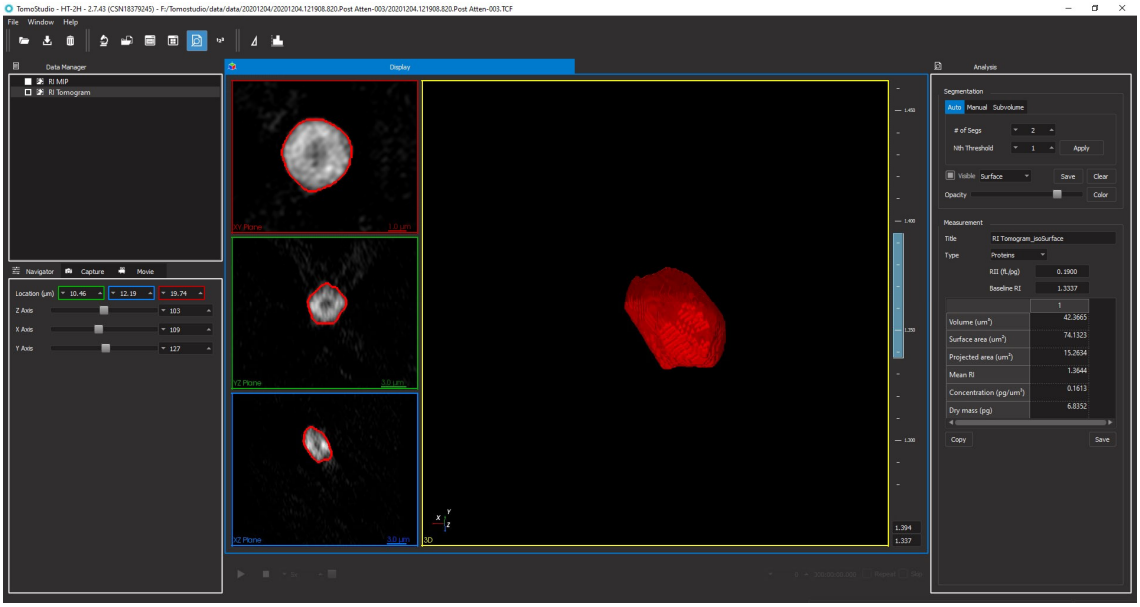

Figure 9.41: Tomographic phase microscopy of MgF_2 beads prepared in an autoclave at 200°C and for 4 days. Displayed are cross-section planes through a representative measured refractive index (RI) tomogram and a rendered 3D representation of the retrieved RI tomogram. The images of the XY, YZ, and XZ planes highlight the microparticle's dimensions and morphology. The measurement data on the right panel include the volume (42.4 µm³), surface area (74.1 µm²), projected area (15.3 µm²) and the mean refractive index (1.364).

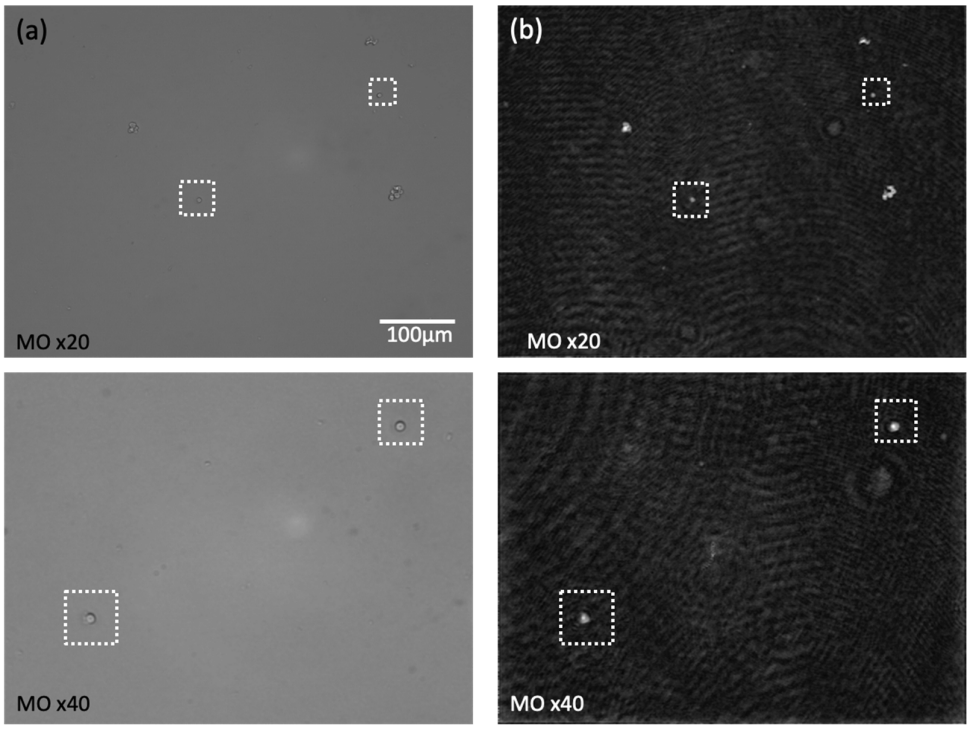

Figure 9.42: Comparison of Imaging Techniques done for MgF_2 beads prepared in an autoclave at 200°C and for 4 days: Brightfield Microscopy vs. Quantitative Phase Imaging (QPI) at Different Magnifications. (a) Brightfield microscopy images at 20x and 40x magnifications. (b) Corresponding QPI images at 20x and 40x magnifications. The dashed squares highlight regions of interest, demonstrating enhanced detail and contrast in QPI images compared to brightfield microscopy.

X STEM-EDX images of functionalized MgF_2 beads with PDEGM-*block*-PAA.

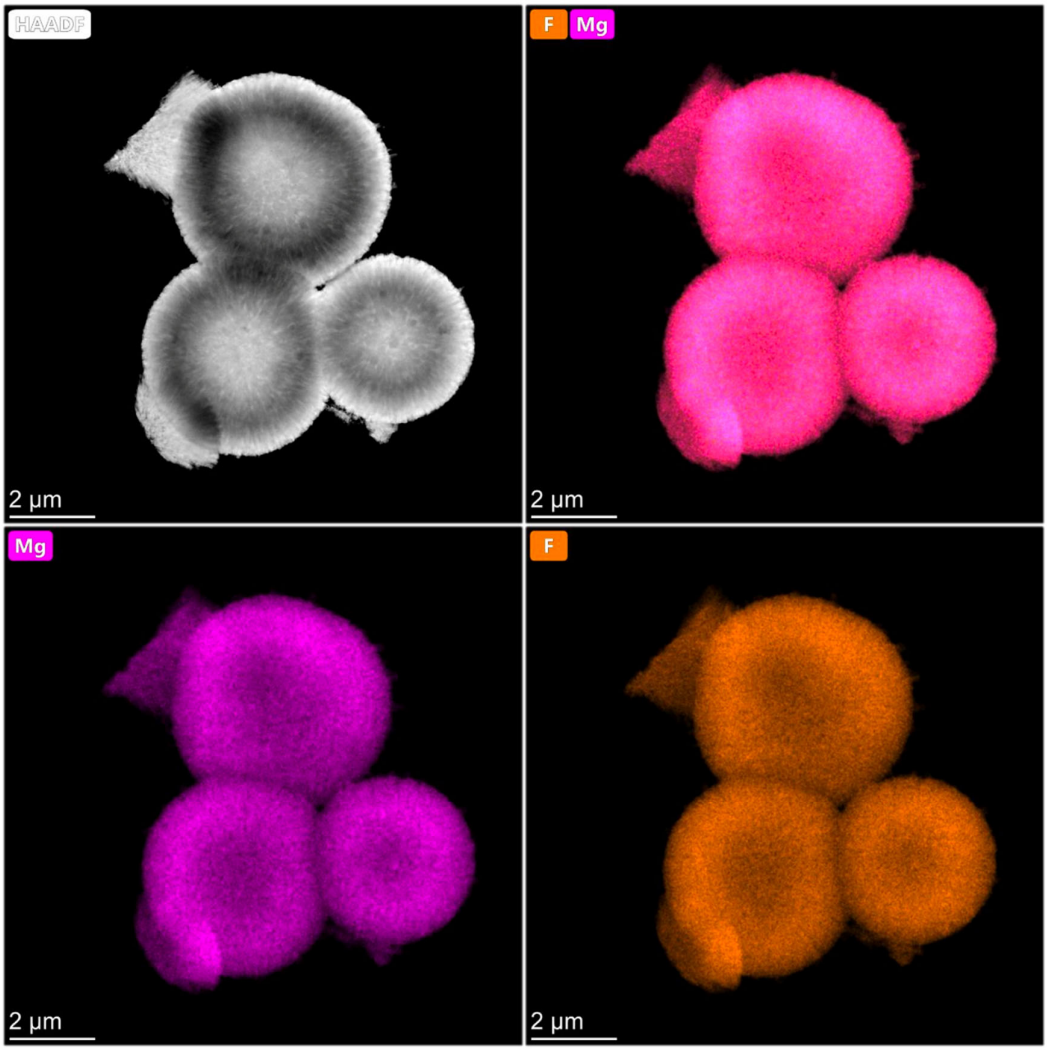

Figure 9.43: High-Angle Annular Dark Field (HAADF) and Elemental Mapping of bare MgF_2 beads: Top-left: HAADF image showing structural details of MgF_2 beads. Top-right: Elemental map highlighting the distribution of Fluorine (F) and Magnesium (Mg). Bottom-left: Elemental map showing the distribution of Magnesium (Mg). Bottom-right: Elemental map showing the distribution of Fluorine (F). Each image provides a 2 µm scale bar for reference, demonstrating the spatial distribution of elements within the MgF_2 beads.

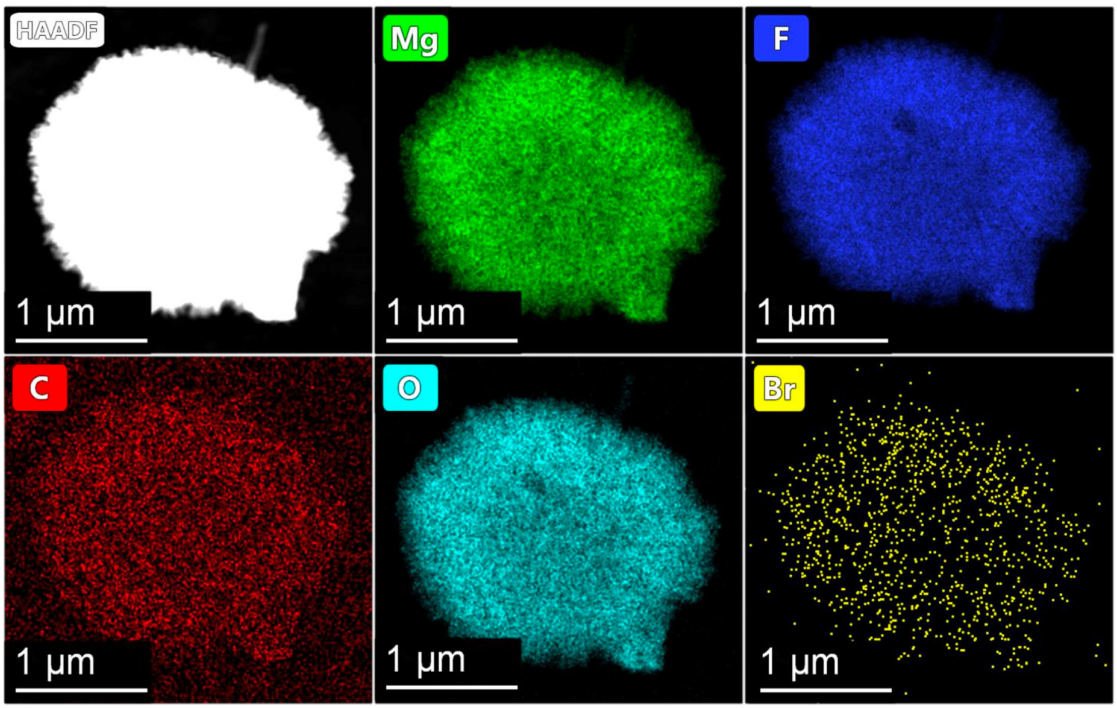

Figure 9.44: HAADF and Elemental Mapping of a MgF_2@MUBiB beads: Top-left: HAADF image showing the overall structure of the MgF_2@MUBiB beads. Top-middle: Elemental map showing the distribution of Magnesium (Mg) in green. Top-right: Elemental map showing the distribution of Fluorine (F) in blue. Bottom-left: Elemental map showing the distribution of Carbon (C) in red. Bottom-middle: Elemental map showing the distribution of Oxygen (O) in cyan. Bottom-right: Elemental map showing the distribution of Bromine (Br) in yellow. Each image includes a 1 µm scale bar, illustrating the spatial distribution of each element within the MgF_2@MUBiB beads.

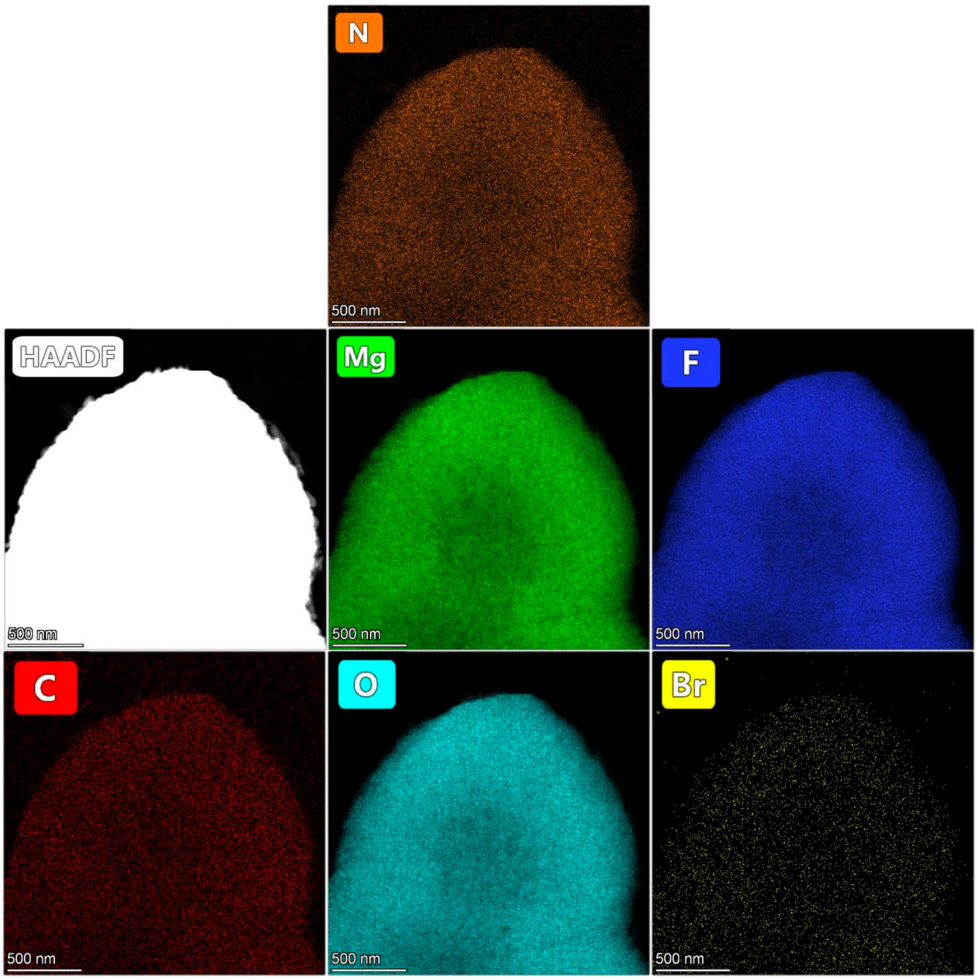

Figure 9.45: HAADF and Elemental Mapping of a MgF_2@PDEGMA-*block*-PAA coated beads: Top row: Elemental maps showing the distribution of Nitrogen (N) in orange, Magnesium (Mg) in green, and Fluorine (F) in blue. Bottom row: HAADF image (left) depicting the MgF_2@PDEGMA-*block*-PAA coated bead's overall structure, and elemental maps showing the distribution of Carbon (C) in red, Oxygen (O) in cyan, and Bromine (Br) in yellow. Each image includes a 500 nm scale bar, providing a detailed spatial distribution of each element within the MgF_2@PDEGMA-*block*-PAA coated beads.

XI Monitoring bacteria growth in the presence of MgF_2 nanowhiskers.

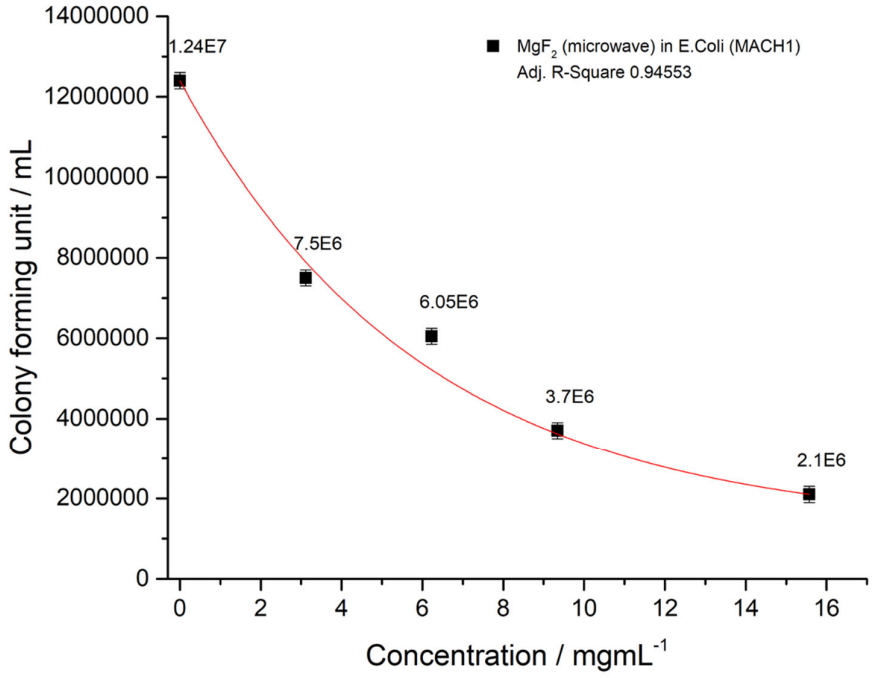

Figure 9.46: Effect of MgF_2 nanowhiskers (prepared in the microwave at 100°C and 100 bar pressure using 5 minutes dwell time) on *E. coli* MACH 1 $T1^R$ Growth: Colony Forming Units per mL vs. Concentration ($mgmL^{-1}$). The graph shows a decreasing trend in the number of colony forming units with increasing MgF_2 concentration, with an adjusted R-square value of 0.94553, indicating a strong fit of the model to the data.

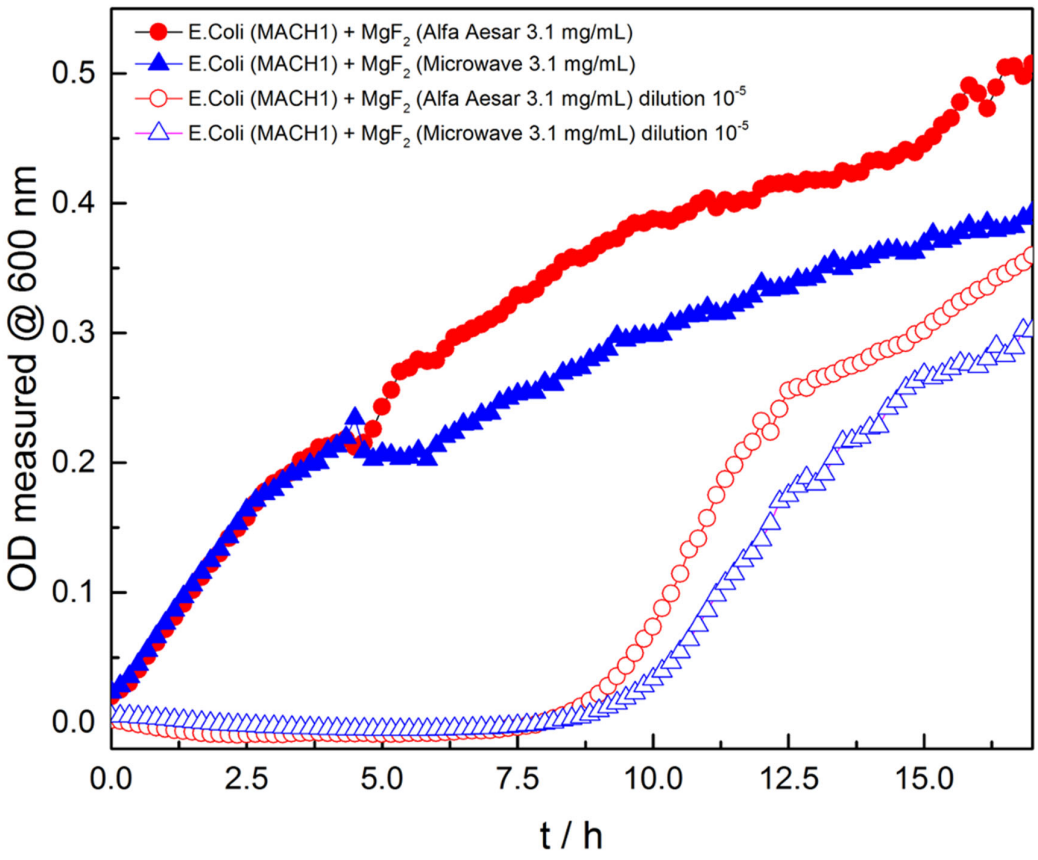

Figure 9.47: Growth Curves of *E. coli* MACH 1 $T1^R$ with MgF_2 nanowhiskers (prepared in the microwave at 100°C and 100 bar pressure using 5 min dwell time) and MgF_2 purchased from Alfa Aesar: Optical Density at 600 nm over time. The graph compares the growth of *E. coli* MACH 1 $T1^R$ with MgF_2 sourced from Alfa Aesar and microwave-assisted synthesis at a concentration of 3.1 mg/mL. Different initial optical densities (OD = 0.5 and a dilution of 10^{-5}) were tested. The growth patterns indicate varying effects of the two MgF_2 sources and initial concentrations on bacterial growth over a 16-h period.

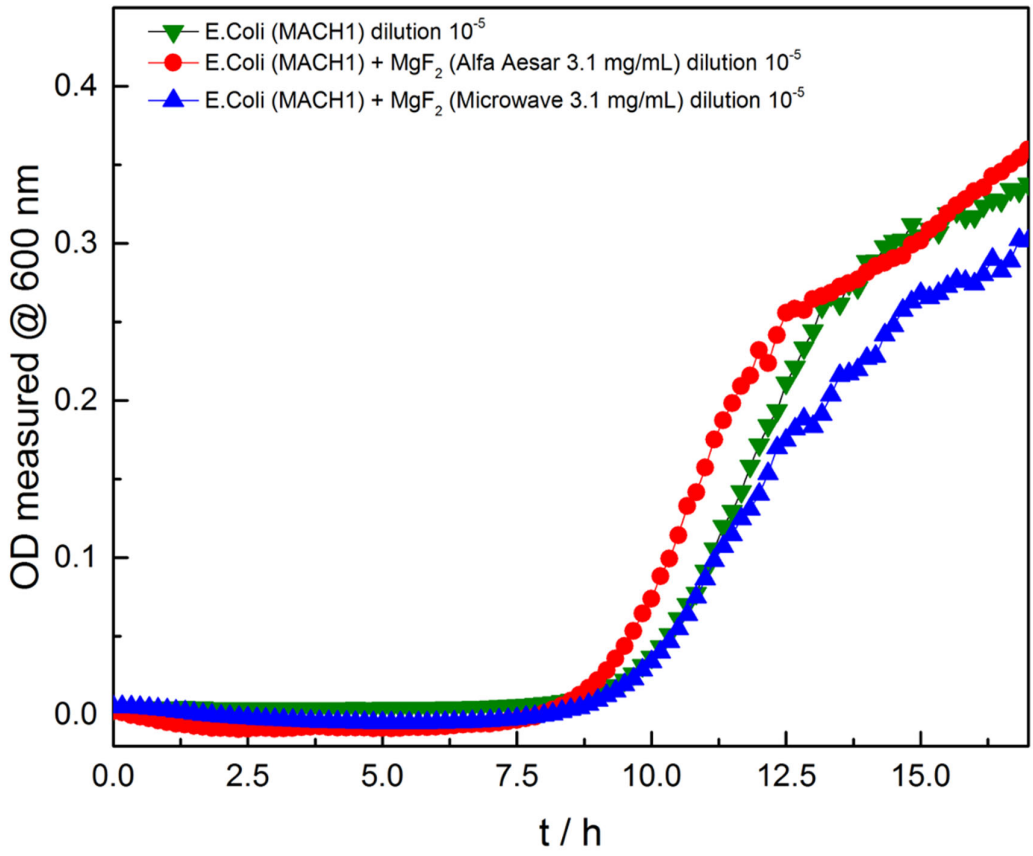

Figure 9.48: Growth Curves of *E. coli* MACH 1 $T1^R$ with MgF_2 nanowhiskers (prepared in the microwave at 100°C and 100 bar pressure using 5 min dwell time) and MgF_2 purchased from Alfa Aesar and without MgF_2: Optical Density at 600 nm Over Time. The graph shows the growth of *E. coli* MACH 1 $T1^R$ diluted to 10^{-5} with MgF_2 from Alfa Aesar and microwave synthesis, both at a concentration of 3.1 mg/mL.
It highlights the differences in growth rates and overall optical density over an 18-h period, demonstrating the effects of different MgF_2 sources on *E. coli* MACH 1 $T1^R$ growth.

XII TGA data for MgF_2, MgF_2@MUBiB and MgF_2@PDEGMA-*b*-PAA

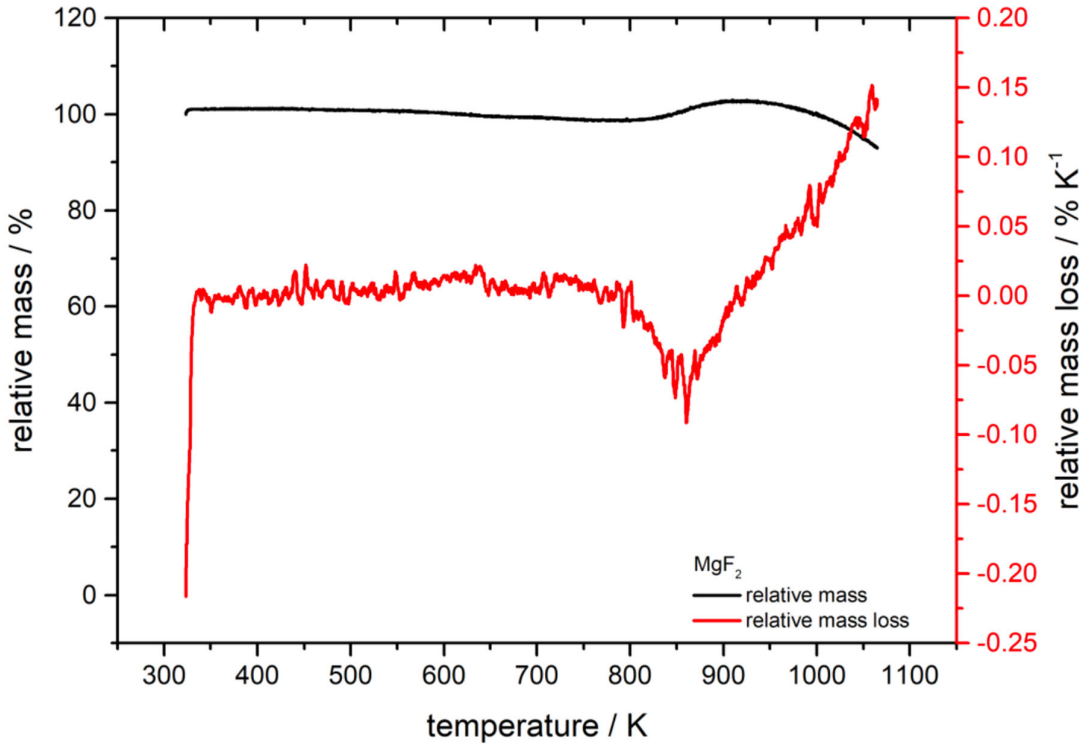

Figure 9.49: TGA and differential thermal analysis DTA of MgF_2. The graph illustrates the relative mass (black line) and relative mass loss (red line) as functions of temperature, ranging from 300 K to 1100 K. The analysis reveals stability in the mass of MgF_2 up to approximately 900 K, followed by a noticeable mass loss at higher temperatures, indicating thermal decomposition or volatilization processes.

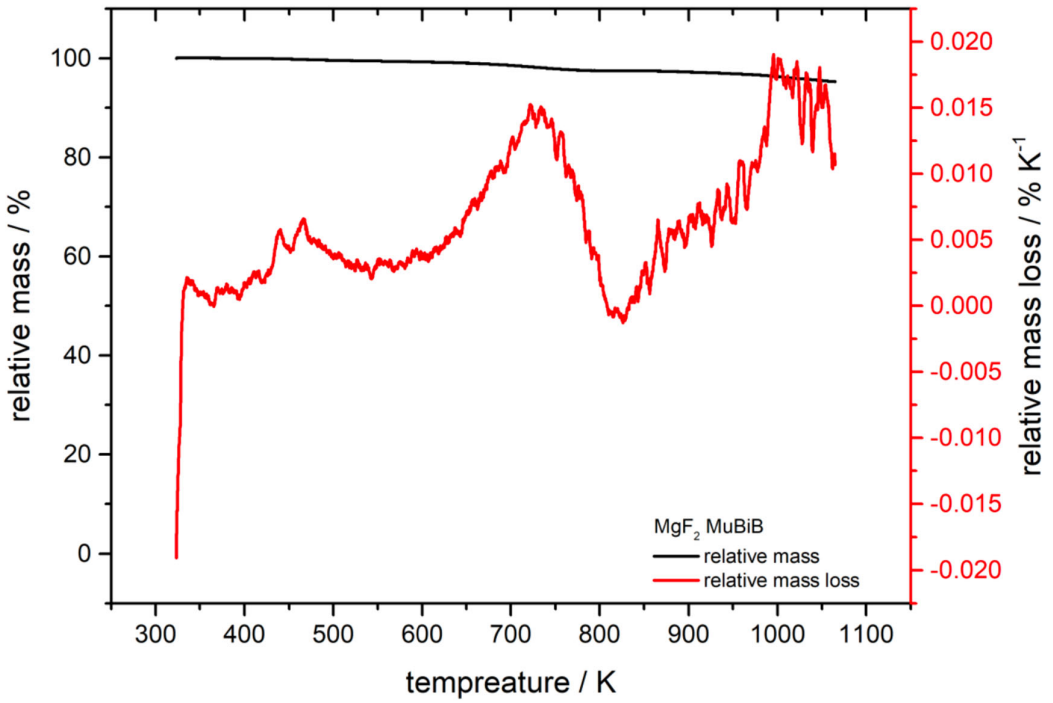

Figure 9.50: TGA and DTA of MgF_2@MUBiB beads. The graph illustrates the relative mass (black line) and relative mass loss (red line) as functions of temperature, ranging from 300 K to 1100 K. The MgF_2@MUBiB beads exhibits a significant mass loss around 700 K, which may indicate thermal decomposition or reactions involving MUBiB. The data reveal distinct thermal stability and decomposition behavior of the MgF_2@MUBiB beads compared to pure MgF_2 beads.

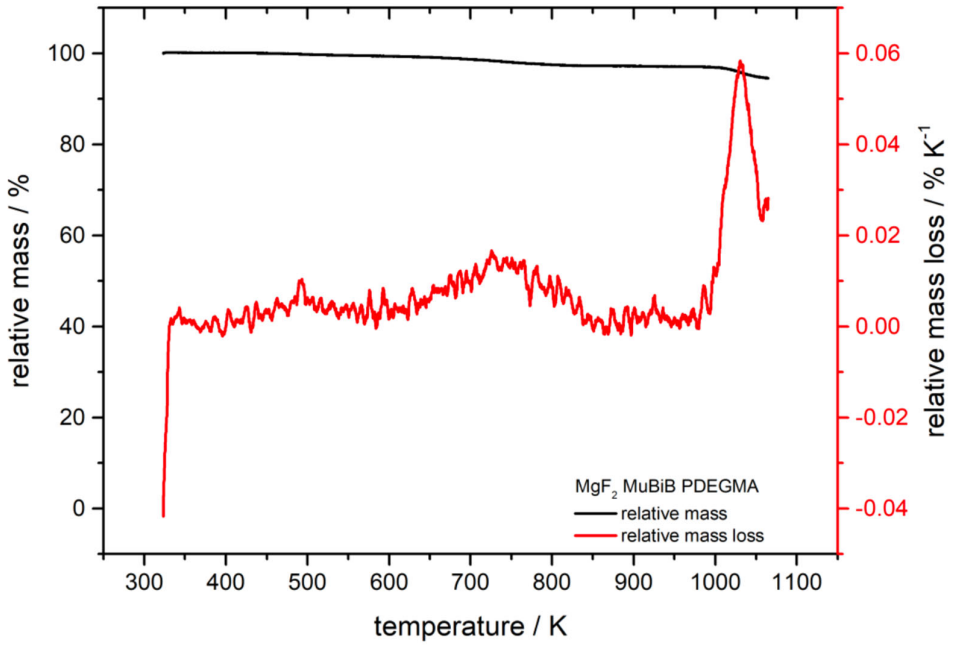

Figure 9.51: TGA and DTA of the MgF_2@PDEGMA beads. The graph shows the relative mass (black line) and relative mass loss (red line) as a function of temperature, ranging from 300 K to 1100 K. The MgF_2@PDEGMA beads exhibit significant thermal events around 700 K and 1050 K, indicating complex decomposition behavior or interactions among MgF_2 and PDEGMA. The sharp increase in mass loss around 1050 K suggests a major thermal degradation or volatilization event.

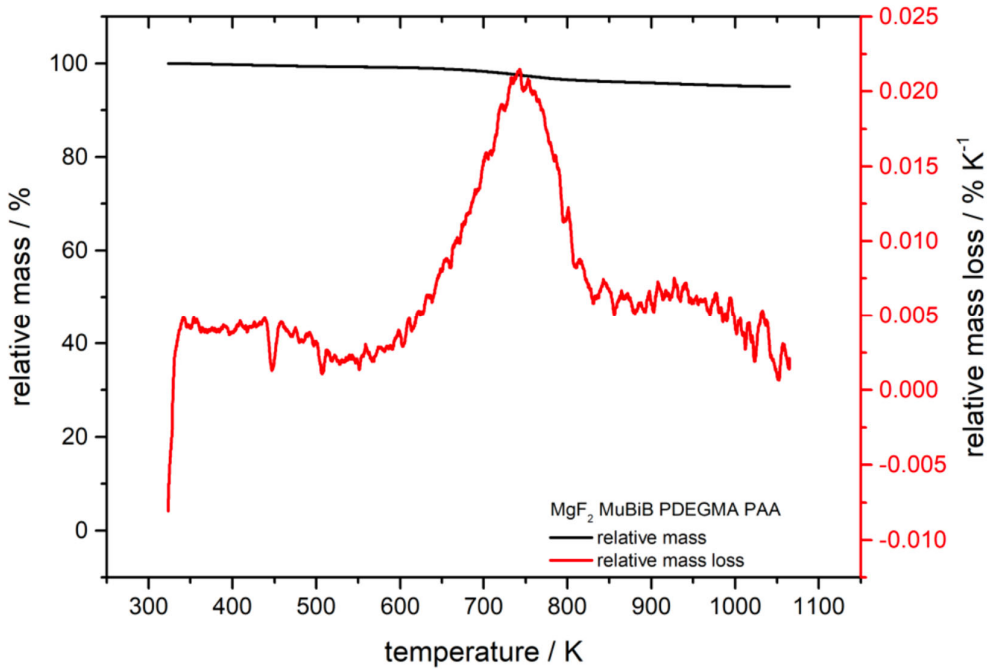

Figure 9.52: TGA and DTA of the MgF_2@PDEGMA-*b*-PAA beads. The graph presents the relative mass (black line) and relative mass loss (red line) as a function of temperature, from 300 K to 1100 K. The MgF_2@PDEGMA-*b*-PAA beads show significant thermal events, particularly around 700 K, where a peak in mass loss is observed.